



**Universidade do Minho**  
Escola de Ciências

Ana Sofia de Sousa Glória e Valadares Souto

**SEDEX heritage in tungsten-gold *skarn* deposits of Serra de Arga metamorphic suite – structural and paragenetical analysis of sulfide-rich calc-silicate rocks and its mineralizations**



**Universidade do Minho**  
Escola de Ciências

Ana Sofia de Sousa Glória e Valadares Souto

**SEDEX heritage in tungsten-gold *skarn*  
deposits of Serra de Arga metamorphic  
suite – structural and paragenetical  
analysis of sulfide-rich calc-silicate rocks  
and its mineralizations**

Master Dissertation  
Master in Geosciences – Valorisation of Geological Resources

Work developed under supervision of  
**Professor Doctor Carlos Augusto Alves Leal Gomes**  
**Professor Doctor Wolfgang Bach**

## **DIREITOS DE AUTOR E CONDIÇÕES DE UTILIZAÇÃO DO TRABALHO POR TERCEIROS**

Este é um trabalho académico que pode ser utilizado por terceiros desde que respeitadas as regras e boas práticas internacionalmente aceites, no que concerne aos direitos de autor e direitos conexos.

Assim, o presente trabalho pode ser utilizado nos termos previstos na licença abaixo indicada.

Caso o utilizador necessite de permissão para poder fazer um uso do trabalho em condições não previstas no licenciamento indicado, deverá contactar o autor, através do RepositóriUM da Universidade do Minho.

### ***Licença concedida aos utilizadores deste trabalho***



**Atribuição**

**CC BY**

<https://creativecommons.org/licenses/by/4.0/>

## ACKNOWLEDGEMENTS

I am very grateful to Professor Doctor C. Leal Gomes for the opportunity to develop this work, and learning experience and Professor Doctor W. Bach for allowing me to learn with him and to have the experience of working in a high tech laboratory of University of Bremen.

Doctor Patrick Monien and Mr. Stefan Sopke for the explanations and help during the procedures and measurements.

To Erasmus program that allowed me to stay in Bremen with its scholarship. And to Professor Doctor Pedro Pimenta and Mrs. Ulrike Wolf-Brozio for their collaboration during the arrangement.

To my *pillows* for their encouragement! And also to some great friends I did while in Bremen.

Although I thank to all the people before, there is no way this work would have come through without my parents and siblings. For being such inspiring and hardworking people that do so well on their jobs as their lives. To my parents and siblings I devote the complete thesis. To my father for challenging me and teaching me how to push my limits by going out of my comfort zone. Because of him, I now know that I am capable of thinking and doing things that I would never thought I would be able of. To my mother for being the person who always brings some light into the darkness and some warmth to the coldest moments I have ever lived. For always having a kind and supportive word for each moment in life. No child can ask for more. To my big brother for showing me that sacrifice and efforts are always recognized. For the little moments when I could feel that I let him proud of me which made me *go for it* in the following challenges. And to my little (enormous) sister for being the person with the greatest mental strenght I have ever knwon, who is able to recognize that *persistance, persistance, persistance* is the key to success.

All in all, I am extremely grateful to God, cosmos, chaos, mysterious setting of coincidences, luck, which name one decides that fits best, because it allowed me to become who I am, owing to somehow be born and grow in this circle of human beings, experiences and influences that drove me until this moment.

Thank you all for your time, experiences and shared thoughts.

*Science is generated by and devoted to free inquiry: the idea that any hypothesis, no matter how strange, deserves to be considered on its merits. The suppression of uncomfortable ideas may be common in religion and politics, but it is not the path to knowledge; it has no place in the endeavor of science. We do not know in advance who will discover fundamental new insights."*

— Carl Sagan, Cosmos

*(Enhanced sentence by my father on his university time)*

## **STATEMENT OF INTEGRITY**

I hereby declare having conducted this academic work with integrity. I confirm that I have not used plagiarism or any form of undue use of information or falsification of results along the process leading to its elaboration.

I further declare that I have fully acknowledged the Code of Ethical Conduct of the University of Minho.

# **Vestígios SEDEX em depósitos de *skarn* tungsto-auríferos na Serra de Arga – análise estrutural e paragenética de rochas calcossilicatadas enriquecidas em sulfuretos e sua mineralização**

## **RESUMO**

Subsequentemente ao estudo estrutural e geoquímico de assinatura vulcanogénica a exalativa de algumas unidades metamórficas da Serra de Arga (Norte de Portugal), atenção centrou-se no Domo de Covas, estrutura localizada nos terrenos silúricos da Serra de Arga. A génese das rochas primitivas, e de algumas fácies exalativas enriquecidas em vanádio, são consistentes com os sistemas de bacias anóxicas de retro-arc, precursoras do início do *rifting* (Dias, 2011). Na mina da Cerdeirinha, um dos jazigos do *Domo de Covas*, a mineralização de tungsténio, embora remobilizada pelo metassomatismo, pode ser considerada parcialmente relacionada com a atividade vulcânica silúrica. Aparentemente, na frente principal da mina a céu aberto da Cerdeirinha, anteriormente à paragénese calcossilicatada do tipo metassomática, existiriam dispositivos estruturais e relíquias de assinaturas singenéticas do tipo SEDEX (Leal Gomes *et al.*, 2011).

O presente estudo teve como foco principal as estruturas do depósito, levantamento e análise detalhada, principalmente da principal frente de mina a céu aberto. Além disso, a análise paragenética, e medições de E.P.M.A. e L.A.-I.C.P.-M.S. foram executadas.

No que respeita à geotermobarometria de metamorfismo regional e minério foram analisados o intercrescimento hornblenda-plagioclase, clorites e arsenopirites.

Relativamente às medições de pirite através de L.A.-I.C.P.-M.S., estas não são claramente conclusivas, contudo podem estar relacionadas apenas com a hipótese sedimentar-exalativa ou com uma assinatura SEDEX sobreposta pela alteração hidrotermal, que terá originado associações mineralógicas típicas de *skarn*. Os conteúdos de terras raras da scheelite e apatite sugerem o fracionamento do fluido e uma ordem de cristalização do centro para a periferia rochosa na frente de mina.

Foi encontrada uma indeterminação enriquecida em Mn, possivelmente relacionada a exalações primordiais ricas em Mn. Este estudo não encontrou uma evidência clara e estrita de uma configuração protolítica SEDEX, contudo mostra algumas indicações deste tipo de deposição pristina, que deve ser pensada em estudos futuros.

Palavras-Chave: Geotermobarometria, L.A.-I.C.P.-M.S., SEDEX, Silurian, *Skarn*.

# **SEDEX heritage in tungsten-gold *skarn* deposits of Serra de Arga metamorphic suite – structural and paragenetical analysis of sulfide-rich calc-silicate rocks and its mineralizations**

## **ABSTRACT**

In the sequence of a structural and geochemical study about the SEDEX to volcanic affiliation of some metamorphic units of Serra de Arga (Northern Portugal), attention was drawn towards *Covas dome*, located in the Silurian terrains of Serra de Arga. A prior geochemical data set for the meta-volcanic rocks suggests a transitional signature between mantle source alkali basalts and transitional-tholeiitic to transitional-calcalkaline magmatic series. The primitive genesis and emplacement of those rocks as well as some contemporary vanadium-rich exhalative facies are consistent with back-arc anoxic basin systems, precursor to rifting onset (Dias, 2011). At Cerdeirinha mine, one of the ore deposits of *Covas Dome*, tungsten mineralization, although remobilized by metassomatism, might be considered partially related to Silurian volcanic activity. Apparently in the main front of Cerdeirinha open pit, previously to the calc-silicate paragenesis of metasomatic type there would be structural devices and relics of syngenetic signatures of the SEDEX-type (Leal Gomes *et al.*, 2011).

The present study was focused mainly in the structures of the deposit, its survey and detailed analysis especially of the main clearing front of the open pit. Also, paragenetic analysis, E.P.M.A., and L.A.-I.C.P.-M.S. measurements were executed.

In what regional metamorphism and ore geothermobarometry concerns, hornblende-plagioclase intergrowth, chlorites and arsenopyrite were analysed.

L.A.-I.C.P.-M.S. pyrite compositions are not clearly conclusive, but could be related with only sedimentary-exhalative setting or with a SEDEX signature overprinted due to hydrothermal alteration, adding up with some *skarn*-like assemblages. Contents of REE scheelite and apatite suggest a fluid fractionation and an order of crystallization sequenced from central to periphery of the rock exposures at the open pit domain.

A Mn-rich indetermination was found, possibly related with a primordial submarine Mn-rich exhalation. This study did not found a clear and strict evidence of a protolithic SEDEX setting, however it shows some indications of this type of pristine depositions that must be thought of in future studies.

Keywords: Geothermobarometry, L.A.-I.C.P.-M.S., SEDEX, Silurian, *Skarn*.

## INDEX

Figures List	ix
Tables List	xxiii
Abbreviations and Acronyms List	xxv
1. Introduction	1
2. Geological setting	2
2.1. Comparative analysis of the protogeoic models	5
2.1.1. <i>Sedimentar protogenic</i> model	5
2.1.2. <i>Volcano-sedimentar to exhalative protogenic</i> model	10
2.1.3. Both models	35
3. Data and methodology	38
3.1. Transmitted and reflected light microscopy	41
3.1.1. Transmitted light microscopy	41
3.1.2. Reflected light microscopy	41
3.2. Scanning electron microscopy and energy dispersive X-ray spectroscopy (S.E.M. & E.D.X.)	42
3.3. Electron microprobe	44
3.4. Laser-ablation inductively coupled plasma mass spectrometry	46
4. Discriminated lithological types	50
5. Mineralogy and paragenesis	54
5.1. Mineralogical checklist	54
5.2. Table of binary intergrowths	62
5.2.1. Arsenopyrite	62
5.2.2. Pyrite & Pyrrhotite	64
5.2.3. Chalcopyrite	65
5.2.4. Mixed phases and mineral clusters	65
5.2.5. Tungstiferous minerals	67
5.2.6. Calc-silicate assemblages	68
5.2.7. Felsic character assemblage	72
5.2.8. Particular textures in CWW-3A	73
5.3. Cerdeirinha paragenetic chronogram	76
6. Ore geochemistry and geothermobarometry of indicative phases	79



6.1. Hornblende and Plagioclase	78
6.1.1. Data treatment	79
6.1.2. Pressure and temperature condition of crystallization	83
6.1.3. Discussion	88
6.2. Chlorite	91
6.2.1. Data treatment	93
6.2.2. Chlorite classification	94
6.2.3. Pressure and temperature condition of crystallization	95
6.3. Arsenopyrite	99
6.3.1. Data treatment	99
6.3.2. Discussion	105
6.3.3. Limitations of Kretschmar & Scott (1976) geothermometer	109
7. Geochemical fractionation and filiation signatures	111
7.1. Geochemical fractionation	111
7.1.1. Sulfides	111
7.1.2. Oxides, tungstates, phosphates and silicates and theirs REE chondrite normalization	114
7.2. Geochemical affinity and genetic relations	118
7.2.1. Sulfides fractionation	118
7.2.2. REE fractionation	134
7.2.3. Mn-indetermination	142
8. Discussion and Conclusions	144
References	150
Webgraphy	157
Annex I – Figure of mineral intergrowth	158
Annex II – Compositions of the diverse minerals applied as geothermomethers (microprobe data)	166
Annex III – Trace-elements concentrations of the diverse minerals (L.A.-I.C.P.-M.S. data)	169
Annex IV – Location of L.A.-I.C.P.-M.S. measurments	173
Annex IV – Notes about the Geological Setting	184

## FIGURES LIST

- Figure 1 – NW Iberia Allochthonous Complexes and terranes emplaced on top of the Central Iberian and West Asturian-Leonese autochthon. (Modified after Ribeiro *et al.*, 2007). 2
- Figure 2 – Geographical and geological setting of Cerdeirinha mine cut. **a)** Geographical localization (image from Minuta (Singular) de revisão da Folha 1c – Caminha). **b)** Overlap of geological map of Portugal (scale 1:50 000; image from Minuta (Singular) de revisão da Folha 1c – Caminha) with the location of Cerdeirinha mine (pink triangle). **c)** Bird's eye view of the Cerdeirinha mine cut, with identification and localization of each studied front. 3
- Figure 3 – Stratigraphic column referring to the study area, relatively to units located below the mineralized zone. (Modified after Coelho (1993)). 5
- Figure 4 – Stratigraphic column referring to the study area, relatively to units located above the mineralized zone. (Modified after Coelho (1993)). 6
- Figure 5 – Stratigraphic column referring to the study area, relatively to units located in the mineralized zone. (Modified after Coelho (1993)). 6
- Figure 6 – Reference lithostratigraphic columns. Location of key sites in figure 1. (After Dias & Leal Gomes, 2013b). 14
- Figure 7 – Transmitted light microscopic (uncrossed polarizers) images of Serro mafic volcanism evidences. **a)** Volcanoclastic protholitic texture. **b)** Porfiric protholitic texture – zoned protoplagioclase enhanced in the black perimeter delineated. **c)** Heterogenous laminar stratification from probable volcanogenic affinity. **d)** Features identified in an amphibolite from Serro. (C. Leal Gomes personal communication, 2019) 19
- Figure 8 – Zebra-alike facies type from Fulão sector. The numbers indicate each image profile location. (Personal communication of C. Leal Gomes, 2015). 20
- Figure 9 – Felsic metavolcanoclastic rocks from Fulão sector. **a)** Outcrop observations. **b)** Hand sample. (Personal communication of C. Leal Gomes, 2015.). 21
- Figure 10 – Representative schemes of Covas Dome formation. **a)** Representative scheme of the former deformation phase, tangential deformation of the dome, during the 2<sup>nd</sup> Variscan deformation phase. **b)** Representative scheme of the second deformation phase, the dome shortening, during the 3<sup>rd</sup> Variscan deformation phase. (Modified after Dias *et al.* (2013a).) 21
- Figure 11 – Covas dome geological map and interpretative profile. (Modified after Dias, 2011). 23

Figure 12 – Structural location of Covas Dome sector in the context of deformational heterogeneity. (Modified from Leal Gomes *et al.*, 2011.) Competent lithologies that set the antiform structure: siliceous metacarbonate rock, amphibolites, polygenic psammitic rocks, polygenic tourmalinites, massive to disseminated sulphide levels, and early aplite-pegmatites. Note: representation of 3D schematic non-isometric with graphic scale, deduced by the cartographic distance between Cerdeirinha and Caminha – about 12 km. 24

Figure 13 – Apical transition of the sulfides unit in the Cerdeirinha south open-pit. Short side of the photo = 2.5m. Lithotype petrography from 1 to 5 referend in the text. EE – exhalation axes = gravitic polarity deduced. (Leal Gomes *et al.*, 2011). 25

Figure 14 – Structures similar to chimneys – lithified anatomies in the 5<sup>th</sup> unit, and whose geometry was preserved in the previous evolution. A – Vertical exposition of the columns with phosphatic sulfate walls but with anhydrite relics, occasional presence of barite and more rarely svambergite; the nuclear portion is richer in sulfides, mainly heterogeneous pyrrhotite. B – Parallel exposition to stratification correspondent to a perpendicular intersection to the previous one. 1 – Core richer in pyrrhotite; 2 – Border richer in phosphatic sulfate; 3 – Compact phyllitic material lithified by recrystallized silica with abundant disseminated sulfides; 4 – Venules with apatite and remobilized sulfides that metasomatized the previous structures. 5 – Overprinted and parallel foliations (probably Variscans S1 and S2) with transposition of mica, chlorite and pyrite. (Leal Gomes *et al.*, 2011). 26

Figure 15 – Preserved proto-small-channels, fulfilled with pyrite-pyrrhotite and by anhydrite in transition to gypsum – microprobe backscattered electrons analysis. Note: in the image of secondary electrons, polyhedral crystals of isocubanite were observed. (Leal Gomes *et al.*, 2011). 27

Figure 16 – Stratigraphic column for the Cerdeirinha sector. The dark lines limit the lithology observed. (Modified after Dias (2011).). 29

Figure 17 – A – Localization of the studied sectors. B – Variation of the Au content depending on the sulfide host and the carrier lithology. (Modified after Dias & Leal Gomes (2013b).). 30

Figure 18 – Punctual analysis results of a heterogeneous and early arsenopyrite, with inclusions of scheelite, that was latter reequilibrated with a mineralization of Bi and Pb. Note: Te and Bi is a venular body with heterogenous distribution of tellurium and bismuth. (From Leal Gomes *et al.*, 2011). 31

Figure 19 – Localization of the diverse tungstiferous mineralization occurrence in the geographic domain involving the granitic massif of Serra de Arga. (From Dias & Leal Gomes, 2010). 31

Figure 20 – Depositional context of Silurian terrains in Serra de Arga, considering coherence between lithological interfaces, protolithic genesis and geometric organization of BHT deposits. **A** – Domo

de Covas; **B** – Serro; **C** – Cumieira-P. Carvalho; **D** – Monteiro. **1** and **2** – Psammpelitic sedimentary sequences; **3** – Basic magmas with affinity to mantle and continental tholeiites; **4** – Felsic-intermediate volcanics and volcanosedimentar products; **5** – Quartzphyllites and quartzites; **6** – Lydites and black shales; **7** – Cryptocrystalline impermeable crust and smoker anatomies; **8** – massive sulfides; **9** – Calc-silicate and carbonated rocks; **10** – Exhalative tourmalinitic products; **11** – Products resulting from carbonate and fenitic alteration of mafic alkaline protoliths. **a** – Fluids with affinity to the mantle (enriched in CO<sub>2</sub>, CH<sub>4</sub>, F, Cl); **b** – Seawater convection; **c** – Metalliferous precipitation in reducing environments, from fluids discharged into the sea water coming from smoker centers. (From Dias & Leal Gomes, 2013a.). 34

Figure 21 – Depositional context of Silurian terrains in Serra de Arga, considering coherence between lithological interfaces, protolithic genesis and geometric organization of BHT deposits (adapted from Dias (2011)). 35

Figure 22 – Representation of the several structures observed on the Cerdeirinha's open pit. **a)** Protolithic structures generalized conceptual profile of Cerdeirinha mine. **b)** Schematic representation of the most occidental domain relatively to the Cerdeirinha's main open pit, where it is possible to observe the primitive structural devices – graded bedding. **c)** Most western sector, where b) was observed. **d)** Detail of c) for the graded bedding structure (from which b)) representative scheme was done. (Images from Souto & Leal Gomes, 2017). 37

Figure 23 – Representation of the several structures observed on the Cerdeirinha's open pit. **a)** Protolithic structures generalized conceptual profile of Cerdeirinha mine. **b)** Schematic representation of the most occidental domain relatively to the Cerdeirinha's main open pit, where it is possible to observe the primitive structural dispositives. The orange codes represent the location of the respective hand samples collected that can be observed in figure 24. 39

Figure 24 – **a), b), c), d), e)** and **f)** Hand samples and polished sections of the samples, whose denomination is on the right down corner of each image. Theirs location is identified in figure 23. 40

Figure 25 – Leica DFC 320 utilized for sample petrography in University of Bremen. 41

Figure 26 – Thin-section carbon coating process. **a)** Cressington carbon coater. **b)** Detail for the moment of carbon coating in two thin-section ate the same time. **c)** Graphite pencil, for the carbon coating. **d)** Piece of paper showing the *before* and *after* carbon coated effect. 43

Figure 27 – Scanning electron microscopy. **a)** Detail for scanning electron microscopy SUPRA 40. **b)** Image of the general equipment required for scanning electron microscopy analysis. 43

Figure 28 – Electron microprobe. **a)** Image of the general equipment required for electron microprobe

use. **b)** Detail for the Cameca SX100 electron microprobe (from “Electron probe microanalysis” in <https://www.ozeankruste.uni-bremen.de/index.php/en/laboratories/electronmicroprobe.html>; accessed on 24<sup>th</sup> of June of 2019). 44

Figure 29 – Laser-ablation inductively coupled plasma mass spectrometry. **a)** General image of the equipment required for laser-ablation inductively coupled plasma mass spectrometry use. **b)** Detail for the New Wave UP193 laser. 47

Figure 30 – Different stages of dehydration for a geliform association. **a)** Perpendicular cut to the stratification. **b)** and **c)** Parallel cuts to stratification of two different levels referred in a). **d)** Texture reconstitution. (Souto & Leal Gomes, 2017). 51

Figure 31 – Cap-rock with 3 generations of apatite, in order of genesis. **a)** Ap I – Crackled-gel texture in green-silica rock. **b)** Representative scheme of a). **c)** Ap II – Crackled and resorbed texture. **d)** Ap III – Crackled, resorbed and recrystallized texture. (Images provided by C. Leal Gomes, 2019). 52

Figure 32 – Backscattered electrons and reflected light microscopy images of arsenopyrite paragenetic observations. The black circumferences indicate the location of L.A.-I.C.P.-M.S. spot measurements. **a)** With inclusions of lollingite and scheelite (CW05). **b)** With pyrrhotite inclusion (CW05). **c)** Without inclusions (CW05). **d)** With quartz and native Bi inclusions (CW05). **e)** Included in pyrrhotite, with inclusions of ilmenite and pyrrhotite, apatite and zircon (C2). **f)** With inclusions of pyrrhotite, titanite and ilmenite (C2). **g)** With inclusions of ilmenite and titanite (C2). **h)** With inclusions of pyrrhotite (C2). **i)** With pyrrhotite inclusion and contacting pyrrhotite (C2). **j)** Porfiroblastic arsenopyrite that includes electrum (CWW-3A). **k)** With pyrite inclusion (CWW-3A). **l)** With pyrrhotite inclusion (CWW-3A). **m)** With inclusions of pyrrhotite, apatite, native bismuth and lollingite (CWW-3A) Black lines limit the detail present in n). **n)** Reflected light microscopy image. Detail of m). Arsenopyrite involving lollingite and native bismuth. **o)** Arsenopyrite crystal observed in the C2 sample. Native bismuth was also observed. 63

Figure 33 – Backscattered electrons images of pyrite and pyrrhotite paragenetic observations. L.A.-I.C.P.-M.S. pyrite measurements. **a)** Outer zone (pyrrhotite dominant) pyrite-pyrrhotite decay (?) (CW05n). **b)** and **c)** Frontier sector pyrite-pyrrhotite decay (?) (CW05n). **d)** and **e)** Inner pyritic sector (CW05n). **f)** Inner pyritic sector close to the center of the nodule (CW05n). **g)** Pyritic matrix (CWW3A). **h)** Pyrite in contact with arsenopyrite that includes quartz and pyrrhotite (CW05). **i)** Pyrite, intergrown with scheelite, quartz and apatite, close to the centre of the *remobilization* sample (CW05). 64

Figure 34 – Chalcopyrite latter than pyrrhotite. **a)** In outer pyrrhotite sector (C2). **b)** Chalcopyrite in triple junction (C2). 65

Figure 35 – Reflected light microscopy images demonstrating pyrite + arsenopyrite + chalcopyrite ± bismuth ± mixed phases (sulfosalts) assemblage (CWW-3A). The orange circumferences and numbers represent the spots locations of L.A.-I.C.P.-M.S. measurements. **a)** Backscatter electrons image. **b)** Reflected light microscopy image of the arsenopyrite, chalcopyrite, *mixed phase* and pyrite intergrown. **c)** Highlighting the location of the L.A.-I.C.P.-M.S. spot analysis of this *mixed phase*. **d)** Evidences of chalcopyrite replacing pyrite and the presence of *mixed phases* formed with the contact of arsenopyrite and chalcopyrite. The white perimeter enhances the chalcopyrite replacing pyrite. **e)** *Pyrite island* indicates that pyrite is being replaced by chalcopyrite. **f)** Detail of pyrite + arsenopyrite + chalcopyrite ± bismuth ± mixed phases (sulfosalts). 65

Figure 36 – Backscattered electrons images of what seems to be a *minerals cluster* in the samples CWW-3A and CW05. The blue circumferences and numbers represent the spots locations of L.A.-I.C.P.-M.S. measurements. **a)** Backscattered electrons image that shows brightness differences that suggest a chemical compositional evolution from *mixed phase* to *minerals cluster* composed by euhedral acicular arsenopyrite intergrowth with chalcopyrite in a pyritic matrix (CWW-3A). **b)** Backscattered electrons image, detailed image of a). **c)** *Minerals cluster* phase included in arsenopyrite and quartz (CW05). **d)** and **e)** Details of c). **f)** *Minerals cluster* that whose content was not measured in L.A.-I.C.P.-M.S. (CW05). **g)** Detail of f). 66

Figure 37 – Backscattered electrons images of tungstiferous minerals. **a)** Scheelite included in pyrite matrix (CW05). **b)** Scheelite included in pyrite (CW05). **c)** Scheelite included in arsenopyrite (CW05). **d)** Scheelite intersected (or included) in arsenopyrite (CW05). **e)** Scheelite included in arsenopyrite and pyrite (CW05). **f)** Scheelite in contact with quartz and pyrite (CW05). **g)** Scheelite in contact with arsenopyrite in a biotitic matrix (C2). **i)** Automorphic scheelite with wolframite included (or exsolved?) in biotitic matrix (C2). **j)** Scheelite and ferberite included in pyrrhotite. **k)** Scheelite included in titanite. **l)** Scheelite, in calcitic matrix with wollastonite needles and in contact with pyroxene. **m)** Scheelite crystal in a fluorite and quartz-rich zone (of the calc-silicate rock) (CEE-S). **n)** Detail of m). 67

Figure 38 – Wollastonite diverse appearances in the calc-silicate rock (CEE-S). **a)** Sector of the calc-silicate rock that contains wollastonite under different crystal shape or thin section plane intersection. **b)** Detail of a), highlighting the diopside-hedenbergite transition. **c)** Wollastonite-almost wollastonite crown and wollastonite crystals in a fluorite-quartz matrix. **d)** Elongated wollastonite crystals. **e)** Wollastonite present in a quartz enriched matrix. Zircon intergrown with quartz. 68

Figure 39 – Backscattered electrons images of examples of clinopyroxenes. **a)** Clinopyroxene in carbonate matrix. **b)** Clinopyroxene (diopside) including quartz, calcite, fluorite and native Bi. 69

Figure 40 – <b>a)</b> Hedenbergite outer zoning diopside, and in contact with vesuvianite. <b>b)</b> Detail of a). <b>c)</b> Pyrite intersected by hedenbergite. <b>d)</b> Detail of c).	40
Figure 41 – Porosity in calc-silicate sample.	70
Figure 42 – Vestigial sphalerites found in the proto-travertine (Dias, 2011) – calc-silicate – sample. <b>a)</b> Sphalerite included in zoned pyroxene. <b>b)</b> Detail of a). <b>c)</b> Sphalerite included in non zoned pyroxene. Apatites were found in both cases in zoned and non zoned pyroxene. <b>d)</b> Sphalerite (remobilized) in contact with quartz, calcite and fluorite. <b>e)</b> Detail of d). <b>f)</b> Three sphalerites were spotted in quartz, fluorite and almost wollastonite crown respectively. <b>g)</b> Detail of f). <b>h)</b> (Remobilized?) sphalerite in contact with quartz and diopside. <b>i)</b> Detail of h).	70
Figure 43 – Backscattered electrons image of galena (?) or molybdenite (?); vesuvianite including calcite and being involved by fluorite. <b>a)</b> General image. <b>b)</b> Detail of the ore mineral present in a).	71
Figure 44 – Backscattered electrons images of zircon in calc-silicate rock.	71
Figure 45 – Felsic character. <b>a)</b> Zircon included in biotite. <b>b)</b> Detail of a). <b>c)</b> and <b>d)</b> Plagioclase intergrown with pyrrhotite. <b>e)</b> Chlorite intergrown with chalcopyrite included in plagioclase matrix. <b>f)</b> Chlorite intergrown with pyrrhotite and ilmenite included in plagioclase. <b>g)</b> Chlorite, with ilmenite inclusion, involved in plagioclase. <b>h)</b> Ilmenite included in chlorite and involved by plagioclase. <b>i)</b> Leucite included in plagioclase. <b>j)</b> Apatite included in biotite. <b>k)</b> Scapolite involving chalcopyrite. <b>l)</b> Detail of k).	72
Figure 46 – Binary intergrowths and mode of contact at the boundaries between each two phases pair. B – Bird eye structure; F – Fracturation/deposition; I – Inclusion; L – Inclusion or successive free deposition; LM - Successive free deposition in meteoric corrosion; S – Synchronism; T – seems to be latter, because it is only present in the borders; Z – Zonation/deuteric??; Black – read in the normal order; Pink – read in the inverse order.	73
Figure 47 – Porphyroblastic arsenopyrite with tungstiferous minerals, native bismuth and Au-Ag alloy included. <b>a)</b> Contact modes verified in the following images. <b>b)</b> Identification of pyrite, arsenopyrite, gold and native Bi in reflected light microscopy. <b>c)</b> Backscattered electrons image of arsenopyrite in pyritic matrix. Backscattered electrons images <b>d)</b> , <b>e)</b> and <b>f)</b> show the arsenopyrite diverse mineralogical inclusions.	74
Figure 48 – Backscattered electrons images of supergene enrichment related with Pb and Bi. <b>a)</b> General image of Pb and Bi minerals in a redox conditions. <b>b)</b> Enhance of galena and native Bi. <b>c)</b> Presence of bismite. <b>d)</b> Anglesite identification close to galena minerals. <b>e)</b> Contact modes verified in the previous images.	75

- Figure 49 – Mineralogical paragenetic sequence of the minerals found in this study (except in the calc-silicate rock). 76
- Figure 50 – Chronogram of the main calc-silicate paragenesis (possible metassomatism of proto-travertin). 77
- Figure 51 – An idealized model of the amphibole structure *sensu lato* showing the chain of tetrahedra, the strip of octahedra, the M(4) site and the A site. (From Hawthorne & Oberti, 2007). 78
- Figure 52 – General classification of the amphiboles, excluding the Mg–Fe–Mn–Li amphiboles (Leake et al., 1997). 80
- Figure 53 – Nodular sample hornblende classification. **a)**  $Na_B$  vs.  $Ca_B+Na_B$  diagram that allows to identify the hornblende group. **b)**  $Mg/(Mg + Fe^{2+})$  and  $Si_T$  diagram that allowed to identify the hornblende type: magnesiohornblende and *actinolitic-hornblende*. 82
- Figure 54 – Microphotography of the sector of nodular sample that contained the only actinolitic hornblende identified. In transmitted light microscopy (uncrossed polarizers – **a)**)(crossed polarizers – **b)**). In reflected light microscopy (**c)**). 83
- Figure 55 – Backscattered electrons images of hornblende-plagioclase intergrowths selected to determine temperatures. The figures **a)**, **b)**, **c)**, **d)** and **e)** are organized from the outer zone to the inner one of the nodule. 84
- Figure 56 – Characterization of the plagioclases that were seen intergrown with hornblende. **a)** Classification of plagioclase intergrown with magnesiohornblende. Pink and green dots represent andesine and labradorite compositions, respectively. **b)** Transmitted light microscopy image of the map of the nodular sample with the limits of the area where andesine (pink) and labradorite (green) intergrown with hornblende were found. White dashed lines represent the nodular orientation observed in the thin-section. 86
- Figure 57 – Temperature–pressure diagram showing the generally accepted limits of the various facies. Boundaries are approximate and gradational. The *typical*/or average continental geotherm is from Brown & Mussett (1993). The 30° C/km geothermal gradient is an example of an elevated orogenic geothermal gradient. The *forbidden zone* is bounded by the 5° C/km (150° C/GPa) gradient beyond which conditions are generally considered unrealized in nature (e.g., Liou et al., 2000). (Modified after Winter (2014)). 89
- Figure 58 – Amphibole chemistry from the nodular sample. Al-Ti diagram (modified after Jin (1991) *in* Li et al. (2017)). 89



Figure 59 – Temperature–pressure diagram showing the three major types of metamorphic facies series proposed by Miyashiro (1973, 1994). Included are the facies boundaries from figure 57 and an  $\text{Al}_2\text{SiO}_5$  phase diagram. Each series is representative of a different type of tectonic environment. The high P/T series is characteristic of subduction zones, medium P/T of continental regional metamorphism, and low P/T of high heat-flow orogens, rift areas, and contact metamorphism. (Modified after Winter (2014)). 90

Figure 60 – Projection of the curves obtained by the application of biotite-garnet and garnet-plagioclase-quartz-sillimanite equilibria. Delimitation of a temperature and pressure mean field, eventually related with partial fusion processes (curves relatives to NaKFMASH system regarding Spear et al. (1999) in Dias (2011)). (From Dias, 2011). 90

Figure 61 – Chlorite structural formula. (After Nelson, 2015). 91

Figure 62 – Si-Al-Fe-Mg tetrahedron for representation of chlorite analyses (solid squares). Plane (stippled) intersecting the tetrahedron is used for ternary Al-chlorite, Fe-chlorite, Mg-chlorite diagrams. Positions of chlorite analyses in this plane (open circles) are obtained by projection through the Si apex (dashed lines). Circled numbers with arrows refer to exchange reactions and vectors of table 16. (From Caritat *et al.*, 1993.). 92

Figure 63 – Classification of chlorites from Cerdeirinha deposit, based on the Hey (1954) diagram, regarding Si content and  $\text{Fe}/(\text{Fe}+\text{Mg})$  cation ratio for chlorites with  $\text{Fe}_2\text{O}_3 > 4\%$  and  $\text{Ca}+\text{Na}+\text{K} < 0.5$  a.p.f.u.. C2 sample data overlapped with Dias (2011) data. Black dashed arrow enhances the trend verified. 95

Figure 64 – Conjugated variation of Fe and Mg chlorites. Cerdeirinha chlorites with  $\text{Fe}_2\text{O}_3 > 4\%$  and  $\text{Ca}+\text{Na}+\text{K} < 0.5$  a.p.f.u. overlapped with Dias (2011) chlorite data. The symbology subtitle is similar to one present in figure 63. 95

Figure 65 –  $\text{Al}^{\text{IV}}$  and  $\text{Fe}/(\text{Fe}+\text{Mg})$  correlation of C2 chlorites. 96

Figure 66 – Comparison of chlorite compositions from the Cerdeirinha deposit with those used for empirical temperature estimation of Cathelineau (1988), Kranidiotis and MacLean (1987), and Zang and Fyfe (1995), regarding  $\text{Ca}+\text{Na}+\text{K} < 0.5$  condition. (Modified after Klein & Koppe, 2000.). 98

Figure 67– Histogram of crystallization temperatures of C2 chlorites calculated by the empirical method of Kranidiotis & MacLean (1987). 99

Figure 68 – Ternary Fe–S–As (at. %) diagram showing compositions of arsenopyrites found in C2, CWW-3A and CW05 thin-sections. The dark pink spot represents a stoichiometric arsenopyrite ( $\text{FeAsS}$ ). The purple dashed line represents the substitution of As for S, while the grey dashed line

represents the Fe-As join – the substitution of As for Fe. The orange area, in the smaller ternary diagram, represents the arsenopyrites domain Argas-Cerquido alignment (Leal Gomes, 1994), and the red area refers to shear zone Argas-Cerquido-Serra de Arga and shear zone networking in Serra de Arga Silurian Terrains (Araújo & Leal Gomes (2014) and Leal Gomes et al. (2015)), respectively. Its values can be seen below and in *Annexe II*. 100

Figure 69 – The numbers subscribed in white circles correspond to the references present in the table 21. The blue ones correspond to composition of early automorphic arsenopyrite, while the green ones correspond to arsenopyrites with hydrothermal paragenetic feature. **a)** Initial arsenopyrite with epitaxial zoning induced by crystal growth, fractionated, and sector zoned due to deformation associated with annealing. It is possible to see variations of the content of Au reticular related to annealing-recovery and polymetallic expressions of Bi and Te, possibly from the same source. (From Araújo & Leal Gomes (2014)). **b)** Arsenopyrite compositional zoning with higher values of Au in the outer zone of crystals (microprobe) and Au exsudations with impoverishment halos in arsenopyrite (expression in S.E.M.-B.E.). **c)** Au, electrum and galena identification in arsenopyrite cracks – location of analysis spots done in reflected light microscopy (uncrossed nicols) and compositions obtained by electron microprobe. Modified images from Leal Gomes *et al.* (2015). 103

Figure 70 – Pseudobinary T-X diagram with arsenopyrite-buffered curves (reprinted from Kretschmar & Scott (1976) and modified after Sharp *et al.* (1985)). Arsenic atomic content of arsenopyrites (and respective mineral assemblage) from Cerdeirinha, Argas-Cerquido alignment (Leal Gomes, 1994) and shear zone networking in Serra de Arga Silurian Terrains (Leal Gomes *et al.*, 2015) are plotted as circles, tetragons and triangles, respectively. 106

Figure 71 – **a)** Phase relations in the system Fe-As-S between 363 and 491 °C (after Kretschmar & Scott, 1976). The stability field of arsenopyrite (shaded) is exaggerated to show the effect of slight deviations from the  $\text{FeS}_2$ - $\text{FeAs}_2$  binary join. **b)** Exploded view of a) in the region of arsenopyrite. The composition of arsenopyrite in equilibrium with pyrite at a constant pressure and temperature can be anywhere along the bold line between A and B, depending on  $f(\text{S}_2)$ . The composition of arsenopyrite in equilibrium with pyrite and pyrrhotite must lie at A. **c)** and **d)** Phase relations in the system Fe-As-S for arsenopyrite lying on the binary join  $\text{FeS}_2$ - $\text{FeAs}_2$ . In this case, arsenopyrite coexisting with pyrite must lie at point C. 107

Figure 72 – Geology of the Penedono area, northern Portugal: a location of the study area in the Iberian Massif. Black continuous line limits the area from which the Cerdeirinha and Argas-Cerquido shear

zone arsenopyrites were collected, while the brown line limits the area studied by Couto (1993). (From Neiva *et al.*, 2019). 108

Figure 73 – Diagram of  $\log a_{S_2}$  – Arsenopyrite temperature, Kretschmar & Scott (1976). Sn-W ore body: SJ=S. Jorge (x; n=8); Sb-Au ore body: M=Montalto (x; n=53); Pb-Zn ore body: RE=Ribeiro da Estivada (6PN sample; n=7). CC= Covas de Castromil and PN= Penedono. 109

Figure 74 – Spider plot of REE normalized to chondrite (Anders & Grevesse, 1989) in ferberite and wolframite. 1 and 2 – represent the wolframites in fig. 37 h). While 3, 4 and 5 correspond to the ferberites in fig. 37 h) and j). Trace elements contents in *Annexe III*. 114

Figure 75 – Spider plot of REE normalized to chondrite (Anders & Grevesse, 1989) in scheelite. Spots location in fig. 37. Black – CW05; Blue – CEE-S; Red – C2. Trace elements contents in *Annexe III*. 115

Figure 76 – Apatites measurements. **a)** In contact with pyrite, biotite and labradorite (CW05n). **b)** In contact with pyrite and micas (CW05n). **c)** Involved by pyrite and labradorite (CW05n). **d)** Included in pyrite (CW05n). **e)** Included in pyroxene (CEE-5a). **f)** Apatite in sericitized plagioclase matrix (C2). 115

Figure 77 – Spider plot of REE normalized to chondrite (Anders & Grevesse, 1989) in apatite. Spots location in fig. 76. Green – CW05n; Blue – CEE-S; Red – C2. Trace elements contents in *Annexe III*. 116

Figure 78 – Vesuvianite measurements in L.A.-I.C.P.-M.S.. **a)** Intergrown with fluorite (CEE-Sa). **b)** Intergrown with calcite and in contact with fluorite and quartz (CEE-Sa). **c)** Included in calcitic matrix (CEE-5b). **d)** Pink line – in contact with fluorite and calcite; yellow line – intergrown with quartz (CEE-Sb). 117

Figure 79 – Spider plot of REE normalized to chondrite (Anders & Grevesse, 1989) in vesuvianite. The numbers correspond to the average of L.A.-I.C.P.-M.S. measurements spots of the same colour in the figure 78. Trace elements contents in *Annexe III*. 117

Figure 80 – Spider plot of depleted REE normalized to chondrite (Anders & Grevesse, 1989) in clinopyroxenes (black), hedenbergite (green) and wollastonites (blue). The numbers correspond to the average of L.A.-I.C.P.-M.S. measurements. 118

Figure 81 – Graphic symbols meaning. 118

Figure 82 – As content in arsenopyrite. **a)** Correlation of As and Bi in arsenopyrite. The 2 main generations of arsenopyrite are identified with the number 1 and 2. **b)** Correlation of As and Au in arsenopyrite. Consult figure 81 for symbology meaning. 118

- Figure 83 – Ag and Au correlation with Sb. **a)** Correlation of Ag and Sb in arsenopyrite. **b)** Correlation of Au and Sb in arsenopyrite. Consult figure 81 for symbology meaning. 119
- Figure 84 – Au and Ag correlation. Consult figure 81 for symbology meaning. 119
- Figure 85 – Comparison of Bi content with In and Te. **a)** Binary plot of In and Bi. **b)** Binary plot of Te and Bi. Consult figure 81 for symbology meaning. 120
- Figure 86 – Tetradymite and Te and Bi composites included in arsenopyrite. **a)** Backscattered electron image of included mineral in arsenopyrite. **b)** Spectrum of tetradymite identified in a). **c)** Table with weight percentage content of element identified in S.E.M.. 120
- Figure 87 – Comparison of Co, Mo, W and Sn content. **a)** Binary plot of Co and Mo. **b)** Binary plot of Co and W. **c)** Binary plot of Mo and Sn. Consult figure 81 for symbology meaning. 121
- Figure 88 – Tungstates compositions present in calc-silicate associations of Covas and amphibolic facies of Monteiro. Note: Covas wolframite compositions include pseudomorphoses and 1<sup>st</sup> generation crystals. **a)** Binary-plot of W (a.p.f.u.) vs. Ca (a.p.f.u.). **b)** Binary-plot of W (a.p.f.u.) vs. Fe (a.p.f.u.). C – Covas compositions (massive sulfide facies, grossularites and metasomatites); S – Serro compositions (calc-silicate rocks); M – Monteiro compositions. (amphibolites and leucocratic periamphibolic facies). (From Dias & Leal Gomes (2010).) 122
- Figure 89 – Backscattered electrons image from Dias (2010). **a)** Pseudomorfose of ferberite II after scheelite - Covas; **b)** Intergrowth between ferberite I and scheelite in the nucleus of a pseudomorfose - Covas; **c)** W-molybdenite crystal – Serro. 123
- Figure 90 – Molybdenite identified in Cerdeirinha mine. **a)** Backscattered electrons image of molybdenite intergrown with pyrite. **b)** Energy-dispersive X-ray spectroscopy – spectrum of molybdenite. 123
- Figure 91 – Paragenetic correlation diagram of metallic trace-elements in arsenopyrite. Green circumferences highlight the best correlations, while the yellow ones indicate the second best. Yellow rectangle evidence the elements that caution should be taken regarding elations. 124
- Figure 92 – Non-auriferous arsenopyrite. **a)** Backscattered electrons image of the porfiroblastic arsenopyrite and the location of theirs measurements found in b). **b)** Table with the content present in a), regarding As, Au, Ag and Bi. **c)** Detail of a). **d)** Representative scheme of the genesis of lollingite particle included in Bi, included in arsenopyrite (hypothesis 1 and 2). 125
- Figure 93 – Lollingite exsolution from arsenopyrite, with native bismuth in the contact of the arsenic minerals. **a)** Reflected light image of lollingite included in arsenopyrite that is in contact with

pyrite. **b)** Detail of a). **c)** Backscattered electrons image of a) with overlap of the L.A.-I.C.P.-M.S. spots locations present in table 26. 126

Figure 94 – Binary plot of Fe and As content in pyrite from samples CW05n and CWW-3A. Consult figure 81 for symbology meaning. 127

Figure 95 – Binary plot of Ag versus Ni (ppm) for pyrite from four different sediment-hosted gold deposits using data presented in Large *et al.* (2009) on Sukhoi Log, Bendigo, Spanish Mountain, and the North Carlin Trend. The distribution of the trace elements in these pyrites provides the basis for distinguishing early diagenetic (red field), versus metamorphic/ hydrothermal orogenic (blue field) and Carlin-type (green filed) pyrite via decoupling/precipitation processes. The green circles are from CW05n pyrite and the orange spot is from CWW-3A. Consult figure 81 for symbology meaning. 128

Figure 96 – Genesis determination of pyrite and pyrrhotite. **a)** Ni vs. Au diagram **b)** Zn vs. Pb diagram. Data of sedimentary pyrite are from Gregory *et al.* (2015) *in* Liu *et al.* (2018). (Modified after Liu *et al.*, 2018.). Consult figure 81 for symbology meaning. 128

Figure 97 – Pyrite (CW05n and CWW-3A) and pyrrhotite (CW05n, CWW-3A and C2) Ni, Co and Fe content. **a)** Binary plot of Fe vs. Ni. **b)** Binary plot of Fe vs. Co. **c)** Binary plot of Fe vs. Ni+Co. Consult figure 81 for symbology meaning. 129

Figure 98 – Ni vs. Co diagrams for pyrite and pyrrhotite from massive and lamellar ores of the Dongguashan copper (gold) deposit (Chen (1995) and Bajwah *et al.* (1987) *in* Liu *et al.* (2018)). I: deposit related to magmatic–hydrothermal solutions; II: Cu–Ni sulfide deposit; III, IV: magmatic and hydrothermal fields; V, VI: sedimentary and sedimentary-reformed field. Consult figure 81 for symbology meaning. 130

Figure 99 – Binary plots showing the distribution of Co, Ni, and Co/Ni for various rock types from the Archean Superior Province (Canada). **a)** Co/Ni versus Ni. **b)** Co versus Co/Ni. **c)** Ni versus Co. The distribution of the elements and elemental ratios in these plots define the corresponding compositional fields: pink corresponds to felsic, light green to mafic, light blue to ultramafic, light purple to lamprophyre, and the brown field to intermediate rocks. Data used to define the fields are from the following sources (*in* Gourcerol *et al.*, 2018b): Arndt & Nesbitt 1982, Arndt 1986, Barrie *et al.* 1991a, b, 1999, Beswick 1983, Canil 1987, Diné *et al.* 2008, Dostal & Mueller 2013, Fan & Kerrich 1997, Feng & Kerrich 1992, Finamore *et al.* 2008, Fralick *et al.* 2009, Gaboury & Pearson 2008, Goldstein & Francis 2008, Hollings & Wyman 1999, Hollings & Kerrich 1999a, b, Hollings *et al.* 2000, Hollings & Kerrich 2000, Innes 1978, Kerrich *et al.* 1999, 2008, Kitayama & Francis 2014, La Fleche *et al.* 1992, La Fleche & Dupuy 1992, Lafrance *et al.* 2000, Lahaye *et al.* 1995, Lahaye & Arndt 1996, Maurice *et al.* 2003, 2009,

MerciLangevin *et al.* 2007, Nesbitt *et al.* 2009, Parks *et al.* 2014, Picard & Piboule 1986, Piercey *et al.* 2008, Polat *et al.* 1999, 2012, Polat & Kerrich 2000, Polat & Münker 2004, Polat 2009, Rinne & Hollings 2013, Sproule *et al.* 2002, Stone *et al.* 1993, 1995, 1996, Stone & Stone 2000, Thurston & Fryer 1983, Ujike & Goodwin 1987, Ujike *et al.* 2007, Wyman & Kerrich 1993, Wyman & Kerrich 1993, 2009, Wyman & Hollings 1998, Wyman 1999, Wyman *et al.* 2000, 2002. Consult figure 81 for symbology meaning.

131

Figure 100 – Binary plot of Ni +Co and As + Fe. Pyrite (CW05n and CWW-3A) and pyrrhotite (CW05n, CWW-3A and C2) and arsenopyrite (CWW-3A, C2, and CW05) Ni, Co and Fe content. Consult figure 81 for symbology meaning.

132

Figure 101 – Binary plot of Au + Ag and Bi. Pyrite (CW05n and CWW-3A) and pyrrhotite (CW05n, CWW-3A and C2) and arsenopyrite (CWW-3A, C2, and CW05) Au, Ag and Bi content. Consult figure 81 for symbology meaning.

132

Figure 102 – Boxplot and whisker of Au, Ag and Bi in the three different sulfides. **a)** Boxplot and respective whiskers of Au L.A.-I.C.P.-M.S. measurements in three sulfides. **b)** Boxplot and respective whiskers of Au + Ag L.A.-I.C.P.-M.S. measurements in three sulfides. **c)** Boxplot and respective whiskers of Bi L.A.-I.C.P.-M.S. measurements in three sulfides (without the Bi-rich measurement in arsenopyrite).

133

Figure 103 – L.A.-I.C.P.-M.S. scheelite and apatite data treatment. The data is in ppm. **a)** REE-scheelite spider plot. **b)** REE-apatite spider plot. **c)** REE-vesuvianite spider plot. **d)** Discernible elements of scheelite in a radar plot. **e)** Discernible elements of apatite in a radar plot.

135

Figure 104 – Zircon in biotitic matrix, found in C2 sample. It did not contain chemical difference in the border, even though they are brighter.

137

Figure 105 – Fields of apatite composition from different rock types, proposed as discriminant plots. **a)** Binary-plot of Sr vs. Y. **b)** Binary plot of Sr vs. Mn. **c)** Binary plot of  $(Ce/Yb)_{CN}$  vs. REE (wt%). **d)** Binary plot of Y vs.  $Eu/Eu^*$ . (Modified after Belousova *et al.*, 2002).

138

Figure 106 – Discrimination diagrams for apatites from carbonatites, various ore deposits, and rocks that are not associated with mineralization. Also shown are literature data (Belousova *et al.*, 2002; Cao *et al.*, 2012 in Mao *et al.* 2016) that were not used in DPA for construction of the discrimination diagrams. **a)** The first discriminant function (DP1-1) vs. the second discriminant function (DP1-2), showing contours of constant Mahalanobis distance outlining bulk of the data in each group. **b)** Log Sr (ppm) vs. log Zr (ppm) with boundary separating bulk of the data for mid-ocean ridge (MOR) from ore

deposits and other rocks based on the lowest Mahalanobis distance. (Modified after Mao *et al.* (2016)).

139

Figure 107 – Discrimination diagrams for apatites from different ore deposits, showing contours of constant Mahalanobis distance outlining bulk of the data in each group. Also shown are literature data (Belousova *et al.*, 2002; Cao *et al.*, 2012 *in* Mao *et al.*, 2016) that were not used in DPA for construction of the discrimination diagrams. The first discriminant function (DP2-1-1) vs. the second discriminant function (DP2-1-2). (Modified after Mao *et al.*, 2016).

140

Figure 108 – Scatterplots for apatites. **a)**  $(La/Sm)_{CN}$  vs.  $(Ce/Yb)_{CN}$ . **b)** Yb (ppm) vs. Mn (ppm). (Modified after Mao *et al.*, 2016).

140

Figure 109 – REE profiles normalized. (Composition of chondrite: C1 of Evensen *et al.* (1978) in Leal Gomes (1994)). (From Leal Gomes, 1994)

109

Figure 110 – Spectra comparison related to phyllic and quartzophilitic facies of Costa da Ventosa – Covas Dome (Dias, 2011). **a)** Comparison with scheelite. **b)** Comparison with apatite. Micaceous tourmalinite with coarse tourmaline porfiroblasts, hosting of quartz-micaceous vein segregations (TCV); muscovitic-biotitic banded quartzphyllite with tourmaline (QFQMCV); tourmalinitic phyllite with garnet (QCV); biotite (BICV); coarse apatite with micaceous matrix that occurs segregated in the periphery of quartz-micaceous venulations (ACV)

110

Figure 111 – Mn-indetermination in CW05.n. **a)** Spheroid sample where Mn-indetermination was identified. **b)** Backscattered electrons image of spots of microprobe analyses; the content present in the letters can be found in the table 28.

142

Figure 112 – REE conclusion. **a)** Protolithic structures generalized conceptual profile of Cerdeirinha mine latter overprinted by igneous fluid. The number represent the order of crystallization. **b), c), d),** and **e)** hand samples and polished sections that allowed the production of thin-sections that allowed to achieve this conclusion.

146

Figure 113 – Current conception of paleogeography, in the context of the Ordovician to the Carboniferous, of the NW Gondwana margin (modified after Ribeiro *et al.* (2007) e Matte (2001) *in* Dias (2011)).

147

Figure 114 – Comparison between Cerecedo-Sáenz *et al.* (2018) and Cerdeirinha open pit field structures.

148

## TABLES LIST

Table 1 – Discrimination of lithotypes ordered according to their space configuration. (This data was compiled from Dias & Leal Gomes (2013a), Dias & Leal Gomes (2013b), Dias (2011), Dias & Leal Gomes (2007)).	15
Table 2 – Discrimination of lithotypes ordered according to their space configuration in Serro sector (from Dias & Leal Gomes, 2008).	20
Table 3 – Samples denomination, respective characterization and analytical methodology applied.	40
Table 4 – Maximum deviation of the control standard for microprobe measurements.	45
Table 5 – Samples, LA-ICP-MS method and minerals analysed under L.A.-I.C.P.-M.S. technique.	48
Table 6 – Control standard evaluation.	49
Table 7 – Control standard evaluation for specific isotopes, with respective compiled value and relative error.	49
Table 8 – Mineralogical checklist of all the minerals identified in Cerdeirinha until now, regarding its author, method (X-Ray Diffractometry, Scanning Electron Microscopy, Wavelength-Dispersive Spectroscopy, Reflected Light Microscopy, Transmitted Light Microscopy and Ultraviolet Light), relative abundance index and subsequent study.	55
Table 9 – Microprobe analysis of amphibole in the nodular sample.	81
Table 10 – Recalculated result of amphibole in the nodular sample.	82
Table 11 – Pressure genesis values determined regarding hornblende microprobe data. The bold method was also used for calculation purposes of Anderson and Smith (1995) and Holland and Blundy (1994), shown latter.	83
Table 12 – Microprobe analysis of plagioclase in the nodular sample.	85
Table 13 – Recalculated result of plagioclase in the nodular sample.	85
Table 14 – Results of Ab, Na and Or, its plagioclase type and hornblende (Hb) intergrowth for each plagioclase sample.	87
Table 15 – Results of pressure and temperature based on iteration using Anderson and Smith (1995) pressure and temperature.	87
Table 16 – Definitive mineral assemblages of metamorphic facies. Blue limit line is evidencing the facies and mineral assemblage studied (modified after Winter, 2014).	88



Table 17 – Chlorite components and exchange reactions. (From Walshe (1986) in Caritat <i>et al.</i> (1993).).	92
Table 18 – Comparison of chlorite compositions of Fe/(Fe+Mg), Al <sup>iv</sup> and Si from the Cerdeirinha deposit with those used for empirical temperature estimation of Cathelineau (1988), Kranidiotis and MacLean (1987), and Zang and Fyfe (1995). (Modified after Klein & Koppe, (2000).).	98
Table 19 – Representative analysis of arsenopyrites from Cerdeirinha open pit, obtained by microprobe with original sulfide program pre-settled in University of Bremen.	101
Table 20 – Representative analysis of arsenopyrites from Argas-Cerquido alignment, obtained by X-ray spectrometry in backscattered electron microscopy with original ASP 200 standard Kretschmar & Scott (1976). (Modified after Leal Gomes (1994).).	102
Table 21 – Representative analysis of arsenopyrites (wt.%), and As recalculations (at. %), associated with the shear zone Argas-Cerquido-Serra de Arga and shear zone networking in Serra de Arga Silurian Terrains, obtained by electron microprobe. (Data from Araújo & Leal Gomes (2014) and Leal Gomes <i>et al.</i> (2015).).	103
Table 22 – Calibration standard features for this study arsenopyrite measurements.	104
Table 23 – Metallic trace-elements present in the mixed phases and in mineral clusters.	113
Table 24 – Variability of the wolframitic mineralization attributed to Covas Dome. (Modified after Dias & Leal Gomes (2010).).	122
Table 25 – L.A.-I.C.P.-M.S. calibration and control standards measurments regarding arsenopyrites measurments.	124
Table 26 – Data from the laser ablation spots present in figure 92 c).	126
Table 27 – Mineral groups with or without REE.	134
Table 28 – TiO <sub>2</sub> , FeO and MnO wt.% content in several ilmenites and indetermination.	143

## ABBREVIATIONS AND ACRONYMS LIST

### **Whitney & Evans (2010)**

Ab – Albite	Gth – Goethite
An – Anorthite	Hbl – Hornblende
Ang – Anglesite	Lct – Leucite
Anh – Anhydrite	Ilm – Ilmenite
Amp – Amphibole	Ms – Muscovite
Ap – Apatite	Pl – Plagioclase
Apy – Arsenopyrite	Po – Pyrrhotite
Apo – Apophyllite	Py – Pyrite
Bt – Biotite	Qz – Quartz
Cal – Calcite	Rt – Rutile
Ccp – Chalcopyrite	Sch – Scheelite
Cel – Celadonite	Stp – Stilpnomelane
Chl – Chlorite	Spn – Sphene (titanite)
Cpx – Clinopyroxene	Scp – Scapolite
Fl – Fluorite	Ves – Vesuvianite
Gn – Galena	Zrn – Zircon

### **Chance (1956)**

Bi – Bismuth
ferb – Ferberite
lab – Labradorite
ty – Tetradymite
wf – Wolframite

lol – Löllingite
Nt – Neustädtelite
And - Andesine

In memory of the most wise, kind, adventurous, fearless and  
inspiring person who has ever crossed my path, *Avô Jorge*.

As you taught me A. Einstein once said  
*Coincidence is God's way of remaining anonymous,*  
and this year there were a lot of them.

See you soon, *Avô*.

(Save me a sit by your side, as you did in my 18<sup>th</sup> birthday,  
now it is my turn to tell you a whole *bunch* of new stories)

## **1. INTRODUCTION**

Following Dias (2011), Leal Gomes *et al.* (2011), Souto & Leal Gomes (2017) and Souto & Leal Gomes (2018) hypothesis, based on the structures and paragenesis observed at the open-pit mine of Cerdeirinha, previously to the calcosilicate paragenesis of metasomatic type there would be structural devices and relics of syngenetic signatures of the SEDEX-type. Apparently in the main front of Cerdeirinha open pit, there would exist some tubuliform structures and mounds fossilized that would represent proto-smokers (Leal Gomes *et al.* (2011) and Souto & Leal Gomes (2017)). Attention was drawn to a strong development of the deposit structure, its survey and detailed structural analysis of the main clearing front of the open cut. Also, paragenetic analysis of the main mineralogical associations and especially to those that were subjected to chemical analysis in Bremen.

In Portugal, during August and September, attention was drawn to specific theoretical preparation and field work. Then during the first semester of the program (from October until middle of April) in University of Bremen (Germany), a set of samples collected from Cerdeirinha open-pit and other set that was collected from previous campaigns, were prepared and analysed. Back to Portugal, during the last semester, the results were interpreted and discussed.

## 2. GEOLOGICAL SETTING

The *Serra de Arga* region belongs to the *galician-transmontano* domain of Variscan Iberian orogenic chain (Dias & Leal Gomes, 2013a). In the sector located in the Western and Central Minho Unit (W.C.M.U.) (*Unidade Minho Central e Ocidental*) between the Orbacém thrust fault and Vigo-Régua shear fault (fig. 1), the terrains that include the *Serra de Arga* granitic massif, whose were considered as metasedimentar-psammopelitic nature, are parautochthonous (fig. 1) and Silurian (Pereira *et al.* (1989) *in* Dias and Leal Gomes (2007) and Dias and Leal Gomes (2013a)). In addition, there is also description of some interstratified levels of short extension *skarns*, *volcanites*, *black shales*, *grey quartzites*, *black shales with intercalations of ampelites* and *lydites* (Dias & Leal Gomes, 2013a).

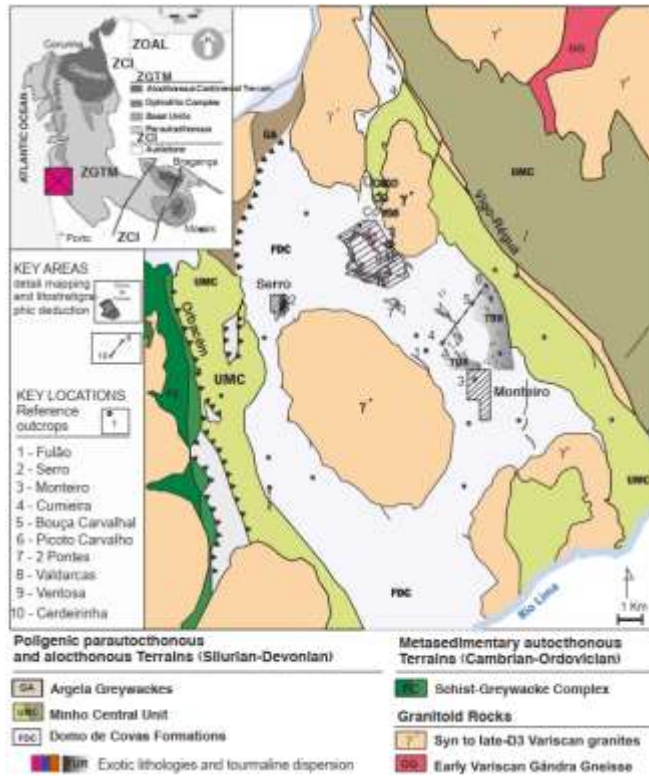


Figure 1 – NW Iberia Allochthonous Complexes and terranes emplaced on top of the Centra-Iberian and West Asturian-Leonese autochthon. (Modified after Ribeiro *et al.*, 2007)

The deposition of the metasediments would have occurred in confined basins with high subsidence and with low oxygenation and epi-continental localization (Pereira (1987) *in* Dias & Leal Gomes, 2013a). Recent geochemical data, available for some outcropping units with exotic aspects, included in W.C.M.U. and located in *Serra de Arga* flanks, allowed to diagnose volcanosedimentar to exhalative polygenesis components (Dias & Leal Gomes, 2008, 2010 *in* Dias & Leal Gomes (2013a)). In these sequence, the amphibolite seems to indicate peralkaline magmatic series consistent with a continental rifting (Dias & Leal Gomes, 2013a). Notice that in the North flank of the granitic massif of *Serra de Arga* there is a mega-structure in antiform  $D_3$ , known as *Covas Dome* (*Domo de Covas*) (Dias & Leal Gomes, 2013b). In *Covas Dome* the tungsten mineralization occurrence – scheelite and wolframite – in calc-silicate rocks (amphibolitic, sulfur alteration, tourmalinic and carbonated siliceous gangue (*skarn*) (Leal Gomes *et. al*, 2011)) motivated the exploitations (open-pit and underground exploitation (Dias, 2011)) of Cerdeirinha, Valdarca, Fervença and Lapa Grande, aggregated under the designation of *Couto Mineiro de Valdarca* (Dias *et. al*, 2013b).

Cerdeirinha mine is located in the NW of Portugal, at N of Serra de Arga, Viana do Castelo district, Caminha, in the Covas mining region (fig. 2). In this mine, the mineralized *skarn* horizon is tendentially sub-horizontal (Dias, 2011).

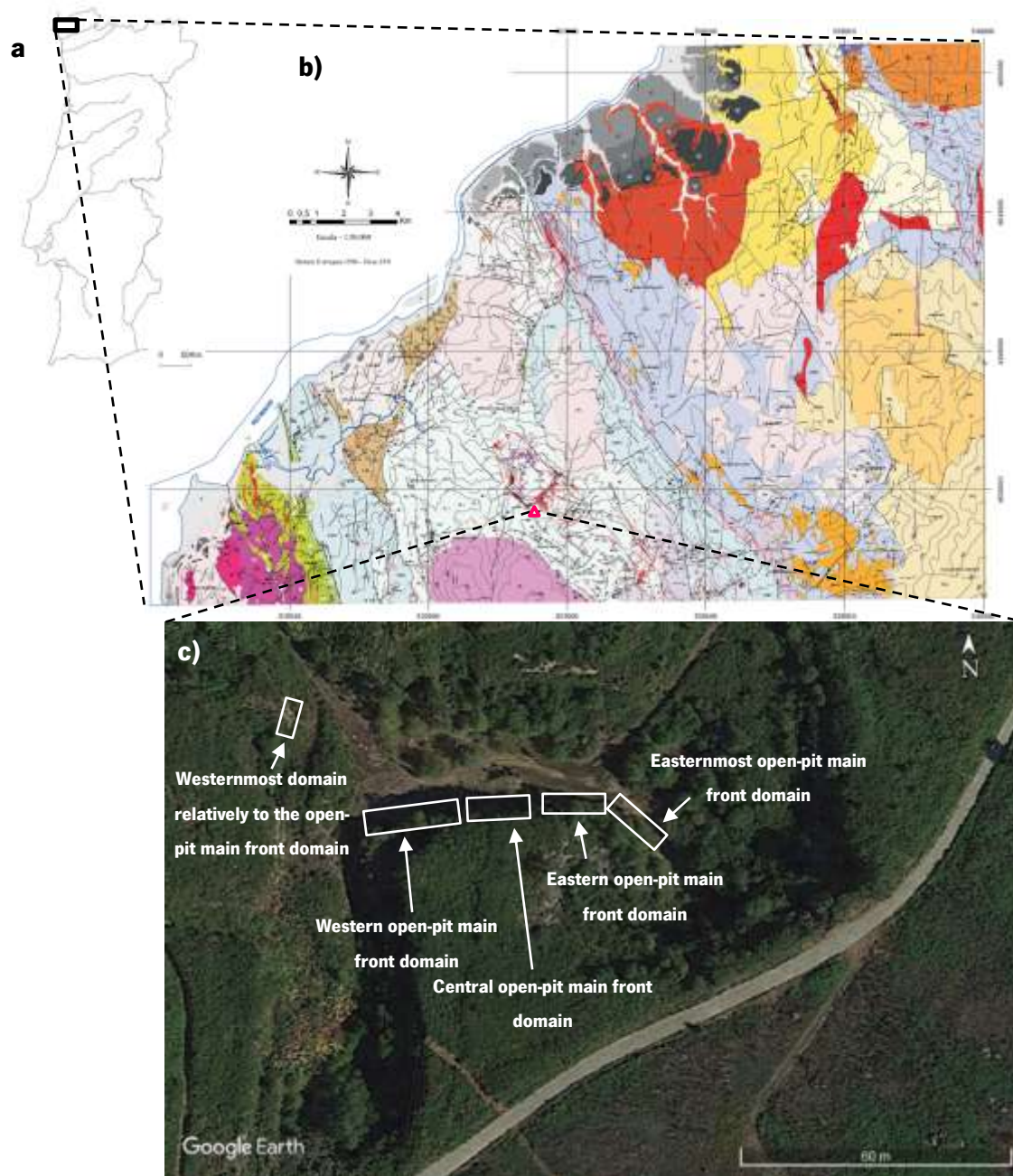


Figure 2 – Geographical and geological setting of Cerdeirinha mine cut. **a)** Geographical localization (image from Minuta (Singular) de revisão da Folha 1c – Caminha). **b)** Overlap of geological map of Portugal (scale 1:50 000; image from Minuta (Singular) de revisão da Folha 1c – Caminha) with the location of Cerdeirinha mine (pink triangle). **c)** Bird's eye view of the Cerdeirinha mine cut, with identification and localization of each studied front (image produced by Google Earth Pro and Microsoft Word).

The figure 1. b) respective subtitles are found below:

### Recent Sedimentar Deposits

- Quaternary to Present (river)**  
 active alluvial and fluvial deposits or underlying storage and
- Quaternary to present (coastal)**  
 current coastal deposits, dunes and beaches
- Pliocene to Quaternary - River**  
 very heterogeneous terrace (sometimes placer with cassiterite, andalusite, col-tan., corundum, tourmaline) (5-8 m)  
 essentially sandy deposits but with some large clasts (15-25 m)  
 extensive and heterogeneous coarse sandy deposits with gravel or clay, clastic or matrixial (30-40 m)  
 sandy loam deposits with rare coarse horizons and levels bearing "lignitized" stems (45-55 m)  
 thick deposits with alternating gravel levels and homogeneous clay horizons (60-70 m)
- Pliocene to Quaternary - Beaches**  
 deposits at different elevations of old beaches (levels correlated with river deposits) (5-8 m)  
 deposits at different elevations of old beaches (levels correlated with river deposits) (15-25 m)  
 deposits at different elevations of old beaches (levels correlated with river deposits) (30-40 m)  
 accumulations of miscegenated slope clasts with old beach deposits from the base of the cliff (45-50)

### Granitoids Rocks

- Post-tectonic biotitic granite for -D3**  
 locally blushed coarse-grained biotitic granite with occasional amphibole (Felgueiras, Castelo das Furnas)
- Porphyroid granites (Sin to tardi-tectonic from D3 and early from D3)**  
 essentially biotitic coarse grain porphyroid granite  
 coarse to medium biotitic granodiorite to quartzdiorite and porphyroid tendency  
 biotitic porphyroid granodiorite
- D3 Syntectonic granites with two mica**  
 medium grain two-mica granite with porfiroid tendency (Cerveira)  
 coarse grain two-mica granite (Covas W, Lanhelas)  
 medium grain two-mica granite (Covas E, Gondarém)  
 thin to medium grain gnaissoid two-mica granite (Romarigães - Sabariz)  
 coarse grain two-mica granite (Arga)  
 medium grain two-mica granite (Moledo)  
 coarse grain two-mica granite (Azevedo)  
 schlierenitic two micas granite sometimes tourmalinitic with thin grain (Cobertorinho)  
 schlierenitic two micas granite sometimes tourmalinitic with medium grain (Cristelo)
- Biotitic and leukocratic granites and granodiorites with occasional amphibole - D3 Syntectonic (subautochthonous to autochthonous)**  
 biotitic granodiorite with occasional amphibole (S. Silvestre)  
 leucocratic inhomogeneous granite essentially plagioclastic with medium to fine grain (Fontoura)  
 fine-grained biotitic gneissoid porphyroid granite (Taião-Mó)  
 migmatite (Taião N)
- D2 Syntectonic granite (subautochthon)**  
 albitic inhomogeneous granite with schlierenitic aggregates overmicaceous and pegmatoid segregations occasionally tourmaline (Taião, Alto dos Teares)
- Ordovician Granites (?)**  
 ocelade gnaisse (Picoto de Penices)  
 gnaisse (Gândara)

### Structures

- Locally more penetrating or continuous surfaces with indication of direction and magnitude of inclination**  
 Metamorphic surfaces (S1, S2, S3, Variscans); magmatic planar fluidalities; geometries s/c no discriminated (\* vertical, \*\* inclined)
- Kinking plans and bands and late chevron fold axial plans**  
 Structures D 3 Variscas and later
- Locally more significant lineations with direction and magnitude of inclination indication**  
 Mineralogical, intersection and stretch lineations (essentially L1, L2 and L3 Variscas); magmatic linear fluidalities
- Low continuity breaks or low thickness fault zones**  
 Confirmed path     Inferred and/or hidden path     Probable path
- High continuity breaks and/or very thick or complex fault boxes - predominant shear-zones**  
 Confirmed path     Inferred and/or hidden path     Probable path
- Extensive tectonic breaks with identified tangential displacement**  
 Proved to confirmed path     Inferred and/or hidden path     Probable path

### Parautoctonous and Allotonous Polygenic Units

- Sobrado Formation – Upper Silurian**  
**Domain of mantles and folds associated with the Covas antiform** – polygenic psamopelitic formations with quartzites, black schists, black phosphate nodules, lydites and exotic psammitic lithologies intercalations:
- Minho Central Unit – indifferenciated Silurian**  
**Formigoso (E) Sr das Neves (W)** – micashist with quartzous segregations and quartz-andalusitic venular and black shales intercalations, quartzites ± silicifiededs, black quartzites and tourmalinites.  
**Sapardos a Gandracho** – metamorphized psamopelitic formations with quartz and quartz-andalusitic diffuse segregations and less schistosity transposition in D3 Varisca.
- Metasomatite**  
**Casteloão** – circumscribed perigranitic domains with strong metasomatism, mixing and venulation.
- Valença and/or Vila Nune Units – Middle Silúrico**  
**Vilar de Mouros** – impure metagruvaques, dark psammopelitic formations and tourmaline grey and/or carbonaceous psammite-quartzitic levels.
- Ribeirda das Pombas** – products of difuse regional metasomatic evolution
- Cerdeirinha** – lithologies of vulcanogenic to carbonate affinity
- Serro a Cumieira** – lithologies of vulcanogenic-exhalative
- Valença** – metamorphosed polygenic psammo-pelitic formations (proto-tuffaceous metavolcanites, quartzites and quartzphyllites) sometimes migmatized with intercalations of dark proto-psammitic levels.

### Metasedimentar Autochthonous Units

- Valongo Formation – Middle Ordovician**  
**Rio Tinto** – roughly carbonous ardosiferous, sometimes with Fe-enriched siltitic shales
- Sta Justa Formation – Lower Ordovician**  
**Pedras Ruivas** – multi-recrystallized silicicous metaconglomerates with segregation of quartz and Fe oxides.
- Desejosa Formation - Cambrian (Indifferenciated)**  
**Cortelhas** – dark heterogeneous banded phyllites with silt beds.
- S. Domingos Formation - Cambrian (Indifferenciated)**  
**Barrocas** – schist-like pelitic matrix metaconglomerates.

### Filonian Intrusives Bodies

- quartziferous microdiorite, quartziferous microdioritic porphyry and kersantite
- granitic apilite-pegmatites and pegmatites sometimes with specialization in rare metals
- ultra-aluminous segregation veins
- quartz veins and quartz breccias
- Units correlated with Pereira et al. (1989).*

### Conventional Signs

- Toponymy, localities
- Level curves (taken from 1: 200 000 geological chart)
- Geodetic vertex; quota
- Main Watercourses (Rivers)

## 2.1. Comparative analysis of the protogenic models

In this chapter, two protogenic models (metasomatic model overprinting carbonated layer (Coelho, 1993) and metasomatic model overprinting a SEDEX sequence (Dias, 2011)) for *Covas Dome* and more precisely for Cerdeirinha open pit domain are confronted. This comparison will allow to clarify which one reunites more accurate features regarding the new data.

### 2.1.1. *Sedimentar protogenic model*

Coelho (1993) considers that the tungstiferous Covas deposit resulted from the interaction of restitic granitic metasomatic fluid of several generations with a carbonated mestassedimentar layer (sporadic carbonated levels that resulted from chemical and/or biochemical sedimentation), interstratified in a Silurian psammo-pelitic sequence, namely with low feldspar in origin. These sequences would have formed in a basin with low oxygen and low sedimentation rates, favourable to the occurrence of efficient grain-selection. This setting was repeated several times in the higher Silurian portions of the series, but with lower frequency.

Coelho (1993) considers that the Paleozoic series of this study area was not influenced by a volcano-sedimentar with significative participation, once the only horizons with volcano-intusive character that were observed in all series correspond to two stratabound bodies:

- A weathered metabasalt;
- Kersantite outcrop in Cerdeirinha.

The features of the basin considered above, with the instability through time, conducted to the appearance of an assimetric sequence:

- a) In the layers between the basement and the mineralization (Valdarcas) (fig. 3):

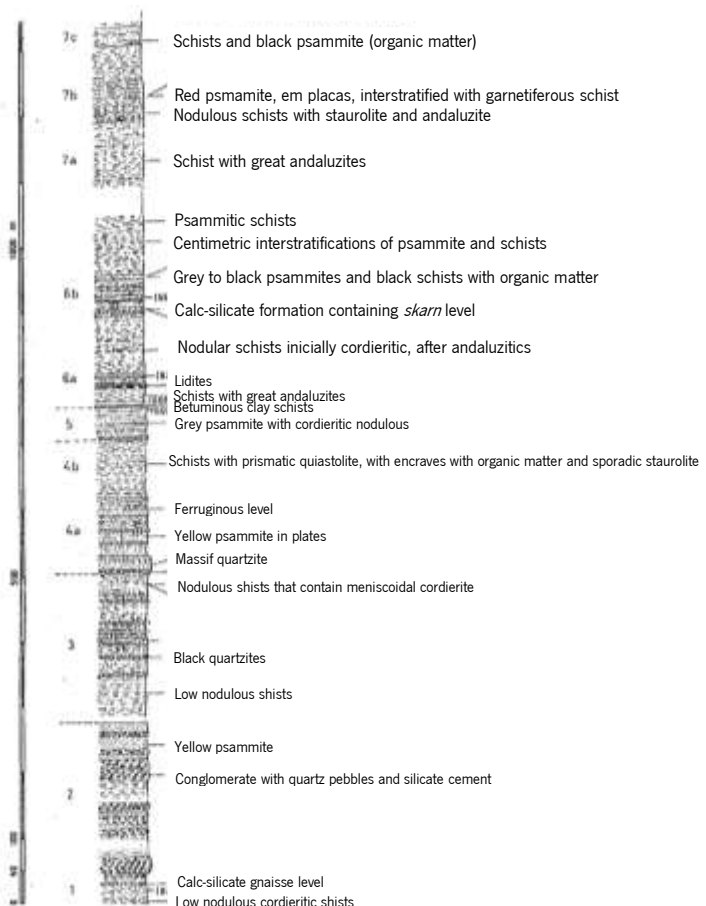


Figure 3 – Stratigraphic column referring to the study area, relatively to units located below the mineralized zone. (Modified after Coelho (1993).)



- Mostly aluminous (argilitic shales), but with sporadic quartzitic intercalations, from a strong sedimentary selection;
- Containing high quantities of dispersed sedimentar organic matter and revealing high concentrations of  $P_2O_5$  and Y.

b) In the layers between the mineralization and the top (Cerdeirinha) (fig. 4):

- Lower sequence in the sedimentar selection expressed in a litology of shales and argilitic psammite with silic-aluminous bipolarization less evident;
- Reduction of the frequency and quantity of the dispersed sedimentar organic matter.

The mineralized levels (fig. 5), developed above the limestone (with chemical and/or biochemical origin), rich in organic matter and contrasting with the poorish in CaO of the host series, they possessed a residual sedimentary fraction that suggest that the genesis of the limestones are related in conditions, with the ones verified at the top of the deposit.

The residual metasedimentar, in a pre-metassomatic time, contained dispersed organic matter, and low quantities of flogopite, pyrite and anhortite.

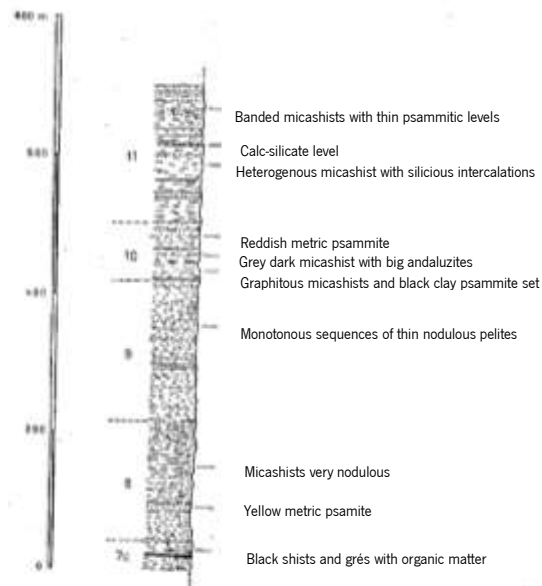


Figure 4 – Stratigraphic column referring to the study area, relatively to units located above the mineralized zone. (Modified after Coelho (1993).)

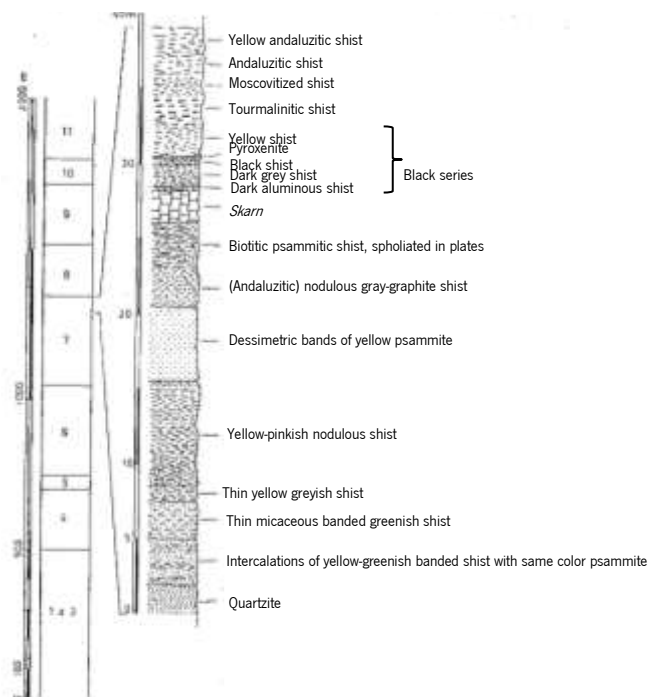


Figure 5 – Stratigraphic column referring to the study area, relatively to units located in the mineralized zone. (Modified after Coelho (1993).)

#### 2.1.1.1. Covas Dome

Coelho (1993) considered that *Covas Dome* resulted of a diapiric domation, promoted by the sub-superficial installation to the dome of a magmatic mass, latter  $F_3$  of an earlier antiform from the same deformation phase.

To prove his idea, he considers the occurrence of sheath folds (Cobbold & Quinquins (1980) *in* Coelho (1993)) associated with flabelliform dispersions formed by folds  $F_2$  and  $F_3$ . Besides this evidence, in a drilling core granite was found under *Covas Dome*, at 150m depth. For last, Dias (1987) *in* Coelho (1993) acknowledged that not only the  $F_3$  antiforms can be favourable structures for the granitoid implementation, but also as a ballooning installation.

#### 2.1.1.1.1. Tungstiferous character

Bayer (1956) *in* Coelho (1993) considered that the Covas tungsten was already found in the original sedimentar environment, where it was syngenetically accumulated by volcanic processes. This author believes that the tungsten was only remobilized and concentrated *in situ* by metamorphism and metassomatic processes of contact.

However, Coelho (1993) believes that the tungsten was introduced by the mineralizing residual granitic fluids of *skarn* (if not totally, at least partially) in Covas system, once the residual marbles in the Covas *skarn* and the genesis of the latter metasomatic stages, would not allow to accept the hypothesis of already existing tungsten in the mineralized layer. One should notice that the volcanic manifestations that Coelho (1993) observed in *Covas Dome* was only the kersantite, without any chemical and petrographic visible hints that could suggest the influence in the mineralized levels or adjacent ones. The marbles that Coelho (1993) observed, revealed three paragenetic expressions, from which only one was considered as totally unaffected by any metassomatic action. The three paragenetic groups are, respectively composed by:

- a) calcite + biotite + organic matter + pyrite  $\pm$  anorthite
- b) calcite + clinopyroxene + potassic feldspar + sphene + <biotite>  $\pm$  pyrite  $\pm$  Na
- c) calcite + clinopyroxene + vesuvianite  $\pm$  pyrite

None of these paragenesis appeared with tungsten mineralization.

Paragenesis a) represents the original limestone facies that was characterized by a calcitic matrix with lower content in dolomite, and by a residual psammo-pelitic fraction constituted by small tabular biotites displayed in thin planar alignments, with parallel strats of organic matter, and also microveins of thin calcitic grains of recrystallized calcite that probably materializes the original stratification, where there is also some grains of anhortite, quartz and pyrite.

Supporting this hypothesis, Ivanova (1986) *in* Coelho (1993) concluded, through the data analysis of the distribution of tungsten in magmatic and sedimentary rocks, that the intervening processes of genesis of these two rock groups are unable to concentrate this element.

Fonteilles (1986) *in* Coelho (1993) considers possible the participation of another compositional origin of the metasomatic fluids, due to the quantity of the resident fluid in the metasediments not being enough to explain the needed volumes involved in the metasomatism.

Coelho (1993) verified that the tungsten was introduced, for the first time, in the deposit in significant quantities, during the V stage of metasomatism, as scheelite I, in the interior of *skarns* and the wolframite in the *endoskarn* and/or aplite-pegmatites. The mechanism of scheelite precipitation seemed to have been controlled, in conditions of pH and favourable temperature, by the CO<sub>2</sub> fugacity. When it achieved lower values than marble, allowed the increasing of the CaO activity in the fluid that could destabilize the oxi-fluor-complexes (possible tungsten carriers). Hence, co-precipitation of scheelite and fluorite would have happened.

The remobilization of the fluids through the porosity of the natural environments presupposed that the fluid pressure was superior or close to the solid pressure ( $P \geq P_s$ ). In these conditions, the velocity of the remobilization of the fluid would have been very high comparatively to the order of velocity in which the chemical reaction would have happened. Hence, the only possibility is that in the fluids trajectory, they had suffered a low diffusion effect with the contacted walls. Being highly improbable that this process was enough to incorporate the responsible tungsten by the mineralization of *Covas Dome*.

Coelho (1993) also considers that if the fluid of the stage V incorporated the tungsten from the metasediments, it would hardly be understandable why none of the previous 4 metasomatic stages produced any mineralization, once the corresponding fluids percolated substrates with similar composition and under the same host-rock. At least, the fluid of the IV stage possessed a chemical composition similar to stage V, alkaline and Al-rich. Therefore, the IV stage fluid contained also some needed features for the tungsten solubilisation, in case this element was present in the sediments (Pascal (1984) and Ivanova (1986) *in* Coelho (1993)). Hence, his evidences point towards to, at least partly, a magmatic origin of the metasomatic fluid and to an introduction of tungsten to the system by this fraction.

In summary, there was a compositional specificity of the generating mineralizing fluid, due to chemical-thermodynamic conditions that influenced the partition coefficient of the tungsten carriers to be favourable to the fluid. These would have promoted the separation of the W from the parental magmatic environment, with which it was in equilibria.

From Coelho's (1993) point of view, the *Covas Dome* genesis might be related with ballooning installation, dependent of the installation of a tardi-hercynic magmatic body, of an antiform a little younger but still in the same phase. *Covas Dome* suffered intensive metasomatic and hydrothermal actions. The

metasomatic set that affected *Covas Dome* began before de  $F_3$  and finished after this phase. The metasomatic stages Ia, Ib and II developed before the  $F_3$  and the stages III, IVa, IVb, Va and Vb occurred after this. Fractures that resulted from the dome distension, associated with the compression of  $F_3$  that closed the structure, played a determinant role in the circulation and access of the latter fluid to the stage II including the mineralizing fluid. Therefore in the mineralized area there is not only metasedimentary rocks series (frequently feldspathic), as well as residual marbles, intrusive stratabound rock, aplite-pegmatites, and rocks that resulted from the intensive metasomatic transformation of the previous ones, which is *skarns* with several origins. Although the intensive transformation that carbonated rocks from *Covas Dome* came through, there are immense marble relics, little or not metasomatized at all, that still exist in the middle of the *skarns*. This shows that the fluids were not enough to transform all the calcitic mass. These relics manifest under different shapes, almost always with an elongation parallel to the marble banded structure. Relic's dimensions range from millimetres or centimetres until several meters of length. The *Covas Dome* marble is composed by a carbonated matrix that contains calcite and dolomite, and a residual psammo-pelitic metasedimentary fraction, formed by biotite, plagioclase, organic matter and quartz.

Notice that the identification of the initial rocks nature can be problematic, except in cases that still exist relics of the primitive materials, or in some very simple cases of metasomatism.

Litologically, this series is dominated by metamorphites composed of argillitic shales and pelitic psammite, although there also exist other metamorphites that were originated from quartzites, lydites, limestones, and carbon-rich levels (Coelho *et al.* (1988) in Coelho (1993)).

Coelho (1993) also suggest that:

- 1) The series polarity is positive;
- 2) Considering the profusion of the aplite-pegmatitic intrusions and the strong hydrothermalization in *Covas Dome* area, its quartzites are mainly transformed facies;
- 3) The lateral variations, sedimentar and thickness, that are observed in the different sector units, are frequent in this series. These variations, that induced great modifications to the materials origin, are dependent on the oscillations of the intrinsic sedimentary character of the basin, on the tectonics present in that region, and also on the metasomatic manifestations, especially in *Covas Dome*.

In summary, regarding Coelho (1993), the Silurian sequence that frames the mineralization is characterized by:

- a) Strong dominance of the pelitic units originated by the argillitic shales;
- b) Appearance of psammitic levels;
- c) Frequency of materials that were formed under low sedimentar rates, associated with high grain-selection and the incorporation of organic matter and carbonates, in the base of the formation until the deposit.
- d) More rarely to the top of the series the sedimentar settling described on c) is also found.

Coelho (1993) did not observe tuffaceous character, therefore he didn't agree with the participation of a significant volcanosedimentar influence in this series genesis. He also added that if it had happened the  $TiO_2/Zr=f(Al_2O_3)$  correlation would have been strongly perturbed.

#### 2.1.2. *Volcano-sedimentar to exhalative protogenic model*

Besides the geological description in *Geological Setting* chapter, Leal Gomes *et al.* (1997) in Dias & Leal Gomes (2007) and Dias & Leal Gomes (2007) also considered other lithologies that promoted the hypothesis of a possible SEDEX protolithic heritage. Such as the presence of quartzites; quartzfilitites; lydites; amphibolites with uncertain protolithic nature; metacarbonated rocks; psammpelitic-alike rocks, occasionally sulfide-enriched (with possible volcanoclastic to tuffaceous nature); argillic rocks with inherited textures that suggested a primordial felsophyric character (Braga *et al.* (1999) in Dias and Leal Gomes (2007)); granatiferous rocks almost monomineralic composed of spessartite to Mn-almandine or grossular; polygenic tourmalinites with several textural expression of schorl-dravite that grade to fosforites, suggesting a primitive evaporitic and/or exhalative nature.

##### 2.1.2.1. *Covas Dome formations*

The tangential deformation is well preserved in low-sloping sectors with low angle reverse displacement and sheath folds sometimes with great development. Therefore, for these contiguous terrains to the granitic massif of Serra de Arga known as *Covas Dome Formations* (C.D.F.) (fig. 1), with a complex polygenic nature, might delineate a mantle-fold configuration, with recumbent inverted replication of the stratigraphic sequences of exhalative affinity, in the zone of Fervença, Valdearcas, Cerdeirinha and Ventosa (fig. 1) (Dias & Leal Gomes, 2013a), which were afterwards folded by D<sub>3</sub> phase.

In the CDF set, the 2<sup>nd</sup> phase of the Variscan deformation (D<sub>2</sub>) and the evolutions in the interface between D<sub>2</sub> and D<sub>3</sub> would have occurred under the P-T conditions of 650-710 °C and 2.9-4.2 Kbar, considering the mineralogical geothermobarometers and the crystallization of hyperalluminous veins from fluids of metamorphic origin (Dias (2011) and Dias & Leal Gomes (2013a)).

The volcanogenic to exhalative components of *Covas Dome* Formations in Serra de Arga show a transitional character between mantle source alkali basalts and transitional-tholeiitic to transitional-calcalkaline magmatic series that gathered with exhalative petrogenesis evidences (registered in lydites, black shales, quartzfilitas, tourmalinites as well as contemporary vanadium-rich exhalative facies) strongly suggest a primordial occurrence of intracontinental extension episodes, precursor to rifting onset. These episodes are more probable in back-arc anoxic basin systems (Dias & Leal Gomes, 2013a).

Dias & Leal Gomes (2013a and 2013b) explained the processes of the geological evolution for the key-sites identified in figure 1 and figure 6. Their results from the petrographic analysis and geochemistry suggest the following essential aspects (table 1):

***Serro, Monteiro and Verdes Amphibolites*** – On one hand these amphibolites, mainly composed by Fe-hornblende and plagioclase (with anomalous titanite (Al-F-rich) content), contain significant concentrations of high-T sulfides (pyrrhotite, arsenopyrite, chalcopyrite, Co-Ni-lollingite) and scheelite. In interface with these alkaline amphibolites, there are green phyllitic facies with mineral assemblage equivalent to those referred in listvenitization products related to carbonate and potassic alteration of mafic precursors, by the intervention of fluids enriched in CO<sub>2</sub> and K.

On the other hand, amphibolites with magnesium mafic precursor are compact or with plagioclasic felsic segregations. From the chemical composition point of view they are similar to M.O.R.B. basalts and continental tholeiites.

Notice that these authors distinguished ortho-derived amphibolites from those representing products of deuteric alteration of intermediate-felsitic volcanogenic rocks which are described as transformed or mixed amphibolites.

***Chloritic rocks with mafic ultrapotassic precursor or superimposed potassic metasomatism in Santa Justa*** – Interpreted as metamorphic evolution products overprinted to a syngenetic hydrothermal alteration, which may in context of analogy and classification establish a petrogenetic equivalence with fenites. The geochemical domain established was traqui-andesite.

***Serro, Santa Justa, Valdarcas, Fulão and Verdes Felsic metavolcanics and granular related terms*** – Sulfide enriched. Correspond to facies where in macroscopic terms suggest a textural volcanogenic affinity:

- Laminated felsophyric tuffs;
- Devitrification products with evidence of polycyclic recrystallization;
- Granular rocks and pelitic feldspathic facies with isotropic granular matrix and likely volcano-sedimentary nature (equivalent to leptites).

In chemical analysis correspond to product evolution of lavas, pyroclastites and subvolcanic rocks owe to felsic to intermediate composition magmas (riodacitic rocks) with calc-alkaline to transitional character (andesitic rock). In the succession of Serro (fig. 1) banded sulfides are particularly abundant in relation to these rocks.

**Tourmalinites** – They are widely represented in the C.D.F. and can be grouped in two main components:

**Cumieira, Duas Pontes, Serro and Monteiro stratiform tourmalinites** – Contain detrital geochemical signature.

**Monteiro and Verdes peri-amphibolitic tourmalinites** – With various modes of occurrence in interface with alkaline mafic amphibolites:

- Phosphatic tourmalinite with apatite ocellar arrangement around individual and aggregated tourmaline crystals (oscillatory precipitation);
- Massive tourmalinite with fine grained tourmaline and clusters of acicular crystals;
- Tourmaline dispersed in the amphibolitic matrix and quartz-tourmaline breccias.

Massive tourmalinites in interface with alkaline amphibolites, show low REE contents, high (La/Yb)<sub>N</sub>, and positive Eu anomaly. Identical patterns have been reported in high-T hydrothermal fluids, vented from current submarine smokers.

The geochemical data, by manifesting similarity between stratiform tourmalinites and metasedimentary rocks, exclude the hypothesis of representing chemically precipitated lithologies. Are more acceptable substitution processes of primitive sediments with pelitic and psammitic feature by hydrothermal fluids enriched in B.

**Quartzites and quartzphyllites** – With greenish mica, lollingite, arsenopyrite and native Bi relatively abundant. Muscovites and tourmalines have high V and Ba average content. According to Canet *et al.* (2004) in Dias & Leal Gomes (2013b) comparable enrichments in sedimentary nature lithotypes with high levels of organic matter, are comparable to increments observed in current hydrothermal fields, and may be an exhalative sourced under redox conditions and low values of  $fO_2$  ((Dias & Leal Gomes, 2007) and Dias & Leal Gomes (2013a)). This interpretation also conciliates with the negative Ce anomalies in that same rocks. In the *Covas Dome W* deposits, Dias (2011) considers that there are some *smoker* structures, lithified in heterogeneous sequences with metasomatized sulfide, sulfate and carbonates (Dias & Leal Gomes (2013a)).

**Metapsammitic rocks with sedimentary organic matter (Lydites and black shales) and phosphates in Cumieira, Picoto do Carvalho and Monteiro** – Correspond to lydites and black

shales often with Al and Fe phosphates as porous nodules, and phosphoric gossanous facies, whose primordial features were accomplished through chemical precipitation ((Dias & Leal Gomes, 2007) and Dias & Leal Gomes (2013a)). Vanadiferous coarse tourmalines occur dispersed in lydite levels conditioned to beds rich in organic matter. Manifestations of significant negative Ce and Eu anomalies (in REE profiles normalized to chondrite) were commonly attributed to precipitation from sea water with or without hydrothermal mixture. Metals enrichment (Ni, Cu, Zn, Co and As) is more distinct in friable black shales where are observed simultaneously high MnO contents. Gossanous metaphosphorites exhibit Fe/Ti enrichment consistent with hydrothermal processes (Dias & Leal Gomes (2013a)).

***Calc-silicate rocks and metamorphosed hydrothermalites*** – In this group are included banded rocks with calc-silicate mineralogy similar to *skarns*, plagioclases with almandine-spessartite and apatite, and cryptocrystalline rocks with quartz and apatite (*green silica rock*) from Covas W mineralized compartments. These authors distinguished almost monomineralic rocks such as grossularites, epidotites, pyroxenites and idocrasites, and more heterogeneous products differentially enriched in Ca, Mg and Fe silicates.

***Heterogenous phyllitic and quartzphyllitic rocks*** – This facies (stratigraphically positioned at the top of the mineralized *skarn* horizons) includes petrographically the following categories:

- Micaceous tourmalinites with coarse tourmaline porphyroblasts and apatites, positioned at metamorphic segregation interfaces;
- Tourmaline and garnet biotites and banded micaceous quartzite with coarse tourmaline (Ventosa, fig. 1).



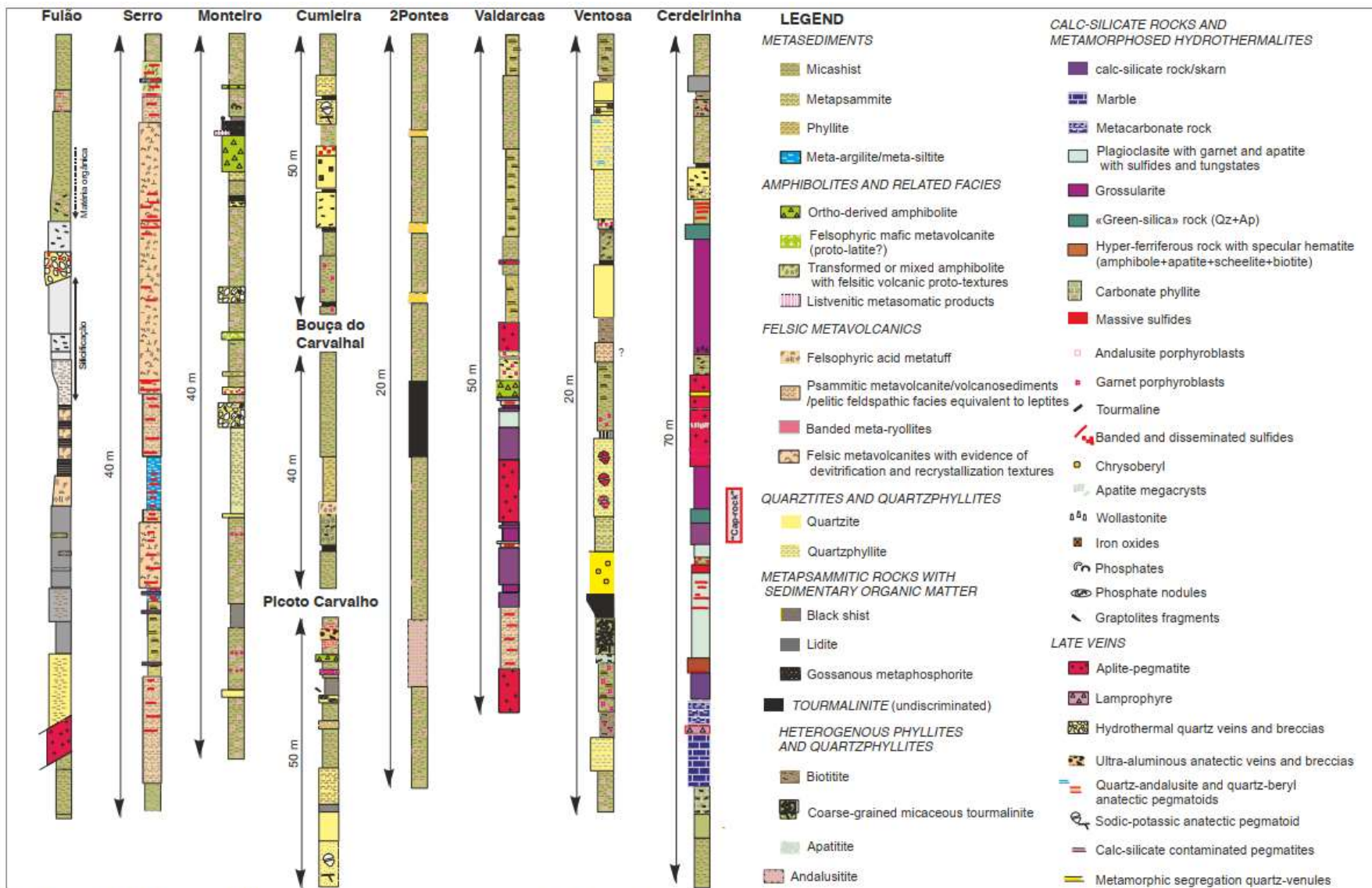


Figure 6 – Reference lithostratigraphic columns. Location of key sites in figure 1. (After Dias & Leal Gomes, 2013b)

Table 1 – Discrimination of lithotypes ordered according to their space configuration. (This data was compiled from Dias & Leal Gomes (2013a), Dias & Leal Gomes (2013b), Dias (2011), Dias & Leal Gomes (2007)). (To be continued.)

Facies Unit		Geochemical Indication	Typomorphic Minerals and Textures	Possible Protolithic Nature
<b>Serro, Monteiro and Verdes Amphibolites</b>	Fe-amphibolite	Strong positive anomalies of TiO <sub>2</sub> , Nb, (La/Yb) <sub>n</sub> and enrichment in Sr, Ni and Cr.	Mineralogical associations including Fe-hornblende, anorthitic plagioclase (with anomalous titanite (rich in Al-F) content), titanite, fluorite, F-apatite and alanite; Concentrations of sulfides (pyrrhotite, arsenopyrite, chalcopyrite, Co-Ni-tollingite) and scheelite.	Intra-plate alkaline basalts originated from metasomatised enriched mantle portions;  In interface with these alkaline amphibolites, there are green phyllitic facies with mineral assemblage equivalent to listvenitization products related to carbonate and potassic alteration of mafic precursors.
	Ca-Mg-amphibolite	Ratios of Zr/Y and (La/Yb) <sub>n</sub> .	Amphibolites with magnesium (calco-magnesian amphibolites with Mg-hornblende) mafic precursor are compact or with plagioclastic felsic segregations.	M.O.R.B. basalts and continental tholeiites.
<b>Chloritic rocks with mafic ultrapotassic precursor or superimposed potassic metasomatism in Santa Justa</b>		Peralkaline fluids influence and Nb/Y relative enrichment;  The geochemical domain established was <i>traqui-andesite</i> .	Ultra-potassic subalkaline nature, with microveins of potassic-feldspar and apatite.	Fenites.
<b>Serro, Santa Justa, Valdarcas, Fulão and Verdes felsic metavolcanics and granular related terms</b>		Felsic to intermediate composition rocks with calc-alkaline to transitional character;  Banded sulfides.	Contain quartz, alkaline feldspar and fengitic muscovite ± flogopite, with significant actinolitic amphiboles;  Macroscopic terms suggest a textural volcanogenic affinity:  Laminated felsophyric tuffs;  Devitrification products with evidence of polycyclic recrystallization;  Granular rocks and pelitic feldspathic facies with isotropic granular matrix and likely volcano-sedimentary nature (equivalent to leptites).	Lavas, pyroclastites and subvolcanic rocks (volcanogenic affinity) of felsic to intermediate and calc-alkaline to transitional magmas.
<b>Tourmalinites</b>	<b>Stratiform T. – Cumieira, Duas Pontes, Serro and Monteiro</b>	Detritic geochemical signature.		Detrital sediments (?).
	<b>Peri-amphibolitic T. – Monteiro and Verdes</b>	Sr, Nb and Ta contents in tourmalinites are consistently higher (mica-schists as background);	With various modes of occurrence in interface with alkaline mafic amphibolites:	Identical patterns have been reported in high-T hydrothermal fluids, vented from current submarine smokers;  Primordial plain exhalative genesis.

Table 1 – Discrimination of lithotypes ordered according to their space configuration. (This data was compiled from Dias & Leal Gomes (2013a), Dias & Leal Gomes (2013b), Dias (2011), Dias & Leal Gomes (2007)). (Continuation.)

		Fixation tendency of Sn, W and As. Massive tourmalinites conditioned to interface with alkaline amphibolites: low REE contents, high (La/Yb) <sub>n</sub> , positive Eu anomaly.	Phosphatic tourmalinite with apatite ocellar arrangement around individual and aggregate tourmaline crystals (oscillatory precipitation); Massive tourmalinite with fine grained tourmaline and fusiform clusters of acicular crystals; Tourmaline dispersed in the amphibolitic matrix and quartz-tourmaline breccias.	<b>Note:</b> The alkaline mafic amphibolites were considered as proto <i>roof-rocks</i> ; Mica-schists, here seen as regional psammopelitic background.
<b><i>Quartzites and quartzphyllites</i></b>		Muscovites and tourmalines with high V and Ba average content; Negative Ce anomalies.	Greenish mica, lollingite, arsenopyrite and native Bi relatively abundant; Tourmaline appears usually dispersed in modal content below 5%, higher concentrations in beds arranged in parallel surfaces as tourmalinite-quartzite alternation rhythms.	Enrichments in sedimentary nature lithotypes with higher levels of organic matter are comparable to increments observed in current hydrothermal fields, and may be exhalative sourced under redox conditions and low values of <i>fO<sub>2</sub></i> ; In <i>Covas Dome</i> were identified “smoker” structures, lithified in heterogeneous sequences with metasomatized sulfide, sulfate and carbonates.
<b><i>Metapsammitic rocks with sedimentary organic matter (Lydites and black shales) and phosphates in Cumieira, Picoto do Carvalho and Monteiro</i></b>		Significant negative Ce and Eu anomalies (normalized to chondrite); Metals enrichment (Ni, Cu, Zn, Co, As) and high MnO contents are more distinct in friable black shales; Moderated Al/(Al+Fe+Mn) values and the U and P; Gossanous metaphosphorites exhibit Mn and Fe/Ti locally high.	Lydites and black shales often with Al and Fe phosphates as porous nodules, and phosphoric gossanous facies; Vanadiferous coarse tourmalines occur dispersed in lydite levels conditioned to beds rich in organic matter.	Primordial chemical precipitation; Precipitation from sea water with or without hydrothermal mixture; Chemical sediments; Hydrothermal processes;
<b><i>Calc-silicate rocks and metamorphosed hydrothermalites</i></b>			Banded rocks with calc-silicate mineralogy (plagioclases with almandine-spessartite and apatite) similar to <i>skarns</i> ; Cryptocrystalline rocks with quartz and apatite; Almost monomineralic rocks: grossularites, epidotites, pyroxenites and idocrasites and more heterogeneous products differentially enriched in Ca, Mg and Fe silicates.	Late metamorphic-metasomatic segregation (?); <i>Green silica rock.</i>

Table 1 – Discrimination of lithotypes ordered according to their space configuration. (This data was compiled from Dias & Leal Gomes (2013a), Dias & Leal Gomes (2013b), Dias (2011), Dias & Leal Gomes (2007)). (Conclusion.)

<p><b><i>Heterogenous phyllitic and quartzphyllitic rocks</i></b></p>		<p>At the top of the mineralized <i>skarn</i> horizons:          Micaceous tourmalinites with coarse tourmaline porphyroblasts and apatites, positioned at metamorphic segregation interfaces;          Tourmaline and garnet biotites and banded micaceous quartzite with coarse tourmaline (Ventosa).</p>	<p>Late metamorphic-metasomatic segregation (?).</p>
---	--	---	--

#### 2.1.2.1.1. Serro

Between 1970 and the beginning of 1980 these deposits were subjected to geophysics exploration (magnetic methods), by the *Serviço de Fomento Mineiro* (S.F.M.) using as magnetic guidance the anomalous high magnetic susceptibility of some stratiform horizons of iron sulfides (particularly pyrrhotite) that have economic contents of W ores. Then the S.F.M. detected several magnetic anomalies not only in *Covas Dome* but also in adjacent areas. One of these anomalies is situated near Serro (A. Rocha Gomes, personal communication (1981) *in* Dias & Leal Gomes (2008)) in terrains separated from the Covas antiform structure by important reverse faults (azimuth N-S to NW-SE) (fig. 1).

Therefore and besides what was written above about Serro, these authors also highlighted other Serro features. The most abundant metasedimentary formations throughout the Serro succession exhibit a psammopelitic nature – andalusitic mica schists and biotite quartzphyllites. These are clearly distinct from the main sub-units with anomalous texture and composition shown on table 2, which summarizes the most relevant hypotheses for the primitive nature of these rock types based on petrographic and geochemical criteria.

Dias & Leal Gomes (2007) enhanced the expression of a bimodal volcanism (previously to the metasomatism induced by granitoid intrusion (Dias & Leal Gomes, 2013b)) (fig. 7), predominantly felsic, with metalogenic potential, capable of producing the high concentration of sulfides observed in metamorphites in the Serro sequence, located in Silurian terrains (Dias & Leal Gomes, 2013b). However Dias & Leal Gomes (2008) recognized some limitations that resulted from the fact that these formations correspond to metamorphites submitted to the main Variscan thermotectonic evolution culminating with the generation of a  $S_3$  highly penetrative cleavage followed by cordierite blastesis.

The establishment of a volcanogenic-exhalitic affinity is supported by:

- Some high Sr and Ba values may be related with peculiar accessory minerals especially phosphates;
- Identification of relic porphyroid and volcanoclastic textures;
- Presence of high amounts of modal Fe-sulfides;
- Albite transformed phenocrysts;
- Unusual Sc, Zn and Mn minerals;
- Tourmaline phyllites with schorl-dravite and Mn-almandine and lithotypes of jaspilitic trend;
- Projections distribution of chemical constituents normally characterized by a lower mobility in Nb/Y - Zr/TiO<sub>2</sub> diagram showed the following lithological correspondences:
  - Amphibolic rocks and felsic granular rocks – protogenic rhyodacite / dacite nature;

- Metavolcanic rock with sulfides – andesite;
- Amphibolite with felsic segregations – basalt.
- In tourmaline phyllites, some accessory sulfides expressing Zn and Pb, are consistent with the exhalitic character attributed to at least some of these formations ((Slack (1996) and Leal Gomes *et al.*, 1997) in Dias & Leal Gomes (2008)).

In Dem (Serro), lollingite with Ni and Co was also identified suggesting the bimodal character signature. In the same local, a grossular garnet (hessonite  $[Ca_3Al_2(SiO_4)_3]$ ) that contained celsian (Ba feldspar –  $BaAl_2Si_2O_8$ ). This data suggested a signature of SEDEX with primitive Ba remobilization that would have been incorporated by a feldspar generating celsian during a metamorphic-metasomatic process (Souto, 2017).

Therefore, the best expression of Silurian (bimodal (fig. 7)) protovolcanism (oxides – mafic volcanites (fig. 7), and sulfides – felsites and felsophyres) in the western area of C.D.F. found until now seems to be settled in the sector of Serro (fig. 1).

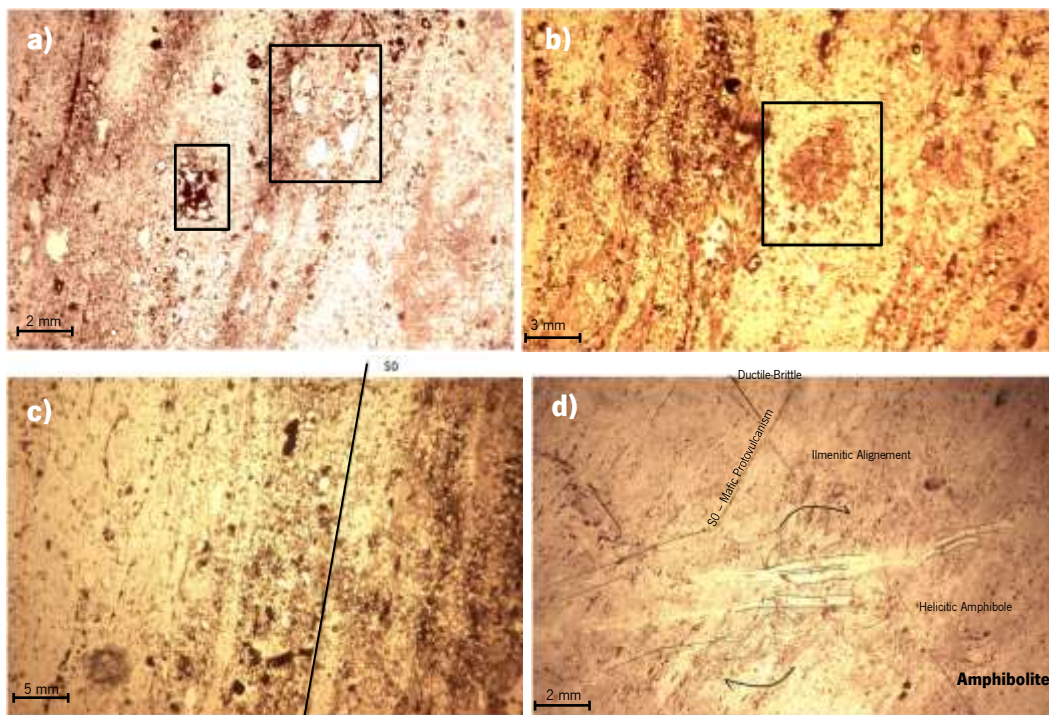


Figure 7 – Transmitted light microscopic (uncrossed polarizers) images of Serro mafic volcanism evidences. **a)** Volcanoclastic protholitic texture. **b)** Porfirc protholitic texture – zoned protoplagioclase enhanced in the black perimeter delineated. **c)** Heterogenous laminar stratification from probable volcanogenic affinity. **d)** Features identified in an amphibolite from Serro. (C. Leal Gomes personal communication, 2019)

Table 2 – Discrimination of lithotypes ordered according to their space configuration in Serro sector (from Dias & Leal Gomes, 2008).

Petrographic type - metamorphite	Geochemical indications for a non phyllitic nature	Typomorphic minerals and textures	Possible protolithic nature
Amphibolites with plagioclasic segregations	TiO <sub>2</sub> =1,91% Fe <sub>2</sub> O <sub>3</sub> = 8% Eu/Eu* = 0,88 (La/Yb) <sub>n</sub> = 2,18 P <sub>2</sub> O <sub>5</sub> =0,27%	scheelite	Late metamorphic segregation to metasomatic terms
Nodular mica schists		andalusite and/or corundum	Metasedimentary pelitic
Quartz-phyllites		ilmenite, REE phosphates., tourmaline	Metasedimentary psammopelitic-exhalitic
Plagioclase felsic phyllites	Ti=407ppm	thortveitite, REE phosphates.	felsite
Felsic phyllites with sulfides	S = 7,19%; Fe = 8%	pyrotite>pyrite>>arsenopyrite	felsite, tuff (?) or felsophyry – volcanite (porphyry)
Clastic quartz-phyllites occasionally enriched in sulfides		pyrotite>pyrite	Volcanoclastic facies
Gossan siliceous rocks		Rare Fe-oxides and sulfides (pyrite, sphalerite, chalcocopyrite, galena)	Facies of jaspilitic appearance
Metamorphized granular rocks	Eu/Eu* = 0,39 (La/Yb) <sub>n</sub> = 4,60-6,36	molybdenite (?)	Primordial porphyry rocks (?) – intermediate composition
Layered amphibolites	SiO <sub>2</sub> =72,7 – 74,1	zircon, ilmenite, Ti-spinel, sphene	Hybridized volcanogenic lithologies
Phyllitic facies with argillic alteration	Zn = 502 ppm Pb = 162 ppm	Fe and Ti oxides; secondary Fe, Zn, Pb and Cu sulfates and phosphates	Late argillic alteration products
Brecciated felsic facies		pyrotite>pyrite>>arsenopyrite	Venular and silicified products
Garnet-tourmaline phyllites		spinel, Mn-almandine, dravite	exhalites
Tourmaline phyllites with sulfides		pyrite>>pyrotite, arsenopyrite, sphalerite, galena, molybdenite, schorl-dravite	Late hydrothermalized exhalite
Mica schists		andalusite-sillimanite	Metasedimentary pelitic

### 1.1.2.1.1. Fulão

In Fulão (fig. 1) C. Leal Gomes (personal communication, 2019) identified a contact that suggests to be a black shales – V.M.S.-SEDEX contact. Regarding to him, zebra-alike facies type was found (figs. 8 and 9), also a dismembered felsitic facies included in a riodacitic metatuff and other arguments present in figure 8.



Figure 8 – Zebra-alike facies type from Fulão sector. The numbers indicate each image profile location. (Personal communication of C. Leal Gomes, 2015)

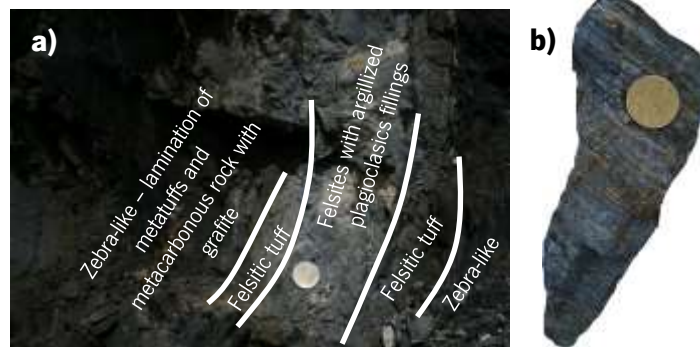


Figure 9 – Felsic metavolcanoclastic rocks from Fulão sector. **a)** Outcrop observations. **b)** Hand sample. (Personal communication of C. Leal Gomes, 2015.)

#### 2.1.2.2. Covas Dome

As previously quoted the *Covas Dome* Formations (C.D.F., fig. 1) correspond to a domain of thrusts and folds determined by tangential activity of the 2<sup>nd</sup> phase of Variscan deformation, that has as reference structure the *Covas Dome* (at the Coura river western margin) (Dias & Leal Gomes (2013b) and Dias & Leal Gomes (2007)). This structure is located at an eastern sector of C.D.F. in comparison with Serro sequence. In the *Covas Dome* area, the diversity of primitive indications of volcanogenesis in C.D.F. terrains are the greatest found until now (Dias & Leal Gomes, 2013a). The mega-structure known as *Covas Dome*, Silurian rocks folded in antiform, is a doubly plunging antiform of the 3<sup>rd</sup> Variscan folding phase superimposed over an earlier recumbent sheath mega-fold (2<sup>nd</sup> Variscan folding phase), where Cerdeirinha orebody is located at the summit in the hinge zone, in a normal limb position attributed to the 2<sup>nd</sup> Variscan folding phase (figs. 1 and 10) (Dias & Leal Gomes (2007), Leal Gomes *et al.* (2011) and Dias (2011)).

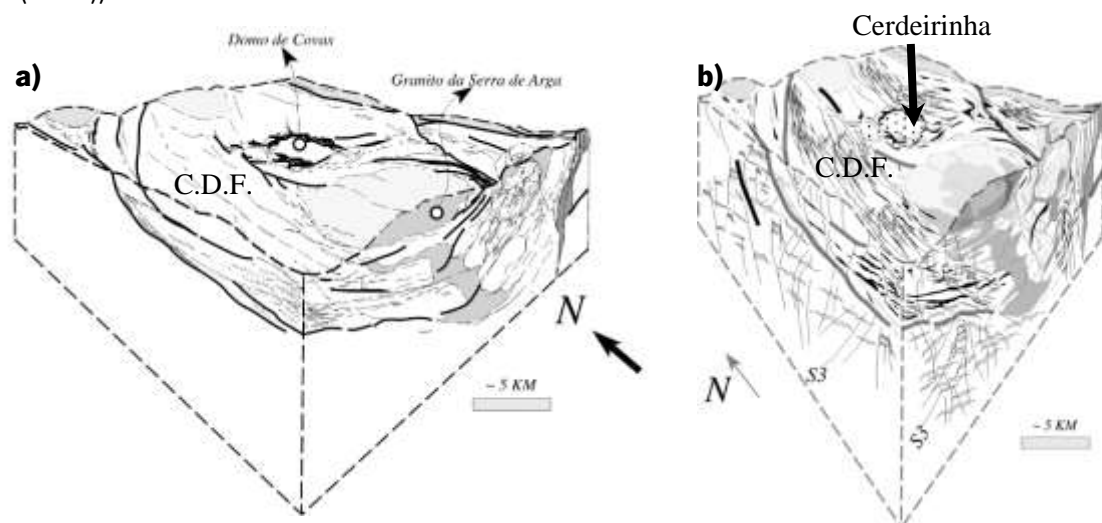


Figure 10 – Representative schemes of *Covas Dome* formation. **a)** Representative scheme of the former deformation phase, tangential deformation of the dome, during the 2<sup>nd</sup> Variscan deformation phase. **b)** Representative scheme of the second deformation phase, the dome shortening, during the 3<sup>rd</sup> Variscan deformation phase. (Modified after Dias *et al.* (2013a).)



As previously demonstrated, the review of protolithic nature of Silurian terrains in the compartment between Orbacém thrust and Vigo-Réguia shear (fig. 1) highlighted a polygenic volcanosedimentary and sedimentary-exhalative nature for the C.D.F., thus, suggesting possibilities for diversification of models that refer to regional petrogenesis, and testing the recognition hypothesis of SEDEX affinity for stratabound deposits of *Couto Mineiro de Valdarças*, prior to metasomatism induced by granitic intrusion. Although superimposed metamorphic-metasomatic remobilizations remain as the most significant in the spatial redistribution of W contents, there are evidences of volcanogenic-exhalative signatures suggesting the contribution of a syngenetic metalliferous stock, similar to that observed in current hydrothermal fields (Dias & Leal Gomes, 2013b). A cross-section of *Covas Dome* can be seen on figure 11.

#### 2.1.2.2.1. Typical mineralization of *Covas dome*

In *Covas Dome*, tungsten ores occur under the shape of scheelite and wolframite in amphibolic, sulfide-rich, plagioclastic, carbonated and silicic gangues. Some paragenetic analysis data on the mineralizations of this compartment, collected by Bayer (1968) in Dias & Leal Gomes (2013b) and Dias (2011), represented at least 4 generations of wolframite (3 of which hubnerites and the 4<sup>th</sup> with ferriferous composition replacing scheelite in pseudomorphosis) and 3 generations of scheelite (Dias & Leal Gomes, 2013b):

- The earliest appears disseminated in calc-silicate beds with wollastonite and vesuvianite;
- *Generation 2* is represented by automorphic disseminated scheelite in *skarn*, generally pseudomorphosed by ferberite;
- *Generation 3* concerns epitaxial scheelite around wolframite, observed in plagioclastic and apatitic lithologic supports.

Sulfides occur in massive horizons below a *crust-shaped* and impermeable horizon represented by *green silica rock* and coexist with Ca sulfates, apatite, amphibole and plagioclase.

- Pyrite is the most abundant primary sulfide occurring in *bird-eye* and botryoidal textures (with Co/Ni relations with values close to 10, typical of primary volcanogenic pyrites) (Dias & Leal Gomes, 2013b).
- Arsenopyrite, trendily automorphic, appears in epitaxy in relation to lollingite. And galena inclusions in zoning oscillatory arsenopyrites (Dias, 2011).
- Pyrrhotite also shows contrasting habits:
  - Earlier crystals are hexagonal and relate persistently with arsenopyrite;
  - Common intergrowths of pyrrhotite-marcassite associated with some isocubanite;

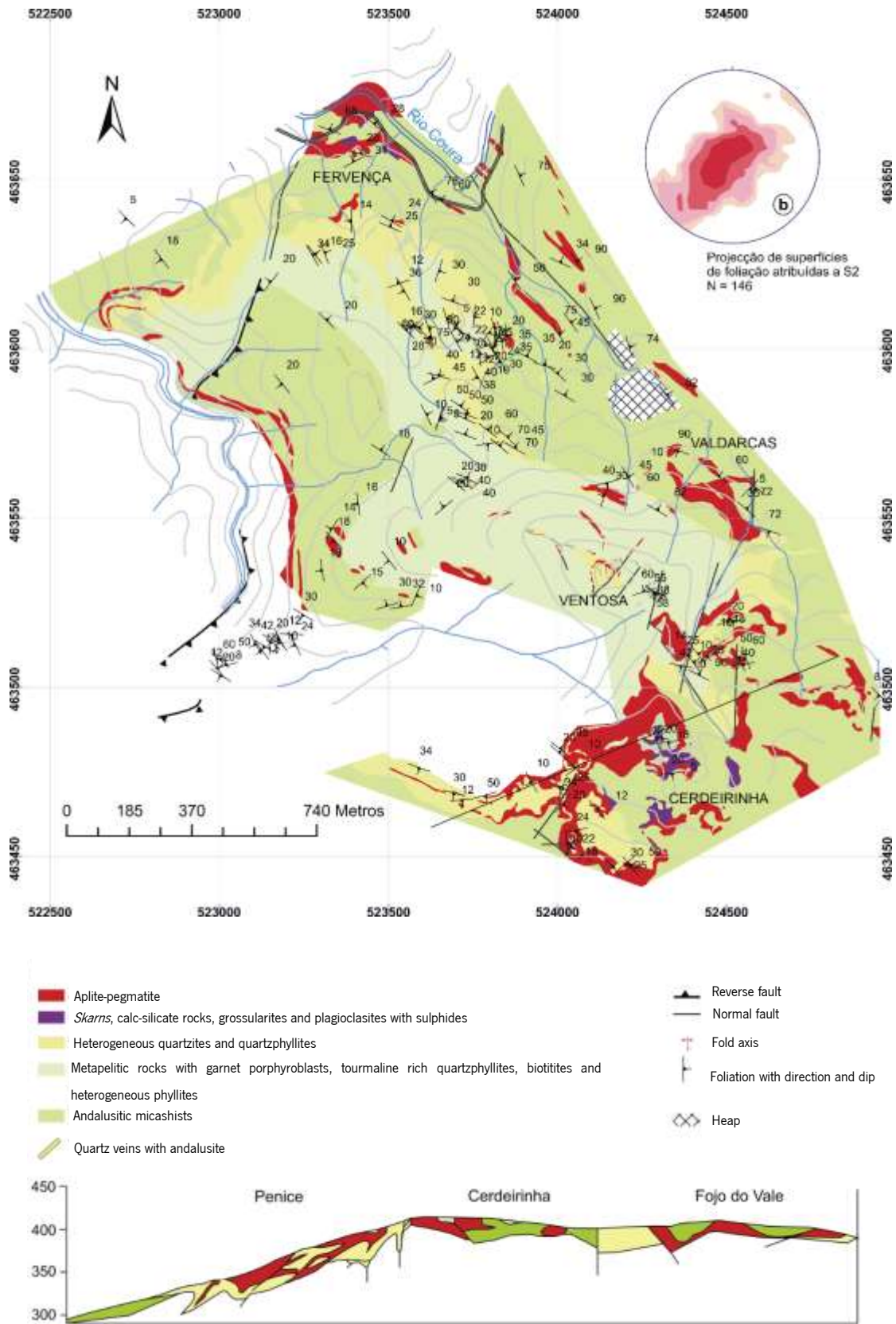


Figure 11 – *Covas dome* geological map and interpretative profile. (Modified after Dias, 2011)

- Sphalerite is associated with chalcopyrite of which reveals exsolutions, with various values of Zn/Cd ratio near of volcanogenic phases;
- Native bismuth (Bi) and bismuthinite were identified as inclusions in lollingite, garnet, scheelite and wolframite. Besides this, native bismuth was also found as inclusions in relic silicates of some pyrrhotite ranges (being sometimes observable the periferic crystallization of wolframite). However, wolframite is the main Bi carrier (and possible zavaritskite that carriers Bi and is rich in F and Fe).

Other referred phases are mackinawite, gersdorffite, tetradymite, nickeline, rutile, ilmenite, magnetite and skutterudite.

#### 2.1.2.2.2. Key character of Cerdeirinha tungstiferous deposit

Due to the lower intensity of the  $D_3$  deformation, in a *shadow zone* between the Arga and Covas granite massifs (fig. 12), previous  $D_2$  structures are still preserved in a position close to the original one (Dias, 2011), where lithified primitive devices compatibles with *smoker-like* fumarolian emergence were identified (Leal Gomes *et al.*, 2011). Besides this, Leal Gomes *et al.* (2011) suggest that, in southern Cerdeirinha's open pit, impermeable competent and more refractory formations (*cap-rock* – represented by a cryptocrystalline facies with *green silica rock*) could retain the syngenetic precursors devices (lithifications of the original exhalative interface) or early metamorphic-deformational ones, at least from the geometrical point of view and eventually through mineralogical and geochemical signatures.

Regarding Leal Gomes (1994) *in* Leal Gomes *et al.* (2011), even after the most intensive Variscan deformation, the *Covas Dome* Formations, mainly the ones exposed at the Cerdeirinha mine south slope, preserved intact

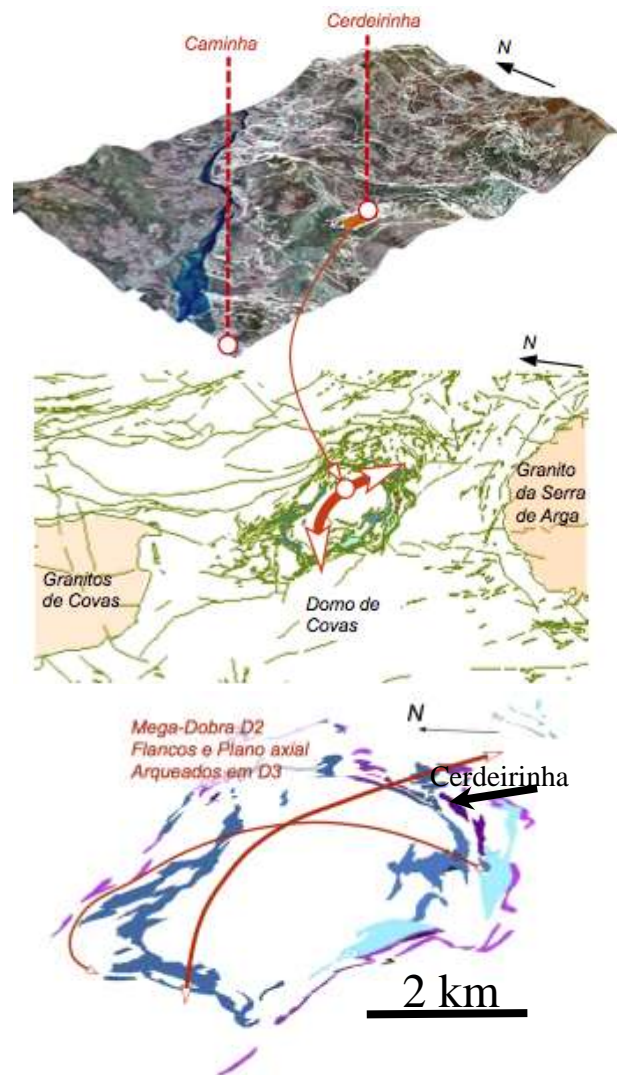


Figure 12 – Structural location of Covas Dome sector in the context of deformational heterogeneity. (Modified from Leal Gomes *et al.*, 2011.) Competent lithologies that set the antiform structure: siliceous metacarbonate rock, amphibolites, polygenic psammitic rocks, polygenic tourmalinites, massive to disseminated sulphide levels, and early aplite-pegmatites. Note: representation of 3D schematic non-isometric with graphic scale, deduced by the cartographic distance between Cerdeirinha and Caminha – about 12 km.

protholitic features. These may be observed in psammitic horizons, compacted calcsilicate rocks, amphibolite and tourmalinites (Leal Gomes *et al.* (2011)). At Cerdeirinha mine (figs. 1 and 12), tungsten mineralization, although related to metasomatism, may be considered partially related to Silurian volcanic activity (Leal Gomes *et al.*, 2011). There are resthitic textures and mineralogical and geochemical signatures suggesting the importance of an initial metal discharge of exhalative type (Leal Gomes *et al.*, 2011). The southern slope of Cerdeirinha open-pit contains some structural organizations lithified correlated with smoker anatomies in a lithological transition between massive sulfides and *green silica rock*, which were also described as proto-tubes with sulfides and phosphatized sulfate walls with anhydrite relics (fig. 1) (Leal Gomes *et al.* (2011) and Dias & Leal Gomes (2013b)). Iron sulfides are the main constituents plus anhydrite, amphibole and polymetallic mineralization of W, Fe, As, Bi > (Au), Te, Zn, Cu, Pb. Scheelite is ubiquitous, and sometimes, in a narrow space and time interval, its association oscillates between, oxidative assemblages with ilmenite and, reductive assemblages with interstitial sulfides. Leal Gomes *et al.* (2011) considered this arrangement as the result of evolution of a SEDEX interface (with normal exhalative polarity –  $S_0$ ).

Regarding the variability found Leal Gomes *et al.* (2011) limited to 5 stratabound rock-type (fig. 13):

- 1 – Quartzphyllite with disseminated sulfides;
- 2 – Greenphyllite with pyrrhotite + pyrite + marcassite ± tourmaline that laterally evolves to silic-metacarbonated rocks (calcite with porous proto-textures filled with vesuvianite and wollastonite – prototravertines (?));

3 – *Green silica rock* – cryptocrystalline rock with apatite + quartz ± amphibole association with Fe sulfide

disseminated – lithology with colloformic textures that correspond to a possible primitive impermeable crust;

4 – Almost massive sulfide level co-existing with calcium sulfate and minerals carriers of polymetallic mineralization, including W – correspond to a succession of *small mounds* with upwards convexity that can be equivalent to *mounds* that resulted from the collapse of anhydritic cones or primitive sulfate chimneys (fig. 14);

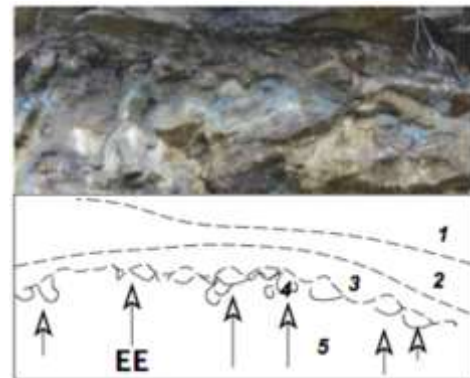


Figure 13 – Apical transition of the sulfides unit in the Cerdeirinha south open-pit. Short side of the photo = 2.5m. Lithotype petrography from 1 to 5 referend in the text. EE – exhalation axes = gravitic polarity deduced. (Leal Gomes *et al.*, 2011)

5 – The most complex unit from the structural and paragenetic point of view. With Fe sulfides, Ca sulfates, apatite and amphibole as well as W, Fe, As, Bi > (Au), Te, Zn, Cu, Pb polymetallic mineralizations. In this unit there are geometric dispositives similar to sulfate-sulfide tubes; at least in the *practical* point of view they were considered as *smokers* (fig. 14).

The same authors noticed that in the most compact Fe sulfide masses (unit 4), the intergrowth of pyrrhotite-marcassite with some isocubanite associated are frequent. In the same porous spaces of the intergrown pyrrhotite with silicates, anhydrite was observed (fig. 15). Besides this, Bi is present since inclusion or exsolution in arsenopyrite until interstitial dissemination in the others sulfides. Venular native tellurium (Te) or bismuth telluride were observed in association with native Bi (fig. 18). At last, some more massive pyrrhotite volumes contain colloformic textures, were it was seen interstitial native Bi (Leal Gomes *et al.*, 2011).

The attribution of a primordial exhalative origin of a structural dispositive under an orogenic system is always discussable, mainly, in cases that several deformation phases, metamorphism, granitic intrusion, with metasomatism associated, originates transformations since the primitive stage (still *smoker*).

Regarding Leal Gomes *et al.* (2011), in this open-pit, three stages were observed (at least partially) in this sequence, where was also verified in a macro and meso exhalative geometric display that seems to be preserved:

- I. Paragenetic and geochemically, a quick change and sometimes concentric of typical mineralogical associations of oxidative-reductive environment associations. The generation of scheelite would be a predictable scenario under syngenetic conditions of thermal and compositional interface, similar to the ones found in present hydrothermal fields:

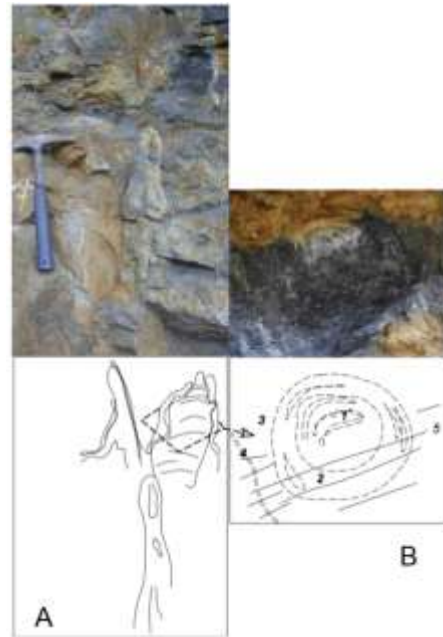


Figure 14 – Structures similar to chimneys – lithified anatomies in the 5<sup>th</sup> unit, and whose geometry was preserved in the previous evolution. A – Vertical exposition of the columns with phosphatic sulfate walls but with anhydrite relics, occasional presence of barite and more rarely svambergite; the nuclear portion is richer in sulfides, mainly heterogeneous pyrrhotite. B – Parallel exposition to stratification correspondent to a perpendicular intersection to the previous one. 1 – Core richer in pyrrhotite; 2 – Border richer in phosphatic sulfate; 3 – Compact phyllitic material lithified by recrystallized silica with abundant disseminated sulfides; 4 – Venules with apatite and remobilized sulfides that metasomatized the previous structures. 5 – Overprinted and parallel foliations (probably Variscans S. and S<sub>2</sub>) with transposition of mica, chlorite and pyrite. (Leal Gomes *et al.*, 2011)

I.1. – The upward drained fluids and their release in the seawater, would promote the chimneys length increase, starting by the anhydrite precipitation from *hot plume – cold seawater* interface. Quickly, the exhaled hydrothermal solution would transit

from acidic and reduced conditions, with  $H_2S \gg SO_4$ , at high temperatures, to typical seawater conditions found in great depths (little above the  $0^\circ C$ , alkaline and oxidative, with  $SO_4 \gg H_2S$ ). The ascension of the

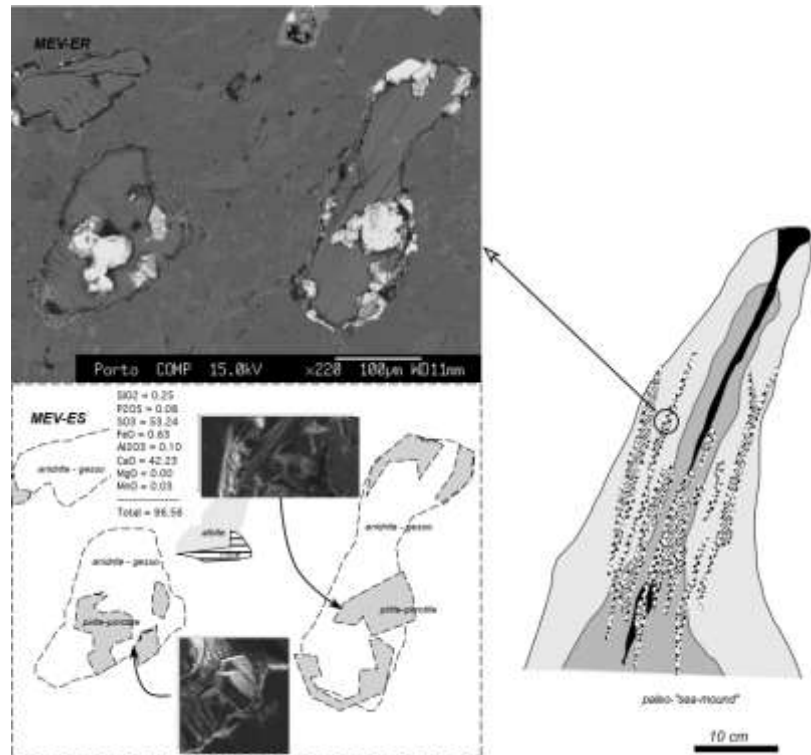


Figure 15 – Preserved proto-small-channels, fulfilled with pyrite-pyrrhotite and by anhydrite in transition to gypsum – microprobe backscattered electrons analysis. Note: in the image of secondary electrons, polyhedral crystals of isocubanite were observed. (Leal Gomes *et al.*, 2011)

hydrothermal solution plume would succeed after the outer cold water penetration in the porous cones and sulfates and sulfide accumulations previously formed. Interactions like this seems to be lithified in the columns with peripheral primordial sulfate and inner sulfide (fig. 14 – A). The cryptocrystalline and recrystallized *green silica rock* (level 3 in fig. 13) would be the evidence of a *crust-shaped* and impermeable original level.

I.2. – Chimneys would grow upwards and the walls from the base would become thicker through time, due to the oscillatory sulfides and sulfates precipitation – this would be the explanation for the sulfide-sulfate alternation (fig. 14 – B).

I.3. – Dominance of pyrrhotite and lower quantities of isocubanite, chalcopyrite and marmatite that would have formed at high temperatures ( $\pm 300^\circ C$ ).

II. During and after the pyrrhotite and Fe, Cu and Zn sulfide deposition also another mineralogical association developed, with much lower volume and composed by sulfur-arsenide, Bi and Au. This association would have been deposited from the highly reduced

and latter fluids that propagated by diffusion through the porous in the cones and chimneys.

- III. During pyrrhotite weathering in seabed other minerals were formed from colloidal particles clusters, that were established in pH gradient between acidic waters retained in the porous and seawater in the surrounding.

Next it is possible to see the stratigraphic column elaborated by Dias (2011), regarding Cerdeirinha (fig. 16).

# Cerdeirinha

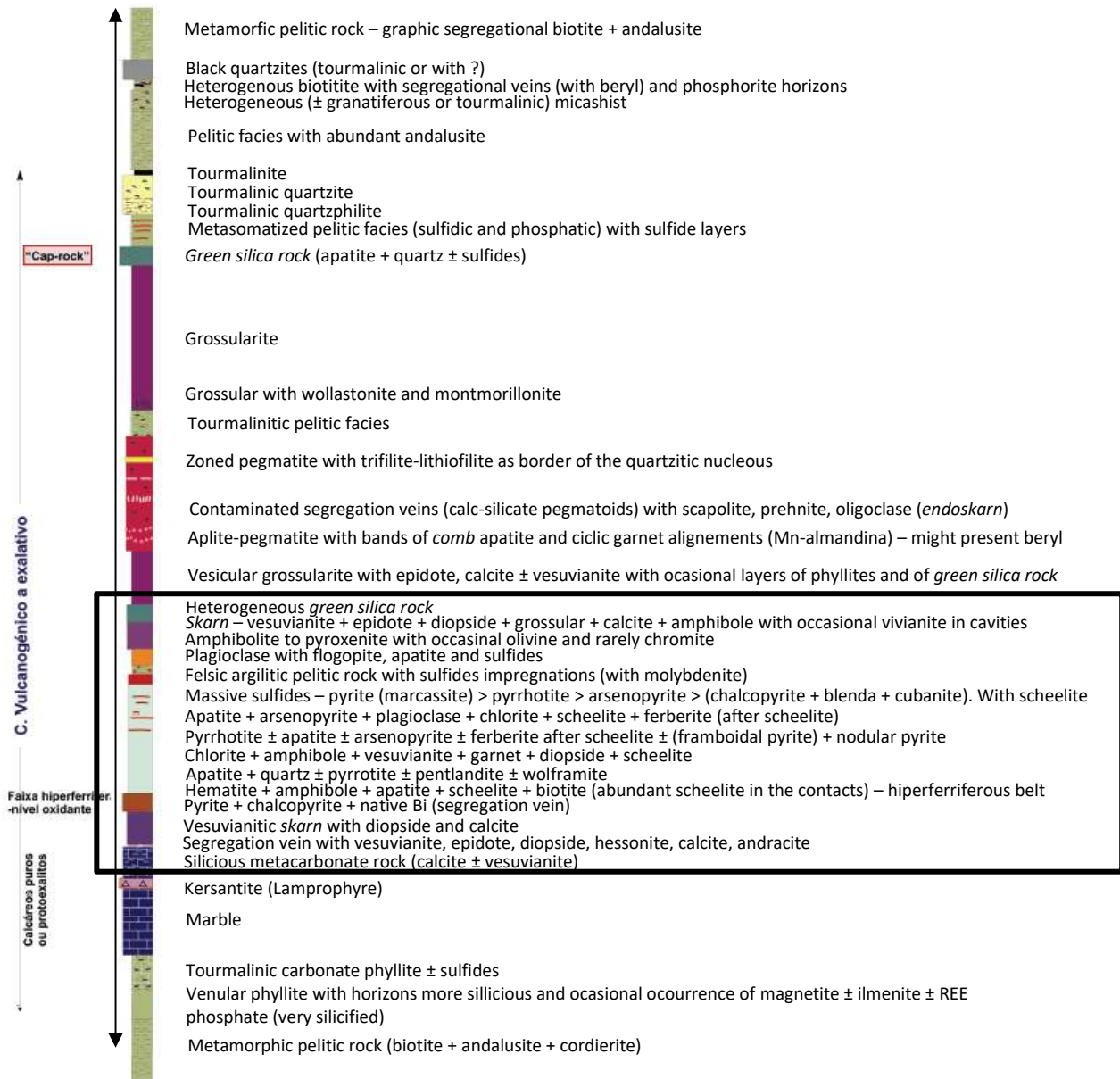


Figure 16 – Stratigraphic column for the Cerdeirinha sector. The dark lines limit the lithology observed. (Modified after Dias (2011).)



2.1.2.3. *Au and W contents supporting exhalative protogenesis hypothesis*

In what Au might concern, Dias & Leal Gomes (2015) showed that in the Silurian sequence of Serra de Arga the global Au content might be high (fig. 17). Considering the host protolithic nature, the development of gold concentrations is envisaged as a result of a combination of processes. A significant gold input appears to be related with felsic-intermediate volcanic episodes (Serro) when highly reactive Fe-S rich hydrothermal fluids led to significant exhalative sulfide deposition. Gold introduction is also correlated to a mafic alkaline volcanic stage and to contemporaneous hydrothermal processes responsible for extensive phyllosilicate formation (likely, listvenites) (Monteiro). Au relative enrichments were also achieved through the establishment of proximal SEDEX systems responsible for seafloor sulfide deposition in the Covas area. The metalliferous fluids vented into distal reduced sedimentary basin compartments (Cumieira and Picoto do Carvalho) might have led to the subsequent introduction of gold in contrasting sediments of exhalative affinity. The development of orogenic Au mineralizations related to shear zones of Late-Variscan age, was likely favoured by the existence of these predecessor metal stocks (Dias & Leal Gomes, 2015).

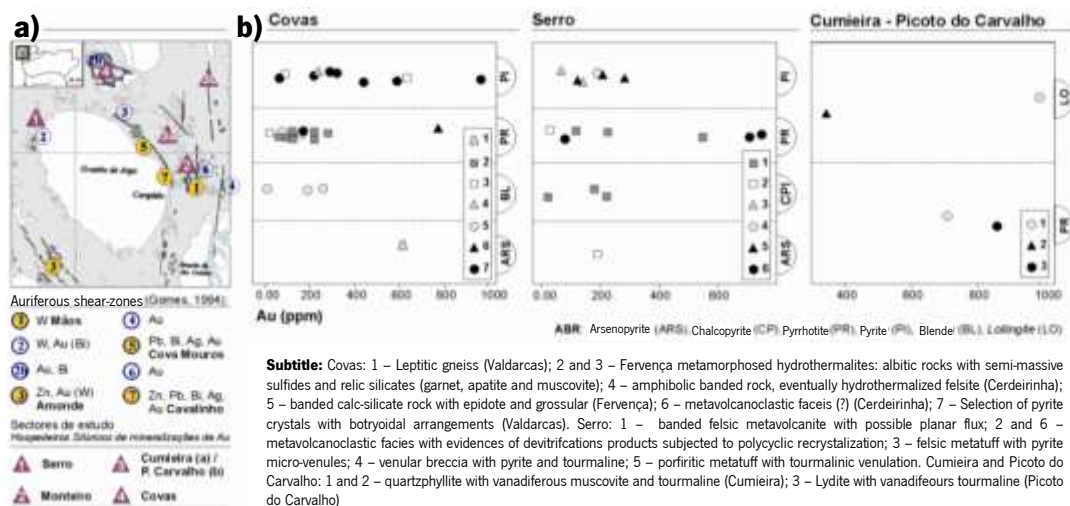


Figure 17 – A – Localization of the studied sectors. B – Variation of the Au content depending on the sulfide host and the carrier lithology. (Modified after Dias & Leal Gomes (2013b).)

The identification of high Au contents in Cerdeirinha arsenopyrites, auriferous particulate in stratiform tourmalinites and simultaneously the achievement of multiple geochemical indexes on whole rock analysis (lyditized black shales (with 0.6 ppm) and listvenitic alteration products with (1.2 ppm)) suggested availability of this metal in the precursor exhalative environment (Leal Gomes *et al.*, 2011).

The most heterogeneous arsenopyrites present domains with high contents of Au, normally in the same domains in which there are also Bi and Te (fig. 18). Although, very rarely, small punctuations of native gold (< 5 µm) were also identified (Leal Gomes *et al.*, 2011).

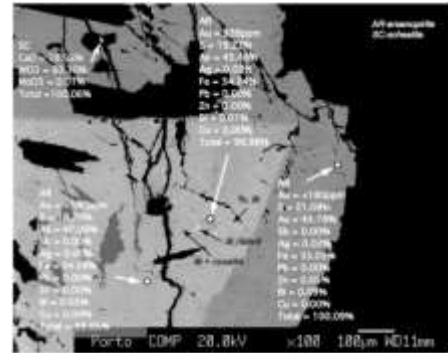


Figure 18 – Punctual analysis results of a heterogeneous and early arsenopyrite, with inclusions of scheelite, that was latter reequilibrated with a mineralization of Bi and Pb. Note: Te and Bi is a venular body with heterogenous distribution of tellurium and bismuth. (From Leal Gomes *et al.*, 2011).

The main W mineralization detected in Serra de Arga (fig. 19) includes scheelite and wolframite and also rarely W-molybdenite. It is hosted in various lithologies: calcsilicate rocks, amphibolites, leucosomes and quartz veins in late-D<sub>3</sub> shear zones. Primary W mineralization, possibly syngenetic to ortomagmatic, and later metamorphic to metassomatic remobilizations allowed the recognition of trends of paragenetic succession and chemical variation, related to *f*O<sub>2</sub> changes (Dias *et al.* (2010) and Dias & Leal Gomes (2010)).



Figure 19 – Localization of the diverse tungstiferous mineralization occurrence in the geographic domain involving the granitic massif of Serra de Arga. (From Dias & Leal Gomes, 2010)

In this region the W concentration processes have been mainly attributed to the metasomatism of contact with aqueous/hydrothermal-magmatic fluids originated from fractionated granites in the presence of carbonated protoliths (permeable and with high reactive potential). Some tungsten indices may however be associated with exhalitic and evaporitic preconcentrations. Authors such as Plimer (1987) in Dias & Leal Gomes (2010) have shown the relationship between W concentration ( $\pm$  Pb-Zn-Ag, Sn, Cu, Ag, Au, Co, U and base metals) and lithological associations considered typomorphic of a sedimentary-exhalitic and volcanogenic-exhalitic origin in sequences with stratiform tourmalinites, rocks rich in spessartite, BIF and rocks rich in granite. Similar associations are observed in some locations of the Silurian terrain surrounding the Serra de Arga (Dias & Leal Gomes, 2010).

In all non-venular occurrences of W minerals, protolithic volcanogenic facies (felsic volcanites and ortho-amphibolites), exhalitics and metacarbonate facies are present. The introduction of W into the system possibly resulted from the exhalation and interaction of hydrothermal systems with volcanites, as well as an orthomagmatic state related to alkaline magmas. The mineralization of Covas primary support was remobilized as a result of metamorphism and regional metasomatism associated with intrusion of syntectonic granites. The predominance of paragenesis with epidote and garnet correlates with the high

$fO_2$  of the late metasomatic stage. Under these conditions W is transported as F-complexes with alkaline ions, being wolframite the more stable ( $CaWO_4 + FeO + 2HF = FeWO_4 + CaF_2 + H_2O$  – pseudomorphic reaction) (Foster (1977) *in* Dias & Leal Gomes (2010)).

#### 2.1.2.4. Summary

The petrologic diversity recognized in these terrains and geochemical signatures of amphibolites and metavolcanites suggest that a possible metavolcanosedimentary protolithic succession may have continental *rifting* relatable signature. Its formulation would be related with early stages of crustal distension that presided the opening of the Paleothetys Ocean in the North Gondwanic margin during the Upper Ordovician – Silurian (between 390 and 420 M.y.) (Ribeiro *et al.* (2007) *in* Dias & Leal Gomes (2013a)), mainly in the distal segments (Dias & Leal Gomes, 2013a). This hypothesis, conveniently accommodates the found petrologic diversity and occurrence of exhalative events. Geochemical and mineralogical signatures deduced an exhalative distal character for sedimentary rocks bearing vanadiferous muscovite and tourmaline and others with high Mn and metals content. By possessing high levels of organic matter, they are also typical of reducing anoxic environments, predictably deposited in deeper compartments of rift-genic basin. Especially metasomatic phenomena adjusted for alkaline and potassic signatures seem to introduce in the previously established sequences, anomalies in concentrations of B, P and F. The widespread evidence of tourmaline may also relate to the role of these fluids. Because B has soluble behaviour in alkaline fluids, can easily be remobilized from metavolcanosedimentary surrounding rocks, occurring its precipitation either by inhalative substitution of pelitic and psammitic rocks in depth, or by exhalation of hydrothermal solution in seawater (Dias & Leal Gomes, 2013b). Dias (2011) was able to evidence some details of the primary evolution of these facies and also of the protolithic hydrothermal alteration related. Dias (2011) supports the rift-genic hypothesis evidencing:

- Alkaline rocks that were originated from the metasomatized portions of the mantle;
- Intermediate to felsic composition with calc-silicate to transitional character;
- Amphibolites related with M.O.R.B.-type basalts and continental tholeiites.

The stratigraphic register preserved in *Covas Dome* contains a lithological diversity whose genesis is compatible with the Silurian existence, of extensional intracontinental episodes, prior rift-genic with specialized mantellic sources (Dias, 2011). The volcanogenic outbreaks were polymodal and locally conditions for the abundant sulfide and syngenetic tungstates precipitation were verified (Dias, 2011).

Although this model explains several petrological and structural elements of a common geodynamics, the correlations still need the complementary geochronological data (Dias & Leal Gomes, 2013a).

In what Cerdeirinha might concern, its apical sulfide transition might really contain proto-sedimentar-exhalative interface with proliferation of *smokers* and *mounds* that would contain the W mineralization and the metallic assemblage of Fe – As – Cu – Zn and Bi – Te – Au, in interbedded metalliferous layers. In the beginning these flows would be spatially short in response to quick oscillatory variations of Eh and pH. The several stages of metasomatism strongly remobilized the initial structure and chemical organization. However, inside the thicker and more competent strata, lithifications of the original exhalative interface are still observable in normal polarity.

The syngenetic metalliferous stock was introduced during the basinal deposition (Leal Gomes *et al.*, 2011) and similar to what is observed in the actual hydrothermal fields (Dias *et al.*, 2013b). For instance, in Waimangu (New Zealand), there are highly W-rich silicate products precipitated, related with the *smokers* activity (50mg/Kg de W (Henley & Roberts (1983) *in* Dias (2011) and Evans (1993)). The connection of W mineralization to SEDEX environments has been suggested in various other metallogenic contexts, in particular deposits referred to as *Broken Hill-type* (B.H.T.), invoking a polyphaser mobility of fluids with mantle signature. In these deposits, the major tungsten outbreaks are associated with massive sulfide precipitation and occur in association with Ca-Fe-Al-Mg silicates, similar to *skarns* (Plimer (1984) *in* Dias (2011) and Dias & Leal Gomes (2013b). Below are listed some mineralogical signatures common to Covas and those situations described in Plimer (1984) *in* Dias & Leal Gomes (2013b):

- Scheelite and wolframite abundance in calc-silicate rocks, grossularites and amphibolites;
- Strong abundance of F-apatite and fluorite from the main mineralized levels;
- *Alkaline-carbonatitic* composition and mobility of elements such as Ti, Nb and Zr arising from protolithic hydrothermal alteration;
- Intercalated levels of stratiform tourmalinites and highly dispersed tourmaline throughout the metavolcansedimentary succession;
- Bimodal nature of volcanism in relation to riftogenic distension;
- Relatively thick enclosing psammopelitic metasedimentary succession;
- Occurrence of sulfide rich plagioclases;
- Evidence of a level impervious to fluid circulation – *cap-rock*.

In conventional models of these deposits, the escape of fluids and alkaline magmas occur along profound rift-genic faults, propagated in the upper mantle, in consequence of its decompression. Previous to fluids with this nature, the possibilities of remobilization of metals from the basinal metavolcanosedimentary sequences were particularly high, observing its easy combination with F. Discharge sites were *smokers* and *mounds* located on the seabed, occurring here the major accumulations of sulfides (Dias & Leal Gomes, 2013b). In turn, the increase in geothermal gradient, correlated with mantle emissions of fluids and basic magmas may induce crustal anatexis and hence production of acid magmas. The felsic volcanogenic sequences of Serro, relatively thicker in C.D.F., may represent evidence of this evolution that generally also relates to the increase of rift-genic distension. Invoking the geometric organization of the BHT-type deposits, the depositional context of Silurian terrains in Serra de Arga region may have the schematic, conceptual representation of figure 20 and a conceptual profile can be observe in the figure 21. This organization can accommodate in coherence successions of facies observed in the study areas of Serro, Monteiro, Domo de Covas and Cumieira - Picoto do Carvalho. Notice that the hypothesis of rift-genic correlation is coherent with the occurrence of dispersive exhalative manifestations and the others evidences present in the *smokers* and *mounds* structures in *Covas Dome* sector (Dias, 2011).

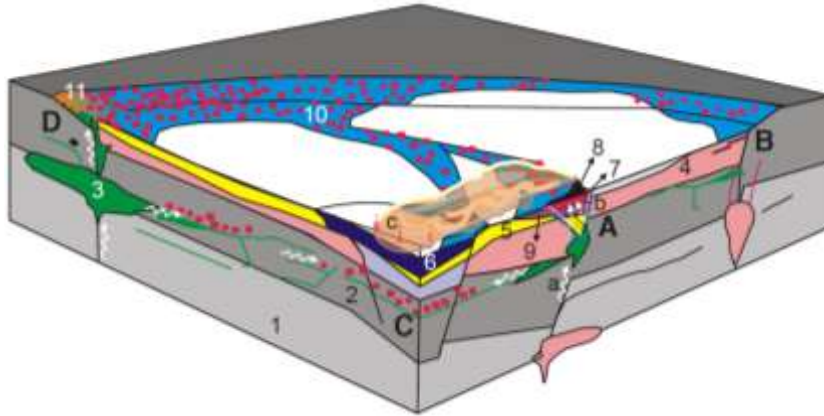


Figure 20 – Depositional context of Silurian terrains in Serra de Arga, considering coherence between lithological interfaces, protolithic genesis and geometric organization of BHT deposits. **A** – Domo de Covas; **B** – Serro; **C** – Cumieira-P. Carvalho; **D** – Monteiro. **1** and **2** – Psammopelitic sedimentary sequences; **3** – Basic magmas with affinity to mantle and continental tholeiites; **4** – Felsic-intermediate volcanics and volcanosedimentar products; **5** – Quartzphyllites and quartzites; **6** – Lydites and black shales; **7** – Cryptocrystalline impermeable crust and smoker anatomies; **8** – massive sulfides; **9** – Calc-silicate and carbonated rocks; **10** – Exhalative tourmalinitic products; **11** – Products resulting from carbonate and fenitic alteration of mafic alkaline protoliths. **a** – Fluids with affinity to the mantle (enriched in CO<sub>2</sub>, CH<sub>4</sub>, F, Cl); **b** – Seawater convection; **c** – Metalliferous precipitation in reducing environments, from fluids discharged into the sea water coming from smoker centers. (From Dias & Leal Gomes, 2013a.)

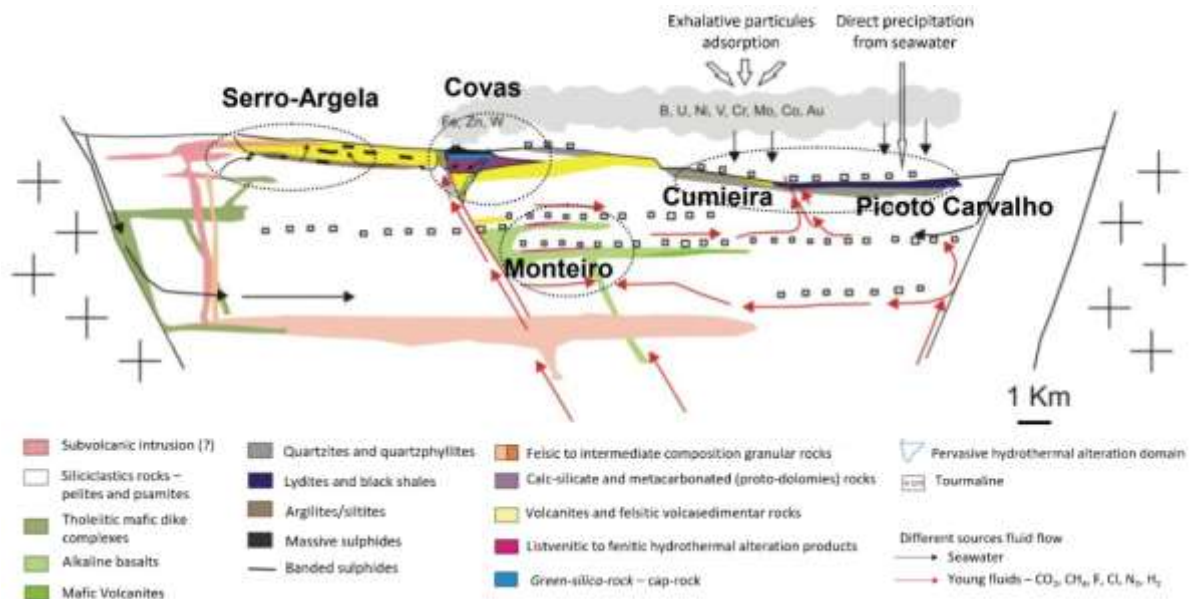


Figure 21 – Depositional context of Silurian terrains in Serra de Argela, considering coherence between lithological interfaces, protolith genesis and geometric organization of BHT deposits (adapted from Dias (2011)).

### 2.1.3. Both Models

Coelho (1993) considers the ore assemblages of *Couto Mineiro de Valdarças*, correspondent to the *Covas Dome*, including those from the Cerdeirinha orebody, as metasomatic tungsten *skarns* (to him, the tungsten was introduced, for the first time, in the deposit in significant quantities, during the V stage of metasomatism, as scheelite I, in the interior of *skarns* and the wolframite in the *endoskarn* and/or aplite-pegmatites), located in discontinuous carbonate levels (from chemical and/or biochemical sedimentation) interlayered in the psammo-pelitic Silurian sequences. These prior *skarn* sequences would have formed in a basin with low oxygen and low sedimentation rates, favourable to the occurrence of efficient grain-selection. Coelho recognizes that this frame was repeated several times in the higher Silurian portions of the series, but with lower frequency.

Nevertheless, Dias & Leal Gomes (2007), Leal Gomes *et al.* (2011) and Dias (2011), although recognizing the metamorphic-metasomatic processes as epigenetic remobilizations, they considered that a primitive volcanic-sedimentary and sedimentary-exhalative polygenesis would have produced an initial metallic stock latter remobilized. However, these authors do not consider that the most significant W content is related with metasomatic fluid of the granitic introduction as Coelho (1993), but also with the Silurian volcanism. To them, this bimodal volcanism seems to locally contain metallogenic SEDEX affiliated conditions that would had been favourable to the precipitation of iron sulfides and syngenetic tungsten minerals (fig. 20). Similar to the *Waimangu* case, and various other metallogenic contexts (in particular deposits with *B.H.*-type signature (Dias & Leal Gomes (2013b)), as previously expressed. Leal

*et al.* (2011), considered once more, that the generation of scheelite would be a predictable scenario under syngenetic conditions of thermal and compositional interface.

The authors gathered several evidences that seem to support a Sillurian primordial SEDEX affinity in the C.D.F.. One should notice that Coelho focused only in *Covas Dome* sector, while Leal Gomes focused in several sectors of C.D.F. (fig. 1) and is still trying to define an early geological setting that incorporated an initial metallic stock that would have been latter remobilized.

Besides the previous comparison, in this stratigraphic sequence, and in the open-pit of Cerdeirinha Mine (fig. 22), an iron sulfide horizon was identified, where spheroidal to framboidal pyrite nodules were concentrated in dense agglomerates. Sometimes, these nodule accumulations showed evidence of graded bedding (fig. 22 b), c) and d)) and with interstitial polymetallic mineral assemblages where tungsten, gold, silver and bismuth mineralizations do occur (Souto & Leal Gomes, 2017). In these paragenesis there is a high phosphate and sulfate contents as well (Souto & Leal Gomes, 2018). However, also isolated spheroids and frambooids (millimetric to pluri-centimetric diameters) were accumulated in sulfide-rich horizons (Souto & Leal Gomes, 2018). These structures underlie a peculiar layer, whose genesis is probably colloformic (with cryptocrystalline quartz + F-apatite) – equivalent to a *cap-rock* (fig. 22 a)). Laterally, orbicular to framboid bearing units are distal relatively to the group of tube and mound geometries, which are currently expressed on the most typical calc-silicate levels. The syngenetic character, the sedimentary-exhalative affinity of the framboidal cumulates and the geometrical organization and crystalline growth of individual nodules suggest a primitive, in equilibrium deposition that still appear preserved after the metamorphic-metasomatic overprint. Therefore, these features still frame the context of the exhalative-sedimentary protogenesis that includes tube and hemispherical structures, eventually smokers fossilized at the calc-silicate rocks that occur nearby (Leal Gomes *et al.* (2011), Dias (2011) and Souto & Leal Gomes (2018)). Supporting this Souto & Leal Gomes (2017) verified the presence of native Au. Until then, Au was only found in arsenopyrites crystal net and as dispersed electrum.

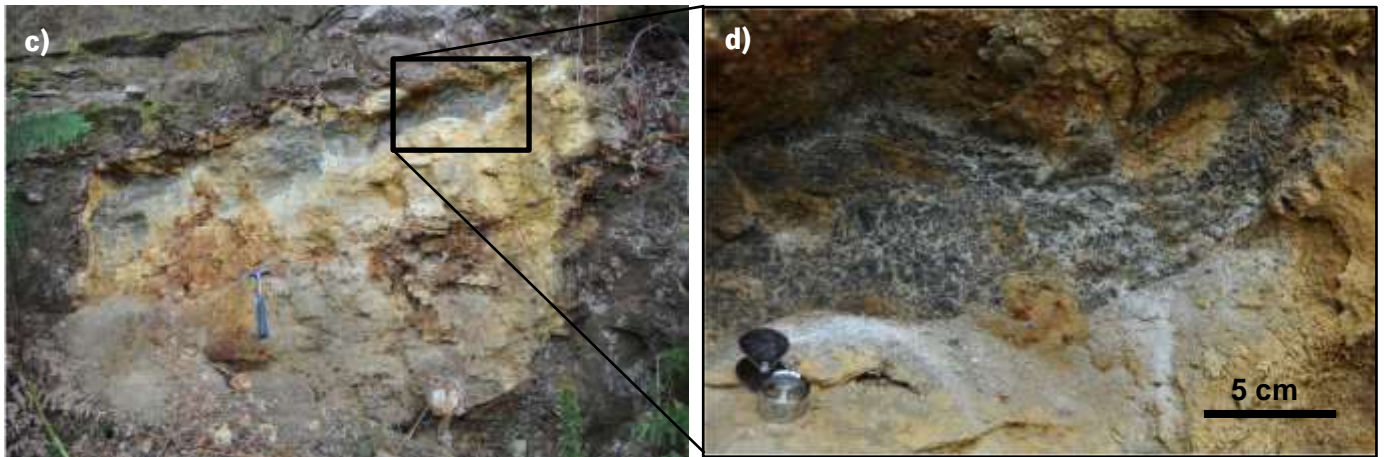
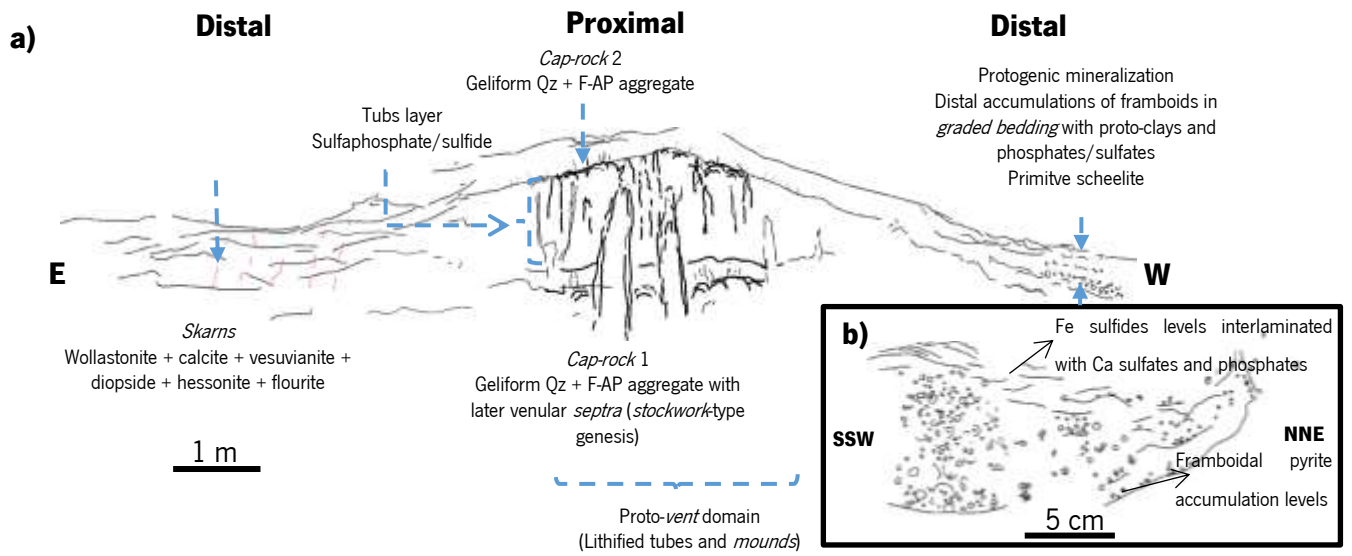


Figure 22 – Representation of the several structures observed on the Cerdeirinha's open pit. **a)** Protolithic structures generalized conceptual profile of Cerdeirinha mine. **b)** Schematic representation of the most occidental domain relatively to the Cerdeirinha's main open pit, where it is possible to observe the primitive structural devices – graded bedding. **c)** Most western sector, where b) was observed. **d)** Detail of c) for the graded bedding structure (from which b)) representative scheme was done. (Images from Souto & Leal Gomes, 2017)



### 3. DATA AND METHODOLOGY

Assuming the SEDEX to volcanogenic nature proposed by Dias (2011), in this study the sulfide layers of Cerdeirinha and a like suites are focused. Thus analysing in detail, from the structural, mineralogical and geochemical point of view, some hypothetically syngenetic, less-reworked features of sedimentary to volcanic and SEDEX affiliation.

Regarding Dias (2011), Leal Gomes *et al.* (2011), and the profile present in Souto & Leal Gomes (2019), the samples were selected in order to characterize best that open-pit. Five samples were selected to a more focused study. Their placement can be found in the figure 23, while the reason for its selection and methodology applied is on table 3.

The petrographic study was accomplished through the thin-section study by transmitted and reflected light microscopy, scanning electron microscope by backscattered electrons. In the case of facies subjected to several cycles of deformation and metamorphism the support for the establishment of the protolithic affinity is essentially textural. Petrography allowed to discern some of these textures and also allowed to guide the punctual chemical analysis of typomorphic minerals and metamorphism through scanning electron microscope, electron microprobe and laser-ablation inductively coupled plasma mass spectrometry. A study in (ore) reflect light microscopy of mineralizations that relate to some more metalliferous levels, with determination of respective specializations expressed in levels with varying proportions of sulfides, which, by hypothesis, correspond to syngenetic paleoconcentrations or later mobilized, as a consequence of metamorphic-metasomatic processes. Through these methods, it was attempted to be close to a primitive geochemical nature of some anomalous facies (representative of the observed lithologic diversity) with homogeneity and lithologic contrast relatively to host rock (characterized by the main demarcated area in the study area (fig. 2).

Apparently, there are textural and structural indicators of the presence of syngenetic smoker type or vent devices and the presence of nodular bodies compatibles with or subjected to gravitational sedimentation. In these conditions will be studied mineralizations paragenesis that may be related to these phenomena and the orechemistry of some phases that can be seen as typomorphic of genesis conditions. Regional metasomatism and the result of Variscan pegmatitic intrusions should be considered and can totally or partially obliterated the most important aspects of the exhalative signature and this has to be checked in each case.

In the mineralchemistry point of view, in this investigation phase, the following phases were privileged:

- *Apatite* – for being an extraordinarily abundant phosphate in these paragenesis.

- *Scheelite* and *wolframite* – for constitute the commodities (main ores) of orebodies that express these processes, and in particular in Cerdeirinha orebody.
- *Inosilicates* (*pyroxene* (*diopside* and *hedenbergite*), *wollastonite* and *hornblende*) – for presenting the inherited syngenetic signature and the signature that resulted from the epigenetic hydrothermal interaction.
- *Plagioclase* and *vesuvianite* – for suggest the composition of the lithotypes that were subjected or not to hydrothermal transformation, and for being relatively abundant.
- *Sulfides* – for representing a class with anomalous content for a situation of only simple metasomatism and for working as geothermometer (arsenopyrite).
- *Chlorite* – by its feature as geothermometer, mainly in latter hydrothermal conditions.

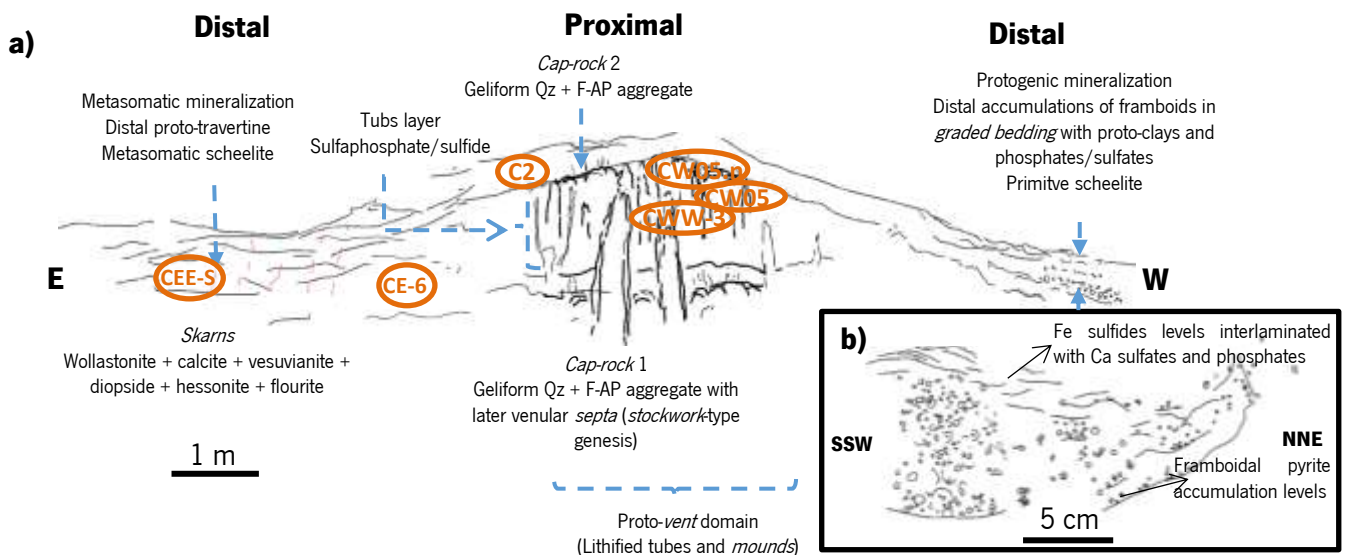


Figure 23 – Representation of the several structures observed on the Cerdeirinha's open pit. **a)** Protolithic structures generalized conceptual profile of Cerdeirinha mine. **b)** Schematic representation of the most occidental domain relatively to the Cerdeirinha's main open pit, where it is possible to observe the primitive structural dispositives. The orange codes represent the location of the respective hand samples collected that can be observed in figure 24.

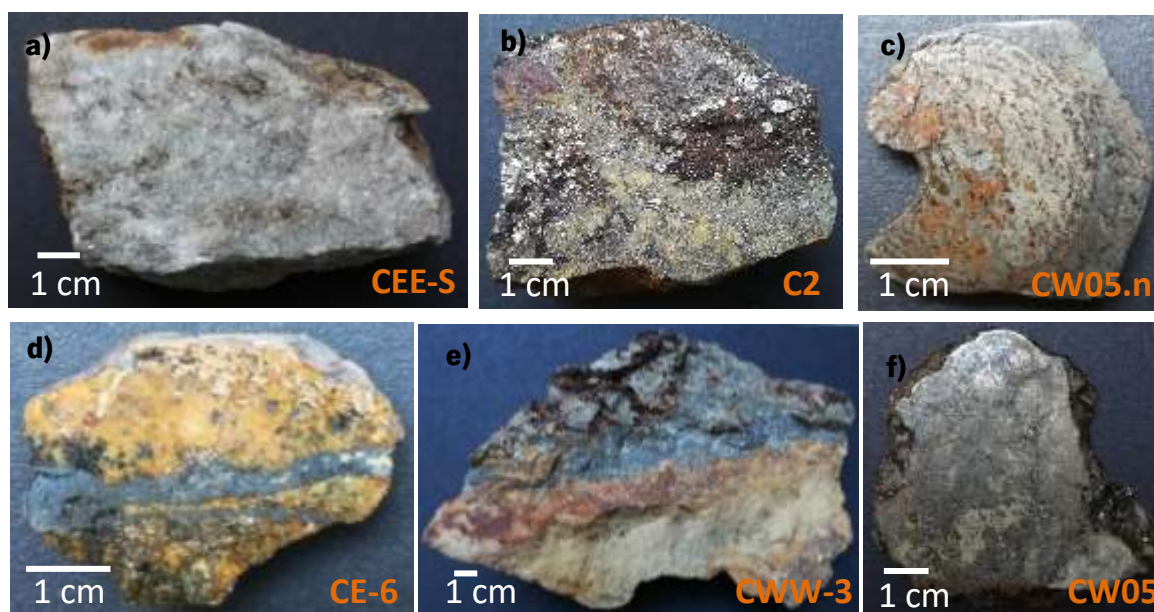


Figure 24 – a), b), c), d), e) and f) Hand samples and polished sections of the samples, whose denomination is on the right down corner of each image. Their location is identified in figure 23.

Table 3 – Samples denomination, respective characterization and analytical methodology applied.

Sample	Characterization	Methodology
C2	Sulfide arcs periphery – distal relatively to apical mounds domain	Electron microprobe L.A.- I.C.P.-M.S.
CEE-S	<i>Skarn</i> with proto-travertine ghost structures (mimetic structure)	Electron microprobe L.A.- I.C.P.-M.S.
CWW-3A	Attributed to sulphide–calc-silicate rock interface in the proximal tubuliform structural domain	MEV Electron microprobe L.A.- I.C.P.-M.S.
CW05	Attributed to apical interface of structural domain of roof with sulfide-phosphate paragenesis and mound geometry	Electron microprobe L.A.- I.C.P.-M.S.
CW05.n	Spheroid – apical sulfide domain with mound structure	MEV Electron microprobe L.A.- I.C.P.-M.S.

The sample preparation was produced by Dettmar Laboratories (Bochum, Germany) and all the methodologies were applied in the Department of Geosciences of the University of Bremen.

The classification of the lithotypes was done by plotting the chemical data in typological diagrams and using GCDkit software for Windows, GCDkit 5.0 IN R 3.4.3 version.

### 3.1. Transmitted and reflected light microscopy

A *Leica DFC 320* light microscope (fig. 25) with transmitted and reflective light was used to analyse the thin-sections. The petrographic microscopy was used as a first instance to mineralogical and assemblages identification as well as textures based on the minerals features.



Figure 25 – Leica DFC 320 utilized for sample petrography in University of Bremen.

#### 3.1.1. Transmitted light microscopy

In transmitted light microscopy the light comes from a source on the opposite side of the specimen to the objective lens. Usually, the light is passed through a condenser to focus it on the specimen to get maximum illumination (“Translucent and opaque mineral microscopy” *in*

[http://petrologyservices.com/transmitted-and-reflected-light-](http://petrologyservices.com/transmitted-and-reflected-light-microscopy)

[microscopy](http://petrologyservices.com/transmitted-and-reflected-light-microscopy); accessed on 24<sup>th</sup> of June of 2019). After, the light passes through the translucent specimen and crosses the objective lens to magnify the image of the sample and then to the oculars, where the enlarged image is viewed (“Translucent and opaque mineral microscopy” *in* <http://petrologyservices.com/transmitted-and-reflected-light-microscopy>; accessed on 24<sup>th</sup> of June of 2019). In this method most data is collected in crossed nicols, where it is possible to observe the mineral extinction angle, shape, birefringence, elongated sign, zoning, twinning, and other features. However, in uncrossed nicols is possible to identify the colour, pleochroism, relief, cleavage and fractures.

#### 3.1.2. Reflected light microscopy

Reflected light microscopy (where the light source is above the thin-section) was used to examine opaque (ore) minerals (and other materials) in order to identify the mineral phases and determine the paragenetic relationships between the different mineral phases (“Translucent and opaque mineral microscopy” *in* <http://petrologyservices.com/transmitted-and-reflected-light-microscopy>; accessed on 24<sup>th</sup> of June of 2019). In this method, most data is obtained in uncrossed nicols, where mineralogical features such as shape, bright, reflectivity, birreflectance, colour, pleochroism, relief and others. While in crossed nicols features such internal reflections are observed (“Translucent and opaque

mineral microscopy” in <http://petrologyservices.com/transmitted-and-reflected-light-microscopy>; accessed on 24<sup>th</sup> of June of 2019). One should take caution before the observation, to see if the sample is freshly polished and does not have any tarnish, illumination level is not too excessive (intensity changes the perceived relative intensity effect), and at last minerals which are pleochroic (non-isotropic minerals) are also birefractant.

Transmitted and Reflected Light Microscopy, image editing and data organization of all samples (CE-6, C2, CEE-5a & CEE-5b, CW05n, CW05, CWW3-A & CWW3-B) lasted for around 3 to 4 months. This textural analysis allowed to:

- Establish different sulfide generations
- Characterize CW05n “*nodule*”
- CW05 *nodule* (zoned sketch from out to inner sector showing different sulfides/tungstates/silicates from each zone)
- *Bird-eye* texture was observed (it appears more in the exterior than in the inner *nodule* (?) in CW05n)
- In the sample CWW-3A, sulfide re-precipitation was observed.
- In the calc-silicate samples CEE-5a & CEE-5b, particular attention was given to wollastonite different shapes and “matrixes that involved it”.

### **3.2. Scanning electron microscopy and energy dispersive X-ray spectroscopy (S.E.M. & E.D.X.)**

These thin-sections were carbon-coated before this technique was applied (fig. 26), by Cressington carbon coater.

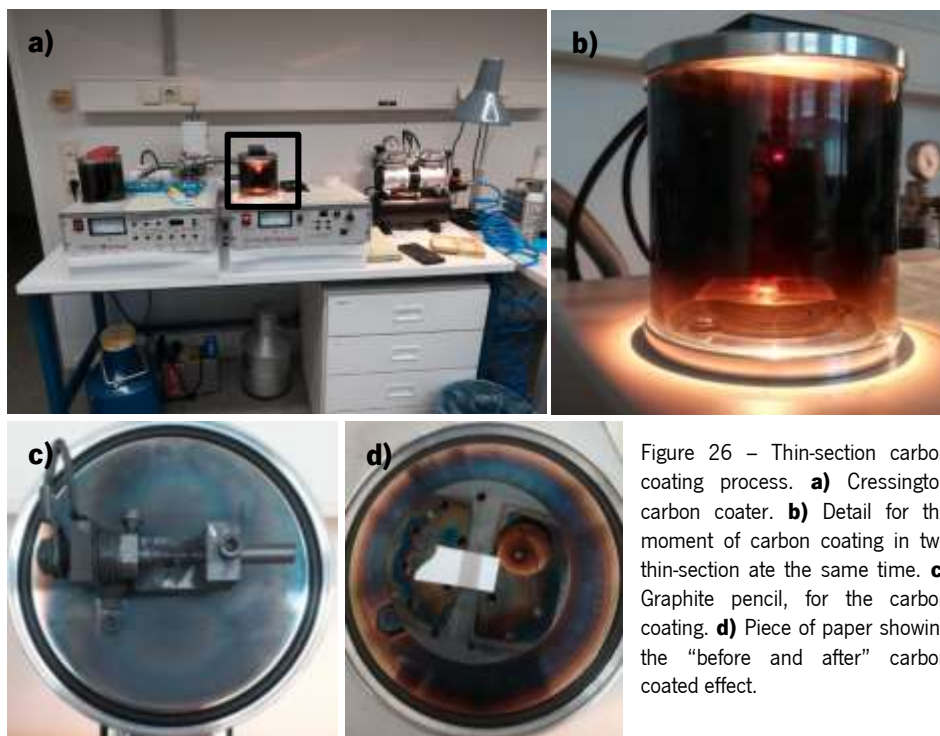
Qualitative and semi-quantitative analysis of elements were performed in scanning electron microscopy and energy dispersive X-ray spectroscopy (S.E.M. and E.D.X.) (fig. 27) (Zeiss field emission electron microscope SUPRA 40 and a Bruker EDS-detector XFlash 6|30) (“REM & EDX” in <https://www.ozeankruste.uni-bremen.de/index.php/en/laboratories/rem-en.html>; accessed on 24<sup>th</sup> of June of 2019).

While the petrographic (polished) thin sections (28 x 48 mm) surface were scanned and screened by a fine focussed electron beam, an interaction with the sample occurs and electrons with different energy levels are released (backscattered electrons – B.S.E.). These electrons are detected (SE2 / Inlens / BSD / EDS) and result in topographical (three-dimensional effect, great resolution and sharpness image)

and chemical compositional data of the sample. Thus B.S.E. allows to obtain the secondary electron (S.E.) images (display structural information, such as habitus of the phases and porosity) of phase contrasting by atomic number contrast. In addition, B.S.E. also allows to accomplish E.D.X. spectroscopy to obtain the qualitative and semi-quantitative compositional spectrums per punctual chemical analysis.

The thin-sections analysed were dry, not degassing and resistant to high vacuum.

S.E.M. and E.D.X. (in a total of 4 session) was used in order to identify sulfides and silicates (samples: CWW3A, CE-6, CW05n). It also allowed to obtain high resolution images, showing textures and minerals intergrowths.



### 3.3. Electron microprobe

X-ray electron microanalysis is a non-destructive analytical method with high spatial resolution for measurement of elemental concentrations in geological samples. Within the microprobe a tungsten cathode produces electrons that are accelerated towards the sample using high voltage. The interaction of the electron beam with the sample leads to emission of characteristic X-rays, the intensity of which is measured. By comparison with measurements of reference materials, the elemental concentrations within the sample can be calculated. With the exception of the light elements (H, He and Li), all elements can be detected by electron microprobe. In addition the microprobe also allows to obtain backscatter electron images (similar to a scanning electron microscope) (“Electron probe microanalysis” *in* <https://www.ozeankruste.uni-bremen.de/index.php/en/laboratories/electronmicroprobe.html>; accessed on 24<sup>th</sup> of June of 2019).

The microprobe used was Cameca SX100 electron microprobe (fig. 28) that contains an energy-dispersive system (EDS) as well as four wavelength-dispersive spectrometers (WDS). The latter are equipped with TAP (2x;  $2d= 25.7\text{\AA}$ ), LIF (2x;  $2d= 4.03\text{\AA}$ ), PC1 (1x;  $2d= 61\text{\AA}$ ) und PET (3x;  $2d= 8.75\text{\AA}$ ) analyzing crystals, which enable the measurement of all elements starting with carbon (or heavier). In addition, the SX100 has a built-in optical microscope and detectors for secondary electrons and backscattered electrons. Prior to analysis thin-sections were carbon-coated (fig. 26). The thin-sections were resistant to vacuum and their formats were 28 x 48 mm and 1 mm thickness. Calibration was done with standards from the Smithsonian National Museum of Natural History (USNM) (Jarosewich et al. 1980) USGS glasses, and further silicates and sulfides.



Figure 28 – Electron microprobe. **a)** Image of the general equipment required for electron microprobe use. **b)** Detail for the Cameca SX100 electron microprobe (from “Electron probe microanalysis” in <https://www.ozeankruste.uni-bremen.de/index.php/en/laboratories/electronmicroprobe.html>; accessed on 24<sup>th</sup> of June of 2019).

For all the cases below the microprobe calibration was done according to the user regulations electron microprobe protocol established.

For this study, the following minerals were quantified under electron microprobe (table 4):

**Hornblende:** Analytical works were performed using 15 kV, 10 nA, beam diameter of 1  $\mu\text{m}$ , and a counting time of 20 s for Na, Mg, Ca, Ti, Fe, Si, Al and 30 s for K and Cr and 40s for Mn. Calibration was done with *Hornblende Kakanui (USNM 143965)* and *Chromium Augite (NMNH 164905)*. In this case the *sili\_Cr* program was applied.

**Chlorite:** Analytical works were performed using 15kV accelerating voltage and 8 nA current and counting time of 20 s for Na, Mg, K, Ca, Ti, Fe, P, Si, Al and 40 s for Mn. Calibration was done with standards of *Plagioclase (USNM 115900)* for Na, K, Si and Al, and *Augite (Kakanui) (NMNH 112142)* for Mg, Ca, Ti, Fe, and Mn. The H<sub>2</sub>O was calculated by stoichiometry and FeO is considered as total iron. The beam size was 5 $\mu\text{m}$  to avoid the migration of light elements. In this case the *silicate* program was applied.

**Arsenopyrite:** Analytical works were performed using 20kV accelerating voltage and 20 nA current, beam diameter of 1  $\mu\text{m}$ , and counting time of 40 s for As and S, and 20 s Mn, Fe, Co, Ni, Cu, Zn, Pb, Sb. Calibration was done with *Arsenopyrite (Arsenkies)*. In this case the *sulfide* program was applied.

**Ilmenite:** Analytical works were performed using 15kV accelerating voltage and 10 nA current and counting time of 20 s for Na, Mg, K, Ca, Ti, Fe, P, Si, Al and 40 s for Mn. Calibration was done with standard of *Ilmenite (NMNH 96189)*. The FeO is considered as total iron. The beam size was 1 $\mu\text{m}$ . In this case the *silicate* program was applied.

The calibration standard data was accessed in *Mikrosondenstandards (2015)* book.

Table 4 – Maximum deviation of the control standard for microprobe measurements.

Hornblende	Na <sub>2</sub> O	MgO	K <sub>2</sub> O	CaO	TiO <sub>2</sub>	FeO	MnO	SiO <sub>2</sub>	Al <sub>2</sub> O <sub>3</sub>	Hornblende
	0.37	0.74	0.12	0.33	0.16	0.32	0.06	0.71	0.82	Augite
Chlorite	0.17	0.20	0.00	0.18	0.06	0.22	0.03	0.42	0.50	
	Na <sub>2</sub> O	MgO	K <sub>2</sub> O	CaO	TiO <sub>2</sub>	FeO	MnO	SiO <sub>2</sub>	Al <sub>2</sub> O <sub>3</sub>	Augite
Arsenopyrite	0.04	0.39	0.02	0.37	0.16	0.33	0.08	1.11	0.18	Plagioclase
	0.31	0.03	0.08	0.44	0.04	0.12	0.05	1.25	0.91	
Ilmenite	Fe	S	As							Arsenopyrite
	1.24	0.97	1.13							
Ilmenite	MgO	TiO <sub>2</sub>	FeO	MnO						Ilmenite
	0.00	0.38	0.32	0.18						

Electron microprobe allowed to obtain temperature & pressure data and WDS (EDX) allowed to confirm some mineral phases (18 days):



- Silicate program:
  - Chlorites (C2) (5 days)
  - Clinopyroxene (CEE-5a & CEE-5b) (6 days)
  - Hornblende (CW05n) (3 days)
- Sulfide program (CW05n; CW05; CWW3-A; C2) (4 days):
  - Arsenopyrite
  - Pyrite
  - Pyrrhotite

During these days, besides microprobe also WDS was used in order to quickly identify mineral phases.

Through the silicates program temperatures data were measured in chlorite and clinopyroxene minerals. Still in the same method, attention was paid to the intergrowth of hornblende (Al-Ti)-plagioclase, once from hornblende is possible to obtain the pressure and its combination with plagioclase allows to obtain temperature data.

The sulfides program allowed to measure different generations of arsenopyrite (C2, CWWA, CW05), in order to find out their genesis temperature according to Krestmar & Scott method. In addition, pyrite and pyrrhotite were also measured with this technique.

The method presented below, are in order of application.

### **3.4. Laser-ablation inductively coupled plasma mass spectrometry**

Laser-ablation inductively coupled plasma mass spectrometry (LA-ICP-MS) was used for quantitative trace-elements analysis of various thin-sections. LA-ICP-MS is a method for microchemical analyses of trace element concentrations and isotope ratios in solid materials. By firing a high-energy laser beam onto the sample surface, material is ablated. The ablated microparticles are removed from the sample chamber by an argon or helium carrier gas, and the aerosol is directly introduced into the hot plasma of an ICP-MS to be analysed. Elements in concentrations as low as 10 ppb can be analysed and quantified.

The LA-ICP-MS used was *New Wave UP193* (fig. 29), the laser wavelength was 193 nm, and an irradiance at the sample of up to 2 GW/cm<sup>2</sup> ("LA-ICP-MS" in <https://www.ozeankruste.uni-bremen.de/index.php/en/laboratories/la-icp-ms/81-la-icp-ms-txt-en.html>; accessed on 24<sup>th</sup> of June of 2019). The pulse rate used was of 1 Hz. Spot sizes selected were 20, 25, 35, 50 and 75 µm (microns)

of diameter. Samples were ablated using individual spots, that were identified through reflected (coax and ring) and transmitted light in this equipment.

Petrographic (polished) thin sections (28 x 48 mm) were analysed by LA-ICP-MS, after electron microprobe analyses of major elements. So, once the coating was not removed, a pre-ablation was done before each ablation.

For determination of elemental concentrations,  $^{43}\text{Ca}$  or  $^{57}\text{Fe}$  (internal standards) were analyzed along with elements of interest in both sample and calibration standard ("LA-ICP-MS" in <https://www.ozeankruste.uni-bremen.de/index.php/en/laboratories/la-icp-ms/81-la-icp-ms-txt-en.html>;



Figure 29 – Laser-ablation inductively coupled plasma mass spectrometry. **a)** General image of the equipment required for laser-ablation inductively coupled plasma mass spectrometry use. **b)** Detail for the New Wave UP193 laser.

accessed on 24<sup>th</sup> of June of 2019).  $^{43}\text{Ca}$  is a better internal standard than  $^{57}\text{Fe}$ , because it is measured more accurately with the standards BHVO-2G and BCR-2G. Their concentrations were determined either by electron microprobe or by stoichiometric calculations (chapter 7. *Geochemical Fractionation And Filiation Signatures*).

The control standard evaluation (table 6) allowed to identify which values range were quantitatively good enough to be used. For the cases that relative error ( $\frac{\text{mean-compiled standard concentration}}{\text{compiled standard concentration}}$ ) was above 10 %, another table (table 7) was constructed in order to alert which range of data values would be acceptable to use in forward work. The calibration standard used was NIST-610.

The *Compiled Value* and a *Preferred Value* were established by GEOREM (verified on 17<sup>th</sup> July 2019).

For calibration and data monitoring, synthetic glasses doped with trace elements (NIST610 and MASS-1) and synthetic glasses from natural rocks (USGS glasses: BCR2G and BHVO2G) were measured

approximately after every eight measurements. Data reduction was carried out using GeoPro(TM) software ("LA-ICP-MS" in <https://www.ozeankruste.uni-bremen.de/index.php/en/laboratories/la-icp-ms/81-la-icp-ms-txt-en.html>; accessed on 24<sup>th</sup> of June of 2019). Quality evaluation of the calibration standards, data integration, and quality evaluation of the data depended on the *GEOPRO* and *INTEG72a* software.

With the L.A.-I.C.P.M.S. different methods were defined (7 days) (table 5):

- Silicates
- Sulfides
- Tungstates
- Titanite

Table 5 – Samples, LA-ICP-MS method and minerals analysed under L.A.-I.C.P.-M.S. technique.

	Silicates						Sulphides				Tungstates				
	Ap	Di	Hd	Ves	Wo	Wo mixture	Apy	lol	Py	Po	mixed phases and mineral clusters		Sch	wf	ferb
CEE-5a	✓	✓	✓	✓	✓	✓									✓
CEE-5b	✓	✓	✓	✓		✓									
C2	✓						✓		✓	✓			✓	✓	✓
CWW-3A							✓	✓	✓	✓		✓			
CW05							✓		✓			✓	✓	✓	
CW05.n	✓								✓	✓					

Data integration and standard evaluation lasted 2 weeks.

Below is possible to observe the element analysed for each *method*:

- *Silicates*: Si, Ti, Al, Fe, Mn, Ca, REE (La, Ce, Pr, Nd, Sm, Eu, Gd, Tb, Dy, Ho, Er, Tm, Yb, Lu), Ba, Co, Cr, Pb, Sr, Th, U, Y and Zr.
- *Sulfides*: Si, Al, Fe, Mn, Ag, As, Au, Bi, Co, Cu, In, Mo, Ni, Pb, Sb, Sn, W, Zn, Te, Ru and Os.

For measuring arsenopyrite the same elements were analysed, except As.

- *Tungstates*: Si, Al, Fe, Mn, Ca, Fe, REE (La, Ce, Pr, Nd, Sm, Eu, Gd, Tb, Dy, Ho, Er, Tm, Yb, Lu), Mo, Nb, Sr, Ta and Y, Ru.

Ca and Fe were used as an internal standard for scheelite (CaWO<sub>4</sub>) and ferberite (FeWO<sub>4</sub>) & wolframite ((Fe,Mn)WO<sub>4</sub>) respectively.

Table 6 – Control standard evaluation.

Element \ Standard	<sup>28</sup> Si	<sup>48</sup> Ti	<sup>27</sup> Al	<sup>56</sup> Fe	<sup>55</sup> Mn	<sup>43</sup> Ca	<sup>139</sup> La	<sup>140</sup> Ce	<sup>141</sup> Pr	<sup>146</sup> Nd	<sup>147</sup> Sm	<sup>151</sup> Eu	<sup>158</sup> Gd	<sup>159</sup> Tb	<sup>163</sup> Dy	<sup>165</sup> Ho	<sup>166</sup> Er	<sup>169</sup> Tm	<sup>172</sup> Yb	<sup>175</sup> Lu	<sup>107</sup> Ag	<sup>75</sup> As	<sup>197</sup> Au	<sup>137</sup> Ba	<sup>209</sup> Bi	<sup>59</sup> Co	<sup>53</sup> Cr	<sup>63</sup> Cu	<sup>115</sup> In	<sup>95</sup> Mo	<sup>93</sup> Nb	<sup>60</sup> Ni	<sup>208</sup> Pb	<sup>121</sup> Sb	<sup>118</sup> Sn	<sup>88</sup> Sr	<sup>181</sup> Ta	<sup>232</sup> Th	<sup>238</sup> U	<sup>51</sup> V	<sup>186</sup> W	<sup>90</sup> Y	<sup>66</sup> Zn	<sup>90</sup> Zr	<sup>128</sup> Te	<sup>101</sup> Ru	<sup>189</sup> Os				
BHVO-2G	✓	✓	✓	✓	✓	✓	✓	✓	✓	✓	✓	✓	✓	✓	✓	✓	✓	✓	✓	✓				✓	*✓ 261.7	✓	✓	✓	✓	✓	✓	*	✓	✓	✓	✓	✓	✓	✓	✓	✓	✓	✓	✓	✓	✓	✓		*	*	
BCR-2G	✓	✓	✓	✓	✓	✓	✓	✓	✓	✓	✓	✓	✓	✓	✓	✓	✓	✓	✓	✓	✓	*			✓	✓	*	✓	✓	*	✓	✓	✓	✓	✓	✓	✓	✓	✓	✓	✓	✓	✓	✓	✓	✓	✓	✓		*	*
MASS-1				✓																		✓	✓	✓	✓	✓	✓	✓	✓	✓	*	✓	*	✓	✓							✓	✓	✓		✓	*	*			

Table 5 legend:

- \* – There was no compiled value, so the comparison value was a *Preferred Value* by GEOREM (on 17<sup>th</sup> July 2019), except in the case of the *MASS-1*, where an average of the extremes values was calculated.
- \* – Isotopes only for correction, not real data.
- ✓ – have less than 10 % of relative error, so it is considered as *acceptable* (compared with *Compiled Value*).
- ✓ – have less than 10 % of relative error, so it is considered as *acceptable* (compared with an approximated reference calculated by its oxide value or with *Preferred Value*).
- ✓ – Only qualitatively, because there is no standard value to compare.
- ✓ – Contains more than 10 % of relative error (compared with *Compiled Value*).
- ✓ – have more than 10 % of relative error (compared with an approximated reference calculated by its oxide value or with *Preferred Value*).

Table 7 – Control standard evaluation for specific isotopes, with respective compiled value and relative error.

Element \ Standard	<sup>107</sup> Ag	<sup>75</sup> As	<sup>197</sup> Au	<sup>209</sup> Bi	<sup>59</sup> Co	<sup>53</sup> Cr	<sup>63</sup> Cu	<sup>115</sup> In	<sup>95</sup> Mo	<sup>60</sup> Ni	<sup>208</sup> Pb	<sup>121</sup> Sb	<sup>118</sup> Sn	<sup>181</sup> Ta	<sup>182</sup> W	<sup>66</sup> Zn	<sup>128</sup> Te
BHVO-2G				0.01 (261.7%)	44 (4.3%)	293 (-1.8%)	127 (0.5%)	0.1 (-0.3%)	3.8 (14.5%)	116 (6.7%)	1.7 (0.2%)	0.3 (-55.1%)	2.6 (-32.7%)	1.15 (-11.7%)	0.23 (3.9%)	102 (13.6%)	
BCR-2G	0.5 (49.6%)			0.05 (43.9%)	38 (-1.0%)	17 (-12.9%)	21 (-17.0%)	0.11 (-1.5%)	270 (-4.3%)	13 (-9.3%)	11 (-5.6%)	0.35 (-5.2%)	2.6 (-17.5%)	0.78 (-8.1%)	0.5 (18.0%)	125 (23.4%)	
MASS-1	67 (2.3%)	65 (-24.1%)	47 (20.3 %)	7 (858.8%)	67 (-0.04%)		134000 (-2.7%)	50 (25%)	61 (-11.1%)	86.5 (14.6%)	74 (-2.3%)	55 (16.2%)	55 (7.7%)			210000 (11.2%)	
Comment	For lower concentration values there are higher uncertainties, while higher values are <i>acceptable</i> .	Qualitatively and value range and comparable with other samples.	Qualitatively and value range and comparable with other samples.	For greater concentration values there are higher uncertainties, while lower values are <i>acceptable</i> .	For the presented range is <i>acceptable</i> .	For lower concentration values there are higher uncertainties, while higher values are <i>acceptable</i> .	For lower concentration values there are higher uncertainties, while higher values are <i>acceptable</i> .	For greater concentration values there are higher uncertainties, while lower values are <i>acceptable</i> .	For lower concentration values there are higher uncertainties, while higher values are <i>acceptable</i> .	It is difficult to measure, therefore even with relative error of 14.6% the value are <i>acceptable</i> .	For the presented range is <i>acceptable</i> .	Qualitatively and value range and comparable with other samples.	For lower concentration values there are higher uncertainties, while higher values are <i>acceptable</i> .	Even with relative error around -12.1% of relative error is <i>acceptable</i> .	Qualitatively and value range and comparable with other samples.	Qualitatively and value range and comparable with other samples.	Reference value absence, however there is 5% of standard deviation with MASS-1.

## 4. DISCRIMINATED LITHOLOGICAL TYPES

The characterization of volcanic and volcanosedimentary affinity lithologies is based on the analysis of textures seeking to screen relic textures, especially those with petrogenetic meaning, which allow the identification of the forming mechanisms. The deduction of the nature of volcanogenic facies in terms of their constituent processes is based on the establishment of petrographic equivalences with the corresponding metamorphic terms.

The current lack of knowledge about the generating mechanisms of some of the lithological types makes the analogical study difficult. Moreover, their mineralogical composition may result from a metamorphic and metasomatic evolution of the primary facies and is still dependent on the overlapping character of the deformation (Dias, 2011).

The petrologic study allowed, among other features, to identify metamorphic rock protoliths and insertion in the context of Silurian heterogeneity and polygenesis. And later on, reformulation of a genetic hypothesis attributed to the tungstiferous Covas deposit, through the conception of a model that explains the lithological diversity and petrogenetic complexity of the sector and includes the dispersion of indexes elsewhere in Serra de Arga (Dias, 2011).

The integrated analysis of the petrological aspects, combining a stratigraphy obtained from the field surveys and survey studies, with cartographic interface analysis, seeks to situate and establish the evolution of the Silurian in the Serra de Arga compartment (Dias, 2011).

Below it is possible to observe some features of the main lithotypes, in the same order from top to bottom as presented in the previous chronostratigraphic column of Cerdeirinha (fig. 16), such as textures, composition and aspects identified through this study and by previous authors (Dias, 2011).

In this present study attention was only drawn for *Phosphorite with sulfides* (sample C2), *Massive sulfides with or without apatite* (sample CW05.n, CW05, CWW-3A) and *Silicious metacarbonate rock* (sample CEE-S).

In Cerdeirinha, Dias (2011) highlighted the following lithological units presented according to the stratigraphic order (from top to bottom):

- Tourmaline quartzphyllites and metasomatized (sulfidic alteration and phosphatized) tourmaline pelitic facies with sulfide beds (Dias, 2011), and **venular bodies** such as contaminated pegmatites, apatitites, quartz veins and zeolitic veins (with clinozoisite and prehnite) (Professor C. Leal Gomes personal Communication, 2019).

– **Phosphorite with sulfides** (*green silica rock*)

Regarding *phosphorite with sulfides*, attention should be drawn towards *green silica rock* (green rock composed by quartz, apatite and sulfides) characterized as a colomorfic or geliform horizon by Leal Gomes *et al.* (2011), that is comparable to a possible *cap-rock* that might allowed the preservation of exhalative structural devices from metamorphic-metassomatic interaction, due to its stratigraphic position and impermeable and competent behaviour.

A small band of *green silica rock* (quartz and F-apatite with some pyrite in *foam structure*) and the contiguous paragenesis seems to present a geliform level resulting from the consolidation of a *mesh*, which in thicker units can behave like a true *caprock* (fig. 30). Gel desiccation polygonizes structures. This geliform structure suggests that this gel suffered polygonal fractures filled by fluids with sulfides. Here, at least 3 generations of apatites can be observed (fig. 31):

- 1<sup>st</sup> – Fracture and filling;
- 2<sup>nd</sup> – Fracture and dissolution;
- 3<sup>rd</sup> – Fracture and recrystallization.

This formation when consolidated becomes competent and hosting veins in stockwork like structure. Horizons of geliform origin such as these may be considered consistent with a sedimentary-exhalative setting.

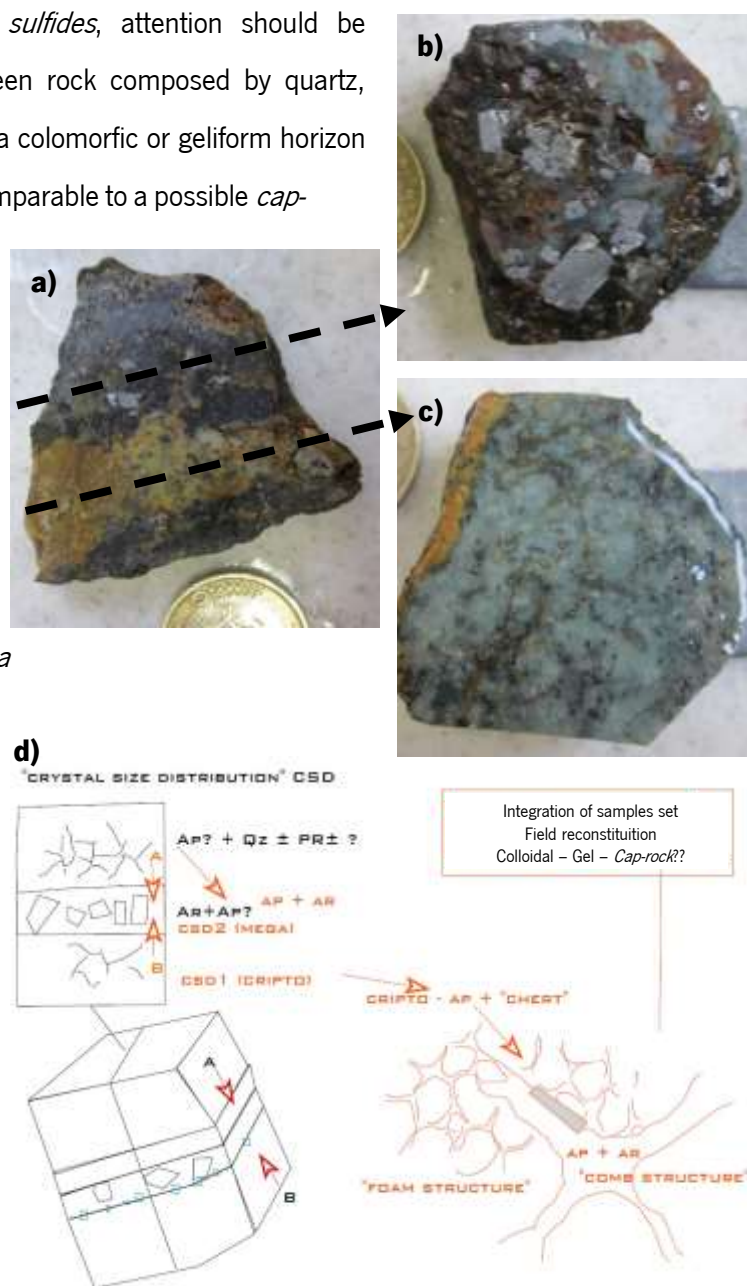


Figure 30 – Different stages of dehydration for a geliform association. **a)** Perpendicular cut to the stratification. **b)** and **c)** Parallel cuts to stratification of two different levels referred in a). **d)** Texture reconstitution. (Souto & Leal Gomes, 2017).

In this study, a thin-section of C2 sample (fig. 24 b)) (similar to figure 30 b)), also considered as *cap-rock* in the conceptual scheme (fig. 23 a)), contained mainly biotite, pyrrhotite, arsenopyrite and scheelite, and lower contents of ilmenite, chlorite, chalcopyrite and scapolite.

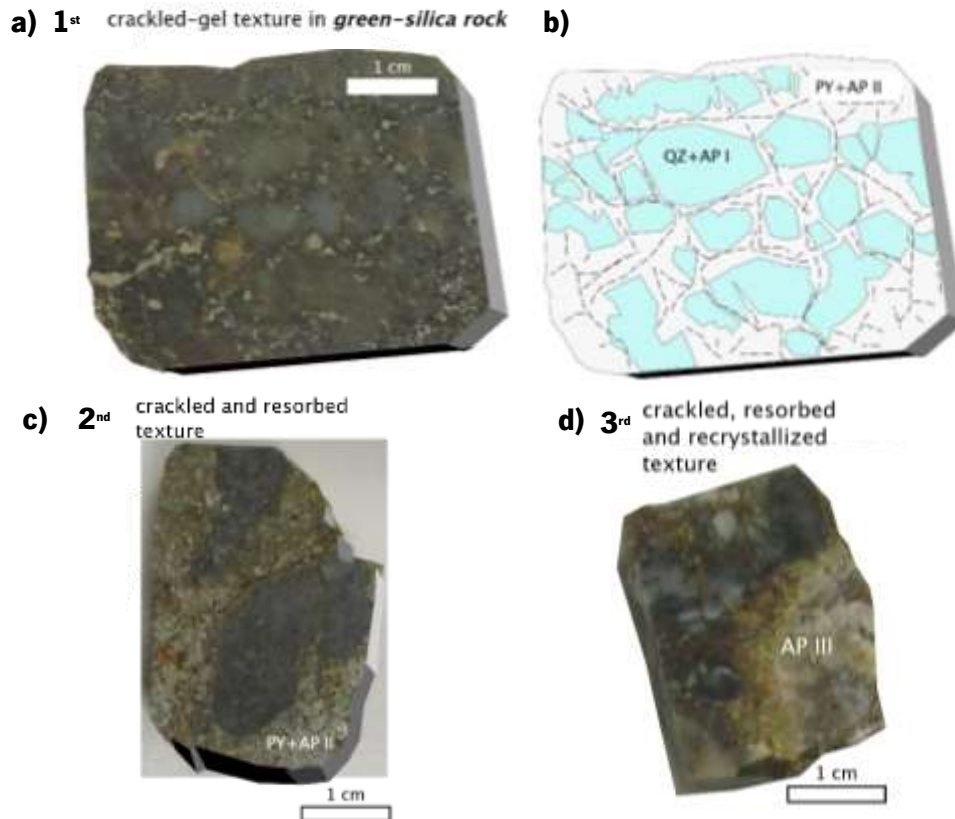


Figure 31 – Cap-rock with 3 generations of apatite, in order of genesis. **a)** Ap I – Crackled-gel texture in green-silica rock. **b)** Representative scheme of a). **c)** Ap II – Crackled and resorbed texture. **d)** Ap III – Crackled, resorbed and recrystallized texture. (Images provided by C. Leal Gomes, 2019)

- **Grossularite** – grossular-enriched levels with some epidote, calcite and vesuvianite (Dias, 2011);
- **Skarn** (calc-silicate rock (in strict sense)) with epidote, diopside, grossular, calcite, amphibole and vesuvianite (Dias, 2011);
- **Plagioclases** with apatite and sulfides (Dias, 2011) and mainly plagioclase of oligoclase composition;
- Feldspatic pelitic rocks with sulfide impregnations (Dias, 2011);
- Massive sulfides with or without apatite
  - **Massive sulfides with** scheelite – Relic silicate paragenesis include associations with chlorite, amphibole, garnet and diopside (Dias, 2011). In this study arsenopyrite, pyrite and quartz were seen intergrown with scheelite (*CW05* fig. 24 f)); Moreover

typical reaction transition was observed: quartz transitioning to apatite, micas and sulfides (and small tungstates crystals on sulfidic matrix) (*CWW-3* – fig. 24 e)).

- **Hyperferriferous band** with *specular* hematite in association with amphibole, apatite, scheelite and biotite; allows to recognize the existence of specific oxidation conditions (Dias, 2011). In this study, a nodule contained mainly sulfides, apatite, hornblende and plagioclase (and Mn-indetermination) was observed (*CW05n* fig. 24 c)).
- Idocrasic (vesuvianitic) **skarn** (calc-silicate rock (in strict sense)) with diopside and calcite;
- **Calc-silicate rocks** and **silicious metacarbonate rocks** with diopside, calcite, vesuvianite, epidote and grossular (Dias, 2011). The calc-silicate rock (*CEE-S* fig. 24 a)) identified in this study contained beds mainly of calcite, fluorite, quartz, vesuvianite, and moreover diopside, hedenbergite and wollastonite.
- **Marbles** – banded-looking rocks in intercalated beds consisting of calcite and vesuvianite (Dias, 2011).



## 5. MINERALOGY AND PARAGENESIS

### 5.1. Mineralogical checklist

The checklist of minerals identified in Cerdeirinha until now by X-ray diffraction (X.R.D.), scanning electron microscopy (S.E.M.), reflected light microscopy (R.L.M.), microscopy transmitted light (T.L.M.), ultraviolet light (U.V.), electron probe microanalyzer (E.P.M.A.), and trace elements analysed under inductively coupled plasma – mass spectrometry (L.A.-I.C.P.-M.S.) is shown in table 8. The same table indicates the confidence level of the identifications, being E.P.M.A., X.R.D. and S.E.M.–energy dispersion mode, the most reliable means of identification. The table is organized by Nickel-Strunz classification.

The meaning of the symbology present in that table is as follows:

T. S. – This study

? – Possibly

?? – Possibly, but low probability

√ – Observed in a specific method of another study

✓ – Observed in a specific method of this study

N.S. – Not Specified

The *relative abundance index* was established through the conjugation of frequency with the respective crystal dimensions:

+ – Rare

++ – Low frequency

+++ – Frequent

++++ – Very frequent

+++++ – Extremely frequent

There were identified 7 *elements*, 20 *sulfides and sulfosalts*, 1 *halogenide*, 16 *oxides, hydroxides and arsenites*, 1 *carbonate*, 14 *sulfates, chromates, molybdates and tungstates*, 7 *phosphates, arsenates and vanadates* and 52 *silicates*.

Table 8 – Mineralogical checklist of all the minerals identified in Cerdeirinha until now, regarding its author, method (X-Ray Diffractometry, Scanning Electron Microscopy, Wavelength-Dispersive Spectroscopy, Reflected Light Microscopy, Transmitted Light Microscopy and Ultraviolet Light), relative abundance index and subsequent study. (To be continued.)

Strunz Classification	Mineral	Author	Method						Relative Abundance Index	Subsequent Studies	
			X.R.D.	S.E.M.	W.D.S.	R.L.M.	T.L.M.	U.V.		L.A.-I.C.P.-M.S.	E.P.M.A.
Elements	Native gold	Souto (2017)		✓							
	Au-Ag alloy	T.S.; Souto (2017)		✓✓		✓			+		
	Bismuth	T.S.; Leal Gomes <i>et al.</i> (2011); Souto (2017)		✓✓	✓	✓✓			+++		
	Graphite (?)	Souto (2017)	✓								
	Polymetallic mineralizations of W, Fe, As, Bi > (Au), Te, Zn, Cu, Pb	Leal Gomes <i>et al.</i> (2011)									
	Tellurium	Leal Gomes <i>et al.</i> (2011)	N.S.	N.S.	N.S.	N.S.	N.S.	N.S.			
	Bismuth telluride	Leal Gomes <i>et al.</i> (2011)	N.S.	N.S.	N.S.	N.S.	N.S.	N.S.			
Sulfides and sulfosalts	Sphalerite	T.S.; Leal Gomes <i>et al.</i> (2011); Souto (2017)			✓	✓			+		
	Chalcopyrite	T.S.; Leal Gomes <i>et al.</i> (2011); Souto (2017)		✓	✓	✓✓			++		
	Greenockite	Souto (2017)				✓					
	Isocubanite	Leal Gomes <i>et al.</i> (2011)	✓						++		✓

Table 8 – Mineralogical checklist of all the minerals identified in Cerdeirinha until now, regarding its author, method (X-Ray Diffractometry, Scanning Electron Microscopy, Wavelength-Dispersive Spectroscopy, Reflected Light Microscopy, Transmitted Light Microscopy and Ultraviolet Light), relative abundance index and subsequent study. (To be continued.)

	Pyrrhotite	T.S.; Leal Gomes <i>et al.</i> (2011); Dias & Leal Gomes, (2015); Souto (2017)		✓✓	✓	✓✓			++++	✓	✓✓
	Galena	T.S.; Souto (2017)		✓	✓						
	Bismuthinite	Souto (2017)		✓		✓					
	Tetradymite	T.S.		✓							
	Molybdenite	T.S.		✓	✓						
	Pyrite	T.S.; Leal Gomes <i>et al.</i> (2011); Dias & Leal Gomes, (2015); Souto (2017)	✓	✓✓	✓	✓✓			++++	✓✓	✓✓
	Marcassite	T.S.; Leal Gomes <i>et al.</i> (2011); Souto (2017)		✓		✓✓			++		✓
	Lollingite	T.S.;		✓	✓	✓			+		
	Arsenopyrite	T.S.; Leal Gomes <i>et al.</i> (2011); Souto (2017)		✓✓	✓	✓✓			++++	✓	✓
	Skutterudite	Souto (2017)				✓					
	Cosalite (??)	Souto (2017)	✓								
	Enargite	Souto (2017)	✓								
	V-Enargite (??)	Souto (2017)	✓								
	Marmatite	Leal Gomes <i>et al.</i> (2011)	N.S.	N.S.	N.S.	N.S.	N.S.	N.S.	+		
	Fe Sulfides	Leal Gomes <i>et al.</i> (2011)	N.S.	N.S.	N.S.	N.S.	N.S.	N.S.			
	Pb-Bi-Ag Sulfosalts	Souto (2017)				✓					
<b>Halogenides</b>	Fluorite	T.S.; Souto (2017); Oliveira (2017)			✓		✓✓		++		✓
	Massicot	T.S.		✓							

Table 8 – Mineralogical checklist of all the minerals identified in Cerdeirinha until now, regarding its author, method (X-Ray Diffractometry, Scanning Electron Microscopy, Wavelength-Dispersive Spectroscopy, Reflected Light Microscopy, Transmitted Light Microscopy and Ultraviolet Light), relative abundance index and subsequent study. (To be continued.)

<b>Oxides, Hydroxides and Arsenites</b>	Magnetite	Leal Gomes <i>et al.</i> (2011)	N.S.	N.S.	N.S.	N.S.	N.S.	N.S.			
	Ilmenite	T.S.; Leal Gomes <i>et al.</i> (2011)			✓	✓			++		✓
	Ilmenorutile	Leal Gomes <i>et al.</i> (2011)	N.S.	N.S.	N.S.	N.S.	N.S.	N.S.			
	Tausonite	Souto (2017)	✓								
	Bismite	T.S.		✓					+		
	Arseniumbismite	Souto (2017)		✓							
	Quartz	T.S.; Dias (2011); Souto (2017); Leal Gomes <i>et al.</i> (2011); Oliveira (2017)		✓✓	✓	✓	✓✓		+++++		
	Cassiterite	Leal Gomes <i>et al.</i> (2011)	N.S.	N.S.	N.S.	N.S.	N.S.	N.S.			
	Rutile	Souto (2017)		✓							
	Ferberite	T.S.		✓	✓				+		
	Wolframite	T.S.; Dias (2011); Leal Gomes <i>et al.</i> (2011); Souto (2017)		✓	✓	✓✓			++		
	Russelite	T.S. (?); Souto (2017); Oliveira (2017)	✓								
	Goethite	T.S.; Souto (2017)		✓✓							
	Bi and (Au) sulfur-arsenites	Leal Gomes <i>et al.</i> (2011)	N.S.	N.S.	N.S.	N.S.	N.S.	N.S.	+		
	Iron Oxides	T.S.; Souto (2017)			✓		✓✓		+		
<b>Carbonates and Nitrates</b>	Calcite	T.S.; Dias (2011); Leal Gomes <i>et al.</i> (2011); Souto (2017); Oliveira (2017); Coelho (1993)			✓	✓	✓✓		++		
<b>Sulfates, Chromates,</b>	Anhydrite	T.S.; Leal Gomes <i>et al.</i> (2011)			✓				+		✓✓

Table 8 – Mineralogical checklist of all the minerals identified in Cerdeirinha until now, regarding its author, method (X-Ray Diffractometry, Scanning Electron Microscopy, Wavelength-Dispersive Spectroscopy, Reflected Light Microscopy, Transmitted Light Microscopy and Ultraviolet Light), relative abundance index and subsequent study. (To be continued.)

<b>Molybdates and Tungstates</b>									Leal Gomes <i>et al.</i> (2011): ++		
	Anglesite	T.S.		✓✓					+		
	Barite	Leal Gomes <i>et al.</i> (2011)							++		
	Alunogéneo, NH4-alunite	Souto (2017)	✓								
	H.O-Jarosite	Souto (2017)	✓								
	Coquimbite	Souto (2017)	✓								
	Gypsum	Leal Gomes <i>et al.</i> (2011); Souto (2017)	✓								✓
	Scheelite	T.S.; Dias (2011); Leal Gomes <i>et al.</i> (2011); Souto (2017); Oliveira (2017); Coelho (1993)	✓	✓	✓	✓✓	✓✓	✓	+++	✓	
	Mo-scheelite	Souto (2017)		✓				✓			
	Powellite	Souto (2017)	✓								
	Tungstates	Souto (2017)				✓					
	Ca sulfates	Leal Gomes <i>et al.</i> (2011)	N.S.	N.S.	N.S.	N.S.	N.S.	N.S.			
	Svambergite	Leal Gomes <i>et al.</i> (2011)	N.S.	N.S.	N.S.	N.S.	N.S.	N.S.	+		
	Phosphatized sulfate	Leal Gomes <i>et al.</i> (2011)	N.S.	N.S.	N.S.	N.S.	N.S.	N.S.			
<b>Phosphates, Arsenates and Vanadates</b>	Neustädtelite	T.S.		✓							
	Apatite	T.S.; Dias (2011); Leal Gomes <i>et al.</i> (2011); Oliveira (2017)			✓		✓	+++	✓		
	F-apatite	T.S.; Souto (2017); Oliveira (2017)	✓	✓✓		✓	✓	(?)			
	Mn-F-apatite	T.S.		✓				+			

Table 8 – Mineralogical checklist of all the minerals identified in Cerdeirinha until now, regarding its author, method (X-Ray Diffractometry, Scanning Electron Microscopy, Wavelength-Dispersive Spectroscopy, Reflected Light Microscopy, Transmitted Light Microscopy and Ultraviolet Light), relative abundance index and subsequent study. (To be continued.)

	Kolbeckite	Souto (2017)		✓							
	Scorodite	Souto (2017)		✓							
	Diadochite	Souto (2017)		✓							
<b>Silicates</b>	Olivine (?)	Souto (2017)	✓								
	Calcic Calderite	Souto (2017)	✓								
	Zircon	T.S.			✓		✓		+		
	Ripidolite	T.S.	N.S.	N.S.	N.S.	N.S.	N.S.	N.S.			✓
	Brungsvite	T.S.	N.S.	N.S.	N.S.	N.S.	N.S.	N.S.			✓
	Pseudothuringite	T.S.	N.S.	N.S.	N.S.	N.S.	N.S.	N.S.			✓
	Sphene	T.S.; Souto (2017); Oliveira (2017)			✓	✓	✓		+		✓
	Garnet	Dias (2011); Oliveira (2017); Coelho (1993)	N.S.	N.S.	N.S.	N.S.	N.S.	N.S.			
	Spessartine	Oliveira (2017)	✓								
	V-Spessartine	Oliveira (2017)	✓								
	Grossular	Dias, 2011; Souto (2017); Oliveira (2017)	✓					✓ (?)			
	Hydrogrossular	Souto (2017)	N.S.	N.S.	N.S.	N.S.	N.S.	N.S.			
	Clinozoisite	Oliveira (2017)	N.S.	N.S.	N.S.	N.S.	N.S.	N.S.			
	Epidote	Dias (2011); Souto (2017); Oliveira (2017)						✓			
	Vesuvianite	T.S.; Dias (2011); Leal Gomes <i>et al.</i> (2011); Souto (2017); Oliveira (2017)	✓		✓			✓✓		++	✓
IMA2009-004 - Sn analogue of baratovite		N.S.	N.S.	N.S.	N.S.	N.S.	N.S.		+		✓

Table 8 – Mineralogical checklist of all the minerals identified in Cerdeirinha until now, regarding its author, method (X-Ray Diffractometry, Scanning Electron Microscopy, Wavelength-Dispersive Spectroscopy, Reflected Light Microscopy, Transmitted Light Microscopy and Ultraviolet Light), relative abundance index and subsequent study. (To be continued.)

Tourmaline	Dias (2011); Leal Gomes <i>et al.</i> (2011)	N.S.	N.S.	N.S.	N.S.	N.S.	N.S.			
Pyroxene	T.S.; Coelho (1993)					✓		++		
Diopside	T.S.; Dias (2011); Souto (2017); Oliveira (2017)	✓	✓	✓				++		✓
Hedenbergite	T.S.			✓				+		✓
Augite	T.S.			✓						
Amphibole	T.S.; Dias, 2011; Leal Gomes <i>et al.</i> (2011); Souto (2017); Oliveira (2017); Coelho (1993)		✓		✓			++		✓
Actinolite-tremolite	Souto (2017)					✓ (?)				
Actinolitic hornblende	T.S.			✓				+		✓
Fe-hornblende (Ca, Fe)	Souto (2017)	✓								
Green hornblende	Souto (2017)					✓				
Mg-hornblende	T.S.			✓				++		✓
Kaolinite	Souto (2017)	✓								
Wollastonite	Oliveira (2017)		✓			✓				
Hydroxyapophyllite-(KOH)	T.S.							+		✓
Celadonite	T.S.							+		✓
Muscovite	T.S.; Souto (2017); Oliveira (2017)	✓		✓		✓✓				
(V/Ba)- Muscovite	Souto (2017)	✓								
(V/Cr)-Muscovite	Souto (2017)	✓								
Biotite	T.S.; Dias (2011)			✓		✓		+++		
Ferrous biotite	Souto (2017)					✓				

Table 8 – Mineralogical checklist of all the minerals identified in Cerdeirinha until now, regarding its author, method (X-Ray Diffractometry, Scanning Electron Microscopy, Wavelength-Dispersive Spectroscopy, Reflected Light Microscopy, Transmitted Light Microscopy and Ultraviolet Light), relative abundance index and subsequent study. (Concluded.)

F-phlogopite	Souto (2017)	✓								
Chlorite	T.S.; Dias (2011); Leal Gomes <i>et al.</i> (2011); Oliveira (2017); Souto (2017)			✓		✓✓		++		✓
Clinochlore (chlorite Mg, Fe)	Souto (2017)	✓								
Stilpnomelane	T.S.			✓				++		✓
Scapolite	T.S.; Souto (2017); Oliveira (2017)			✓		✓		+		✓
Scapolite (marialite, Na)	Souto (2017)	✓				✓				
Plagioclase	T.S.; Dias (2011); Souto (2017); Oliveira (2017)					✓ (?)	✓✓	++++		
Albite	T.S.; Leal Gomes <i>et al.</i> (2011); Souto (2017); Oliveira (2017)		✓	✓			✓✓	+		
Anorthite	T.S.; Souto (2017); Oliveira (2017)	✓		✓				+		
Andesine	T.S.			✓				+		✓
Labradorite	T.S.			✓				+++		✓
Oligoclase	Souto (2017)	✓	✓							
Feldspar	Dias (2011); Souto (2017); Coelho (1993)						✓			
Mica	T.S.; Leal Gomes <i>et al.</i> (2011)						✓✓	+++		
Filosilicates	Leal Gomes <i>et al.</i> (2011)									
Adularia (?)		✓								



## 5.2. Table of binary intergrowths

When minerals crystalize they can intergrowth with others. Hence, the mode they contact with each other (in some cases only with particular minerals) and develop intergrowths allow to establish a possible generation order. Figure 46 was established due to microscope observations (the mineral intergrowths, and their black circumferences that indicate the location of L.A.-I.C.P.-M.S. procedures that were latter executed, can be found in figures 32 to 37, and others are in *Annexe 1*). The mineral assemblage contacts considered for the construction of the figure 46 are represented with “ $\diamond$ ” in the following pictures and in *Annexe 1*.

Hence, in order to achieve a possible order of crystallization (figs. 49 and 50) (subchapter *5.3. Cerdeirinha paragenetic chronogram*), three diagrams were established. The first with all the minerals (fig. 46) that were found, except the ones present in the next two diagrams. The second was devoted only on particular minerals and their intergrowths found in a porfiroblastic arsenopyrite crystal that contained an Au-Ag alloy (fig. 47). And the last one, with only the Pb-Bi intergrowth sector found in the same sample (fig. 48).

### 5.2.1. Arsenopyrite

Arsenopyrite is one of the main ore minerals (fig. 32), and was found including and intergrowing with several minerals. A detailed paragenetic description of this geothermometer is present in the subchapter *6.3. Arsenopyrite*.

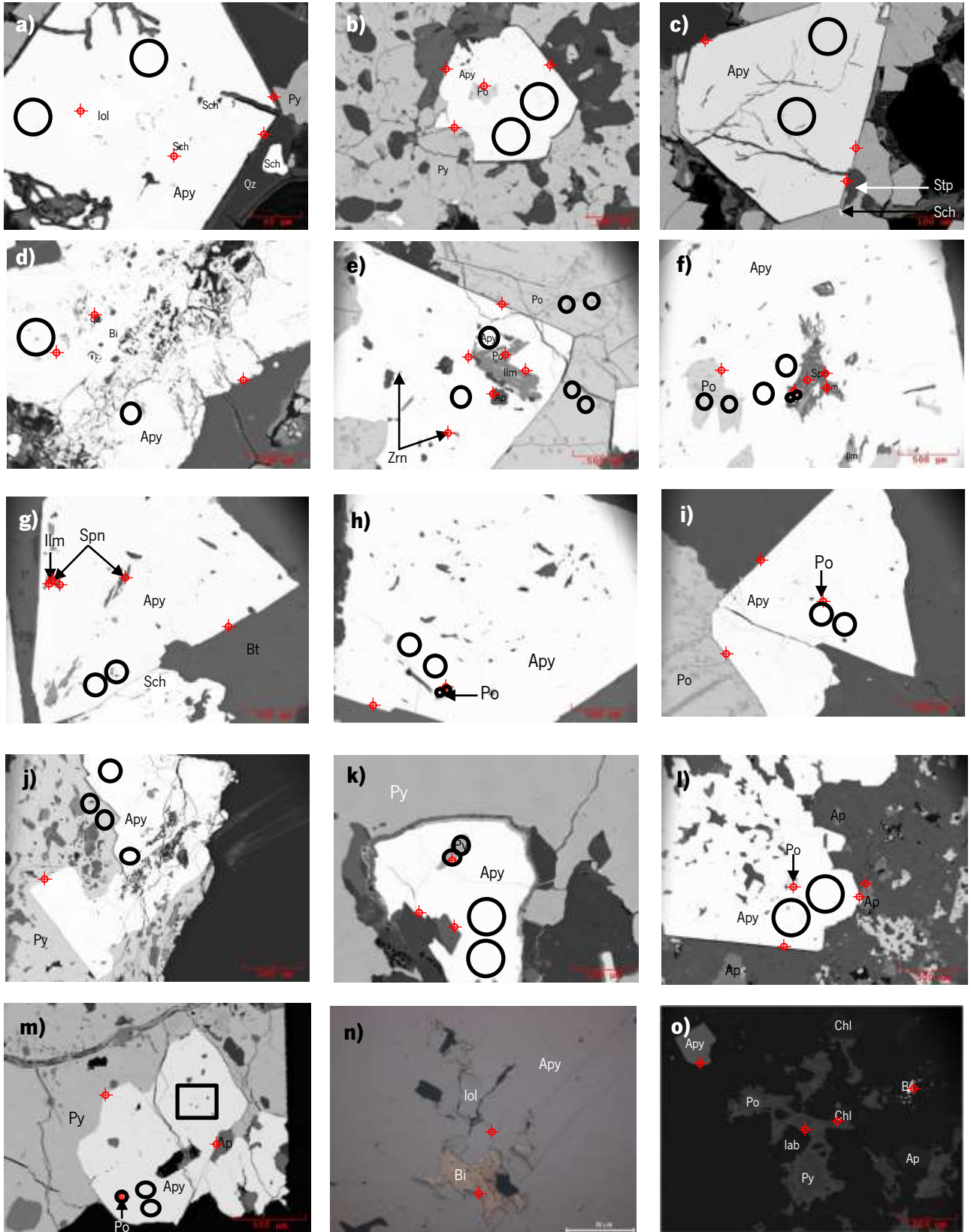


Figure 32 – Backscattered electrons and reflected light microscopy images of arsenopyrite paragenetic observations. The black circumferences indicate the location of L.A.-I.C.P.-M.S. spot measurements. **a)** With inclusions of lollingite and scheelite (CW05). **b)** With pyrrhotite inclusion (CW05). **c)** Without inclusions (CW05). **d)** With quartz and native Bi inclusions (CW05). **e)** Included in pyrrhotite, with inclusions of ilmenite and pyrrhotite, apatite and zircon (C2). **f)** With inclusions of pyrrhotite, titanite and ilmenite (C2). **g)** With inclusions of ilmenite and titanite (C2). **h)** With inclusions of pyrrhotite (C2). **i)** With pyrrhotite inclusion and contacting pyrrhotite (C2). **j)** Porfiroblastic arsenopyrite that includes electrum (CWW-3A). **k)** With pyrite inclusion (CWW-3A). **l)** With pyrrhotite inclusion (CWW-3A). **m)** With inclusions of pyrrhotite, apatite, native bismuth and lollingite (CWW-3A) Black lines limit the detail present in n). **n)** Reflected light microscopy image. Detail of m). Arsenopyrite involving lollingite and native bismuth. **o)** Arsenopyrite crystal observed in the C2 sample. Native bismuth was also observed.

## 5.2.2. Pyrite & Pyrrhotite

Pyrites and pyrrhotites were analysed in L.A.-I.C.P.-M.S. considering the diverse mineral assemblages (fig. 33). However, the results of pyrrhotites spots present in figures 32 f), h), and m) and pyrite spots in figure 32 k), and in figures 33 h) and i) contained contaminations, due to their low crystal dimensions, therefore their values are not present in the graphics in the chapter 7. *Geochemical fractionation and filiation signatures*. The sample CW05n presented a spheroid structure (*spheroid – apical sulfide domain with mound structure*) (fig. 24 c)), and therefore in the subtitle of the figure 33, it is discriminated if the respective image corresponds to the *outer*, *frontier* or *inner* sector – for a greater image description of this particular sample consult *Annexe I*.

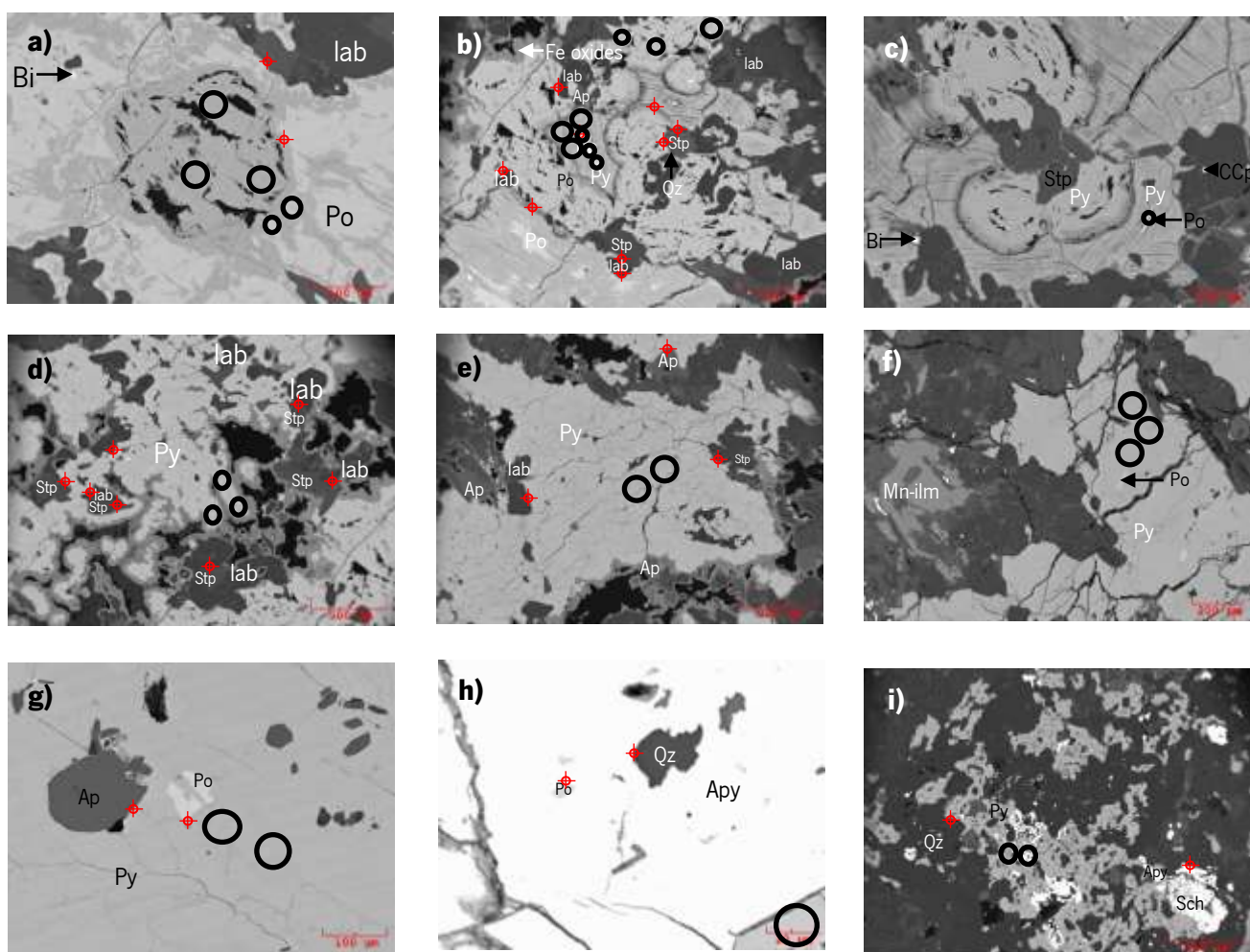


Figure 33 – Backscattered electrons images of pyrite and pyrrhotite paragenetic observations. L.A.-I.C.P.-M.S pyrite measurements. **a)** Outer zone (pyrrhotite dominant) pyrite-pyrrhotite decay (?) (CW05n). **b)** and **c)** Frontier sector pyrite-pyrrhotite decay (?) (CW05n). **d)** and **e)** Inner pyritic sector (CW05n). **f)** Inner pyritic sector close to the center of the nodule (CW05n). **g)** Pyritic matrix (CWW-3A). **h)** Pyrite in contact with arsenopyrite that includes quartz and pyrrhotite (CW05). **i)** Pyrite, intergrown with scheelite, quartz and apatite, close to the centre of the *remobilization* sample (CW05).

### 5.2.3. Chalcopyrite

Chalcopyrite was identified in all samples, except in the calc-silicate one. In the figure 34 its latter aspect is enhanced.

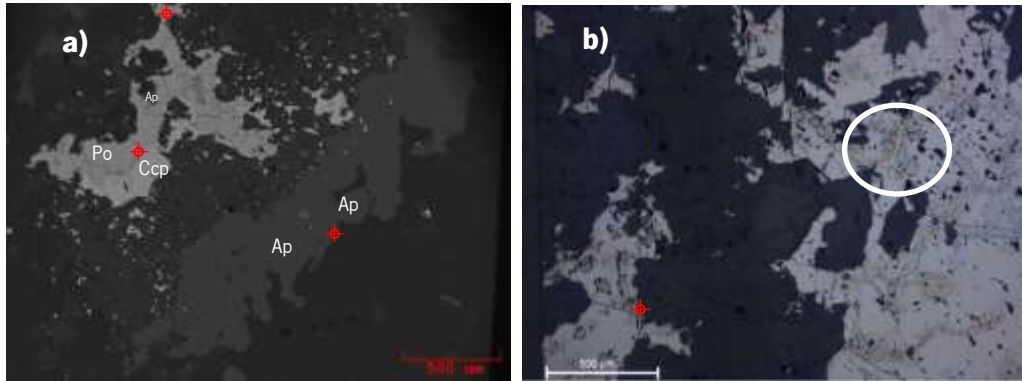


Figure 34 – Chalcopyrite latter than pyrrhotite. **a)** In outer pyrrhotite sector (C2). **b)** Chalcopyrite in triple junction (C2).

### 5.2.4. Mixed phases and mineral clusters

Besides all the sulfides that were previously presented, *mixtures of minerals* were also identified, where the higher dimension particles were around 10  $\mu\text{m}$  in size (figs. 35 and 36). These microscale intergrowths can be considered as masses of *mixed phases* sometimes similar to

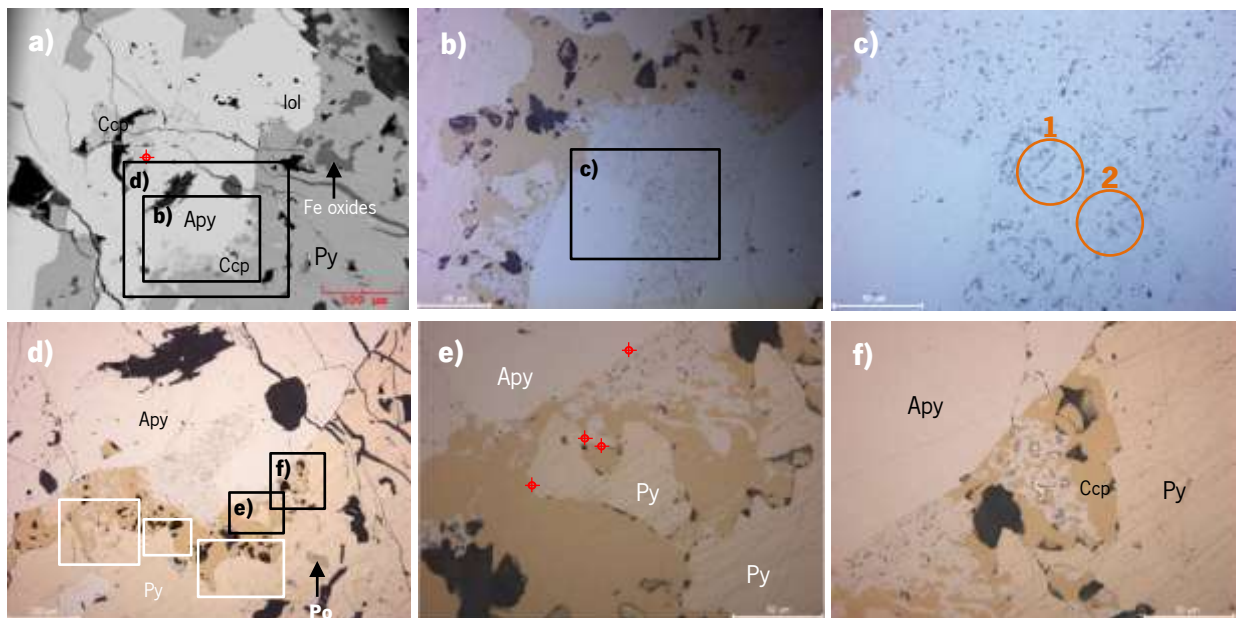


Figure 35 – Reflected light microscopy images demonstrating pyrite + arsenopyrite + chalcopyrite  $\pm$  bismuth  $\pm$  *mixed phases* (sulfosalts) assemblage (CWW-3A). The orange circumferences and numbers represent the spots locations of L.A.-I.C.P.-M.S. measurements. **a)** Backscatter electrons image. **b)** Reflected light microscopy image of the arsenopyrite, chalcopyrite, *mixed phases* and pyrite intergrown. **c)** Highlighting the location of the L.A.-I.C.P.-M.S. spot analysis of this *mixed phase*. **d)** Evidences of chalcopyrite replacing pyrite and the presence of *mixed phases* formed with the contact of arsenopyrite and chalcopyrite. The white perimeter enhances the chalcopyrite replacing pyrite. **e)** *Pyrite island* indicates that pyrite is being replaced by chalcopyrite. **f)** Detail of pyrite + arsenopyrite + chalcopyrite  $\pm$  bismuth  $\pm$  *mixed phases* (sulfosalts)

*mineral clusters*, because they seem to be more likely to present mineral aggregates with some well identified minerals (fig. 36).

When arsenopyrite contacts with chalcopyrite, the *mineral cluster* contains bismuth minerals with arsenopyrite (?).

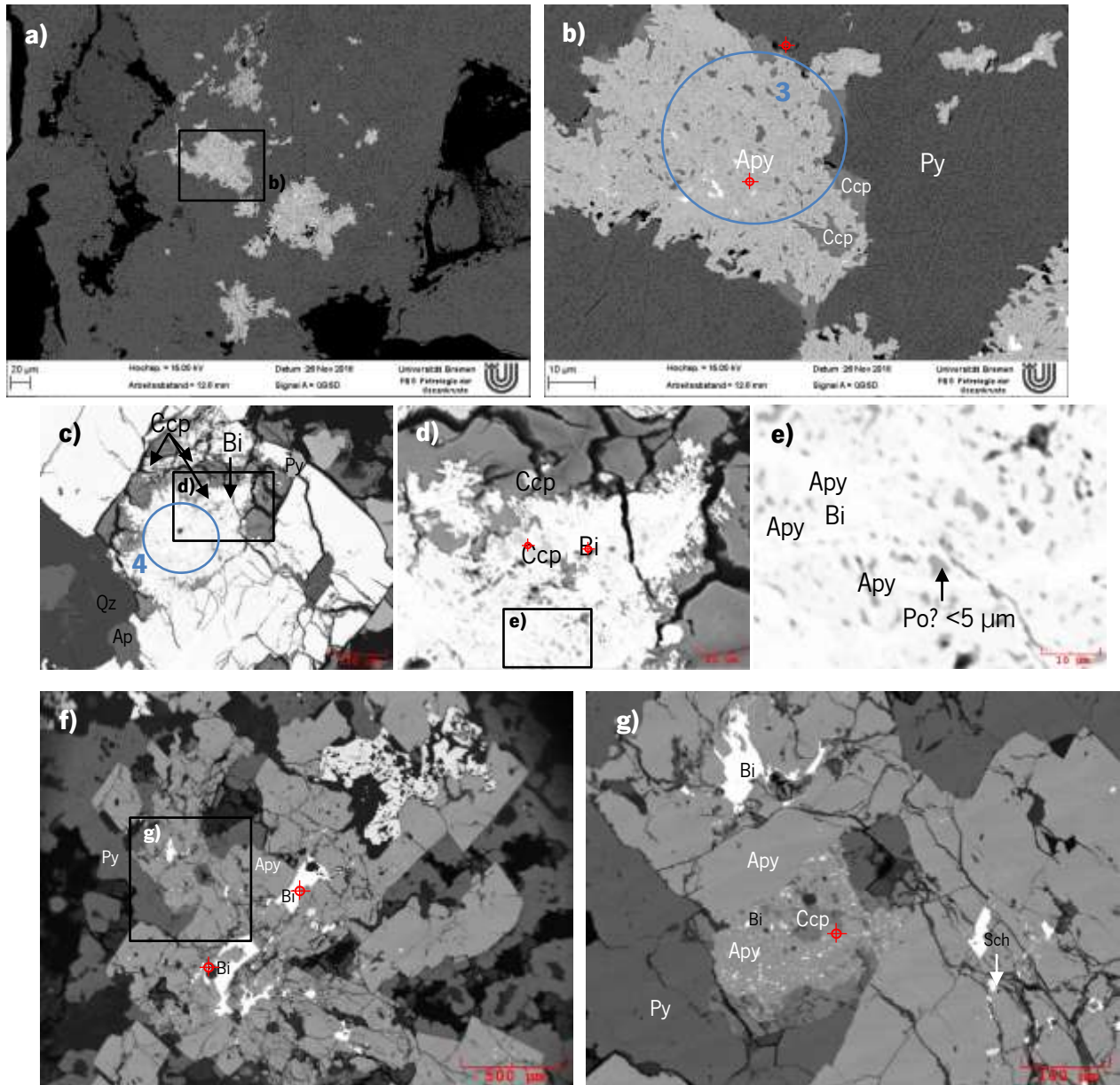


Figure 36 – Backscattered electrons images of what seems to be a *mineral cluster* in the samples CWW-3A and CW05. The blue circumferences and numbers represent the spots locations of L.A.-I.C.P.-M.S. measurements. **a)** Backscattered electrons image that shows brightness differences that suggest a chemical compositional evolution from *mixed phase* to *mineral cluster* composed by euhedral *acicular* arsenopyrite intergrowth with chalcopyrite in a pyritic matrix (CWW-3A). **b)** Backscattered electrons image, detailed image of a). **c)** *Mineral cluster* phase included in arsenopyrite and quartz (CW05). **d)** and **e)** Details of c). **f)** *Minerals cluster* that whose content was not measured in L.A.-I.C.P.-M.S. (CW05). **g)** Detail of f).

### 5.2.5. Tungstiferous minerals

Scheelite (fig. 37) is an ubiquitous mineral. It was observed mainly in sulfidic matrix (intergrown with pyrite and arsenopyrite). However, it was also observed in a biotitic matrix.

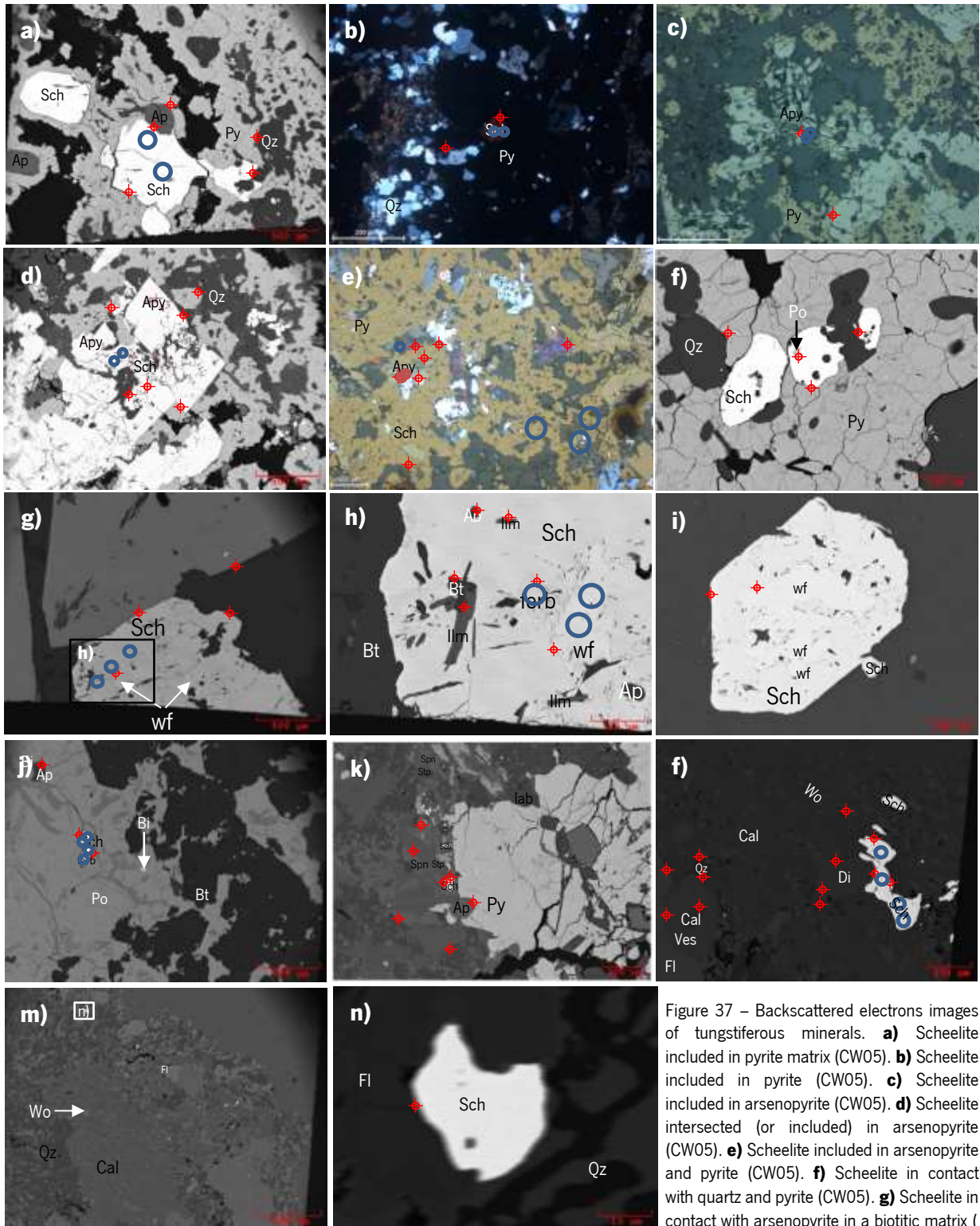


Figure 37 – Backscattered electrons images of tungstiferous minerals. **a)** Scheelite included in pyrite matrix (CW05). **b)** Scheelite included in pyrite (CW05). **c)** Scheelite included in arsenopyrite (CW05). **d)** Scheelite intersected (or included) in arsenopyrite (CW05). **e)** Scheelite included in arsenopyrite and pyrite (CW05). **f)** Scheelite in contact with quartz and pyrite (CW05). **g)** Scheelite in contact with arsenopyrite in a biotitic matrix (C2). **i)** Automorphic scheelite with wolframite included (or exsolved?) in biotitic matrix (C2). **j)** Scheelite and ferberite included in pyrrhotite. **k)** Scheelite included in titanite. **l)** Scheelite, in calcitic matrix with wollastonite *needles* and in contact with pyroxene. **m)** Scheelite crystal in a fluorite and quartz-rich zone (of the calc-silicate rock) (CEE-S). **n)** Detail of m).

### 5.2.6. Calc-silicate assemblages

The calc-silicate rock (*Skarn with proto-travertine ghost structures (mimetic structure)*) was considered as a proto-travertine by Dias (2011).

The dominant minerals found in this assemblage were clinopyroxenes, vesuvianite, calcite, quartz, fluorite and wollastonite.

#### 5.2.6.1. Wollastonite

Wollastonites appeared with different crystal habits, varying according to the matrix. In fluorite matrix, wollastonite generates zones with *almost wollastonitic crown* (Fig. 38 c)). Calcitic matrix includes wollastonite *needles* (Fig. 38 a) – in transition zone with calcitic-quartzous matrix it was possible to observe calcite, quartz and wollastonite surrounded by fluorite, and native Bi included. In quartz matrix wollastonite appeared elongated (Fig. 38 d)). Hydroxy-apophyllite is present at the contact between wollastonite and fluorite (Fig. 38 d)). In the interface between quartz and wollastonite the formation of hydroxy-apophyllite occurred.

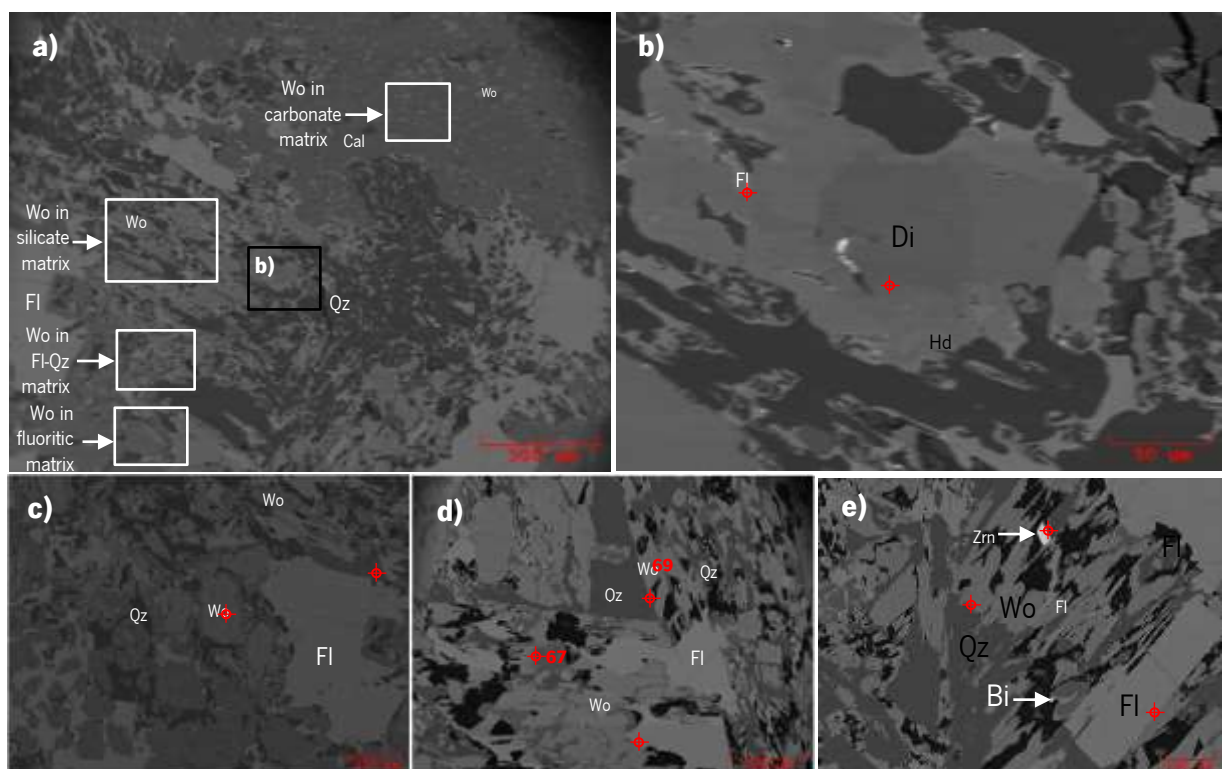


Figure 38 – Wollastonite diverse appearances in the calc-silicate rock (CEE-S). **a)** Sector of the calc-silicate rock that contains wollastonite under different crystal shape or thin section plane intersection. **b)** Detail of a), highlighting the diopside-hedenbergite transition. **c)** Wollastonite-*almost wollastonitic crown* and wollastonite crystals in a fluorite-quartz matrix. **d)** Elongated wollastonite crystals. **e)** Wollastonite present in a quartz enriched matrix. Zircon intergrown with quartz.

### 5.2.6.2. Diopside

Clinopyroxenes have subrounded shapes and in figure 37 f) the scheelite is *almost envolving* / adapted to the pyroxene. Clinopyroxenes are present in calcitic matrix, indicating that they predate calcite (fig. 39). In this situation, bismuth was observed included in clinopyroxene (diopside) (fig. 39 b))

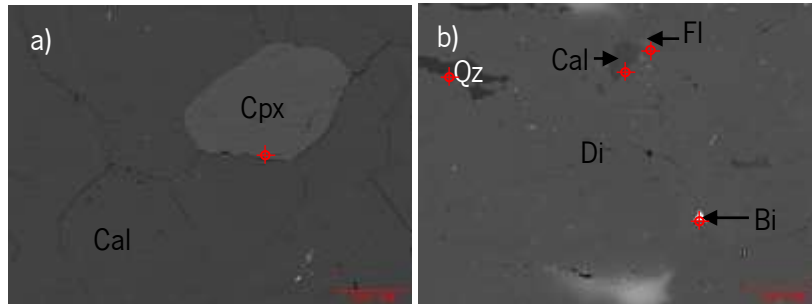


Figure 39 – Backscattered electrons images of examples of clinopyroxenes. **a)** Clinopyroxene in carbonate matrix. **b)** Clinopyroxene (diopside) including quartz, calcite, fluorite and native Bi.

Hedenbergite zonations were also observed in the peripheric boundary of the diopside crystals (fig. 40), suggesting being latter when compared with diopside. Pyrite was found including hedenbergite (fig. 40 d)).

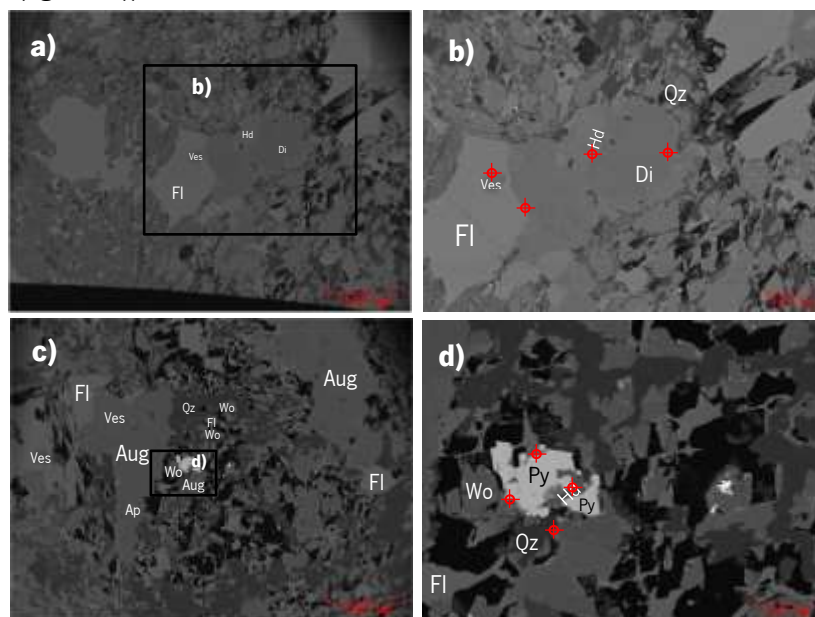


Figure 40 – **a)** Hedenbergite outer zoning diopside, and in contact with vesuvianite. **b)** Detail of a). **c)** Pyrite intersected by hedenbergite. **d)** Detail of c).



In sectors whose matrix is less constant, in particular the quartz-fluorite reaction, porosity increased (fig. 41).

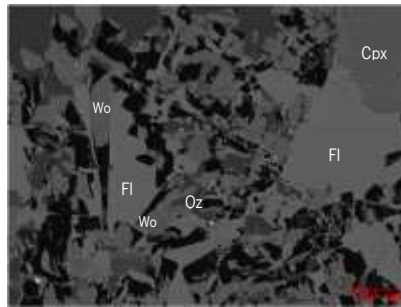


Figure 41 – Porosity of the calc-silicate rock.

### 5.2.6.3. Sphalerite

Vestigial content of sphalerite was found in the calc-silicate rock (fig. 42).

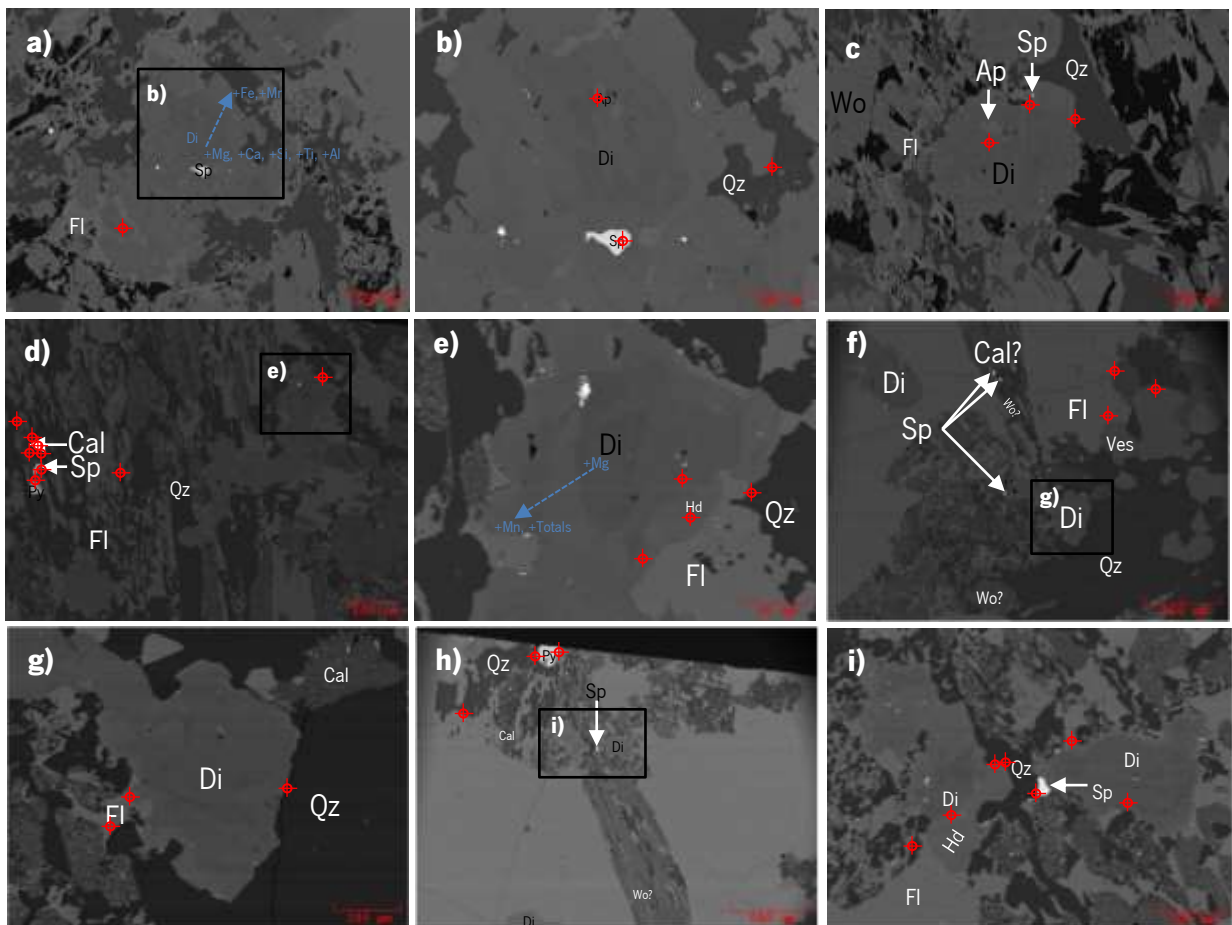


Figure 42 – Vestigial sphalerites found in the proto-travertine (Dias, 2011) – calc-silicate – sample. **a)** Sphalerite included in zoned pyroxene. **b)** Detail of a). **c)** Sphalerite included in non zoned pyroxene. Apatites were found in both cases in zoned and non zoned pyroxene. **d)** Sphalerite (remobilized) in contact with quartz, calcite and fluorite. **e)** Detail of d). **f)** Three sphalerites were spotted in quartz, fluorite and *almost wollastonite crown* respectively. **g)** Detail of f). **h)** (Remobilized?) sphalerite in contact with quartz and diopside. **i)** Detail of h).

#### 5.2.6.4. Galena

Galena was observed in the contact between vesuvianite and fluorite (fig. 43).

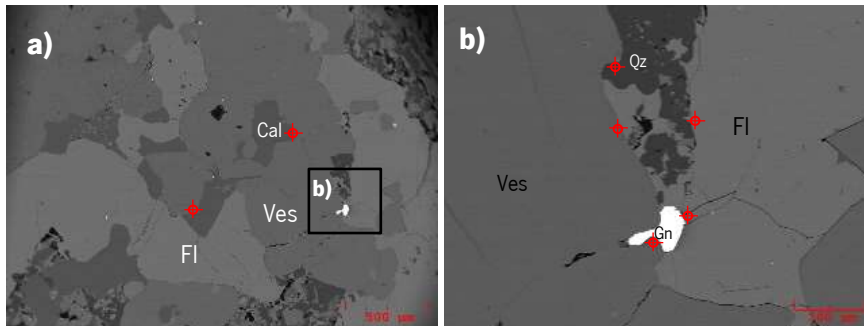


Figure 43 – Backscattered electrons image of galena (?) or molybdenite (?); vesuvianite including calcite and being involved by fluorite. **a)** General image. **b)** Detail of the ore mineral present in a).

#### 5.2.6.5. Zircon

Zircon was found in the felsic C2 sample (*sulfide arcs periphery – distal relatively to apical mounds domain*) (fig. 45 b)), but also in the calc-silicate one (fig. 38 e) and fig. 44)).

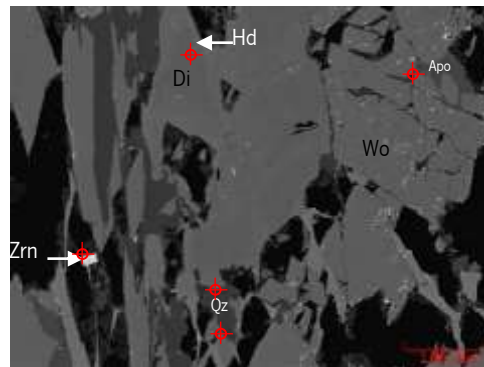


Figure 44 – Backscattered electrons images of zircon in calc-silicate rock.

### 5.2.7. Felsic character assemblage

C2 sample suggest a strong acidic and felsic character formation, due to presence of minerals such as biotite, sulfides and tungstates (fig. 45).

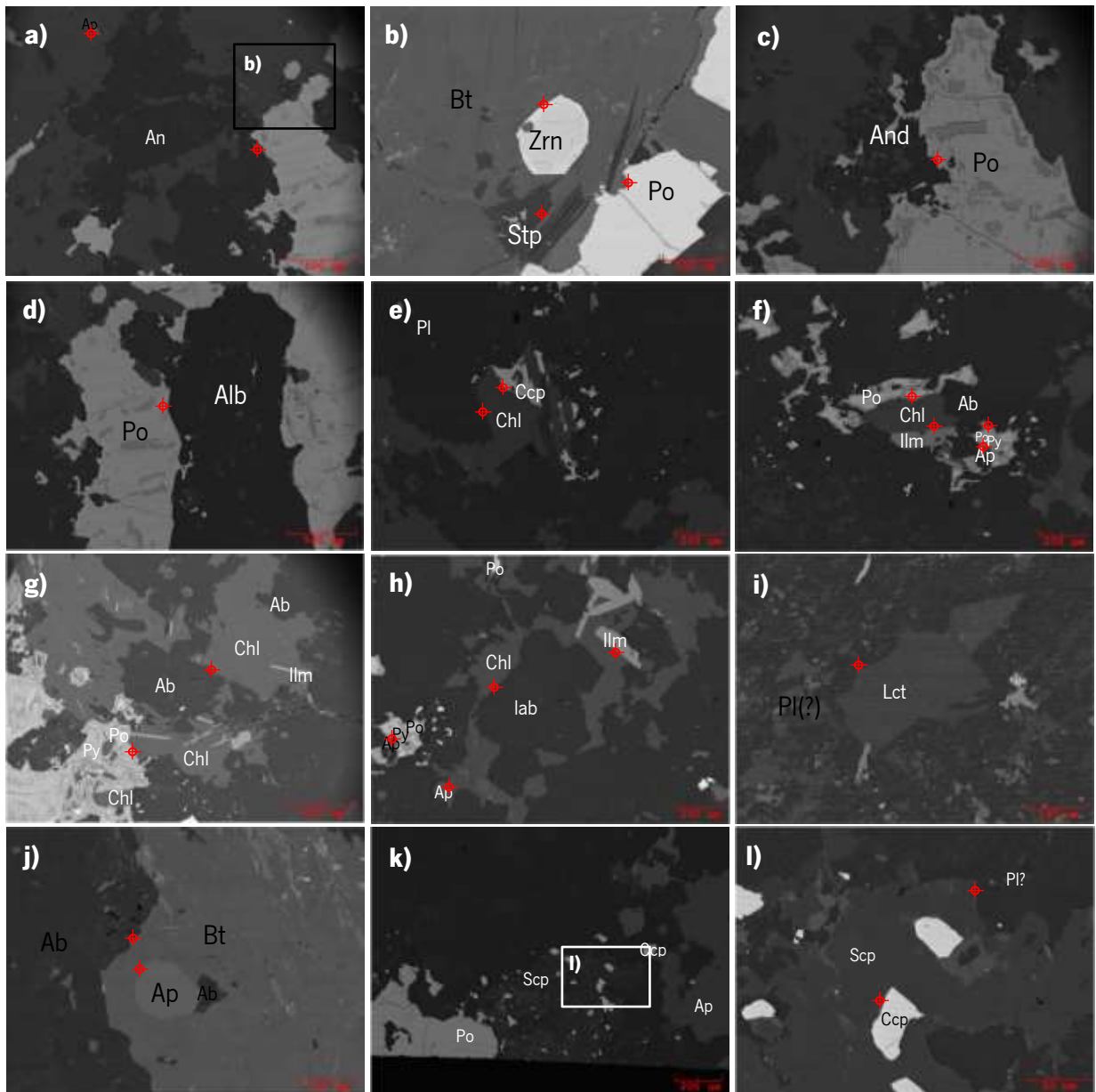


Figure 45 – Felsic character. **a)** Zircon included in biotite. **b)** Detail of a). **c)** and **d)** Plagioclase intergrown with pyrrhotite. **e)** Chlorite intergrown with chalcopyrite included in plagioclase matrix. **f)** Chlorite intergrown with pyrrhotite and ilmenite included in plagioclase. **g)** Chlorite, with ilmenite inclusion, involved in plagioclase. **h)** Ilmenite included in chlorite and involved by plagioclase. **i)** Leucite included in plagioclase. **j)** Apatite included in biotite. **k)** Scapolite involving chalcopyrite. **l)** Detail of k).



### 5.2.8. Particular textures in CWW-3A

In several samples, some peculiar assemblages were observed containing native bismuth, lollingite, wolframite and scheelite in arsenopyrite crystal. This is the example of CWW-3A (*attributed to sulfide-calcsilicated rock interface in the proximal tubuliform structural domain*) thin-section (fig. 47), where Au-Ag was found.

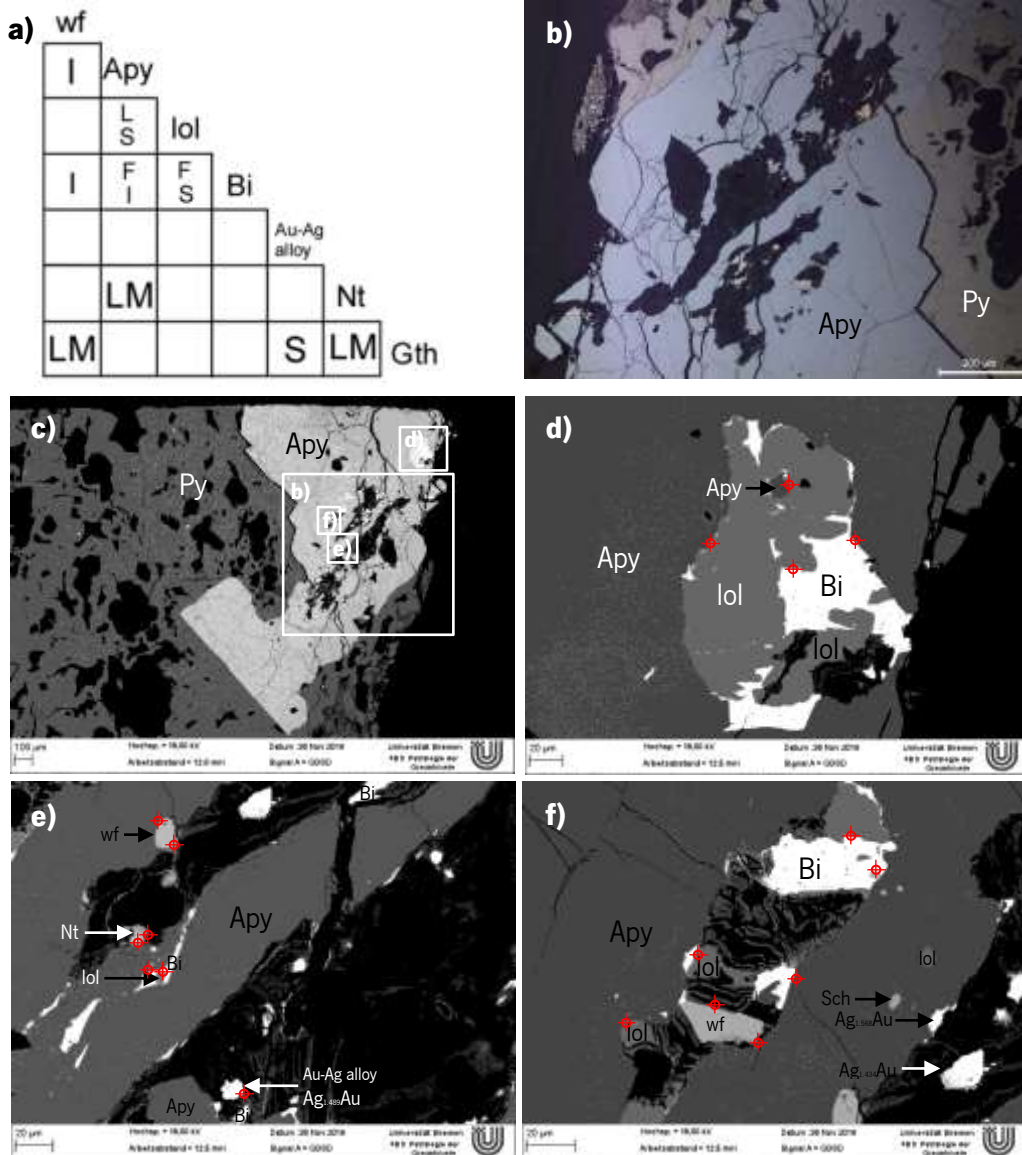


Figure 47 – Porphyroblastic arsenopyrite with tungstiferous minerals, native bismuth and Au-Ag alloy included. **a)** Contact modes verified in the following images. **b)** Identification of pyrite, arsenopyrite, gold and native Bi in reflected light microscopy. **c)** Backscattered electrons image of arsenopyrite in pyritic matrix. Backscattered electrons images **d)**, **e)** and **f)** show the arsenopyrite diverse mineralogical inclusions.

Besides, still in the same rock, more peculiar intergrowths, that seem to be correlated with supergene enrichment related with Pb and Bi content, were also observed (fig. 48).

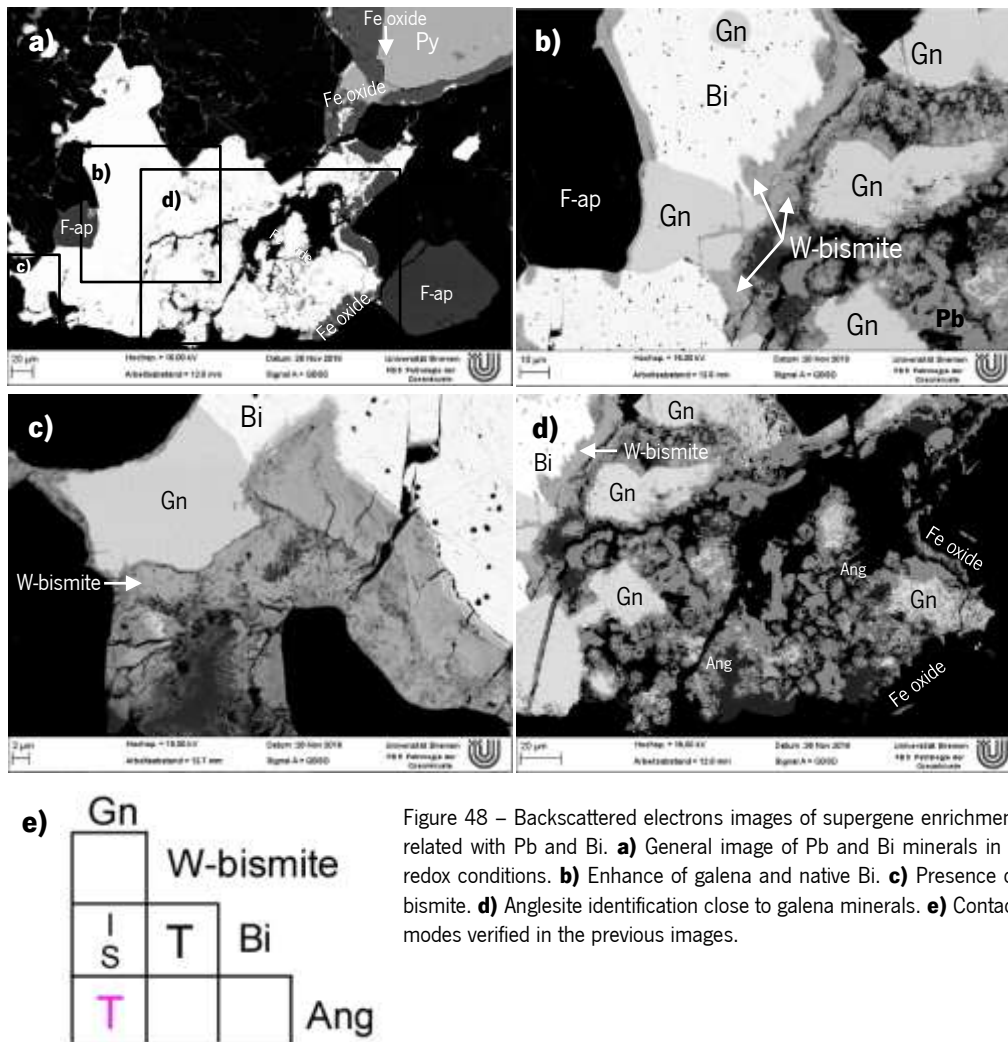


Figure 48 – Backscattered electrons images of supergene enrichment related with Pb and Bi. **a)** General image of Pb and Bi minerals in a redox conditions. **b)** Enhance of galena and native Bi. **c)** Presence of bismite. **d)** Anglesite identification close to galena minerals. **e)** Contact modes verified in the previous images.

### 5.3. Cerdeirinha paragenetic chronogram

A paragenetic diagram with the reduce-oxidizing conditions (fig. 49) was established for the textures observed in the set of samples analysed. For the most typical calc-silicate assemblages the paragenetic diagram is presented in figure 50. In both cases, the relative abundance is established in a roughly approximate way. The minerals are presented considering Nickel-Strunz classification.

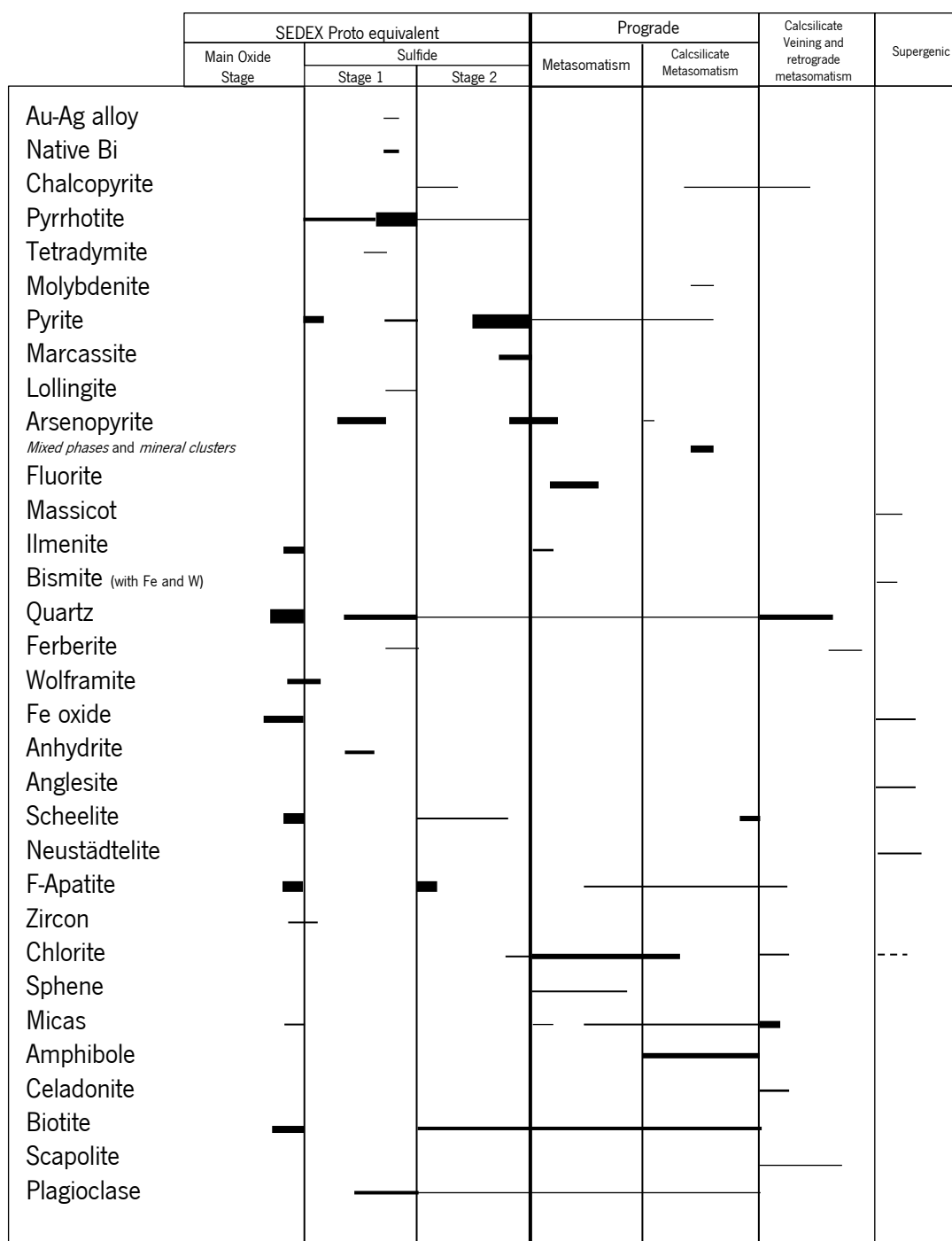


Figure 49 – Mineralogical paragenetic sequence of the minerals found in this study (except in the calc-silicate rock)

	Metasomatic assemblages	Infilling and vein assemblages
Native Bi	—	
Sphalerite	—	
Galena		—
Pyrite	—	
Fluorite	—	—
Quartz	—	—
Calcite	—	
Scheelite	—	
Apatite	—	
Zircon	—	
Vesuvianite	—	
Clinopyroxene	—	
Wollastonite	—	
Hydroxy-apophyllite		—

Figure 50 – Chronogram of the main calc-silicate paragenesis (possible metassomatism of proto-travertin).



## 6. ORE GEOCHEMISTRY AND GEOTHERMOBAROMETRY OF INDICATIVE PHASES

The data is scarce, but some diagnostic phases already allow to extract some guidance relations, regarding temperature (hornblende, hornblende-plagioclase intergrowth, chlorite and arsenopyrite) and pressure (hornblende, and hornblende-plagioclase intergrowth) of typical mineral assemblage formation. Hornblende and plagioclase allowed to characterize the regional metamorphism, while chlorite and arsenopyrite allowed a preliminary insight into the temperature of ore genesis.

### 6.1. Hornblende and Plagioclase

The amphibole structure consists of two main features, a double chain of cornersharing tetrahedra and a strip of edge-sharing octahedra, both of which extend in the *c*-direction (fig. 51). Both the tetrahedrally coordinated sites and the tetrahedra themselves are denoted as *T*, and the octahedrally coordinated sites and the octahedra are denoted as *M*. There are two topologically distinct types of tetrahedra in the double chain that are designated *T1* and *T2*, and three distinct types of octahedra that are designated *M1*, *M2* and *M3* (fig. 51). At the junction of the strip of octahedra and the chain of tetrahedra is the *M4* site, and below the hexagonal ring of tetrahedra is the *A* site at the center of a large cavity (Hawthorne & Oberti, 2007).

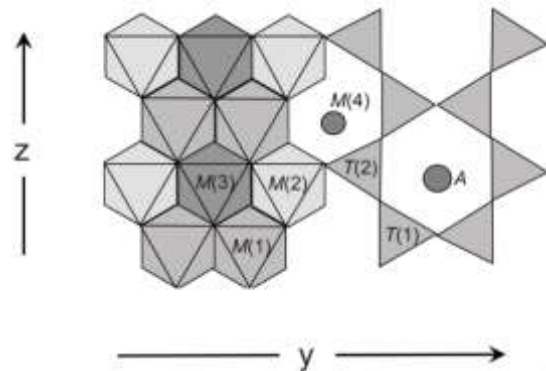
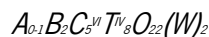


Figure 51 – An idealized model of the amphibole structure *sensu lato* showing the chain of tetrahedra, the strip of octahedra, the *M4* site and the *A* site. (From Hawthorne & Oberti, 2007)

At the junction of the strip of octahedra and the chain of tetrahedra is the *M4* site, and below the hexagonal ring of tetrahedra is the *A* site at the center of a large cavity (Hawthorne & Oberti, 2007).

The amphibole classification is based on the chemical contents of the standard amphibole formula. Its complex chemical composition can be expressed by (Leake, 1978; Deer *et al.*, 1992; Leake, *et al.*, 1997; Hawthorne & Oberti, 2007):



where

- A = Na, K, □, Ca, Li;
- B = Na, Ca, Mg, Fe<sup>2+</sup>, Mn<sup>2+</sup>, Li;
- C = Mg, Fe<sup>2+</sup>, Al, Fe<sup>3+</sup>, Mn<sup>2+</sup>, Mn<sup>3+</sup>, Zn<sup>2+</sup>, Cr<sup>2+</sup>, Ti<sup>4+</sup>, Li;
- T = Si, Al, Ti<sup>4+</sup>;
- W = (OH), F, Cl, O<sup>2-</sup>.

As seen above, regarding the *B* layer, nearly complete substitution may take place between sodium (Na) and calcium (Ca) and among magnesium (Mg), ferrous iron (Fe<sup>2+</sup>), and manganese (Mn). Regarding the *C* layer, there can exist limited substitution between ferric iron (Fe<sup>3+</sup>) and aluminium (Al) and between titanium (Ti) and other *C*-type cations (Safei *et al.*, 2015). Also, minor elements such as zinc (Zn), nickel ion (Ni<sup>2+</sup>), cobalt ion (Co<sup>2+</sup>), vanadium ion (V<sup>3+</sup>), scandium (Sc), chromium ion (Cr<sup>3+</sup>) and zirconium (Zr) are also observed as *C* cations (Hawthorne & Oberti, 2007). Aluminium (Al) can partially substitute silicon (Si) in the tetrahedral (*T*) site. Beside this, as it is possible to see through the presented chemical formula, also partial substitution of fluorine (F), chlorine (Cl), and oxygen (O) for hydroxyl (OH) in the hydroxyl site is also common (Safei *et al.*, 2015).

In structural terms the *A*, *B*, *C* and *T* atoms are respectively located in *A* sites, *M4*, *M1+M2+M3*, and *T* (tetrahedral) (Deer, 1992). Also Leake (1978) summarizes the standard formula for amphiboles and the procedure for its calculation from chemical analysis:  $A_{0-1}B_2C_5^{VI}T_8^{IV}O_{22}(OH,F,Cl)_2$ . This formula translated into the site terminology of crystallographers reads:  $A_{0-1}(M4)_2(M1,2,3)_5^{VI}(T1)_4(T2)_4^{IV}O_{22}(OH,F,Cl)_2$ .

In a mineral group as chemically complicated as the amphiboles, there are many problems connected with (1) the measurement of chemical compositions, and (2) the calculation of the chemical formula (Hawthorne & Oberti, 2007).

Considering the complexity of the amphibole formula, the classification of this mineral group is divided into four principal subdivisions based on *B*-group cation occupancy (fig. 52): iron-magnesium-manganese amphibole group, the calcic amphibole group, the sodic-calcic amphibole group, and the sodic amphibole group (Leake *et al.*, 1997).

#### 6.1.1. Data treatment

In order to determine the chemical composition of the amphiboles present in the nodular sample found in Cerdeirinha's open pit mine, electron microprobe analysis were performed (table 9). This technique allowed to obtain the mineral chemical composition as weight percentage of the oxides of the elements, except for the halogens. To determine the chemical composition of the crystals, microprobe analyses were performed at the University of Bremen, using a Cameca SX100 electron probe microanalyzer (E.P.M.A.) coupled with an energy-dispersion microprobe system. Analytical works were performed using 15 kV, 10 nA, beam diameter of 1 µm, and a counting time of 20 s for Na, Mg, Ca, Ti, Fe, Si, Al and 30 s for K and Cr and 40 s for Mn. Calibration was done with *Hornblende Kakanui* (USNM 143965) and *Chromium Augite (NMNH 164905)*. The calculation applied was based on scaling the ratios of the cations and/or anions to some quantity that one believes is constant and known within the unit

cell. Classically, the atomic contents of the unit cell are normalized to the density of the mineral, however this procedure is not followed here due to the difficulty of measuring accurately the minerals density

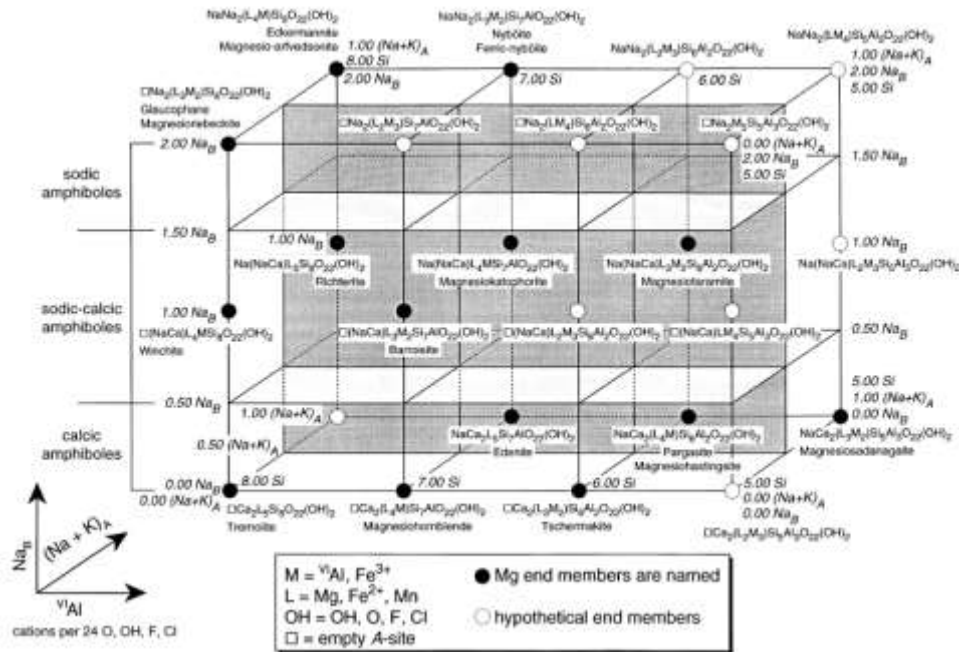


Figure 52 – General classification of the amphiboles, excluding the Mg–Fe–Mn–Li amphiboles (Leake *et al.*, 1997).

(Hawthorne & Oberti, 2007).

Calculations of a structural formula from complete wet chemical analysis should begin with evaluation of the H<sub>2</sub>O, F and Cl analysis and evidence for replacement of OH by O. If these analysis were considered extremely reliable, then the formula should be calculated on the basis of 24 (O, OH, F, Cl) (Hawthorne & Oberti, 2007). However, based on the results of electron microprobe analysis, as there is some uncertainty about the element previously referred in the Cerdeirinha data, it is safer to assume 2 (OH, F, Cl) and to calculate the formula on the basis 23 O (Doolan *et al.*, 1982). Therefore, the 23 O calculation assumes that (O,OH,F,Cl) = 2 apfu (Hawthorne & Oberti, 2007). According to Doolan *et al.* (1982) and to the available data, cations were then assigned to sites as follows:

*T site*: Added Si and then Al to sum to 8.00.

*C sites* (M1, M2, M3): Added left-over Al, Ti, Fe<sup>3+</sup>, Mg, Mn, Fe<sup>2+</sup> and Ca in that order to sum to 5.00.

*B sites* (M4): Added left-over Fe<sup>2+</sup>, Ca and Na in that order to sum to 2.00.

*A site*: Added left-over Ca, then Li, then Na, then K to sum no exceeding 1.00. Crystallographic data suggests that occupancy by any amount of Na + K between 0 and 1 is possible, and it is this variability in total cation occupancy that makes amphibole chemistry difficult to deal with (Doolan *et al.*, 1982).

Therefore, the number of cations was recalculated on the basis of 23 oxygens (O) (hence the sum of cations was close to 15), once this method is the most recommended regarding to Hawthorne & Oberti (2007). The calculation of the iron type of  $Fe^{2+}$  and  $Fe^{3+}$  was from Lawford Anderson (University of Southern California) excel sheet.

The recalculated mineral structure of amphiboles can be seen in the table 10. Leake (1968) suggested that analysis of a calcic amphibole should be rejected if  $Mg + Fe^{2+}$  in *B* is greater than 0.25. This was not verified in the present case.

Table 9 – Microprobe analysis of amphibole in the nodular sample.

Sample	Na <sub>2</sub> O	MgO	K <sub>2</sub> O	CaO	TiO <sub>2</sub>	Cr <sub>2</sub> O <sub>3</sub>	FeO	MnO	SiO <sub>2</sub>	Al <sub>2</sub> O <sub>3</sub>	Total
CW05n-1	1.09	11.52	0.61	11.92	0.18	0.04	15.30	1.17	47.67	6.76	96.26
CW05n-2	1.05	10.56	0.60	11.80	0.26	0.00	16.90	1.37	46.13	8.18	96.83
CW05n-3	1.23	10.90	0.65	11.94	0.19	0.03	16.28	1.14	46.49	7.98	96.82
CW05n-4	0.97	11.30	0.54	11.92	0.19	0.03	15.52	1.16	49.35	5.46	96.45
CW05n-5	1.12	10.15	0.70	11.67	0.16	0.05	16.79	1.34	45.97	8.69	96.64
CW05n-12	0.84	11.77	0.60	11.94	0.22	0.02	16.75	1.42	48.06	6.28	97.88
CW05n-13	0.94	10.90	0.63	11.85	0.26	0.01	17.60	1.37	47.73	7.32	98.61
CW05n-14	1.22	10.07	0.63	11.73	0.23	0.02	17.83	1.38	46.05	9.03	98.19
CW05n-19	0.95	11.32	0.62	11.90	0.23	0.03	17.00	1.38	47.81	6.76	98.00
CW05n-21	1.08	10.06	0.78	11.88	0.26	0.05	17.34	1.34	45.94	8.83	97.54
CW05n-25	1.17	10.06	0.70	11.87	0.19	0.07	17.46	1.50	45.85	8.61	97.46
CW05n-31	1.09	10.55	0.76	11.74	0.21	0.03	16.88	1.25	46.34	8.71	97.58
CW05n-44	0.97	11.52	0.61	11.83	0.17	0.06	16.45	1.36	48.05	6.77	97.79

To determine the amphibole mineral groups of the study area, the chemical composition determined was plotted on  $Na_B$  vs.  $Ca_B + Na_B$  diagram (Hawthorne, 1981). This diagram (fig. 53 a)), shows that the analysed amphiboles belongs to the *calcic group*. In addition, the correlation between  $Mg/(Mg + Fe^{2+})$  and  $Si_T$  allowed to identify the amphiboles as mainly *magnesiohornblende* and one as *actinolitic-hornblende* (fig. 53 b)). However, Leake *et al.* (1997) recommended that *actinolitic hornblende* should be considered as *magnesiohornblende* as well.

The low content of Ti present in hornblende indicates its secondary genesis instead of a magmatic genesis (Otten, 1984).

Table 10 – Recalculated result of amphibole in the nodular sample.

Sample	T site			C site								
	Si	Al <sup>IV</sup>	Sum T	Al <sup>VI</sup>	Ti	Fe <sup>3+</sup>	Mg	Mn	Fe <sup>2+</sup>	Cr	Ca	Sum C
CW05n-1	7.13	0.87	8.00	0.33	0.02	0.28	2.57	0.15	1.63	0.00	0.02	5.00
CW05n-2	6.89	1.11	8.00	0.33	0.03	0.53	2.35	0.17	1.59	0.00	0.00	5.00
CW05n-3	6.95	1.05	8.00	0.36	0.02	0.37	2.43	0.14	1.67	0.00	0.01	5.00
CW05n-4	7.37	0.63	8.00	0.33	0.02	0.17	2.51	0.15	1.77	0.00	0.05	5.00
CW05n-5	6.90	1.10	8.00	0.44	0.02	0.40	2.27	0.17	1.70	0.01	0.00	5.00
CW05n-12	7.07	0.93	8.00	0.16	0.02	0.60	2.58	0.18	1.45	0.00	0.00	5.00
CW05n-13	7.00	1.00	8.00	0.27	0.03	0.54	2.38	0.17	1.61	0.00	0.00	5.00
CW05n-14	6.81	1.19	8.00	0.39	0.03	0.54	2.22	0.17	1.66	0.00	0.00	5.00
CW05n-19	7.05	0.95	8.00	0.22	0.03	0.53	2.49	0.17	1.57	0.00	0.00	5.00
CW05n-21	6.85	1.15	8.00	0.40	0.03	0.45	2.23	0.17	1.71	0.01	0.01	5.00
CW05n-25	6.85	1.15	8.00	0.36	0.02	0.49	2.24	0.19	1.69	0.01	0.01	5.00
CW05n-31	6.88	1.12	8.00	0.40	0.02	0.47	2.33	0.16	1.62	0.00	0.00	5.00
CW05n-44	7.08	0.92	8.00	0.26	0.02	0.47	2.53	0.17	1.55	0.01	0.00	5.00

Sample	B site				A site			Sum cations	
	Fe	Ca	Na	Sum B	Ca	Na	K		
CW05n-1	0.00	1.89	0.11	2.00	0.00	0.21	0.12	0.33	15.33
CW05n-2	0.00	1.89	0.11	2.00	0.00	0.19	0.11	0.30	15.30
CW05n-3	0.00	1.90	0.10	2.00	0.00	0.26	0.12	0.38	15.38
CW05n-4	0.00	1.85	0.15	2.00	0.00	0.13	0.10	0.24	15.24
CW05n-5	0.00	1.88	0.12	2.00	0.00	0.21	0.13	0.34	15.34
CW05n-12	0.00	1.88	0.12	2.00	0.00	0.12	0.11	0.23	15.23
CW05n-13	0.01	1.86	0.13	2.00	0.00	0.14	0.12	0.26	15.26
CW05n-14	0.01	1.86	0.13	2.00	0.00	0.22	0.12	0.34	15.34
CW05n-19	0.00	1.88	0.12	2.00	0.00	0.15	0.12	0.27	15.27
CW05n-21	0.00	1.89	0.11	2.00	0.00	0.20	0.15	0.35	15.35
CW05n-25	0.00	1.89	0.11	2.00	0.00	0.23	0.13	0.36	15.36
CW05n-31	0.01	1.87	0.12	2.00	0.00	0.19	0.14	0.33	15.33
CW05n-44	0.01	1.87	0.12	2.00	0.00	0.15	0.11	0.27	15.27

Regarding the above explanation magnesianhornblende mineral formula was  $(\text{Na}_{0.12-0.26}, \text{K}_{0.11-0.15})(\text{Ca}_{1.86-1.90}, \text{Fe}_{0.00-0.01}, \text{Na}_{0.10-0.13})(\text{Mg}_{2.22-2.58}, \text{Mn}_{0.14-0.19}, \text{Fe}^{3+}_{0.28-0.61}, \text{Fe}^{2+}_{1.45-1.71}, \text{Al}_{0.16-0.44}, \text{Ti}_{0.02-0.03}, \text{Cr}_{0.00-0.01}, \text{Ca}_{0.00-0.02})(\text{Si}_{6.81-7.14}, \text{Al}_{0.87-1.19})\text{O}_{22}(\text{OH})_2$ .

While, for the actinolitic hornblende the calculated formula was  $(\text{Na}_{0.14}, \text{K}_{0.10})(\text{Ca}_{1.86}, \text{Na}_{0.15})(\text{Mg}_{2.51}, \text{Mn}_{0.15}, \text{Fe}^{3+}_{0.17}, \text{Fe}^{2+}_{1.77}, \text{Al}_{0.33}, \text{Ti}_{0.02}, \text{Cr}_{0.00}, \text{Ca}_{0.05})(\text{Si}_{7.37}, \text{Al}_{0.63})\text{O}_{22}(\text{OH})_2$ .

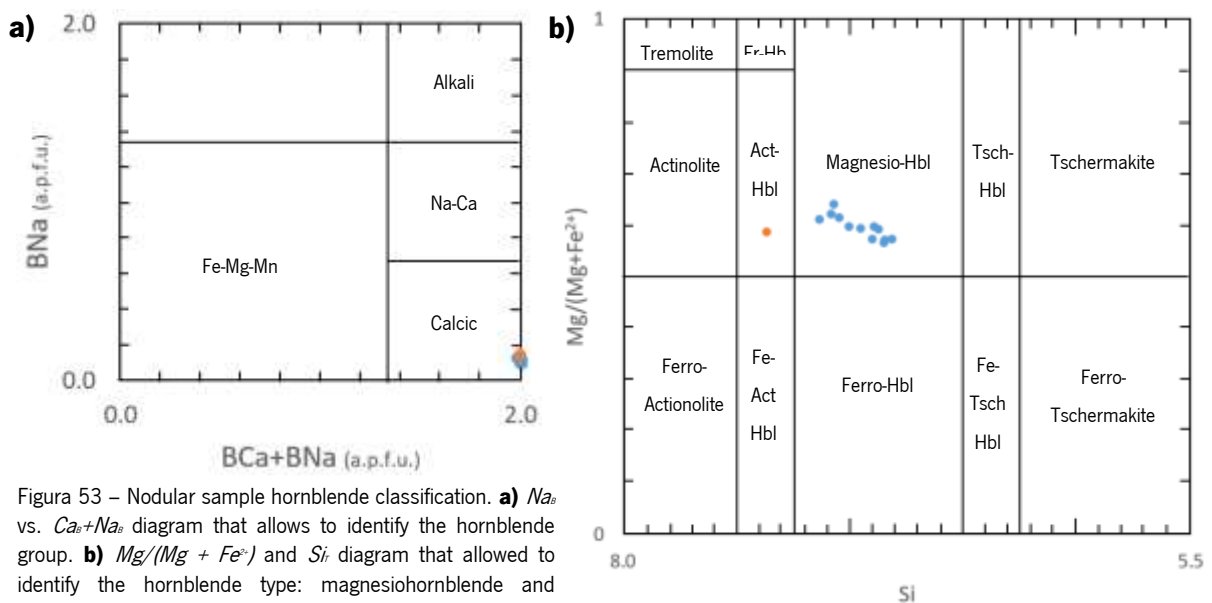


Figura 53 – Nodular sample hornblende classification. **a)**  $\text{Na}_a$  vs.  $\text{Ca}_a + \text{Na}_a$  diagram that allows to identify the hornblende group. **b)**  $\text{Mg}/(\text{Mg} + \text{Fe}^{2+})$  and  $\text{Si}$  diagram that allowed to identify the hornblende type: magnesianhornblende and actinolitic-hornblende.

The only *actinolitic-hornblende* identified can be seen in the figures 54 and 55 a), in contact with two *magnesiohornblendes*.

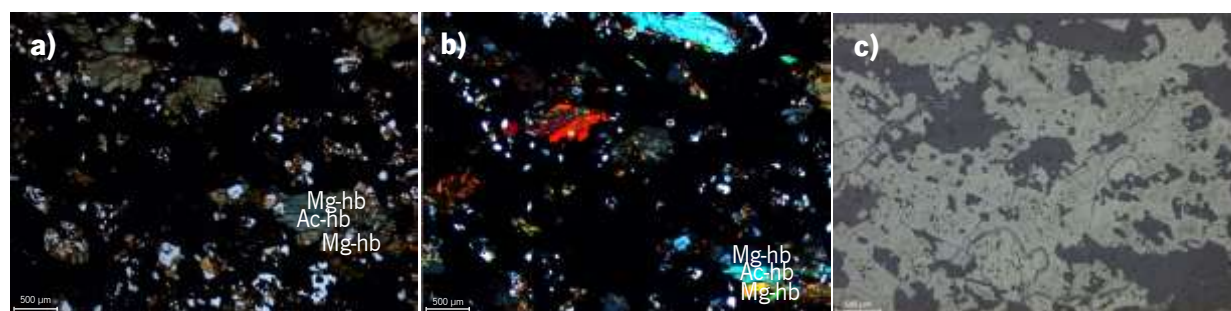


Figure 54 – Microphotography of the sector of nodular sample that contained the only actinolitic hornblende identified. In transmitted light microscopy (uncrossed polarizers – **a**)(crossed polarizers – **b**). In reflected light microscopy (**c**).

### 6.1.2. Pressure and temperature condition of crystallization

In the sample nodule (CW05.n), twelve Mg-hornblende points were analysed under microprobe. From these measurements it was possible to estimate its pressure of generation.

A excel sheet built by Tindle & Webb (1994) allowed to calculate the pressure conditions for each crystal during the hornblende genesis, according to different authors (table 11). However, for the actinolitic-hornblende, pressure conditions were not calculated (table 11; fig. 54). Latter, the Lawford Anderson's (University of Southern California) excel sheet allowed to confirm the pressure determination through Schmidt (1992) method and also determinate the temperature conditions, regarding the intergrowth of hornblende-plagioclase.

Table 11 – Pressure genesis (unit: Kbar) values determined regarding hornblende microprobe data. The bold method was also used for calculation purposes of Anderson and Smith (1995) and Holland and Blundy (1994), shown latter. (To be continued)

Sample \ Authors	Hammarstrom & Zen (1986)	Hollister <i>et al.</i> (1987)	Johnson & Rutherford (1989)	<b>Schmidt (1992)</b>
CW05n-1	2.1	2.0	1.6	2.7
CW05n-2	3.3	3.4	2.6	3.8
CW05n-3	3.2	3.2	2.5	3.7
CW05n-5	3.8	3.9	3.0	4.3
CW05n-12	1.6	1.4	1.1	2.2
CW05n-13	2.4	2.4	1.9	3.0
CW05n-14	4.0	4.1	3.2	4.5
CW05n-19	2.0	1.9	1.5	2.6
CW05n-21	3.9	4.0	3.1	4.4
CW05n-25	3.7	3.8	2.9	4.2
CW05n-31	3.7	3.8	3.0	4.2

Table 11 – Pressure genesis values determined regarding hornblende microprobe data. The bold method was also used for calculation purposes of Anderson and Smith (1995) and Holland and Blundy (1994), shown latter. (Concluded.)

CW05n-44	2.0	1.9	1.5	2.6
Mean	3.0	3.0	2.3	3.5
Standard deviation	0.9	1.0	0.7	0.8

The pressure was calculated due to hornblende crystal structure. The plagioclase (andesine and labradorite) intergrown with hornblende (fig. 55) allowed the estimation of the temperature.

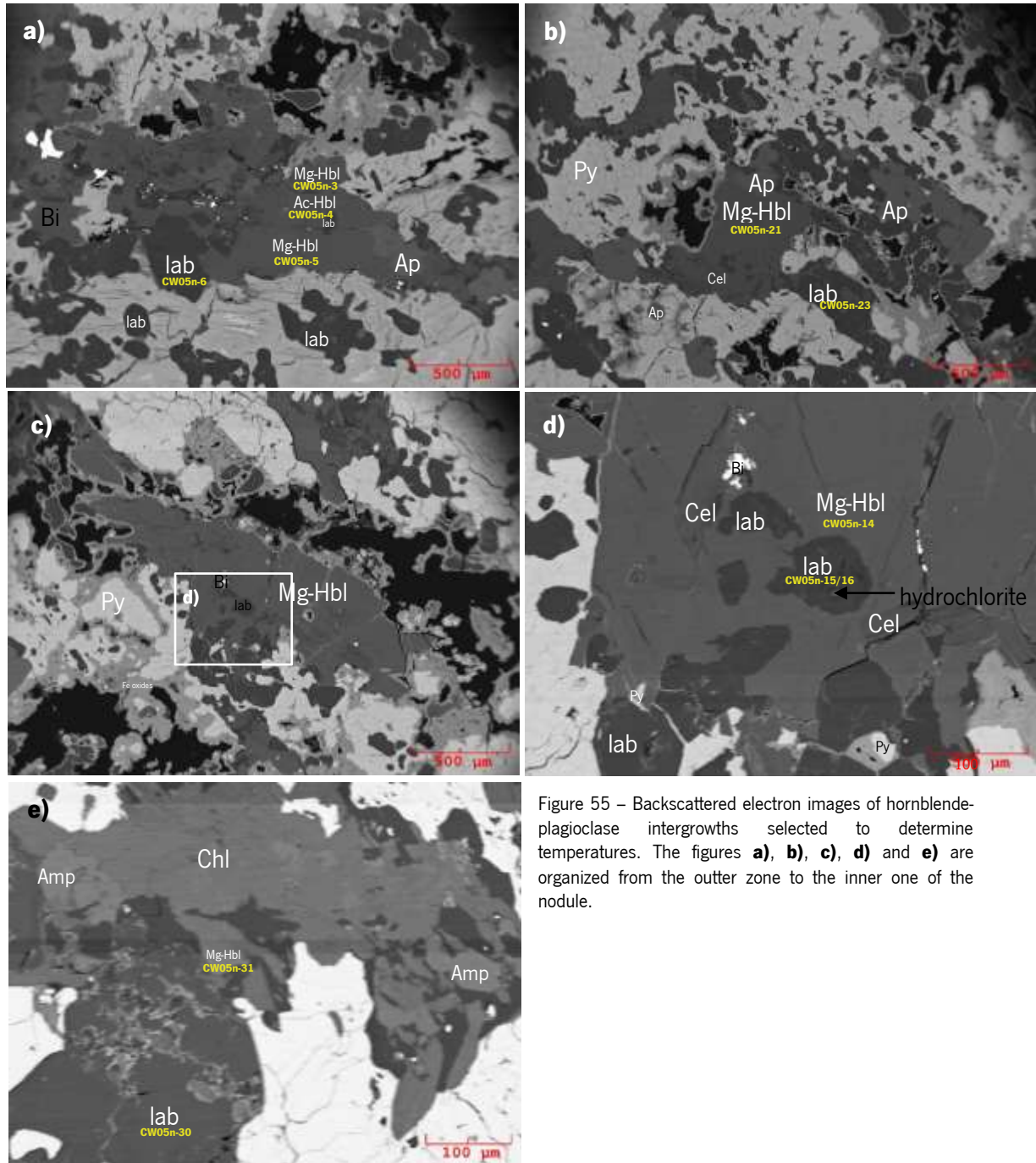


Figure 55 – Backscattered electron images of hornblende-plagioclase intergrowths selected to determine temperatures. The figures **a)**, **b)**, **c)**, **d)** and **e)** are organized from the outer zone to the inner one of the nodule.

For temperatures calculations, 3 different methods were applied. On the one hand, temperatures based only on hornblende. This temperature method based on Ti (Otten, 1984) is used to determine magmatic versus secondary compositions, however, in what temperature concerns,

$$T(^{\circ}\text{C}) = 273 \times (\text{Ti}/23 \text{ O}) + 877 \quad T > 970^{\circ}\text{C}$$

$$T(^{\circ}\text{C}) = 1,204 \times (\text{Ti}/23 \text{ O}) + 545 \quad T < 970^{\circ}\text{C}$$

Where  $Ti/23O$  is the number of Ti cations per unit formula (23 oxygens). When applied, and according to Otten (1984), the calculated temperatures were considered as low temperature range,  $\approx 567.0\text{--}579.8^{\circ}\text{C}$ . Therefore, the  $\approx 567.0\text{--}579.8^{\circ}\text{C}$  range indicates that this is not associated with a magmatic process but somehow related to fluid percolation. This values are low due to the low content of Ti present in hornblende that indicates its secondary crystallization or remobilization and recrystallization, as written above (Otten, 1984).

In addition, in the same sample hornblende-plagioclase intergrowth was verified (fig. 55). So, temperatures based on hornblende-plagioclase intergrowth were also determined. Its calculations were based on Schmidt (1992) method. Other methods applied were Anderson and Smith (1995) and Schmidt (1992).

Values obtained with Otten (1984) method were very low compared with the ones obtained through the hornblende-plagioclase intergrowth method (table 15).

In both cases of hornblende-plagioclase intergrowth, to determine the generation temperatures it was necessary to calculate the XAb and XAn for each plagioclase intergrown with hornblende.

#### 6.1.2.1. Plagioclases

Plagioclase chemical compositions were measured by electron microprobe (table 12), and a.p.f.u. calculated on the basis of 8 oxygens as in Deer *et al.* (1992) (table 13).

Table 12 – Microprobe analysis of plagioclase in the nodular sample.

Sample	Na <sub>2</sub> O	MgO	K <sub>2</sub> O	CaO	TiO <sub>2</sub>	Cr <sub>2</sub> O <sub>3</sub>	FeO	MnO	SiO <sub>2</sub>	Al <sub>2</sub> O <sub>3</sub>	Total
CW05n-6	5.33	0.00	0.06	10.45	0.01	0.01	0.13	0.03	55.74	28.43	100.19
CW05n-16	4.39	0.04	0.06	11.39	0.00	0.01	0.35	0.04	54.87	29.74	100.90
CW05n-23	5.14	0.00	0.05	9.92	0.02	0.01	0.25	0.00	56.54	27.98	99.91
CW05n-30	3.96	0.01	0.04	12.27	0.00	0.01	0.27	0.00	53.42	30.05	100.03

Table 13 – Recalculated result of plagioclase in the nodular sample.

Sample	Si	Al	Ti	Fe	Mn	Mg	Ca	Na	K	$\Sigma_{\text{cations}}$	Ab	An	Or
CW05n-6	222.95	151.65	0.03	0.00	0.22	0.00	83.59	85.28	0.94	544.66	0.50	0.49	0.01
CW05n-16	219.49	158.59	0.00	0.00	0.28	0.34	91.14	70.30	0.93	541.08	0.43	0.56	0.01
CW05n-23	226.16	149.23	0.07	0.00	0.00	0.00	79.35	82.26	0.86	537.93	0.51	0.49	0.01
CW05n-30	213.67	160.28	0.00	0.00	0.00	0.08	98.12	63.42	0.67	536.25	0.39	0.60	0.00



To discriminate these plagioclases, their chemical composition were plotted on Ab-An-Or diagram, where the plagioclases were identified as andesine ( $An_{0.49}Ab_{0.50}Or_{0.01}$ ) and labradorite ( $An_{0.56}Or_{0.61}Ab_{0.39}Or_{0.00}Or_{0.01}$ ) (figs. 55 and 56 c)).

Close to the exterior of the nodule the plagioclase in contact with hornblende is mainly andesine, while labradorite exists in the middle part of the nodule.

#### 6.1.2.2. Condition estimates

As seen before the calculation of pressure-temperature (P-T) conditions of metamorphism present in the nodular sample is hampered by the absence of suitable mineral phases such as garnet. However, some conventional quantitative geothermometers and geobarometers as hornblende-plagioclase equilibrium (Safei *et al.*, 2015) could be tested. To temperatures during metamorphism were estimated using the hornblende-plagioclase thermometer of Holland and Blundy (1994). This thermometer is based on the Ca and Na equilibrium exchange between plagioclase and amphibole (Safei *et al.*, 2015). The temperatures were calculated for plagioclase-amphibole pairs that show clear boundaries between them (fig. 55).

Anderson (1996) and Holland and Blundy (1994) hornblende-plagioclase expression for *edenite + albite = richterite + anorthite* equilibrium was used. The former author considered that the results derived from the calibration of reaction edenite-richterite of Holland and Blundy (1994) yield the lowest and are considered to be the most reliable (when compared with *edenite + 4 quartz = tremolite + albite* equilibrium), once they reproduce more precisely the temperatures derived from other thermometers. Besides this, as the nodular sample did not contain quartz, and also the plagioclases found were andesine

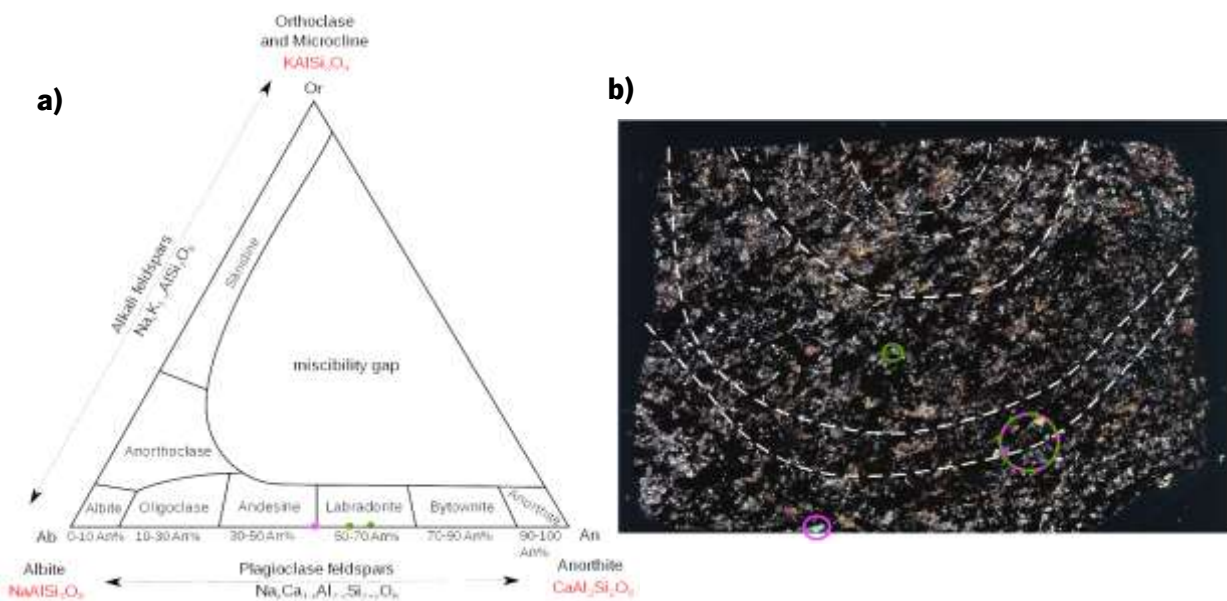


Figure 56 – Characterization of the plagioclases that were seen intergrown with hornblende. **a)** Classification of plagioclase intergrown with magnesianhornblende. Pink and green dots represent andesine and labradorite compositions, respectively. **b)** Transmitted light microscopy image of the map of the nodular sample with the limits of the area where andesine (pink) and labradorite (green) intergrown with hornblende were found. White dashed lines represent the nodular orientation observed in the thin-section.

and labradorite (both solid solutions compositions related with minerals present in the first reaction), this expression of equilibrium was the one selected.

For this equilibria the ideal solution model for hornblende was discarded and used a symmetrical formalism to account for non-ideality. This calibration is sensitive to the Fe<sup>3+</sup> content of hornblende which, in turn, affects the occupancy of several sites. Holland and Blundy (1994) follow an amphibole normalisation scheme similar to that of Spear and Kimball (1984) and, as it was used as a basis for calibrations, their procedure must be followed in the application of the thermometers (Anderson, 1996).

Regarding Anderson & Smith (1995), Schmidt (1992) and tables 14 and 15, a mean pressure of 3.8 kbar was established for the nodular sample. Regarding Holland and Blundy (1994), the mean temperature was determined, through Anderson & Smith (1995), as 718.0 °C. Notice that hornblende-plagioclase interaction calculated by Anderson & Smith (1995) are based on the Schmidt (1992) method. The estimated P–T conditions are in favour of their metamorphism under amphibolite (692 °C – 742 °C and 3.3 – 4.1 kbar) facies.

Table 14 – Results of Ab, Na and Or, its plagioclase type and hornblende (Hb) intergrowth for each plagioclase sample.

<b>Sample</b>	<b>Hb intergrown</b>	<b>Ab</b>	<b>Na</b>	<b>Or</b>	<b>Plagioclase</b>
CW05n-6	CW05n-5	0.50	0.49	0.01	Andesine
CW05n-16	CW05n-14	0.43	0.56	0.01	Labradorite
CW05n-23	CW05n-21	0.51	0.49	0.01	Andesine
CW05n-30	CW05n-31	0.40	0.66	0.00	Labradorite

Table 15 – Results of pressure and temperature based on iteration using Anderson and Smith (1995) pressure and temperature.

<b>Sample</b>	<b>T (°C)</b>	<b>P (Kb)</b>
CW05n-6	691.7 ± 23.0	4.13 ± 0.35
CW05n-16	739.4 ± 23.0	3.59 ± 0.35
CW05n-23	698.5 ± 23.0	4.11 ± 0.35
CW05n-30	742.4 ± 23.0	3.32 ± 0.35

### 6.1.3. Discussion

Amphibole and plagioclase are the main silicate minerals observed in the nodular sample. Based on the results of electron microprobe analysis, the amphiboles belong to the calcic group including several *magnesio-hornblende* terms and one *actonilitic-hornblende*. Intergrown with the former andesine ( $\text{An}_{0.49}\text{Ab}_{0.50-0.51}\text{Or}_{0.01}$ ) and labradorite ( $\text{An}_{0.56-0.61}\text{Ab}_{0.39-0.43}\text{Or}_{0.00-0.01}$ ) were identified.

A suitable mineral phase such as garnet was absent in the nodular sample, therefore some conventional quantitative geothermometers and geobarometers were tested specially hornblende-plagioclase.

Using hornblende-plagioclase intergrowths and its microprobe measurements, pressure and temperature of their generation were determined, being  $(3.80 \pm 0.35)$  Kb and  $(718.0 \pm 23.0)$  °C, respectively. The pressure was calculated, according to Schmidt (1992) and Anderson and Smith (1995), whereas the temperature was determined according to Holland and Blundy (1994). The estimated P-T conditions are in favour of their metamorphism under amphibolite ( $691.7^\circ\text{C} - 742.4^\circ\text{C}$  and 3.32-4.13 Kb) facies.

Regarding the mineral assemblages studied, the table 16 suggests that this is coherent with the amphibolitic facies (Hornblende + Plagioclase ( $\text{An} > 20\%$ )), where all the XAn in plagioclase was above 20% (Winter, 2014).

Table 16 – Definitive mineral assemblages of metamorphic facies. Blue limit line is evidencing the facies and mineral assemblage studied (modified after Winter, 2014)

Facies	Definitive Mineral Assemblage in Mafic Rocks
Zeolite	zeolites: especially laumontite, wairakite, analcime (in place of other Ca-Al silicates such as prehnite, pumpellyite, and epidote).
Prehnite-pumpellyite	prehnite + pumpellyite (+ chlorite + albite)
Greenschist	chlorite + albite + epidote (or zoisite) + actinolite ± quartz
<b>Amphibolite</b>	<b>hornblende + plagioclase (oligoclase, andesine) ± garnet</b>
Granulite	orthopyroxene + clinopyroxene + plagioclase ± garnet
Blueschist	glaucophane + lawsonite or epidote/zoisite (± albite ± chlorite ± garnet)
Eclogite	pyralpsite garnet + omphacitic pyroxene (± kyanite ± quartz). No plagioclase.
Contact facies	mineral assemblages in mafic rocks of the facies of contact metamorphism do not differ substantially from those of the corresponding regional facies at higher pressure.

After Spear (1993), Fettes and Desmons (2007).

Although the interpolation of these results suggested amphibolitic facies, it also showed that the conditions could be close to the granulite facies (fig. 57). But caution should be taken regarding these relations, due to the fact of existing a metasomatic overprint. The mineral assemblage that was found and is present in the table above agrees with the figure 57. In the figure 57 amphibolitic facies was obtained due to the interaction of magnesianhornblende with andesine compositions (pink spots on the fig. 57). While, the possible granulitic facies conditions was determined due to the magnesianhornblende-labradorite interaction (green spots on the fig. 56).

Focusing only on the hornblende compositions, actinolitic-hornblende suggests that the mineral assemblages considered appeared under greenschist facies, while the magnesiohornblendes chemical composition suggests a low amphibolite facies (fig. 58).

Since the temperature and pressure control the Ti and Al contents of the amphibole, the low Ti and high Al content indicate a low temperature and pressure of the amphibolites (Li *et al.*, 2017).

This hypothesis agrees with the conclusions obtained on the temperature–pressure of metamorphic facies diagram that includes the magnesio-hornblende–plagioclase interaction of Anderson and Smith (1995) and Holland and Blundy (1994) present on the figure 57. Regarding figure 58, it appears that this mineral assemblage was generated under low amphibolite facies (III) and the figure 59 indicates that it followed low P/T suite.

Considering the figures 57 and 58 and mainly the figure 59, the metamorphic facies is characterized by the low

P/T conditions of high heat-flow orogenic belts, rift areas, and contact metamorphism. Besides this, the sequence of facies may be a low-pressure version of the medium P/T series such as amphibolite facies.

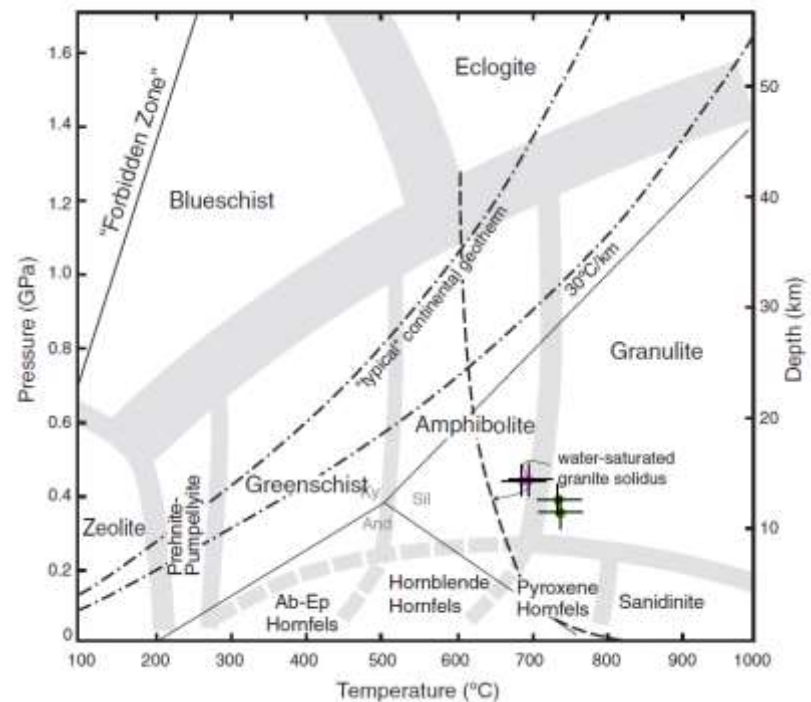


Figure 57 – Temperature–pressure diagram showing the generally accepted limits of the various facies. Boundaries are approximate and gradational. The *typical* or average continental geotherm is from Brown & Mussett (1993). The 30 °C/km geothermal gradient is an example of an elevated orogenic geothermal gradient. The *forbidden zone* is bounded by the 5 °C/km (150 °C/GPa) gradient beyond which conditions are generally considered unrealized in nature (e.g., Liou *et al.*, 2000). (Modified after Winter (2014)).

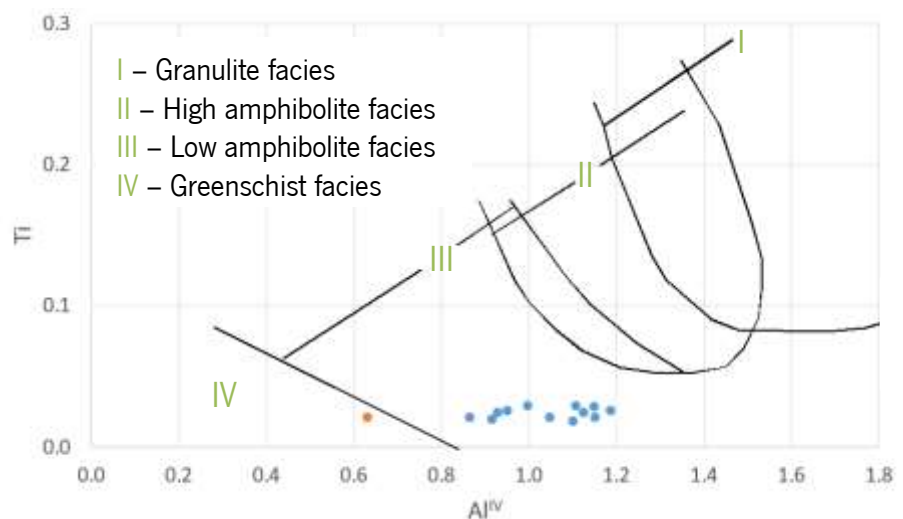


Figure 58 – Amphibole chemistry from the nodular sample. Al-Ti diagram (modified after Jin (1991) in Li *et al.* (2017)).

Still in the medium P/T series, the crustal melting under H<sub>2</sub>O-saturated conditions occurs in the upper amphibolite facies (the H<sub>2</sub>O-saturated granite solidus is indicated in figure 57). The granulite facies, therefore, occurs only in H<sub>2</sub>O-deficient rocks, either dehydrated lower crust or areas with high X<sub>CO<sub>2</sub></sub> in the intergranular fluid.

The pressure ((3.80±0.35) Kb) and temperature ((718.0± 23.0) °C) determined are in accordance with the ones established by Dias (2011) and Dias & Leal Gomes (2013a) for D<sub>2</sub> and the evolutions in the interface between D<sub>2</sub> and D<sub>3</sub> that would have occurred under the P-T conditions of 2.9-4.2 Kbar and 650-710 °C (these

values represent general mean boundaries), in the C.D.F. set. These authors achieved these conclusion by studying the mineralogical geothermobarometers (biotite-garnet pair and garnet-plagioclase-quartz-sillimanite system) and the crystallization of hyperalluminous veins from fluids of metamorphic origin (fig. 60). Regarding Dias (2011), the different mobilization processes may have occurred in variable P-T-μ.

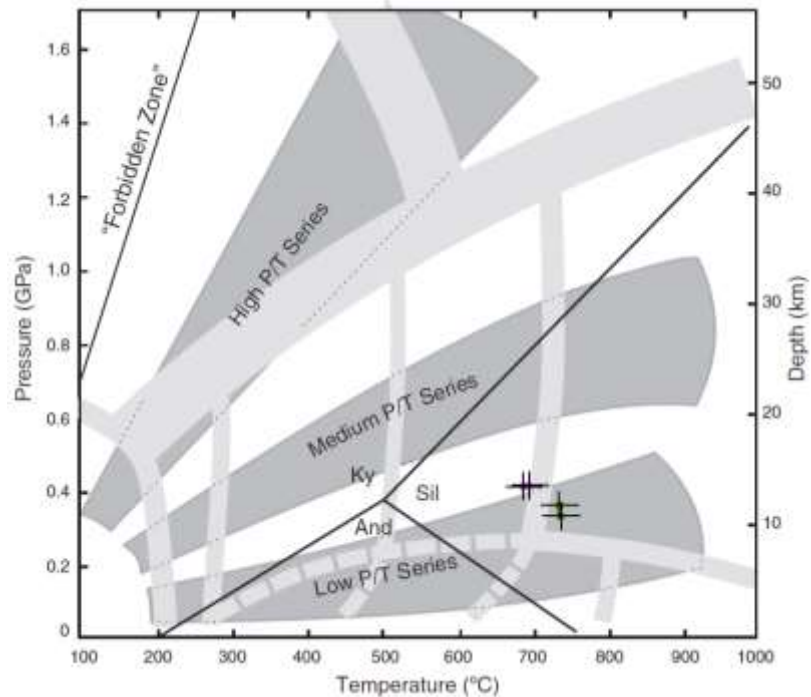


Figure 59 – Temperature–pressure diagram showing the three major types of metamorphic facies series proposed by Miyashiro (1973, 1994). Included are the facies boundaries from figure 57 and an Al<sub>2</sub>SiO<sub>5</sub> phase diagram. Each series is representative of a different type of tectonic environment. The high P/T series is characteristic of subduction zones, medium P/T of continental regional metamorphism, and low P/T of high heat-flow orogens, rift areas, and contact metamorphism. (Modified after Winter (2014)).

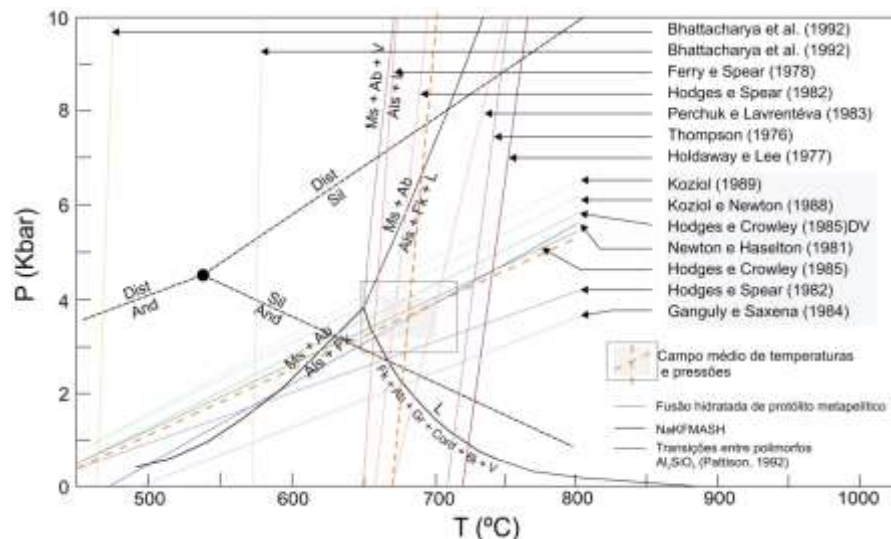


Figure 60 – Projection of the curves obtained by the application of biotite-garnet and garnet-plagioclase-quartz-sillimanite equilibria. Delimitation of a temperature and pressure mean field, eventually related with partial fusion processes (curves relatives to NaKFMASH system regarding Spear et al. (1999) in Dias (2011)). (From Dias, 2011)

## 6.2. Chlorite

Chlorite, a phyllosilicate found in a variety of geological environments including sedimentary, low-grade metamorphic and hydrothermally altered rocks (Deer *et al.*, 1966), can either replace pre-existing (generally, ferro-magnesian) minerals or precipitate directly from solution (Klein & Koppe (2000) and Caritat *et al.* (1993)). Chlorites form solid solutions, hence show variable degree of substitution. Especially, Al substitutes Si in tetrahedral sites and Mg substitutes Fe in octahedral sites, which makes chlorites chemical composition also variable. It is currently known that these variations are related to the bulk composition of the host rock increasing effects of metamorphism and to hydrothermal alteration, and that they record the physico-chemical conditions of chlorite crystallization (Walshe, 1986; Cathelineau, 1988; Laird, 1988; Schiffman & Fridleifsson, 1991; Caritat *et al.*, 1993; Walker, 1993; Zang & Fyfe, 1995; Xie *et al.*, 1997 *in* Klein & Koppe (2000)).

Chlorite group has a structure that consists of T-O-T layers sandwiching brucite-like (with some Al) octahedral layer (fig. 61) (Nelson, 2015). The ideal structure of this hydrous aluminosilicate is characterized by regularly alternating octahedral, *brucite-like* sheets (also known as the hydroxide sheets) and tetrahedral-octahedral-tetrahedral, *talc-like* sheets (also known as the 2:1 sheets) (Bailey (1988a) *in* Caritat *et al.* (1993)). The mineral displays a wide range of composition and

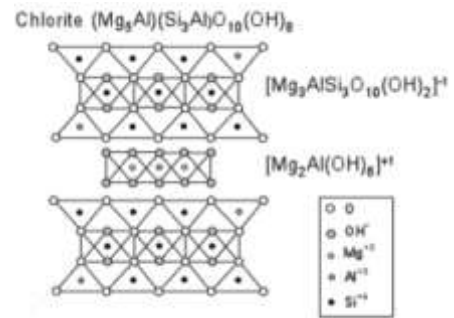
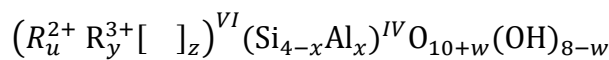


Figure 61 – Chlorite structural formula. (After Nelson, 2015).

a general crystallochemical formulation for chlorite has been suggested to be (modified from Wiewióra & Weiss (1990) *in* Caritat *et al.* (1993)):



where

- $u + y + z = 6$ ;
- $z = \frac{y-w-x}{2}$ ;
- $w$  generally is zero or a small number;
- $R^{2+}$  generally represents  $Mg^{2+}$  or  $Fe^{2+}$ ;
- $R^{3+}$  generally represents  $Al^{3+}$  or  $Fe^{3+}$ ;
- $[ ]$  represents structural vacancies.

Notice that *octahedral* sites (superscript *VI*) are differentiated from *tetrahedral* sites (superscript *IV*) in this general formula. Octahedral occupancy represents the sum of all cations in the octahedral site, and is given by  $\Sigma = u + y$ . Figure 62 illustrates how chlorite compositions can be plotted in terms of the major cations, Si, Al, Fe, and Mg.

Not represented in the formula are components that commonly occur in minor amounts in the octahedral site of chlorite, such as Cr, Ti, Ni, Mn, V, Cu, and Li.

These, together with the major chlorite constituents Mg, Fe<sup>2+</sup>, Fe<sup>3+</sup>, Al, and Si, contribute to the wide ranging compositional variability, or non-stoichiometry, that makes chlorite a potentially attractive geothermometer.

By virtue of this non-stoichiometric behaviour, chlorite has the potential to record invaluable information about the physicochemical conditions under which it formed. It has been observed, for instance, that the effects of increasing burial depth, metamorphic grade, or hydrothermal alteration upon chlorite composition include a decrease in Si<sup>IV</sup>, Al<sup>VI</sup>, and [ ]<sup>VI</sup> and an increase in Al<sup>IV</sup>, (Fe + Mg), and  $\Sigma^{VI}$ .

In addition to compositional changes, structural changes have been noted to occur in natural chlorites, and these polytype transitions have been suggested to depend on environment temperature as well (Caritat *et al.*, 1993).

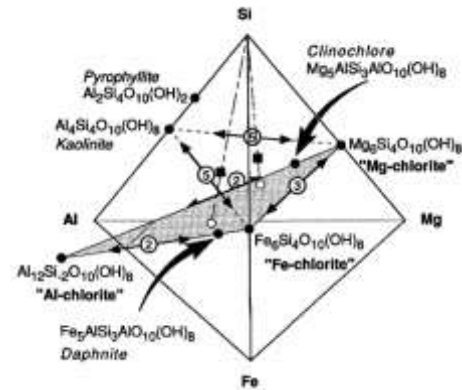


Figure 62 – Si-Al-Fe-Mg tetrahedron for representation of chlorite analyses (solid squares). Plane (stippled) intersecting the tetrahedron is used for ternary *Al-chlorite*, *Fe-chlorite*, *Mg-chlorite* diagrams. Positions of chlorite analyses in this plane (open circles) are obtained by projection through the Si apex (dashed lines). Circled numbers with arrows refer to exchange reactions and vectors of table 17. (From Caritat *et al.*, 1993.)

Table 17 – Chlorite components and exchange reactions. (From Walshe (1986) in Caritat *et al.* (1993).)

	Oxide component	Molecular component	Exchange reaction	Exchange vectors
1	SiO <sub>2</sub>	Mg <sub>x</sub> Si <sub>4</sub> O <sub>10</sub> (OH) <sub>8</sub>	—	—
2	MgO	Mg <sub>x</sub> AlSi <sub>3</sub> AlO <sub>10</sub> (OH) <sub>8</sub>	(Si <sup>IV</sup> ) <sup>x</sup> (Mg <sup>2+</sup> ) <sup>VI</sup> ↔ (Al <sup>IV</sup> ) <sup>x</sup> (Al <sup>VI</sup> ) <sup>VI</sup>	Al <sub>2</sub> Si <sub>1-x</sub> Mg <sub>x-1</sub>
3	FeO	Fe <sub>2-x</sub> AlSi <sub>3</sub> AlO <sub>10</sub> (OH) <sub>8</sub>	(Mg <sup>2+</sup> ) <sup>VI</sup> ↔ (Fe <sup>2+</sup> ) <sup>VI</sup>	FeMg <sub>-1</sub>
4	Fe <sub>2</sub> O <sub>3</sub>	Fe <sub>2-x</sub> Fe <sup>3+</sup> Si <sub>3</sub> Fe <sup>3+</sup> O <sub>10</sub> (OH) <sub>8</sub>	(Al <sup>IV</sup> ) <sup>x</sup> ↔ (Fe <sup>3+</sup> ) <sup>VI</sup>	Fe <sup>3+</sup> Al <sub>-1</sub>
5	Al <sub>2</sub> O <sub>3</sub>	Al <sub>4-x</sub> Si <sub>2</sub> O <sub>10</sub> (OH) <sub>8</sub>	3(Mg,Fe <sup>2+</sup> ) <sup>VI</sup> ↔ 2(Al <sup>IV</sup> ) <sup>VI</sup> □ <sup>VI</sup>	Al <sub>2</sub> (Mg,Fe <sup>2+</sup> ) <sub>-3</sub>
6	H <sub>2</sub> O	Fe <sub>2-x</sub> Fe <sup>3+</sup> AlSi <sub>3</sub> AlO <sub>10</sub> (OH) <sub>8</sub>	(Fe <sup>2+</sup> ) <sup>VI</sup> 2(OH) <sup>-</sup> ↔ (Fe <sup>3+</sup> ) <sup>VI</sup> O <sup>2-</sup> (OH) <sup>-</sup>	Fe <sup>3+</sup> O <sup>2-</sup> -Fe <sub>2</sub> OH <sub>-1</sub>

The value of *x* in the formula varies mostly between 0.6 and 1.6 in metamorphic/hydrothermal chlorites, however in C2 sample (*sulfide arcs periphery – distal relatively to apical mounds domain*) this is not verified, instead Al<sup>IV</sup> content ranges between 1.87 and 3.30 a.p.f.u. (Foster (1962) in Caritat *et al.* (1993)).

Chlorites from low-temperature environments, such as those found in sedimentary rocks from the diagenetic to low-grade metamorphic realms, exhibit some compositional differences compared to higher-grade metamorphic or hydrothermal chlorites (Curtis *et al.*, 1985). For instance, the diagenetic (or sedimentary) chlorites:

- Tend to have higher *Si* contents and lower *Fe + Mg* contents and octahedral totals than metamorphic chlorites of similar alumina content (Curtis *et al.* (1985) and Hillier and Velde, (1991) *in* Caritat *et al.* (1993)).
- Tend to have problems in interlayering and compositional purity. Chlorites from low-temperature settings are indeed commonly interstratified with smectite, vermiculite, saponite, and/or illite (Caritat & Walshe (1990) *in* Caritat *et al.* (1993)).

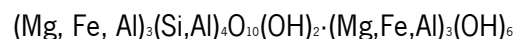
The resolution of the electron microprobe, the most commonly used analytical instrument for acquiring mineral compositional data on chlorites, does not allow the user to ascertain directly the purity of the chlorite analysed (Caritat *et al.*, 1993).

During the passage from diagenesis to metamorphism, chlorites apparently become less siliceous, richer in *Fe + Mg*, and octahedral occupancy increases. And this transition must be accompanied by an increase in Al<sup>IV</sup> and a decrease in Al<sup>VI</sup> if aluminium is to be conserved at the chlorite structure scale (Hillier and Velde (1991) *in* Bourdelle *et al.* (2013)).

#### 6.2.1. Data treatment

The microprobe analyses were calculated on the basis of chlorite formula with 36 oxygen atoms (O, OH), 16 groups of OH and 8 atoms of *Si + Al<sup>IV</sup>*, based on 28 oxygens as recommended by Deer *et al.* (1966), with Fe<sup>2+</sup>/Fe<sup>3+</sup> and OH calculated assuming full site occupancy (excel sheet provided by Matthew Brzozowski (2014) and Ahmed Hassan Ahmed (2017)).

Cerdeirinha's chlorite general formula is as follows (regarding its tetrahedral and octahedral content):



With atoms per formula unit as follows:

- Si<sub>4.70–6.13</sub>
- Al<sup>IV</sup><sub>1.87–3.30</sub>
- Al<sup>VI</sup><sub>2.70–3.10</sub>
- Ti<sub>0.00–0.18</sub>
- Fe<sup>3+</sup><sub>0.00–0.51</sub>
- Fe<sup>2+</sup><sub>4.58–6.62</sub>
- Mn<sub>0.14–0.28</sub>
- Mg<sub>2.44–3.26</sub>



- Ca<sub>0.00–0.02</sub>
- Na<sub>0.00–0.12</sub>
- K<sub>0.00–1.38</sub>
- (OH)<sub>16.00</sub>

The table with all the data can be found in the *Annexes II*. The H<sub>2</sub>O was calculated by stoichiometry and FeO was considered as total iron. The measurement conditions are referred in the subchapter *3.1.3. Electron microprobe*.

#### 6.2.2. Chlorite classification

According to Hey (1954) diagram (fig. 63), chlorites projected (with only  $Ca + Na + K < 0.5$  a.p.f.u.) were identified as belonging to *chamosite-clinocllore* solid-solution series. There were observed a majority of *ripidolite* (a clinocllore variety), followed by *pseudothuringite* (a chamosite variety) and *brunsvigite* (magnesian variety of chamosite) (fig. 63). These chlorites contain high iron content, that might be explained by the iron sulfides decay, once some ripidolites were in contact with sulfide minerals (fig.45). In addition, the exactly same chlorite minerals were identified in the study of chlorite geothermometry and physicochemical conditions of gold mineralization in Paleoproterozoic Caxias Deposit (Klein & Koppe, 2000).

In the diagram (from Hey (1954); based on 28 oxygens) proposed by Dias (2011), the chlorites from ultrapotassic mafic rocks of Santa Justa plotted in the *ripidolite* and *pycnoclhorite* fields with high Si content. Other points of analyse, obtained in chlorites of Serro tuffacic precursors, metamafites with fenocrystalline feldspar (described as proto-latites) from Monteiro and hydrothermal plagioclasites with massive sulfides from Covas, have ripidolitic trend.

The majority of chlorites (ripidolite) identified in the C2 sample (*Sulfide arcs periphery – distal relatively to apical mounds domain*) match with *metamorfized hidrotermalites from the Covas* sequence from Dias (2011) (fig. 63). In figure 63 is possible to verify a trend (black dashed arrow), that according with C. Leal Gomes (personal communication, 2019) can suggest an evolution from VMS (Dias, 2011) to SEDEX primordial setting regarding Fe, Mg and Si (a.p.f.u.) content (in ripidolite and pseudothuringite).

The compositions are discerned by the Fe and Mg content (fig. 64). Dias (2011) graphic suggests the presence of 3 populations expressed in the slopes of the compositional drift implying the Mg/Fe ratios, while the Cerdeirinha data agrees with the Covas (Fervença) data, once more.

The Mg/Fe content is higher in Santa Justa chlorites ( $Mg/Fe \approx 2$ ), while the chlorite from samples with Fervença massive sulfides and from the Cerdeirinha pyrrhotite rich sample were plotted to the lowest values of that quotient ( $Mg/Fe \approx 0.5$ ). Monteiro's ultrapotassic proto-latite-like facies and hydrothermal evolution products from Serro's tuffacic precursors have  $Mg/Fe \approx 1$  (Dias, 2011).

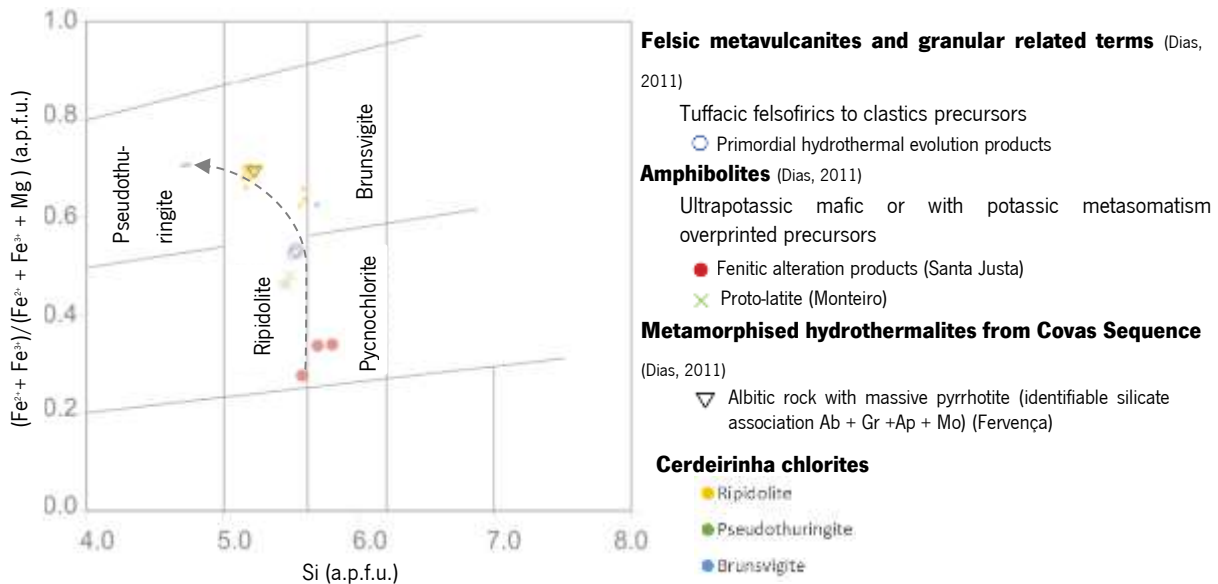


Figure 63 – Classification of chlorites from Cerdeirinha deposit, based on the Hey (1954) diagram, regarding Si content and  $Fe/(Fe+Mg)$  cation ratio for chlorites with  $Fe_2O_3 > 4\%$  and  $Ca+Na+K < 0.5$  a.p.f.u.. C2 sample data overlapped with Dias (2011) data. Black dashed arrow enhances the trend verified.

### 6.2.3. Pressure and temperature condition of crystallization

On one hand, the chlorite geothermometer could probably be applied successfully to chlorites from diagenetic, hydrothermal or metamorphic origin, as the  $Al^{IV}$  content seems to be independent of the rock lithology or the fluid composition (Caritat *et al.*, 1993). On the other hand, Klein *et al.* (2006) considers that the  $Fe/(Fe + Mg)$  ratio and formation temperatures may be influenced by the fluid to rock ratio,  $f O_2$ ,  $f S_2$ , pH, and the composition of the hydrothermal fluid and host

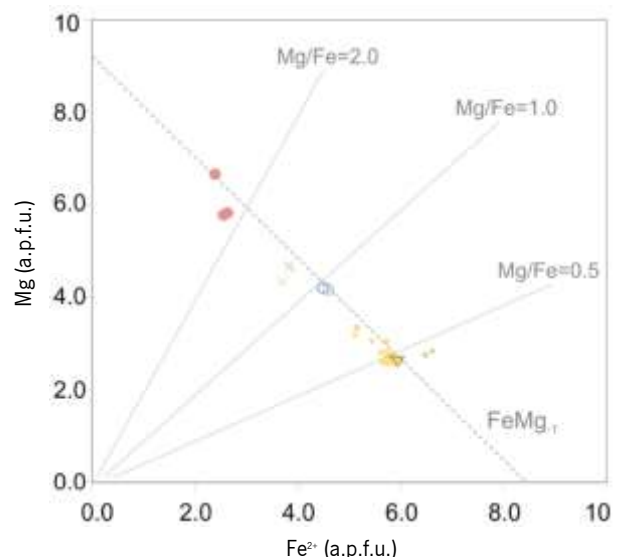


Figure 64 – Conjugated variation of Fe and Mg chlorites. Cerdeirinha chlorites with  $Fe_2O_3 > 4\%$  and  $Ca+Na+K < 0.5$  a.p.f.u. overlapped with Dias (2011) chlorite data. The symbology subtitle is similar to one present in figure 63.

rock (Kranidiotis and MacLean (1987) and Jiang *et al.* (1994) in Klein *et al.* (2006) and Caritat *et al.* (1993)), note that these parameters are not always readily available.

The empirical chlorite thermometry (Kranidiotis and MacLean (1987), Cathelineau (1988) and Zang and Fyfe (1995) in Caritat *et al.* (1993)) is based on the variation of  $Al^{IV}$  content and  $Fe/(Fe + Mg)$  ratios of chlorites as a function of temperature. Some problems in the application of this empirical geothermometer include contamination of chlorites (therefore, chlorite geothermometry should be used with caution and only in combination with alternative methods of estimating paleotemperatures (Caritat *et al.* (1993)) by submicroscopic inclusions or interlayers (Schiffman & Fridleifsson (1991) and Jiang *et al.*, (1994) in Klein *et al.* (2006)). Contaminated chlorites typically have variable amounts of  $Ca + Na + K$ . To avoid this concern, analyses with only  $Ca + Na + K < 0.5$  a.p.f.u. have been used in the temperature calculations, as suggested by Vidal *et al.* (2001) in Klein *et al.* (2006). Thus, in this study they were plotted in figure 63, but they were not considered for further calculations.

Despite these limitations, the use of the chlorite chemical composition to estimate the temperature of ore formation is an effective procedure, provided that some basic principles are observed, namely:

- (1) Consistency between the chemical data of the studied chlorites and those of chlorites used in the calibration of the geothermometers;
- (2) Correlation between the  $Fe/(Fe + Mg)$  ratio and  $Al^{IV}$  contents;
- (3) The results are compared with independent temperature estimations.

In what the second point might concern, the  $Fe/(Fe + Mg)$  ratios and  $Al^{IV}$  show a positive correlation (fig. 65), regarding the  $Ca + Na + K < 0.5$  condition.

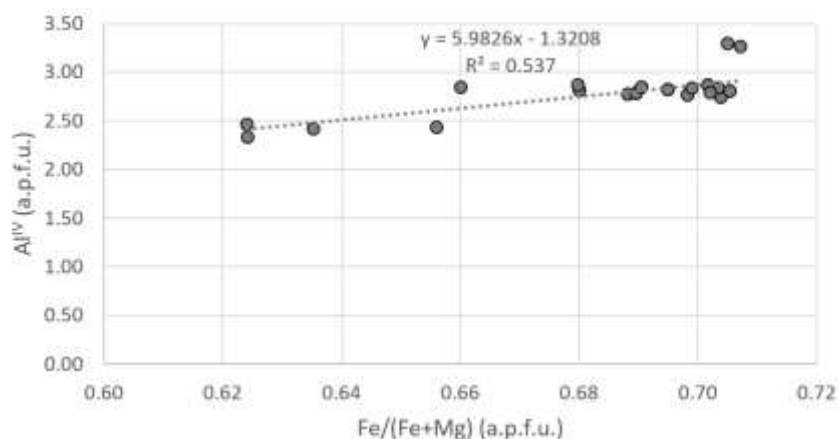


Figure 65 –  $Al^{IV}$  and  $Fe/(Fe+Mg)$  correlation of C2 chlorites.

Overall, the compositional variation trends conditioned to the ratio  $Fe/(Fe+Mg)$  enhanced positive correlations with  $Al^{IV}$  and Mn, culminating in Al in the Monteiro facies, and in Mn mafic precursors with phenitic alteration in Santa Justa, which impose the compositional drift (fig. 63). Mn values are even higher in the massive pyrrhotite of Fervença sample and are consistent with high Mn concentrations

achieved in exhalative facies (Dias, 2011). Mn values in C2 sample were even higher than the one verified in Fervença (Covas Dome), which can support the hypothesis of a primordial exhalation facies in Cerdeirinha sector. However, petrographically, chlorites in the C2 sample suggest to be originated by the alteration of biotite.

#### 6.2.3.1. Condition estimates and discussion

On one hand, Cathelineau (1998) (CAT) proposed that the number of tetrahedral Al cations in chlorite increases and octahedral vacancies decrease with increasing temperature (Klein & Koppe, 2000) and therefore it can be used as a geothermometer (Schiffman & Howard (1995)). On the other hand, Kranidiotis & MacLean (1987), studied volcanogenic deposits, adding an  $Al^{IV}$  correction value, as function of the variation of Fe/(Fe+Mg) ratio (Klein & Koppe, 2000). Zang & Fyfe (1995) revised Cathelineau (1998) and Kranitoids & MacLean (1987) geothermometers and argued that for high Fe/(Fe+Mg) ratios, the calculated temperatures tend to be too high, since the calibration of the geothermometer was done for lower ratios (<0.37 (Cathelineau, 1988) and 0.18 to 0.64 (Kranidiotis & MacLean, 1987)) (Klein & Koppe, 2000).

Comparison between the chemical compositions of chlorites from Cerdeirinha deposit and chlorites used in the calibration of empirical geothermometers Cathelineau (1998) (CAT), Kranitoids & MacLean (1987) (KM) and Zang & Fyfe (1995) (ZF) (data obtained by Klein & Koppe (2000)) is present in figure 66.

Among these approaches, the Cerdeirinha chlorite data ranges between the KM and ZF chlorite composition used to establish their geothermometers (table 18), therefore both geothermometers were applied for this new data (meeting the principle (1) previously established). Cathelineau (1998) geothermometer was established for chlorites with Fe/(Fe+Mg)<0.37, once this range is not close to Fe/(Fe+Mg) Cerdeirinha chlorite range (0.62 to 0.71), this geothermometer was discarded.

The equations employed in the chlorite formation temperatures (table 18) are as follows ( $Al^c$  is the corrected value for Al) (Klein & Koppe, 2000):

$$T(^{\circ}C) = -61.92 + 321.98Al^{IV}, \text{ eq. 1}$$

$$Al^{IV}_c = Al^{IV} + 0.7\left(\frac{Fe}{Fe+Mg}\right), \text{ eq. 2}$$

$$T(^{\circ}C) = 106Al^{IV}_c + 18, \text{ eq. 3}$$

$$Al^{IV}_c = Al^{IV} - 0.88\left(\frac{Fe}{Fe+Mg} - 0.34\right), \text{ eq. 4}$$

Table 18 – Comparison of chlorite compositions of Fe/(Fe+Mg), Al<sup>iv</sup> and Si from the Cerdeirinha deposit with those used for empirical temperature estimation of Cathelineau (1988), Kranidiotis and MacLean (1987), and Zang and Fyfe (1995). (Modified after Klein & Koppe, (2000).)

	CAT	KM	ZF	Cerdeirinha
Fe/(Fe+Mg) (a.p.f.u)	0.24 to 0.37	0.18 to 0.64	0.78 to 0.81	0.62 to 0.71
Al <sup>iv</sup> (a.p.f.u)	0.59 to 1.93	1.89 to 2.83	2.49 to 2.64	1.78 to 3.25
Si (a.p.f.u)	2.80 to 3.41	5.17 to 5.80	5.36 to 5.51	4.75 to 6.22
equations	<i>1</i>	<i>2 and 3</i>	<i>3 and 4</i>	<i>2 and 3</i> <i>3 and 4</i>

These geothermometers are useful when environmental conditions are similar to those in which the calibration has been done (Klein & Koppe, 2000). Therefore, according to figure 66, Cerdeirinha chlorites data is not similar to any of previous authors chlorites used in the calibration of empirical geothermometers, however the majority of data is closer to Kranitoids & MacLean (1987). Hence, C2 chlorites description was more focused on this geothermometer.

According to Kranidiotis & Mac Lean (1987) equations, the studied chlorites show a temperature range from 257.13 °C to 419.72 °C, while according Zang & Fyfe (1995) calculations they vary from 173.94 °C to 333.37 °C. Overlapping both methods, there is a temperature range in common from 257.13 °C to 333.37 °C.

The histogram of chlorites calculated crystallization temperatures by the empirical method of Kranidiotis & MacLean (1987), the maximum value obtained owes to the presence of pseudothuringite (fig. 67) 416.13 °C to 419.72 °C, while the minimum was obtained because of the presence of brunsvigite (257.13 and 311.81 °C). The values obtained from 355 °C to 375 °C were obtained through the presence of ripidolite. The temperature range between 315 °C and 335 °C was obtained because 3 ripidolites minerals contained the lowest content of Fe/(Fe+Mg) ratio and Al<sup>iv</sup> content after brunsvigite.

The 3<sup>rd</sup> principle is not accomplished in this study, once it was not possible to compare these results with independent temperature estimations.

The Kettara deposit consists of a sub-vertical pyrrhotite-rich massive sulfide hosted by sedimentary rocks, located in centre of the Variscan Jebilet massif, north of Marrakech, Morocco. The

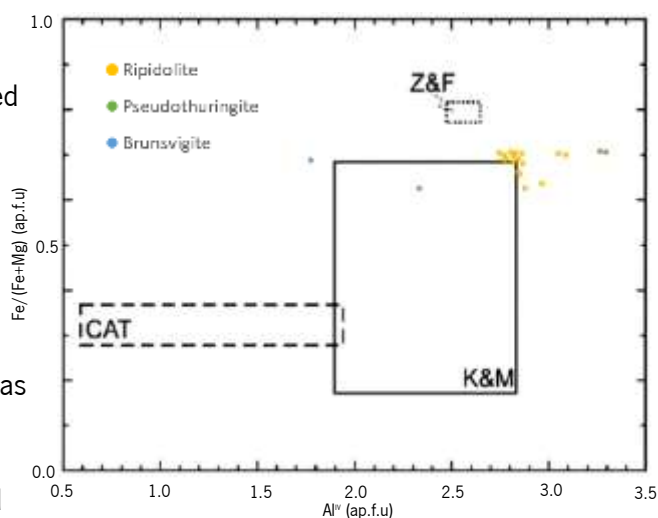


Figure 66 – Comparison of chlorite compositions from the Cerdeirinha deposit with those used for empirical temperature estimation of Cathelineau (1988), Kranidiotis and MacLean (1987), and Zang and Fyfe (1995), regarding Ca+Na+K<0.5 condition. (Modified after Klein & Koppe, 2000.)

host rocks are deformed and weakly metamorphosed to greenschist facies. They are composed of pelite, sandstone, and calcareous beds and cross cut by dolerite dikes. The sulfide ore are massive to semi-massive pyrrhotite with fragments of the host schists, brecciated pyritic ore and mineralized veins. The mineralization is composed of two main paragenetic assemblages:

- Pyrrhotite dominant with chalcopyrite, magnetite, sphalerite, arsenopyrite, galena and native bismuth, associated with quartz, chlorite ± talc and mica gangues;
- Pyrite-dominant with marcasite and associated with Fe-rich carbonate minerals; formed via replacement of the pyrrhotite-rich mineralization by carbonates.

The chlorites associated with Kettara pyrrhotite-rich massive sulfide are Fe-rich with mean values of Fe/Fe+Mg of 0.62, 0.73 and 0.70 (similar to Cerdeirinha's) for chlorite from hydrothermal alteration (320 to 375°C), massive to semi-massive ore (347 to 370°C) and mineralized veins (325 to 342°C), respectively. The temperatures

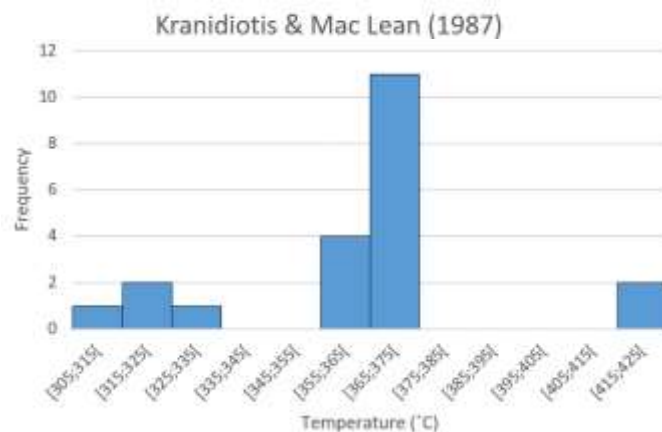


Figure 67– Histogram of crystallization temperatures of C2 chlorites calculated by the empirical method of: Kranidiotis & MacLean (1987).

were calculated from chlorite compositions using Kranidiotis and Mac Lean (1987) geothermometer. They correspond all to ripidolite excepted two chlorites from hydrothermal alteration that are brunsvigite and corundophylite (Hey (1954) and N'Diaye *et al.* (2015)). Oxygen and hydrogen isotope indicate that these chlorites were formed from metamorphic fluid.

### 6.3. Arsenopyrite

The paragenetic study suggests the existence of several arsenopyrite generations. Several arsenopyrites paragenetically referenced were studied, in the attempt to verify the possibility of existence of diverse compositional populations, and to study their estimative of formation conditions. The a.p.f.u. of this study arsenopyrites can be found in *Annexe II*.

#### 6.3.1. Data treatment

The set of arsenopyrite, from the Cerdeirinha deposit, projections is coherent with the known non-stoichiometry of arsenopyrite. They are plotted in a zone parallel to the S-As axis indicating substitution of As for S (purple trend) and also parallel to the Fe-As join indicating substitution of As for Fe (grey trend) (figure 68) (Kretschmar & Scott (1976) and Rajabpour *et al.* (2017)).

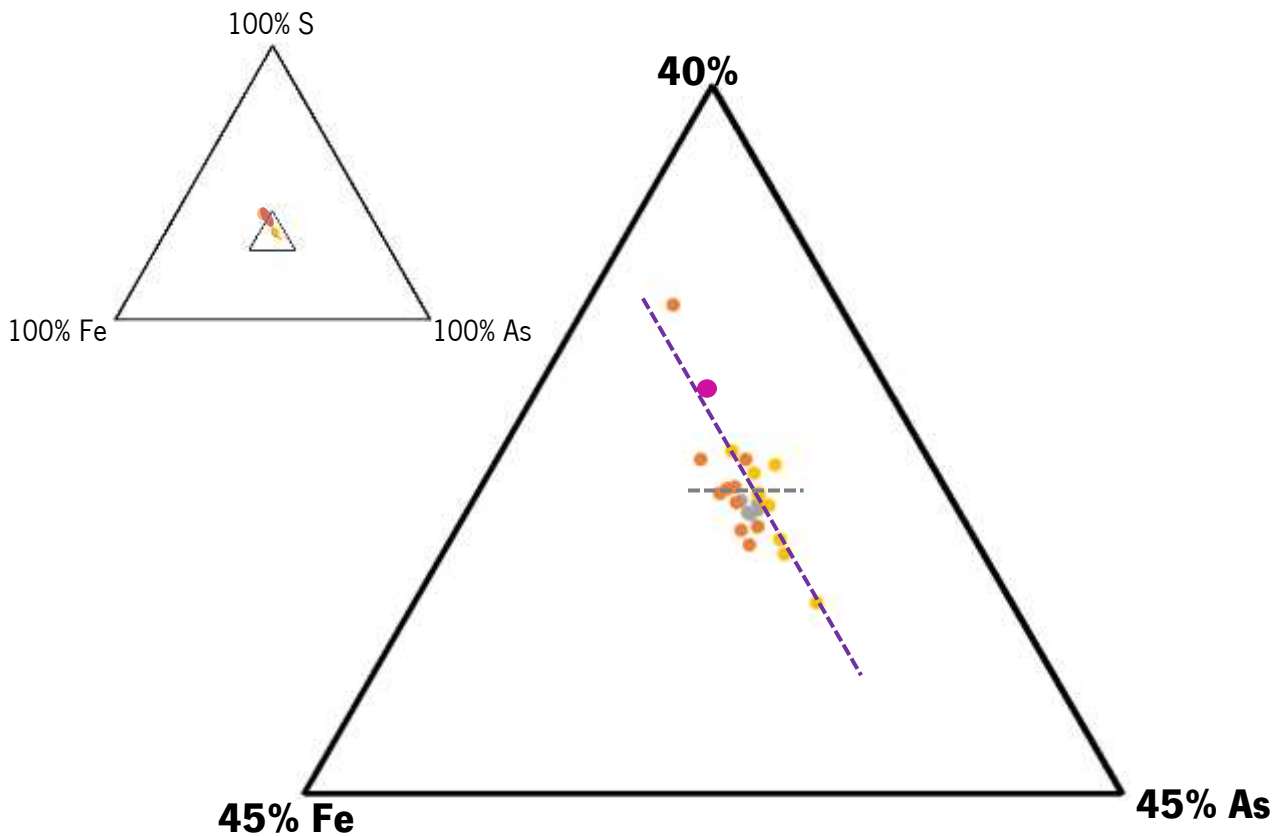


Figure 68 – Ternary Fe–S–As (at. %) diagram showing compositions of arsenopyrites found in C2, CWW-3A and CW05 thin-sections. The dark pink spot represents a stoichiometric arsenopyrite (FeAsS). The purple dashed line represents the substitution of As for S, while the grey dashed line represents the Fe-As join – the substitution of As for Fe. The orange area, in the smaller ternary diagram, represents the arsenopyrites domain Argas-Cerquido alignment (Leal Gomes, 1994), and the red area refers to shear zone Argas-Cerquido-Serra de Arga and shear zone networking in Serra de Arga Silurian Terrains (Araújo & Leal Gomes (2014) and Leal Gomes *et al.* (2015)), respectively. Its values can be seen below and in *Annexe II*.

According to Craig & Vaughan (1994), phase diagrams are important in providing geothermometric and geobarometric data. The geothermometers can be one of two types – *sliding scale* or *fixed point*. The *sliding-scale* type is based on the temperature dependence of the composition of a mineral or pair of minerals when it is part of a specified assemblage. However, in some cases (e.g.: pyrrhotite coexisting with pyrite), its composition determination would uniquely define the temperature of equilibration. Therefore, unfortunately the rapid rates of sulfide reequilibration processes have limited the usefulness of many *sliding scale* geothermometers. However, arsenopyrite when equilibrated with pyrite and pyrrhotite (and some other less common assemblages) is one of two notable exceptions (the other is coexisting magnetite-ulvospinel and ilmenite-hematite) that involve refractory minerals that retain their high temperature compositions during cooling and thus are applicable as *sliding scale* geothermometers (Craig & Vaughan, 1994).

Kretschmar & Scott (1976) work considers that the stoichiometry of arsenopyrite can differ from the FeAsS stoichiometric formula. These variations refers essentially to the As/S relation, once the Fe may change just a little. Besides this, some elements such as Co and Ni can replace Fe, while Sb can

replace As. The use of arsenopyrite as a geothermometer can contain some limitations, namely when the concentrations of Ni, Co and Sb are above 0.2 at. %, or when the crystals are zoned (Sundblad *et al.* (1984) *in* Couto (1993)). In this study, analysed crystals (samples and control standard) did not show any zoning evidence in petrographic microscope nor backscattered electrons images. The non-essential elements (Mn, Co, Ni, Cu, Zn, Pb and Sb) were not above 1% in all measurements. Ni, Co and Sb were always below 0.2 at. %, except in one case where Co was 0.22 at. %.

On figure 70 is possible to observe the reference formation temperature range of arsenopyrites, determined regarding their stoichiometric variation and respective mineral assemblage (figs. 32 and 33) (and, hence their temperatures of equilibration). The red dots represent the spots measured from C2 sample, the black from CWW-3A and the brown from CW05 (fig. 24). Most of them were seen intergrown with pyrrhotite. However, some of them contained lollingite.

Although several of them were seen intergrown with pyrite, they were projected with another mineral that they were seen also with, or not plotted at all. This happened due to the broad range of arsenopyrite inconsistent compositions with the geothermometer of Kretschmar & Scott (1976), since arsenopyrite with  $X(\text{As}) \geq 34$  at. % (table 19 and table 20) and  $X(\text{As}) \leq 29$  at. % (table 21) are not possible to project with pyrite intergrowth. The Cerdeirinh's mineral assemblage considered to be plotted in Kretschmar & Scott (1976) diagram is in bold in table 19.

It is also important to notice that the range of compositions analysed within a single sample may be too broad to reasonably constrain temperatures of formation (Sharp *et al.*, 1985). For this reason, 3 different thin-sections were submitted to EPMA analysis.

Table 19 – Representative analysis of arsenopyrites from Cerdeirinha open pit, obtained by microprobe with original *sulfide* program pre-settled in University of Bremen. (to be continued)

<b>Sample</b>	<b>Mineral Assemblage</b>	<b>As (at. %)</b>	<b>Plot</b>
C2	<b>Apy + Po</b> ( $\pm$ Ilm $\pm$ Po $\pm$ Ap $\pm$ Zr inclusions)	34.95	
	<b>Apy + Po</b> ( $\pm$ Po $\pm$ Ccp inclusions)	34.87	
	<b>Apy + Po + Bt</b> $\pm$ ferb ( $\pm$ Spn $\pm$ Ilm $\pm$ Sch inclusions)	34.59	
	Apy + Bt + Sch ( $\pm$ Spn $\pm$ Ilm inclusions)	34.88	no
	<b>Apy + Bt</b> ( $\pm$ Po inclusion)	34.87	
	<b>Apy + Po + Bt</b> ( $\pm$ Po inclusion)	34.80	
CWW-3A	<b>Apy + Py</b> ( $\pm$ electrum (close))	34.82	no
	<b>Apy + Py</b> ( $\pm$ electrum (distant))	34.51	no



Table 19 – Representative analysis of arsenopyrites from Cerdeirinha open pit, obtained by microprobe with original *sulfide* program pre-settled in University of Bremen. (concluded)

	<b>Apy + Py (± lol inclusion)</b>	34.84	
	<b>Apy + Py (± Po inclusion)</b>	36.77	Note: Co was 0.222%
	<b>Apy + Ap + Pl (± Po inclusion)</b>	35.58	
	<b>Apy + Py + Ap + Ilm+ Spn + Rt + Ab (± Po ± Ccp inclusions)</b>	34.78	
	<b>Apy + Py + (± lol + Native Bi + Ap inclusions)</b>	35.08	
	<b>Apy + Py + Ab (± Py inclusion)</b>	33.97	no
CW05	<b>Apy + Py + Qz + Stp</b>	34.37	no
	<b>Apy + Py + Qz (± native Bi + Qz + Sch inclusions)</b>	34.26	no
	<b>Apy + Sch</b>	35.18	no
	<b>Apy + Py + Qz (± Po + Qz inclusions)</b>	34.19	
	<b>Apy + Py + Qz (± lol + Sch + Qz + native Bi)</b>	35.10	
	<b>Apy + Py + Qz + Stp (± Po inclusions)</b>	34.50	

In the same diagram also arsenopyrites of Argas-Cerquido alignment were plotted (tetragons in fig. 70; table 20) (Leal Gomes, 1994).

Table 20 – Representative analysis of arsenopyrites from Argas-Cerquido alignment, obtained by X-ray spectrometry in backscattered electrons microscopy with original ASP 200 standard Kretschmar & Scott (1976). (Modified after Leal Gomes (1994).)

<b>Mineral Assemblage</b>	<b>Fe</b> (at.%)	<b>As</b> (at. %)	<b>S</b> (at. %)	<b>Plot</b>
Apy + Py + Po ± wf	33.33	32.95	33.71	
Apy + Py ( <i>crack-seal</i> )	33.14	30.13	36.73	
Apy + Py ( <i>crack-seal</i> )	33.39	29.87	36.74	
Apy + Py (normal venular)	33.33	29.64	37.03	
Apy + Py (normal venular)	32.49	29.81	37.70	
Apy + Py (normal venular)	33.30	29.97	36.73	
Apy + Py (miarolitic)	33.40	29.61	36.99	
Apy ± Cordierite ± Po ± Py (no plain evidence of pyrrhotite and pyrite syncrystalization)	32.96	28.85	38.19	no

Other arsenopyrites from C.D.F. were measured. Early automorphic arsenopyrite and arsenopyrite with hydrothermal paragenetic feature, associated with shear zone Argas-Cerquido-Serra de Arga (Araújo

& Leal Gomes, 2014) and shear zone networking in Serra de Arga Silurian Terrains present in Leal Gomes *et al.* (2015), respectively (fig. 69 and table 21), were intergrown with pyrite (C. Leal Gomes personal communication (2019)). Their As weight percentage data was recalculated to atomic percentage in this study (*Annexe II*), in order to plot them in the Kretschmar & Scott (1976) diagram (figure 70). For this calculation the formula applied was

$$As (at. \%) = \left( \frac{\frac{As (wt. \%)}{As_{conventional\ atomic\ weight}}}{\frac{Fe (wt. \%)}{Fe_{conventional\ atomic\ weight}} + \frac{As (wt. \%)}{As_{conventional\ atomic\ weight}} + \frac{S (wt. \%)}{S_{conventional\ atomic\ weight}}} \right) \times 100$$

where (IUPAC Periodic Table of Elements, 2019):

$$As_{conventional\ atomic\ weight} = 74.92$$

$$Fe_{conventional\ atomic\ weight} = 55.85$$

$$S_{conventional\ atomic\ weight} = 32.06$$

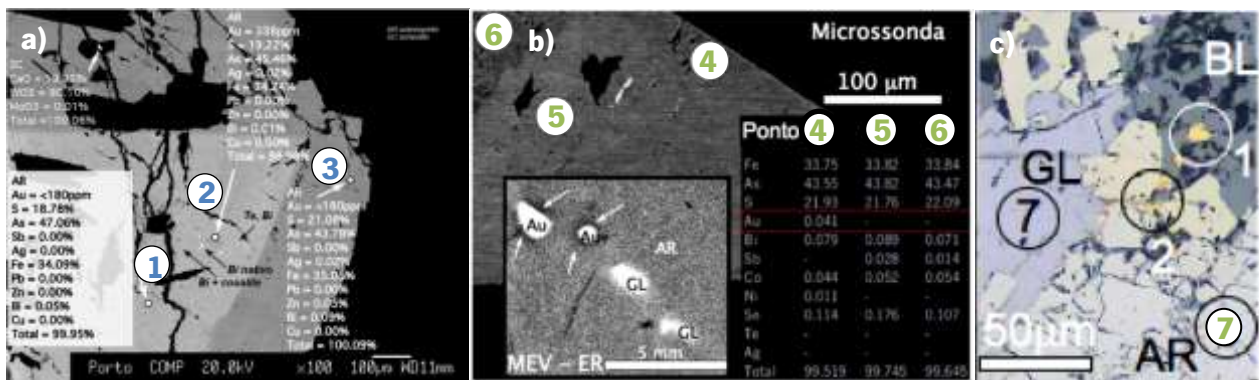


Figure 69 – The numbers subscribed in white circles correspond to the references present in the table 21. The blue ones correspond to composition of early automorphic arsenopyrite, while the green ones correspond to arsenopyrites with hydrothermal paragenetic feature. **a)** Initial arsenopyrite with epitaxial zoning induced by crystal growth, fractionated, and sector zoned due to deformation associated with annealing. It is possible to see variations of the content of Au reticular related to *annealing-recovery* and polymetallic expressions of Bi and Te, possibly from the same source. (From Araújo & Leal Gomes (2014).) **b)** Arsenopyrite compositional zoning with higher values of Au in the outer zone of crystals (microprobe) and Au exsudations with impoverishment halos in arsenopyrite (expression in S.E.M.-B.E.). **c)** Au, electrum and galena identification in arsenopyrite cracks – location of analysis spots done in reflected light microscopy (uncrossed nicols) and compositions obtained by electron microprobe. Modified images from Leal Gomes *et al.* (2015).

Table 21 – Representative analysis of arsenopyrites (wt.%), and As recalculations (at. %), associated with the shear zone Argas-Cerquido-Serra de Arga and shear zone networking in Serra de Arga Silurian Terrains, obtained by electron microprobe. (Data from Araújo & Leal Gomes (2014) and Leal Gomes *et al.* (2015).)

Mineral Assemblage	Wt. %				At. %	Plot	A.P.F.U.			
	Fe	As	S	Total	As		Fe	As	S	
<b>1</b>	Apy + Py	34.09	47.06	18.78	99.93	34.43	no	1.01	1.11	1.00
<b>2</b>	Apy + Py	34.24	45.46	19.22	98.92	33.35	no	1.02	1.08	1.02
<b>3</b>	Apy + Py	35.05	43.78	21.08	99.91	31.26		1.04	1.04	1.12
<b>4</b>	Apy + Py	33.75	43.55	21.93	99.23	31.09		1.00	1.03	1.17
<b>5</b>	Apy + Py	33.82	43.82	21.76	99.40	31.29		1.00	1.04	1.16
<b>6</b>	Apy + Py	33.84	43.47	22.09	99.40	30.94		1.00	1.03	1.18
<b>7</b>	Apy + Py	36.15	42.26	22.07	100.48	29.69		1.07	1.00	1.17

However, in this study, the *sulfide program* pre-settled in EPMA was used, hence the calibration standards are present in table 22 (only As was measured with an arsenopyrite (*Arsenkies*) (Freiberg, Germany)), while the calibration standard used by Leal Gomes (1994) was *ASP 200* (natural, homogeneous, S-rich arsenopyrite without detectable Co or Ni, from the Lucie pit of the Helen siderite mine near Wawa, Ontario as recommend by Kretschmar & Scott (1976). This latter standard calibration was absent in University of Bremen. Therefore, it is crucial to highlight the application of different calibration standards towards the results comparison. Besides this, there is no description about the arsenopyrites calibration standards measured by Araújo & Leal Gomes (2014) and Leal Gomes *et al.* (2015).

The condition of measurement were 20kV and 20 nA.

Table 22 – Calibration standard features for this study arsenopyrite measurements.

Sine $\theta$	Element	Standard	Radiation	Crystal	Counting time (sec.)
37673	As	<i>Arsenopyrite Arsenkies</i>	L $\alpha$	TAP	40
52186	Mn	Ilmenite	K $\alpha$	LiF	20
48079	Fe	Pyrite	K $\alpha$	LiF	20
44431	Co	Co	K $\alpha$	LiF	20
41148	Ni	Ni	K $\alpha$	LiF	20
38235	Cu	Chalcopyrite	K $\alpha$	LiF	20
35627	Zn	Sphalerite	K $\alpha$	LiF	20
61399	S	Pyrite	K $\alpha$	PET	40
60396	Pb	Galena	M $\alpha$	PET	20
39297	Sb	Stibnite	L $\alpha$	PET	20

For the control standard, a spot on a single crystal (arsenopyrite *Arsenkies*) was analysed at the beginning and end of each set of analyses throughout this study. The program normalized the final results to 100%. The arsenopyrite *Arsenkies* content measured were as follows:

Fe = 35.89 wt. %, As = 44.05 wt. % and S = 21.83 wt. %;

Fe = 35.99 wt. %, As = 44.11 wt. % and S = 22.42 wt. %;

Fe = 35.89 wt. %, As = 44.03 wt. % and S = 22.11 wt. %;

Fe = 35.78 wt. %, As = 43.89 wt. % and S = 21.55 wt. %;

Fe = 35.82 wt. %, As = 42.67 wt. % and S = 22.34 wt. %;

Fe = 36.31 wt. %, As = 41.99 wt. % and S = 22.89 wt. %;

Fe = 35.90 wt. %, As = 43.83 wt. % and S = 22.20 wt. %.

Fe = 35.85 wt. %, As = 43.30 wt. % and S = 21.94 wt. %.

These values are acceptable, once they manifest a good approximation to the ones proposed by Kretschmar & Scott (1976) for ASP 200:

$$\text{Fe} = (34.43 \pm 0.66) \text{ wt. \%}, \text{As} = (43.91 \pm 1.49) \text{ wt. \%} \text{ and } \text{S} = (21.24 \pm 0.43) \text{ wt. \%}.$$

The analytical error attributed to the quantitative analysis results (table 19), can be considered as non-significant to the arsenopyrite characterization and for their use as metalgenesis markers.

### 6.3.2. Discussion

Regarding the plotted data in Kretschmar & Scott (1976) diagram (fig. 70) some interpretations were established from the 3 authors. On Cerdeirinha arsenopyrites ( $\text{Fe}_{1.02-1.12}\text{As}_{1.04-1.24}\text{S}_{0.98-1.00}$ ) several temperature ranges were estimated:

- 1 – **Apy** + Py ( $\pm$  **Po** inclusion)  $\approx$  634 °C
- 2 – **Apy** + Ap + Pl ( $\pm$  **Po** inclusion)  $\approx$  589 °C
- 3 – **Apy** + **Po** ( $\pm$  Ilm  $\pm$  Po  $\pm$  Ap  $\pm$  Zr inclusions) from  $\approx$  564 °C, to **Apy** + Py + Ap + Ilm + Spn + Rt + Ab ( $\pm$  **Po**  $\pm$  Ccp inclusions)  $\approx$  557 °C
- 4 – **Apy** + **Po** + Bt  $\pm$  Fb ( $\pm$  Tit  $\pm$  Ilm  $\pm$  sch inclusions)  $\approx$  550 °C, to **Apy** + Py + Qz + Stp ( $\pm$  **Po** inclusions)  $\approx$  545 °C
- 5 – **Apy** + Py + Qz ( $\pm$  **Po** + Qz inclusions)  $\approx$  534 °C
- 6 – **Apy** + Py + Qz ( $\pm$  **lol** + Sch + Qz + native Bi) from  $\approx$  509 °C, to **Apy** + Py + ( $\pm$  **lol** + Native Bi + Ap inclusions)  $\approx$  505 °C
- 7 – **Apy** + Py ( $\pm$  **lol** inclusion)  $\approx$  491 °C

Leal Gomes (1994) ( $\text{Fe}_{1.09-1.14}\text{As}_{1.00}\text{S}_{1.22-1.32}$ ) established:

- 1 – Massive arsenopyrite co-existing with cordierite  $\approx$  630 °C (P=3Kb)
- 2 – Arsenopyrite + pyrite + pyrrotite co-existing with wolframite (?)  $\approx$  490 °C
- 3 – Arsenopyrite + pyrite  $\approx$  360 °C (*crack seal*) – 325 °C (miarolitic – co-existing with euhedric quartz). Here also belongs arsenopyrite co-existing with sphalerite in the zinciferous ore.

The 3<sup>rd</sup> arsenopyrite population shows the ubiquitous arsenopyrite that appear in all kind of ores. Yet, the most abundant crystallizations are due to former arsenopyrites in the venular ores or the firsts *crack seal* crystallizations, that demonstrated the higher temperatures in the considered range (Leal Gomes, 1994). Apparently, in the case of As-poor arsenopyrite (28.85 at. % As), the difficulty of its formation temperature estimative (it is not possible to plot in the Kretschmar & Scott (1976) diagram) can be explained by the co-existence with cordierite. This mineral might have been formed at the

metamorphism conditions suggested by Dias (1987), 630 °C – 3 Kb (which fits with the syncrystallization textural appearance between cordierite and arsenopyrite) (Leal Gomes, 1994).

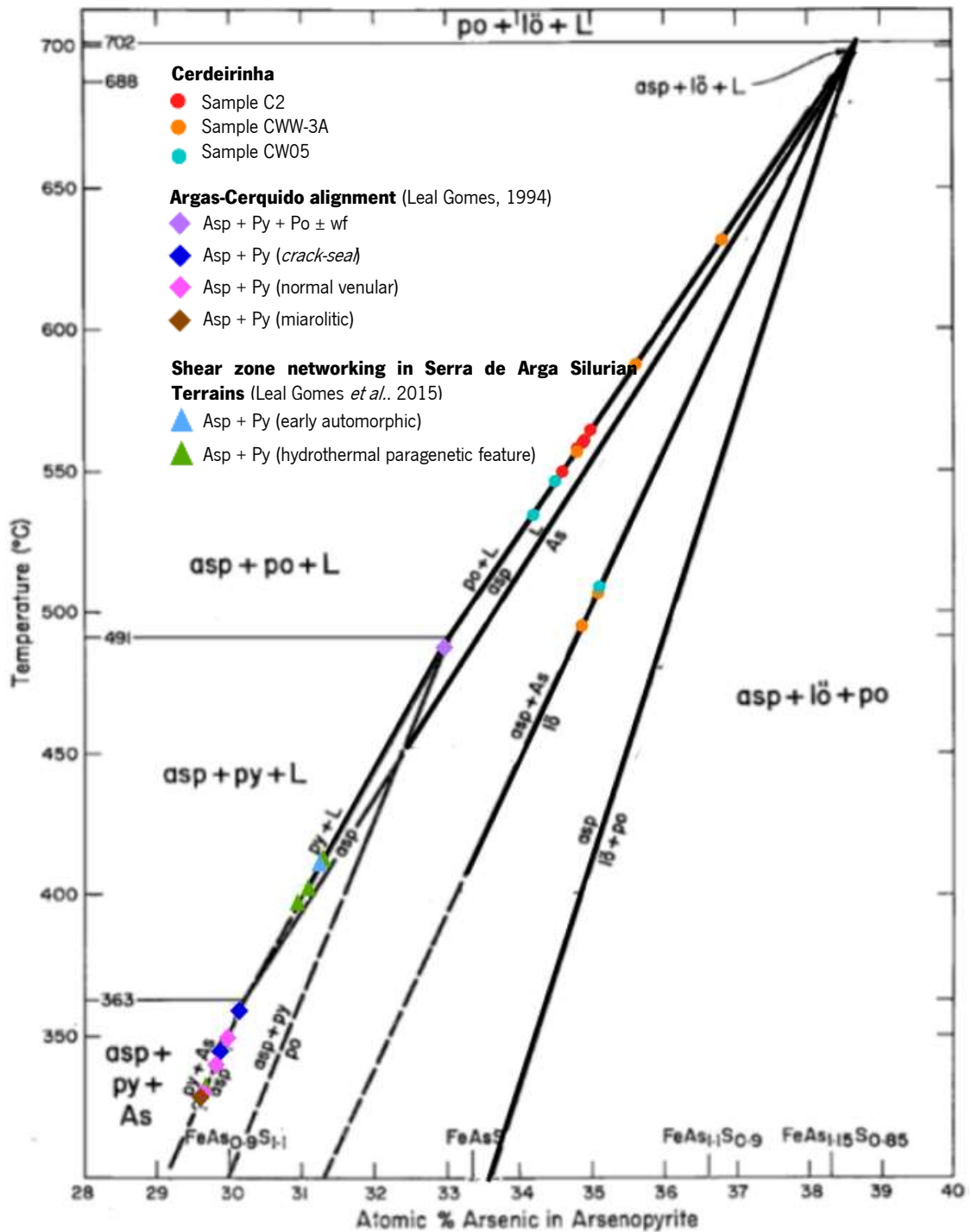


Figure 70 – Pseudobinary T-X diagram with arsenopyrite-buffered curves (reprinted from Kretschmar & Scott (1976) and modified after Sharp *et al.* (1985)). Arsenic atomic content of arsenopyrites (and respective mineral assemblage) from Cerdeirinha, Argas-Cerquido alignment (Leal Gomes, 1994) and shear zone networking in Serra de Arga Silurian Terrains (Leal Gomes *et al.*, 2015) are plotted as circles, tetragons and triangles, respectively.

Regarding the data ( $\text{Fe}_{1.00-1.07}\text{As}_{1.00-1.11}\text{S}_{1.00-1.18}$ ) plotted from Araújo & Leal Gomes (2014) and Leal Gomes *et al.* (2015), it is possible to estimate that:

- 1 – Inner zoned arsenopyrite (where the higher As (at. %) is in the inner zone) from  $\approx 413^\circ\text{C}$  (fig. 69 b)) to  $\approx 408^\circ\text{C}$  (fig. 69 a))
- 2 – Outer zoned arsenopyrite from  $\approx 402^\circ\text{C}$  to  $\approx 395^\circ\text{C}$  (fig. 69 b))
- 3 – Arsenopyrite  $\approx 333^\circ\text{C}$  (fig. 69 c))

The two *Asp* + *Py* assemblages (**1** and **2** in fig. 69) were not possible to plot in the diagram, due to their As-rich content (34.43 at. % As and 33.35 at. % As, respectively).

The former population, obtained in crystals that co-exist with pyrite, equilibrated its As atomic content between 30.94 at. % (Leal Gomes *et al.*, 2015) and 31.26 at. % (Araújo & Leal Gomes, 2014), at temperatures below  $490^\circ\text{C}$ . Lowest As content arsenopyrite (29.69 at. %) (of Leal Gomes *et al.*, 2015) temperature agrees with Leal Gomes (1994) arsenopyrites that ranges from  $333^\circ\text{C}$  to  $330^\circ\text{C}$ .

In summary, regarding these elements, might exist several crystal generations that represent a primitive equilibrium and an expression of the non-stoichiometry (fig. 71), which should depend on the *annealing/recovery* readjustment related with primordial metamorphism/metasomatism (from  $634^\circ\text{C}$  to  $491^\circ\text{C}$ ). Succeeding this, all the arsenopyrites analysed by Leal Gomes (1994), Araújo & Leal Gomes (2014) and Leal Gomes *et al.* (2015), whose composition and pyrite equilibrium suggest conditions of precipitation hydrothermal or deuteric alteration (temperatures under  $\approx 490^\circ\text{C}$  to  $\approx 395^\circ\text{C}$ , fig. 72). Furthermore, seems to exist compositions of cataclastic readjustment and remobilization/recrystallization at low temperature (mesothermal domain – shear zones;  $360^\circ\text{C}$  to  $330^\circ\text{C}$ ) (Leal

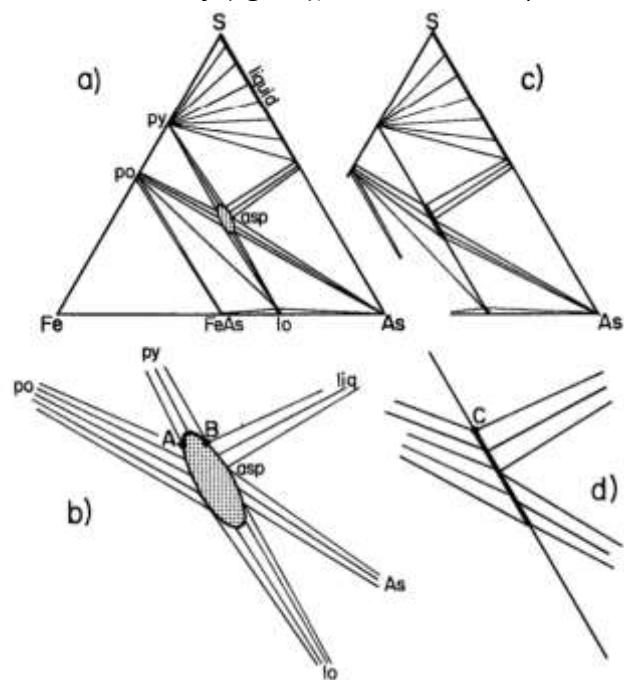


Figure 71 – **a)** Phase relations in the system Fe-As-S between  $363$  and  $491^\circ\text{C}$  (after Kretschmar & Scott, 1976). The stability field of arsenopyrite (shaded) is exaggerated to show the effect of slight deviations from the  $\text{FeS}_2$ - $\text{FeAs}_2$  binary join. **b)** Exploded view of **a)** in the region of arsenopyrite. The composition of arsenopyrite in equilibrium with pyrite at a constant pressure and temperature can be anywhere along the bold line between A and B, depending on  $f(\text{S}_2)$ . The composition of arsenopyrite in equilibrium with pyrite and pyrrhotite must lie at A. **c)** and **d)** Phase relations in the system Fe-As-S for arsenopyrite lying on the binary join  $\text{FeS}_2$ - $\text{FeAs}_2$ . In this case, arsenopyrite coexisting with pyrite must lie at point C.

Gomes (1994) and Leal Gomes *et al.* (2015)).

In Monteiro, the dominant As mineral is lollingite with Co (tending to skutterudite). Arsenopyrite occurs in epitaxial overprinting situations over lollingite and pyrrhotite, which enhances the reaction:  $2 \text{FeAsS (Asp)} \Leftrightarrow \text{FeAs}_2(\text{Lo}) + \text{FeS}(\text{Po}) + \frac{1}{2} \text{S}_2$ . The persistent occurrence of lollingites in the various facies is typical of an evolution under even higher T conditions ( $T > 702^\circ \text{C}$  regarding Kretschmar & Scott, 1976) (Dias & Leal Gomes, 2010).

For last, just a short note regarding the values that fall in the Asp+As $\rightarrow$ lol field (fig. 70): although this is an unstable field due to the free As, it would be expectable to find a more stable association with a pyrrhotite or pyrite intergrowth (C. Leal Gomes personal communication, 2019), this was not found nor possible to plot.

#### 6.3.2.1. Comparison with other Silurian terrains

All the arsenopyrites analysed from Cerdeirinha, and the ones from Argas-Cerquido alignment (Leal Gomes, 1994), and from shear zone Argas-Cerquido-Serra de Arga (Araújo & Leal Gomes, 2014) and also from shear zone networking in Serra de Arga Silurian Terrains (Leal Gomes *et al.*, 2015) came from C.D.F., which means they all came from parautochthonous domain. The stratigraphy of parautochthonous domains is very similar to Central Iberian Zone (autochthonous domain) (Rodrigues *et al.*, 2013). So, in order to compare these two domains (fig. 72), in figure 73 are presented arsenopyrites from Couto (1993). However, the only orebody present in Silurian terrains studied by Couto (1993) was in *Ribeira da Estivada* region, where it occurs in a narrow belt, in the W flank (where is possible to observe black shales).

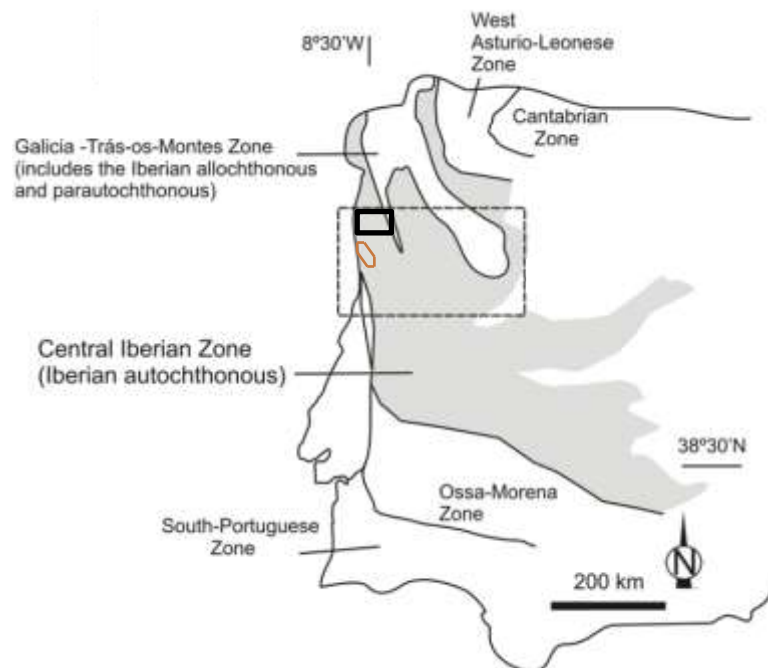


Figure 72 – Geology of the Penedono area, northern Portugal: a location of the study area in the Iberian Massif. Black continuous line limits the area from which the Cerdeirinha and Argas-Cerquido shear zone arsenopyrites were collected, while the brown line limits the area studied by Couto (1993). (From Neiva *et al.*, 2019)

The greater temperature range ( $520^\circ \text{C}$  to  $580^\circ \text{C}$ ) corresponds to Sn-W *S. Jorge* orebody, followed by *Montalto* (Sb-Au) orebody (around  $440^\circ \text{C}$ ) (Couto, 1993). While one of the lowest one ( $380^\circ \text{C}$ ) corresponds to Au-As *Covas de Castromil* orebody, this arsenopyrite seems to be equivalent to

arsenopyrite I (ferri-arseniferous stage) Sb-Au and Au-As orebodies. This temperatures were for cases where  $Sb < 0.2\%$  (Couto, 1993).

Couto (1993) used 2 kind of standards:

- ASP 200 (Fe=34.52%; As=44.45%; S=21.03% from siderite mine in Helen, Ontario, used by Kretschmar & Scott (1976)) in BRGM – Orléans;
- Roche-Baloue sample (Fe=34.00%; As=47.05%; S=19.20%) (Móelo *et al.* 1984 *in* Couto (1993)).

Besides this, the element conditions including voltage and elements counting time were also different in each case.

As it is possible to observe the Couto (1993) data related with Silurian terrains (*Ribeira da Estivada* region) ( $\approx 340^\circ\text{C}$ ) was formed under lower temperatures than the ones obtained in this study ( $\approx 491^\circ\text{C}$  to  $\approx 634^\circ\text{C}$ ). However, it fits among the temperatures measured by Leal Gomes (1994), Araújo & Leal Gomes (2014) and Leal Gomes *et al.* (2015) ( $\approx 330^\circ\text{C}$  to  $\approx 491^\circ\text{C}$ ).

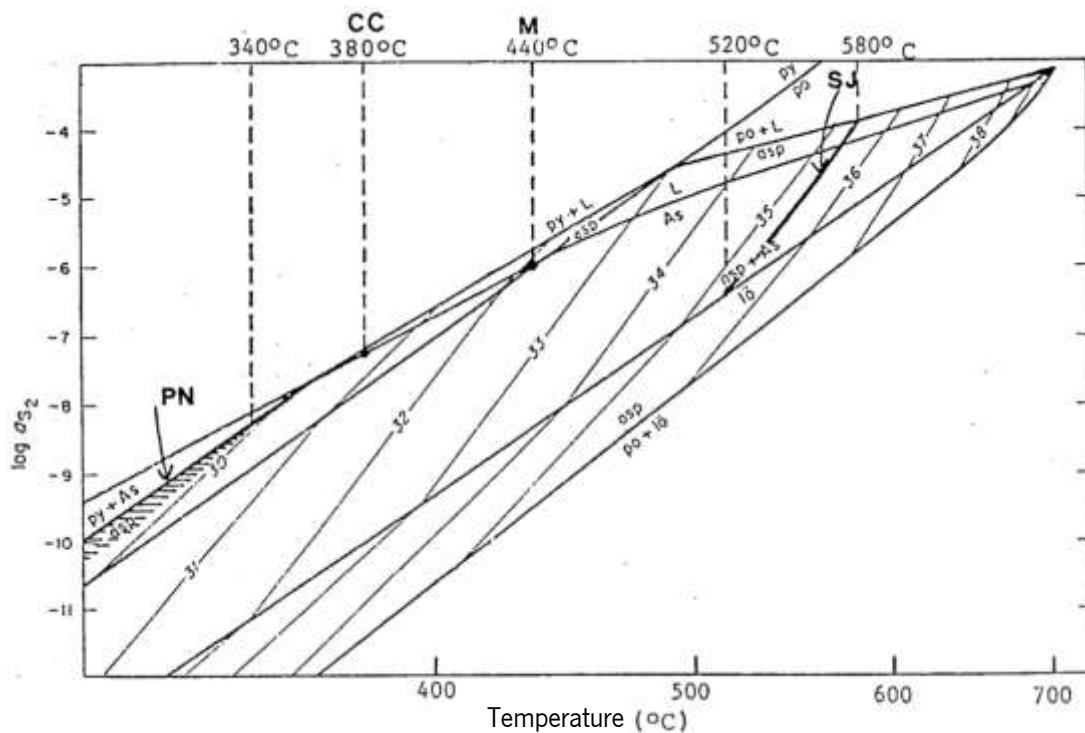


Figure 73 – Diagram of  $\log aS$  – Arsenopyrite temperature, Kretschmar & Scott (1976). Sn-W ore body: SJ=S. Jorge ( $x$ ;  $n=8$ ); Sb-Au ore body: M=Montalto ( $x$ ;  $n=53$ ); Pb-Zn ore body: RE=Ribeiro da Estivada (6PN sample;  $n=7$ ). CC= Covas de Castromil and PN= Ribeira da Estivada (Couto, 1993).

### 6.3.3. Limitations of Kretschmar & Scott (1976) geothermometer

There are some studies that have alert for some issues using this geothermometer.

On one hand, the effect of pressure on arsenopyrite composition being buffered by two other phases is not large and can be ignored for low-pressure hydrothermal deposits. On the other hand, pressure will affect the composition of arsenopyrite in metamorphosed deposits, and should not be



ignored. The most dramatic effect of pressure is to extend the stability field of coexisting arsenopyrite and pyrite to higher temperatures by approximately 14°C/kbar. The commonly accepted upper limit of 491°C for these two phases is probably incorrect for regional metamorphic assemblages of moderate to high grade (Sharp *et al.*, 1985).

Arsenopyrite geothermometry appears to be valid for ore deposits metamorphosed at low or intermediate grades, but the accuracy is less than desirable (Sharp *et al.*, 1985). Application of the arsenopyrite geothermometer to samples formed under conditions other than greenschist and amphibolite facies is not recommended (Sharp *et al.*, 1985). Scott (1983) noticed that sphalerite barometry yields anomalously high pressures (6-8 kbar), and arsenopyrite thermometry give anomalously low temperatures (360-480 °C) for rocks associated with middle amphibolite-facies schists. However, in the Cerdeirinha mine case study, the sample that allowed to estimate amphibolite facies did not contain arsenopyrite.

Berglund & Ekström (1980) proposed that local  $f(S_2)$  variations exist in medium-grade metamorphic rocks, based on varying compositions of arsenopyrite on a fine scale.

In cases with arsenopyrite from high-grade metamorphic rocks appears to have reset, and arsenopyrite from hydrothermal deposits may not have attained equilibrium. Wide compositional ranges of arsenopyrite have been interpreted as effects of temperature variation or fluctuation in sulfur fugacity within the hydrothermal system (Lowell & Gasparri (1982), Kalogeropoulos (1984)).

Arsenopyrite geothermometry has been used for temperature estimation without additional data from other conventional geothermometers (Berglund & Ekström (1980) among other authors). Sharp *et al.* (1985) suggest that the arsenopyrite geothermometer can be used with discretion, preferably in conjunction with other, better-calibrated thermometers (e.g., Essene 1982). Tightly reversed experiments are still needed before the arsenopyrite geothermometer can be regarded as fully quantified. For instance, the coexistence of arsenopyrite from Panasqueira with pyrrhotite indicates temperatures between 410 ° and 635 °C, whereas actual temperatures of formation as assessed by fluid-inclusion data are less than 350 °C. However, and unfortunately, there are only few calibrated geothermometers other than the arsenopyrite geothermometer that can be applied sulfide deposits. For this reason several authors consider this geothermometer as an estimative indicator mainly when arsenopyrite crystallizes close to pyrite-pyrrhotite (Leal, 1994). Sharp *et al.* (1985) also consider that an understanding of the low-temperature behavior of arsenopyrite and the effect of minor-element substitution would be valuable.

## 7. GEOCHEMICAL FRACTIONATION AND FILIATION SIGNATURES

### 7.1. Geochemical fractionation

In order to study the geochemical fractionation of vestigial constituents in sulfides, L.A.-I.C.P.-M.S. measurements were done, and latter graphics of co-relation among metallic elements present in pyrite, pyrrhotite and arsenopyrite were established. In the specific situation of arsenopyrite, a correlation diagram (fig. 91) was done depending on the elements co-relation previously established. While, to study trace elements in the oxides, tungstates, phosphates and silicates (Nickel-Strunz classification), the REE content was normalized to chondrite.

In order to calculate the normalization of trace-elements contents, it was necessary the implementation of one element content (e.g.:  $^{57}\text{Fe}$  or  $^{43}\text{Ca}$ ). This is presented next.

#### 7.1.1. Sulfides

The complexity of the mineralogical expressions of each metal is very variable. Some metals correspond to one and only one phase, deposited in a single metallogenic episode, while other metals appear expressed in more than one phase in a single episode or in only one phase but in several episodes. This finding, emanating from the observation of the intergrowths, proposes an accurate characterization of the potentially recurrent phases and a fine decomposition of the mineralogical phase associations that express a given mineralization. The compromise between admission and reception of cations and crystalline structure instability is organized as follows (descending order): pyrrhotite, arsenopyrite, and pyrite.

The microprobe and L.A.-I.C.P.-M.S. analysis were executed as explained in the chapter 3. *Data and Methodology*.

##### 7.1.1.1. Arsenopyrite data preparation

The standard element for arsenopyrite was  $^{57}\text{Fe}$ , and this standard element was determined through E.P.M.A.. On the sulfide table in *Annexe IV*, one can see the corresponding values of Fe for each case, ranging from 33.84 to 35.05 % of Fe. The correspondent trace elements can be seen on table III.1 in *Annexe III*.

Below, in chapter 7.2. *Geochemical Affinity and Genetic Relations* (fig. 81), dark blue squares represent the arsenopyrites found in different assemblages from the sample CW05 (*attributed to apical interface of structural domain of roof with sulfide-phosphate paragenesis and mound geometry*) (fig. 24

f)). While the yellow represent the arsenopyrite crystals found in C2 sample (*sulfide arcs periphery – distal relatively to apical mounds domain*) (fig. 24 b)). At last, the orange ones evidence the valid measurement present in the CWW-3a (*attributed to sulfide-calcsilicate rock interface in the proximal tubuliform structural domain*) (fig. 24 e)).

#### 7.1.1.2. Pyrite

The standard element for pyrite was  $^{57}\text{Fe}$ , and this standard element was determined through E.P.M.A.. On the sulfide table in *Annexe IV*, one can see the corresponding values of Fe for each case, ranging from 43.34 wt. % to 48.18 wt. % of Fe. The correspondent trace elements can be seen on table III.1 in *Annexe III*.

Below, in chapter 7.2. *Geochemical Affinity and Genetic Relations* (fig. 81), the green circles represent the pyrite found in different assemblages from the sample CW05.n (*spheroid – apical sulfide domain with mound structure*) (fig. 24 c)). While the orange represent the one measurement done in pyrite crystal found in CWW-3a (*attributed to sulfide-calcsilicate rock interface in the proximal tubuliform structural domain*) (fig. 24 – e)).

#### 7.1.1.3. Pyrrhotite

The standard element for pyrrhotite was  $^{57}\text{Fe}$ , and this standard element was determined through E.P.M.A.. On the sulfide table in *Annexe IV*, one can see the corresponding values of Fe for each case, ranging from 60.20 to 61.41 wt. % of Fe. The correspondent trace elements can be seen on table III.1 in *Annexe III*.

Below, in chapter 7.2. *Geochemical Affinity and Genetic Relations* (fig. 81), the green triangle represent pyrrhotites found in different assemblages from the sample CW05.n (*spheroid – apical sulfide domain with mound structure*) (fig. 24 c)). While the yellow represent pyrrhotite crystals found in C2 sample (*sulfide arcs periphery – distal relatively to apical mounds domain*) (fig. 24 b)). At last, the orange triangles evidence the measurements executed in the CWW-3a (*attributed to sulfide-calcsilicate rock interface in the proximal tubuliform structural domain*) (fig. 24 e)).

#### 7.1.1.4. "Mixed phases" and "mineral clusters"

In order to present the metallic trace-elements that were present in these micro *mixed phases*, and once arsenopyrite is the dominant mineral here present (fig. 35 and 36), its Fe content was considered. Fe (wt. %) of the spots **1** and **2** intergrown with arsenopyrite in CWW-3A (fig. 35) were determined, once this was not measured in the microprobe.

$$FeAsS = \frac{A_{Fe}}{M_{FeAsS}} = \frac{55.845}{55.845 + 74.922 + 32.06} \cong 0.34297 = 34.30\% \text{ of Fe}$$

Regarding table 23 is possible to observe that *mixed phases* contain higher values than the *minerals clusters* for the majority of metallic trace-elements, except for Bi and Te, which the higher values were found in spot **4** (native Bi dominant). These metallic trace elements values are greater when compared with the ones present in arsenopyrite, pyrite and pyrrhotite. This suggests a latter remobilization (?).

The W and Mo values in these both *mixed phases* and *mineral clusters* are not significant comparing with the previous sulfides.

Table 23 – Metallic trace-elements present in the *mixed phases* and in *mineral clusters*.

	<i>Mixed Phases</i>		<i>Mineral Clusters</i>	
	<b>1</b>	<b>2</b>	<b>3</b>	<b>4</b>
Fe (% wt.)	34.30		33.06	30.36
Au (ppm)	290.31	330.61	103.14	10.50
Ag (ppm)	104.94	113.89	59.41	20.19
Bi (ppm)	37533.39	55195.57	1385.41	150738.96
Te (ppm)	157.74	159.77	72.49	264.69
Co (ppm)	3033.06	4769.62	4047.40	2007.42
Ni (ppm)	8206.08	10724.75	7520.43	5753.05
Pb (ppm)	2822.01	3299.62	1519.39	57.15
Sb (ppm)	579.67	645.66	506.32	465.59
Mo (ppm)	0.12	0.10	0.27	0.14
W (ppm)	0.12	0.02	93.93	1.47

## 7.1.2. Oxides, tungstates, phosphates and silicates and their REE chondrite normalization

### 7.1.2.1. Ferberite & Wolframite

The standard element for ferberite and wolframite was Fe, and this standard element was calculated considering the ferberite ( $\text{FeWO}_4$ ) and wolframite  $[(\text{Fe},\text{Mn})\text{WO}_4]$  chemical formula, respectively.

$$\text{FeWO}_4 = \frac{A_{\text{Fe}}}{M_{\text{FeWO}_4}} = \frac{55.845}{55.845 + 183.84 + (4 \times 15.999)} \cong 0.1839 = 18.39\% \text{ of Fe}$$

Therefore, the Fe content considered for ferberite was 18.39 wt. %.

For wolframite the chemical formula was considered as  $[(\text{Fe}_{0.5},\text{Mn}_{0.5})\text{WO}_4]$

$$(\text{Fe}, \text{Mn})\text{WO}_4 = \frac{A_{\text{Fe}}}{M_{\text{FeWO}_4}} = \frac{0.5 \times 55.845}{((0.5 \times 55.845) + (0.5 \times 54.938)) + 183.84 + (4 \times 15.999)} \cong 0.0921 = 9.21\% \text{ of Fe}$$

Therefore, the Fe content for wolframite was 9.21 wt. % (*Annexe III*).

This was only analysed in the C2 sample.

In the spider plot (fig. 74), the red squares represent the wolframite in the sample C2 sample (*sulfide arcs periphery – distal relatively to apical mounds domain*) (fig. 24 b)), while the ones in black evidence the ferberites that were measured in the same sample (number 3 included in a scheelite crystal, while numbers 4 and 5 in a pyrrhotitic matrix).

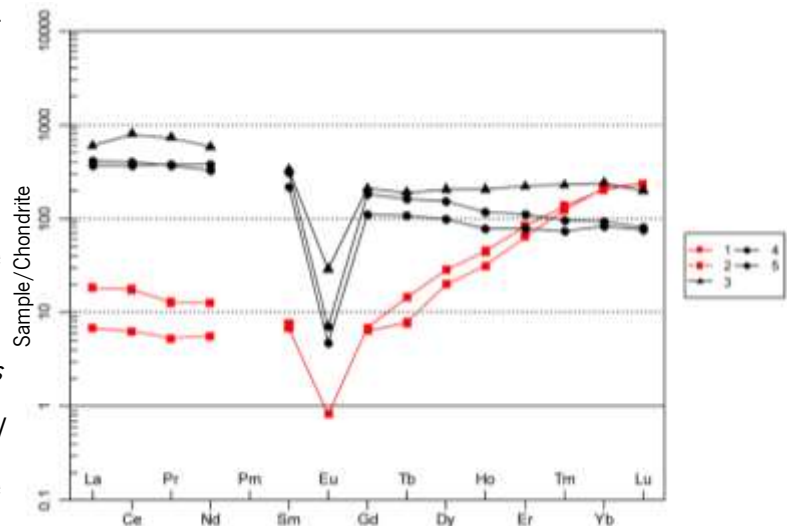


Figure 74 – Spider plot of REE normalized to chondrite (Anders & Grevesse, 1989) in ferberite and wolframite. 1 and 2 – represent the wolframites in fig. 37 h). While 3, 4 and 5 correspond to the ferberites in fig. 37 h) and j). Trace elements contents in *Annexe III*.

### 7.1.2.2. Scheelite

The standard element for scheelite was Ca, and this standard element was calculated considering the scheelite chemical formula ( $\text{CaWO}_4$ )

$$\text{CaWO}_4 = \frac{A_{\text{Ca}}}{M_{\text{CaWO}_4}} = \frac{40.078}{40.078 + 183.84 + (4 \times 15.999)} \cong 0.1392 = 13.92\% \text{ of Ca}$$

Therefore, the Ca content used was 13.92 wt. % (*Annexe III*).

In the spider plot (fig. 75) the black spots represent the scheelite found in different mineral assemblage from the sample CW05 (*attributed to apical interface of structural domain of roof with sulfide-phosphate paragenesis and mound geometry*) (fig. 24 f)). While the blue represent four measurements

done in the only scheelite crystal found in CEE-S (*skarn with proto-travertine ghost structures (mimetic structure)*) (fig. 24 a)). At last, the red line evidence the measurements present in the C2 sample (*sulfide arcs periphery – distal relatively to apical mounds domain*) (Fig. 24 b)).

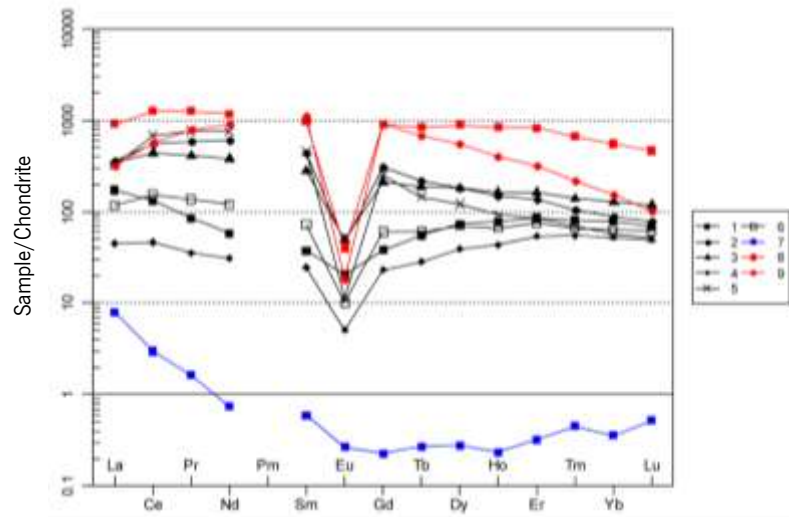


Figure 75 – Spider plot of REE normalized to chondrite (Anders & Grevesse, 1989) in scheelite. Spots location in fig. 37. Black – CW05; Blue – CEE-S; Red – C2. Trace elements contents in *Annexe III*.

### 7.1.2.3. Apatite

Apatite was analysed in L.A.-I.C.P.-M.S. regarding the diverse mineral assemblage (fig. 76).

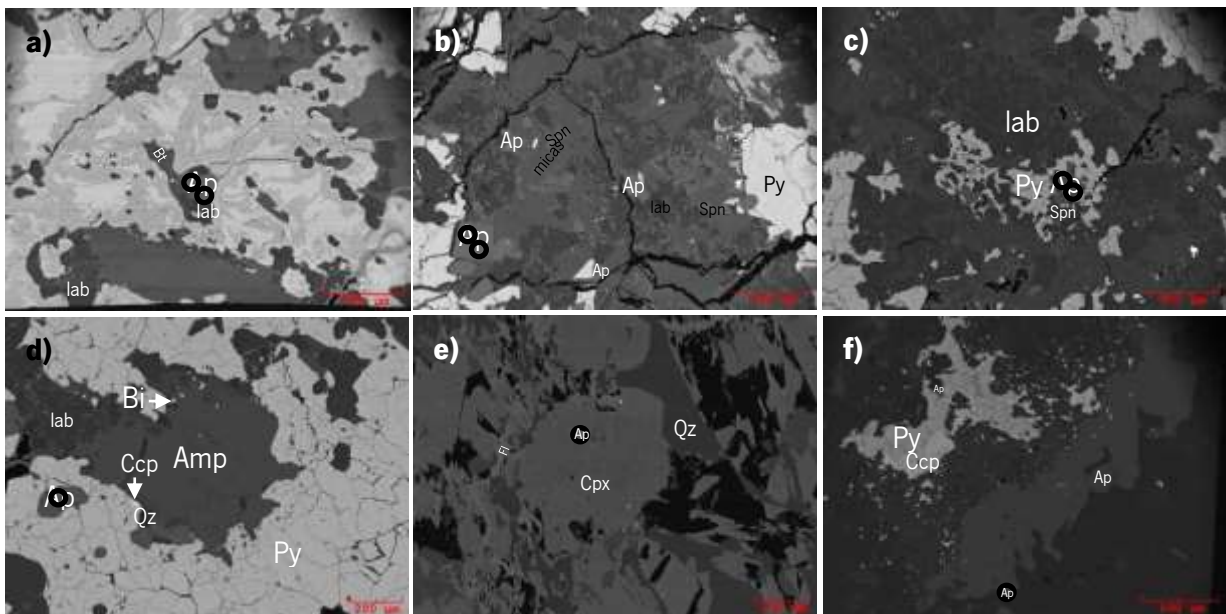


Figure 76 – Apatites L.A.-I.C.P.-M.S. location measurements. **a)** In contact with pyrite, biotite and labradorite (CW05n). **b)** In contact with pyrite and micas (CW05n). **c)** Involved by pyrite and labradorite (CW05n). **d)** Included in pyrite (CW05n). **e)** Included in pyroxene (CEE-S). **f)** Apatite in sericitized plagioclase matrix (C2).

The standard element for apatite was  $^{43}\text{Ca}$ , and this standard element was calculated considering the apatite chemical formula  $[\text{Ca}_5(\text{PO}_4)_3(\text{OH},\text{F},\text{Cl})]$ , for the calculations it was considered as  $\text{Ca}_5(\text{PO}_4)_3(\text{OH})_{0.33}\text{F}_{0.33}\text{Cl}_{0.33}$

$$\text{Ca}_5(\text{PO}_4)_3(\text{OH})_{0.33}\text{F}_{0.33}\text{Cl}_{0.33} = \frac{5 \times A_{\text{Ca}}}{M_{\text{Ca}_5(\text{PO}_4)_3(\text{OH})_{0.33}\text{F}_{0.33}\text{Cl}_{0.33}}}$$

$$= \frac{5 \times 40.078}{(5 \times 40.078) + (3 \times (30.974 + (4 \times 15.999))) + (0.33 \times (15.999 + 1.008)) + (0.33 \times 18.998) + (0.33 \times 35.45)}$$

$$\cong 0.39326 = 39.33\% \text{ of Ca}$$

Therefore, the Ca content used was 39.33 wt. % (*Annexe III*).

The green lines in figure 77 represent the apatite measured in different assemblage from the sample CW05.n (*spheroid – apical sulfide domain with mound structure*) (fig. 24 c)). While the blue represent the one measurement done in an apatite crystal found in CEE-S (*skarn with proto-travertine ghost structures (mimetic structure)*) (fig. 24 a)). At last, the red line evidence the measurement present in the C2 sample (*sulfide arcs periphery – distal relatively to apical mounds domain*) (fig. 24 b)).

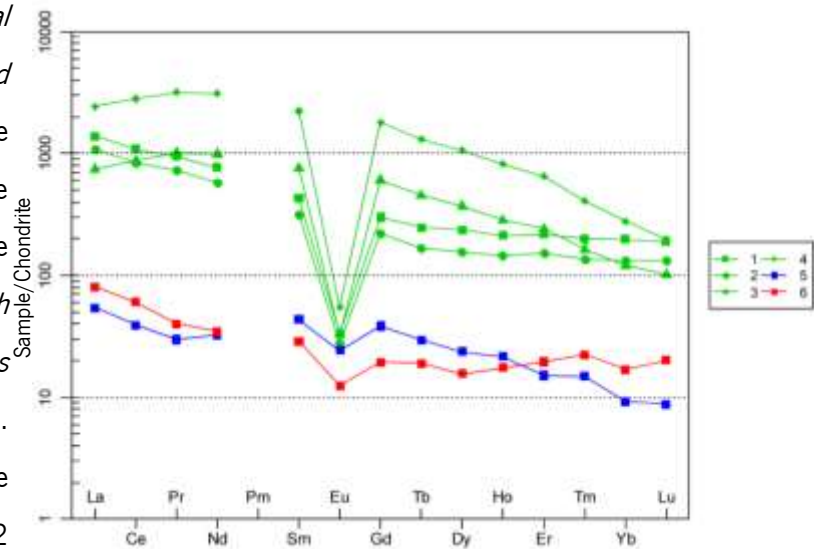


Figure 77 – Spider plot of REE normalized to chondrite (Anders & Grevesse, 1989) in apatite. Spots location in fig. 76. Green – CW05n; Blue – CEE-S; Red – C2. Trace elements contents in *Annexe III*.

In the graphic below there is no location difference in the CW05n apatites to justify its diverse content observed in 1 and 2 vs. 3 and 4, once 1 and 2 were found further and closest to the nucleus respectively, and 3 and 4 were found in intermediate positions.

#### 7.1.2.4. Vesuvianite

Vesuvianite was analysed in L.A.-I.C.P.-M.S. regarding the diverse mineral assemblage (fig. 78).

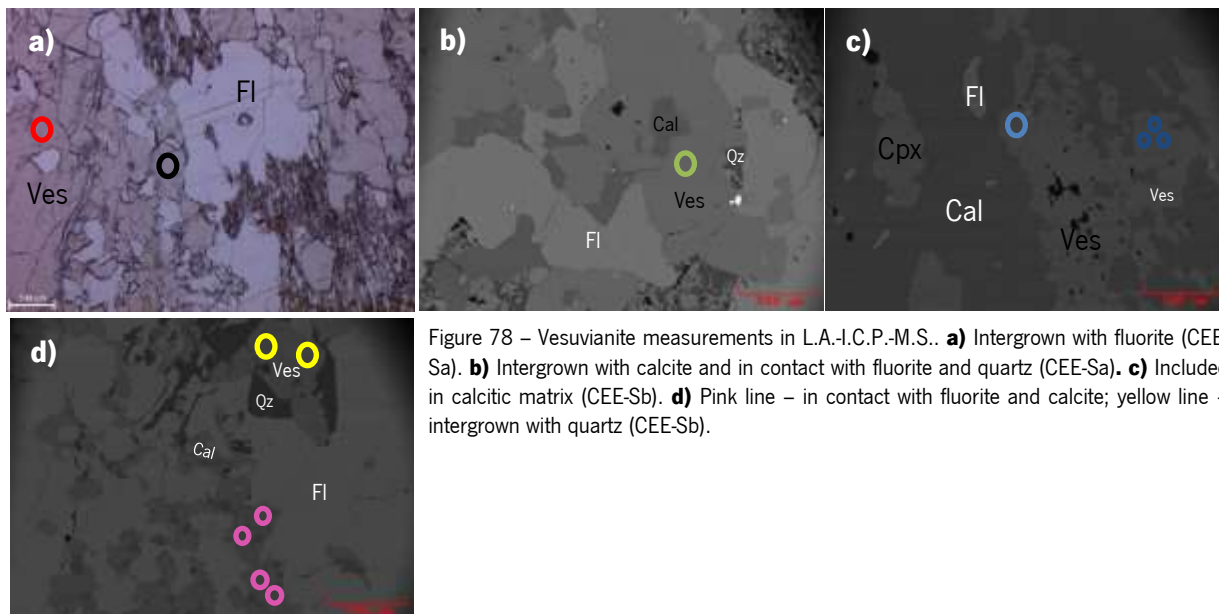


Figure 78 – Vesuvianite measurements in L.A.-I.C.P.-M.S.. **a)** Intergrown with fluorite (CEE-Sa). **b)** Intergrown with calcite and in contact with fluorite and quartz (CEE-Sa). **c)** Included in calcitic matrix (CEE-Sb). **d)** Pink line – in contact with fluorite and calcite; yellow line – intergrown with quartz (CEE-Sb).

In the case of vesuvianite (fig. 79), the standard element was also  $^{43}\text{Ca}$ . However, Ca weight percentage contents of six vesuvianites (24.973%; 25.191%; 25.256%; 25.486%; 25.687%; 25.505%) were measured under microprobe. Therefore this average of Ca content of these six vesuvianite was determined:  $25.34967\% \approx 25.350\%$ . After, this value was implemented to calculate the concentration of trace elements present in the other vesuvianite crystals (*Annexe III*). Notice that vesuvianite was only found in this sample CEE-S (*skarn with proto-travertine ghost structures (mimetic structure)*) (fig. 24 a)).

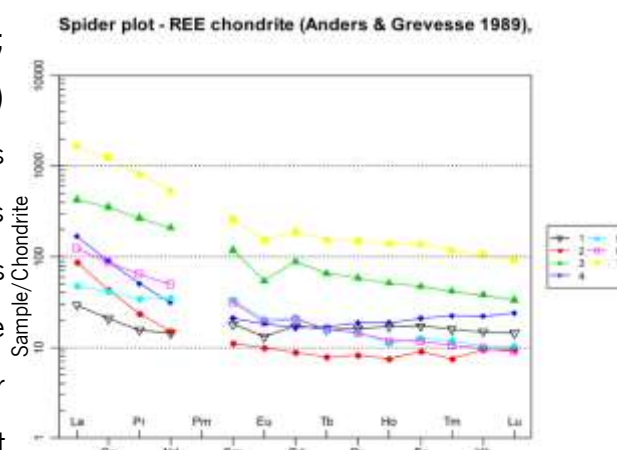


Figure 79 – Spider plot of REE normalized to chondrite (Anders & Grevesse, 1989) in vesuvianite. The numbers correspond to the average of L.A.-I.C.P.-M.S. measurements spots of the same colour in the figure 78. Trace elements contents in *Annexe III*.

Therefore, the Ca value used was 25.687 wt. % for one vesuvianite crystal, 25.486 wt. % for other crystal and 25.350 wt. % for all others.

#### 7.1.2.5. Pyroxene (diopside & hedenbergite) & Wollastonite

In these cases the standard element was also Ca. However, the Ca weight percentage contents of each diopside, hedenbergite and wollastonite was previously measured by microprobe. Notice that these minerals were only found in this sample CEE-S (*skarn with proto-travertine ghost structures (mimetic structure)*) (fig. 24 a)). In figure 80, represent black spots diopside, green spots represent hedenbergite, and for last blue indicates wollastonite measurements in L.A.-I.C.P.-M.S..



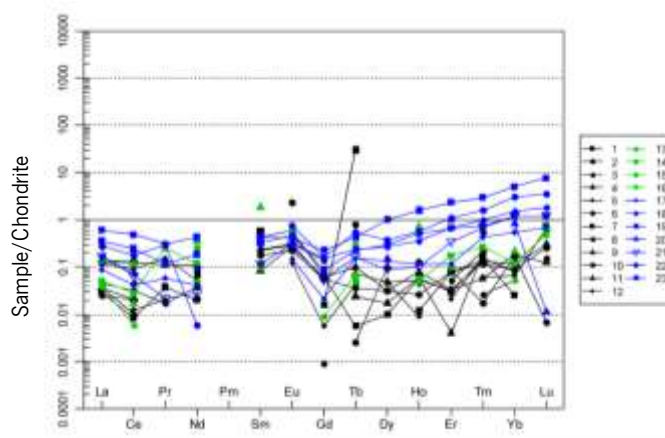


Figure 80 – Spider plot of depleted REE normalized to chondrite (Anders & Grevesse, 1989) in clinopyroxenes (black), hedenbergite (green) and wollastonites (blue). The numbers correspond to the average of L.A.-I.C.P.-M.S. measurements.

## 7.2. Geochemical affinity and genetic relations

### 7.2.1. Sulfides fractionation

Regarding the following subchapter the symbols in the graphics can be found in figure 81.

The binary-plots, from which the paragenetic correlation diagram of metallic trace-elements in arsenopyrite was based, contained both axis with logarithmic scale, therefore the respective correlation curve was the type  $y = ax^k$ .

- ◆ Arsenopyrite CW05
- ◆ Arsenopyrite C2
- ◆ Arsenopyrite CWW-3
- ◆ Pyrite CWW-3A
- Pyrite CW05n
- ▲ Pyrrhotite C2
- ▲ Pyrrhotite CWW-3
- ▲ Pyrrhotite CW05n

Figure 81 – Graphic symbols meaning.

#### 7.2.1.1. Arsenopyrite

In what Bi concerns, it is possible to identify 2 generations of arsenopyrite (fig. 82 a)). One exhibits a negative correlation, whereas the other are positive. While, in the correlation of As and Au, it suggests that Au was in arsenopyrite crystal net and was exsudated or exsolved. Fractures were filled by electrum,

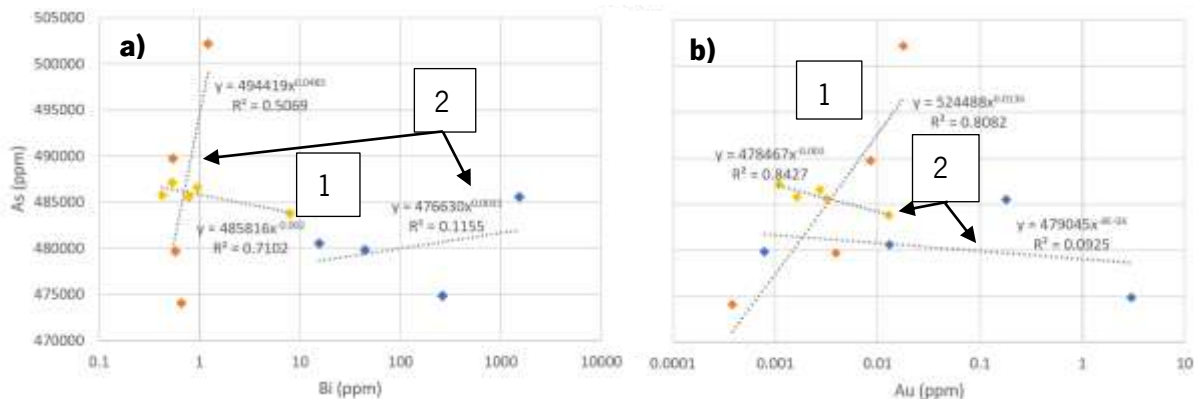


Figure 82 – As content in arsenopyrite. **a)** Correlation of As and Bi in arsenopyrite. The 2 main generations of arsenopyrite are identified with the number 1 and 2. **b)** Correlation of As and Au in arsenopyrite. Consult figure 81 for symbology meaning.

native Bi and bismutinite. In this case (fig. 82 b)), it is possible to observe a positive As-Au correlation and two other negative. However, one should enhance that some Au content is below the detection limit (0.01 ppm).

Still in arsenopyrite, regarding Sb vs. Ag, all correlations are positive (fig. 83 a)), while in the Sb vs. Au plot, there are two positive correlation, and one that is negative. These elements correlation indicates a low temperature genesis. However, one should take in consideration what was said above about Au.

In the correlation of Au and Ag (fig. 84), all the measurements considered in arsenopyrite were plotted under the Au/Ag ratio, except one, which means that there is higher content of Ag than Au in general. However, most of Au contents are below detection limit, and therefore it is not right to comment on its correlation.

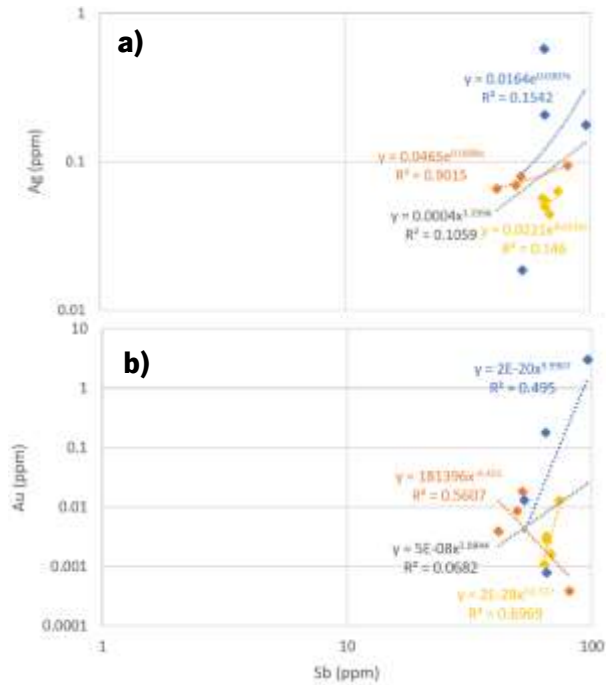


Figure 83 – Ag and Au correlation with Sb. **a)** Correlation of Ag and Sb in arsenopyrite. **b)** Correlation of Au and Sb in arsenopyrite. Consult figure 81 for symbology meaning.

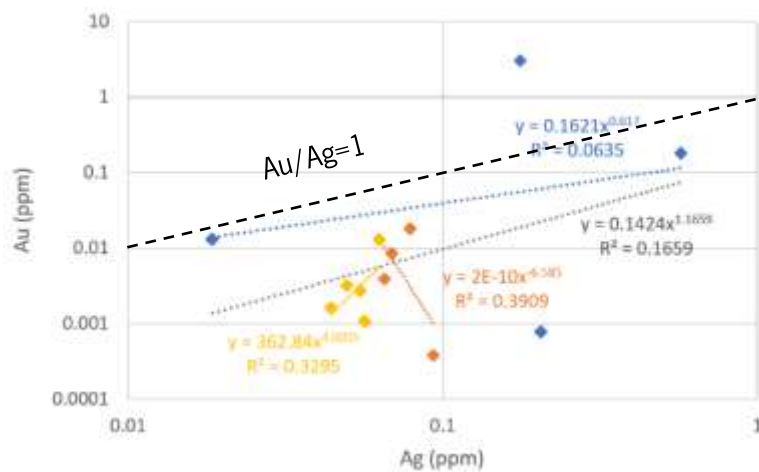


Figure 84 – Au and Ag correlation. Consult figure 81 for symbology meaning.

In the In and Bi (fig. 85 a)) binary-plot, it seems to exist some correlations, once there are two cases where they came as positive and one has a slightly negative trend. However, in the case of Te vs. Bi (fig. 85 b)) the two observed correlations are positive. This seems to be correlated with the presence of tetradymite and Te and Bi composites that were seen included in arsenopyrite (fig. 86).

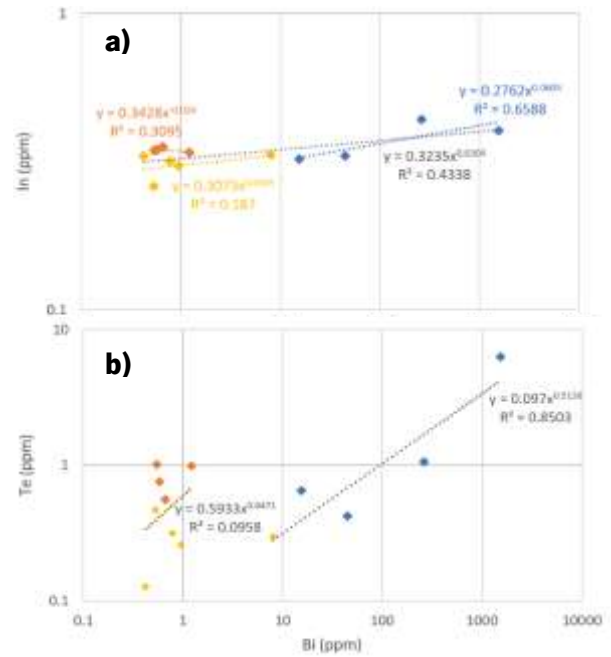


Figure 85 – Comparison of Bi content with In and Te. **a)** Binary plot of In and Bi. **b)** Binary plot of Te and Bi. Consult figure 81 for symbology meaning.

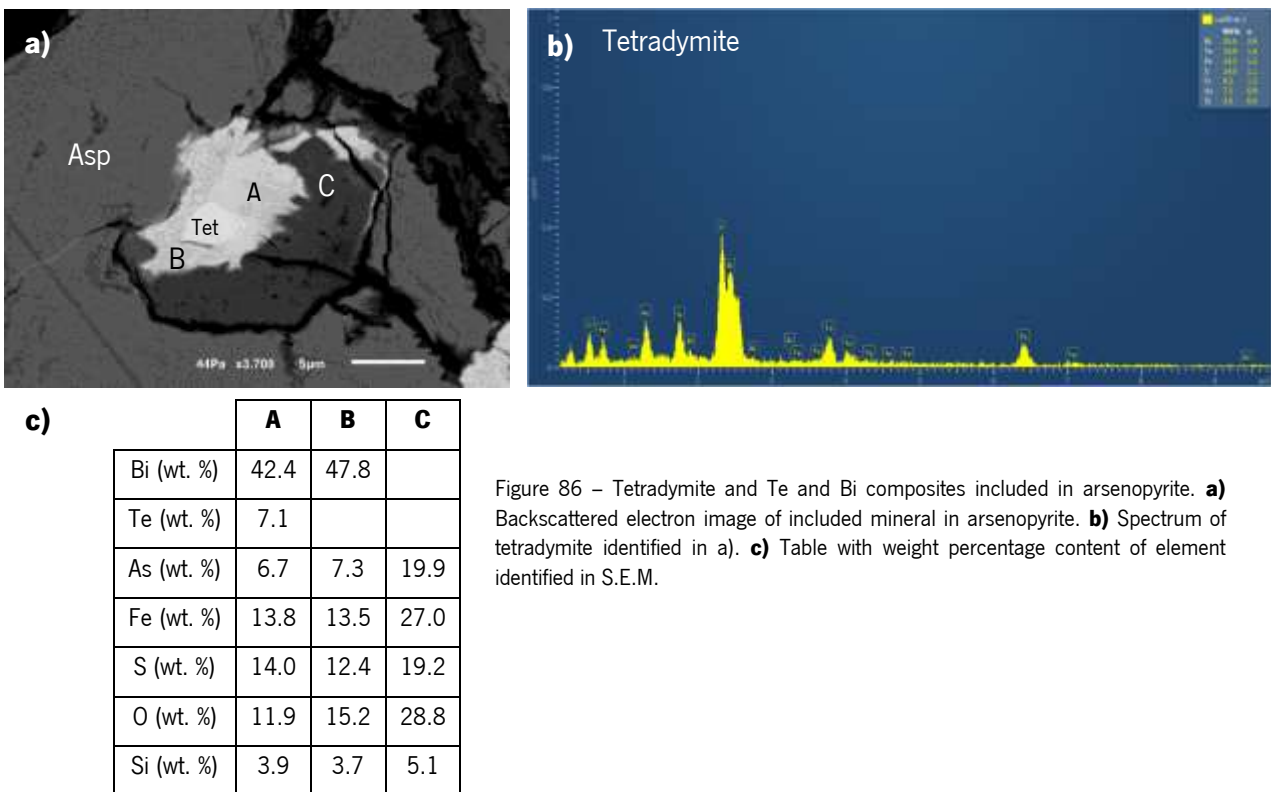


Figure 86 – Tetradymite and Te and Bi composites included in arsenopyrite. **a)** Backscattered electron image of included mineral in arsenopyrite. **b)** Spectrum of tetradymite identified in a). **c)** Table with weight percentage content of element identified in S.E.M.

Moreover, on one hand, Co and Mo correlation is low (fig. 87), and the same applies to Co and W. Some contents of W are below the detection limit (0.01 ppm). On the other hand, although Sn determinations are not accurate (table 25), Mo and Sn indicate higher and positive correlations, suggesting that their presence might be correlated.

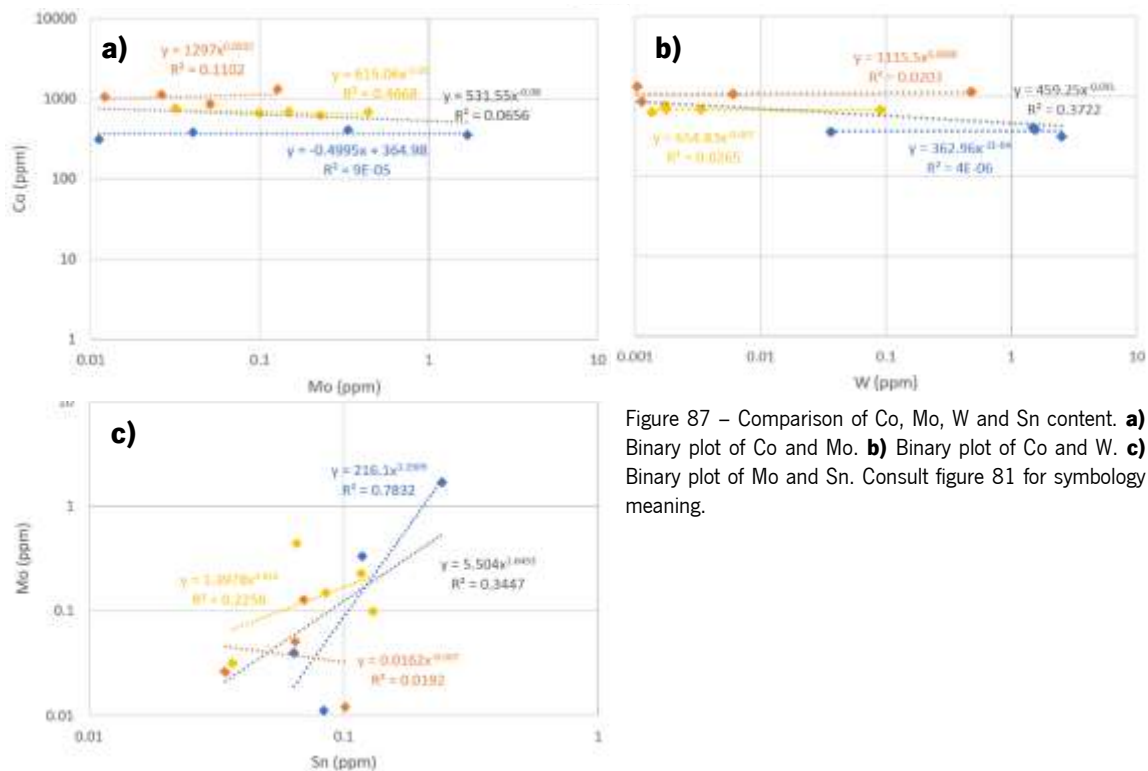


Figure 87 – Comparison of Co, Mo, W and Sn content. **a)** Binary plot of Co and Mo. **b)** Binary plot of Co and W. **c)** Binary plot of Mo and Sn. Consult figure 81 for symbology meaning.

Although W and Mo correlation is not evident in arsenopyrites in particular, these chemical elements characterize a strong mobilization in Serra de Arga, as seen in sub-chapter 2.1.2.3. *Au and W contents supporting Exhalative Protogenesis hypothesis*. Regarding tungstiferous content only in the non-venular facies (Dias, 2010):

*I. Covas Dome* – several generations of scheelite and wolframite in sulfide mineralized stratabound bodies and calc-silicate lithologies; In the context of Covas lithostratigraphy, the discrimination of facies also suggested the existence of volcanogenic and exhalitic carriers neighbouring the metacarbonate and calc-silicate formations; these are hyperferriferous formations with magnetite and hematite and granite-rich gneissic textured rocks (attributed to a SEDEX petrogenesis) (table 24).

*II. Serro* – scheelite dispersed in calc-silicate rocks; disseminated W-molybdenite in metamorphosed felsic tuffs with sulfides; scheelite in venular leucosome of amphibolites.

*III. Monteiro* – abundant scheelite in amphibolites that co-exist with tourmalinites, phosphate horizons, and graphite calc-silicate rocks – W content can reach 2883 ppm in melanocratic facies; scheelite present in phyllitic facies related to metasomatic periamphibolic products (W = 368 ppm) – paragenesis includes lollingite, arsenopyrite, pyrrhotite and chalcopyrite.

Table 24 – Variability of the wolframitic mineralization attributed to Covas Dome. (Modified after Dias & Leal Gomes (2010).)

Localization	Host-rock	Mineralogical assemblage	Typology of W mineralization	Habit and textures of W ores
<i>I. Covas Dome</i>	Massive pyrrhotite in metavulcanic-exhalitic facies	Albite + Mn-almandine - spessartite + muscovite + biotite + F-apatite + pyrrhotite + chalcocopyrite ± quartz	Scheelite	
	Massive pyrrhotite in metavulcanic-exhalitic facies	Pyrrhotite + plagioclase + biotite (chlorite) + K-feldspar + muscovite.	Wolframite+scheelite	Pseudomorphose of ferberite after scheelite (locally called <i>peões</i> ( <i>spinning top</i> ) due to the crystals morphology)
	Grossularite	Garnet (grossular) + andesine + pyrrhotite + arsenopyrite + chalcocopyrite + zavariskite + pyrite (Co/Ni=5)	Scheelite+wolframite	Scheelite and wolframite intergrowths.
	Albitic Metasomatite	Albite + apatite + biotite + pyrite + pyrrhotite + chalcocopyrite + arsenopyrite + native Bi	Scheelite	Thin crystals included in pyrite. Thick crystals.

Scheelite present in amphibolitic facies (Monteiro) are richer in Ca than most scheelites in calc-silicate rocks; scheelites hosted on calc-silicate rocks of Serro are richer in W.

On one hand, in Covas *skarn*, in facies with massive pyrrhotite were observed ferberitization textures of wolframite I (richer compositions in Fe; (fig. 88)) and the occurrence of ferberite II in pseudomorphose

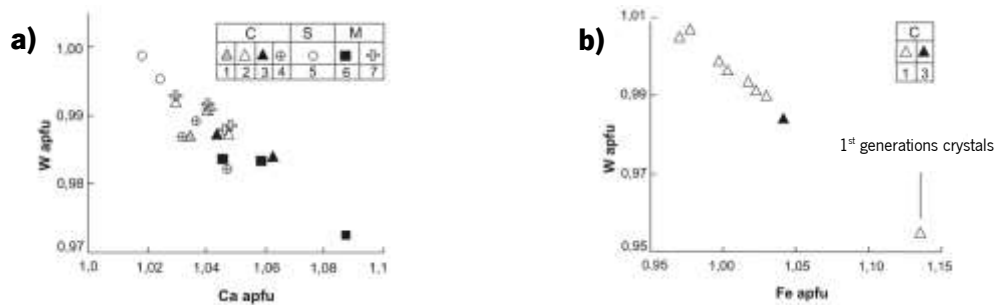


Figure 88 – Tungstates compositions present in calc-silicate associations of Covas and amphibolitic facies of Monteiro. Note: Covas wolframite compositions include pseudomorphoses and 1<sup>st</sup> generation crystals. **a)** Binary-plot of W (a.p.f.u.) vs. Ca (a.p.f.u.). **b)** Binary-plot of W (a.p.f.u.) vs. Fe (a.p.f.u.). C – Covas compositions (massive sulfide facies, grossularites and metasomatites); S – Serro compositions (calc-silicate rocks); M – Monteiro compositions. (amphibolites and leucocratic peri-amphibolitic facies). (From Dias & Leal Gomes (2010).)

after scheelite. Wolframite is the major carrier of Bi minerals (native Bi and zavaritskite with Bi, F and Fe) and is often hosted in massive pyrrhotite and in intergrowths of chalcocopyrite and sphalerite. It was also observed early homogeneous wolframite associated with biotite with native Bi inclusions (Dias & Leal Gomes, 2010).

In Cerdeirinha mine, scheelite that included wolframite was found included in biotite matrix, and one small crystal of scheelite and other of ferberite were found in pyrrhotite in the same sample (C2 – *sulfide arcs periphery – distal relatively to apical mounds domain*). Besides this, scheelite was also seen intergrown with arsenopyrite and quartz, and scheelite that included wolframite was seen intergrown with

quartz (CW05 – attributed to apical interface of structural domain of roof with sulfide-phosphate paragenesis and mound geometry).

On the other hand, in Serro, the presence of W-molybdenite in felsic meta-volcanics suggests peculiar conditions to the evolution in a primordial hydrothermal stage. The observed crystals oscillatory zoning and aspects of corrosion suggest rebalancing with several and repeated fluctuations of oxidation degree ( $fO_2$ ) and W and Mo contents variations in the growth environment (Dias & Leal Gomes (2010) and Dias *et al.* (2010)):

- W enrichment in molybdenite is correlated with high sulfur activity – reductor stage – during early crystallization (Holl & Weber-Diefenbach (1973) and Hsu (1977) in Dias *et al.* (2010)
- Mo-rich overgrowths tend to be accompanied by increasing  $fO_2$  (Hsu, 1977);

The introduction of W in the system possibly accompanied water-interaction, concomitant with the deposition of sulfide mineralization, in a VHMS type model. The evolution to an oxygenated environment would reflect the observed deposition of vein tourmalinites (Cr-rich dravite) in tuffitic protoliths including W-molybdenite (fig. 89), possibly due to exhalitic remobilization. Also, it would facilitate the occurrence of molybdenite, without W content, which is observed in metafelsites, and scheelite, occurring in calc-silicate rocks and amphibolites of the same suites (Dias *et al.* (2010)).

Subsequently, shear zones such as Argas-Cerquido or Castelão focus W mineralizations on successive late-Variscian hydrothermal reactivations of wolframitic sequestration until late stolzite formation.

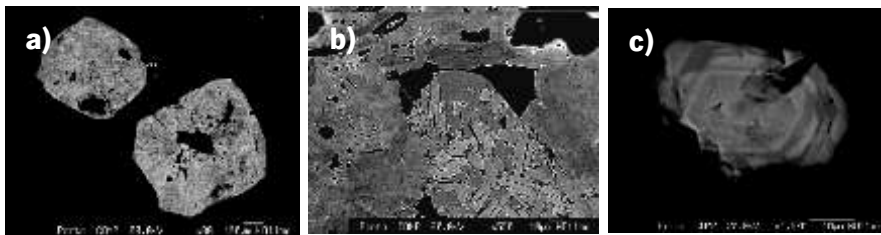


Figure 89 – Backscattered electrons image from Dias (2010). **a)** Pseudomorphose of ferberite II after scheelite - Covas; **b)** Intergrowth between ferberite I and scheelite in the nucleus of a pseudomorphose - Covas; **c)** W-molybdenite crystal – Serro.

Also in this study, a molybdenite (fig. 90) with its typical plastic character and hence deformed aspect, was identified.

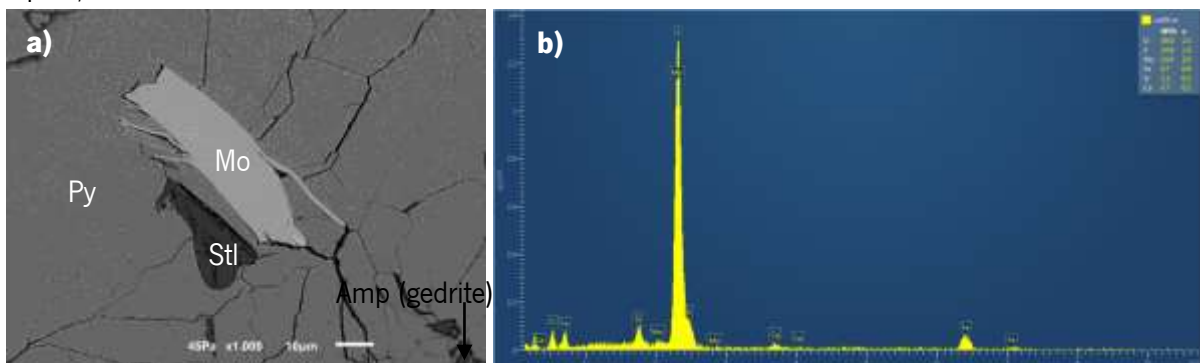


Figure 90 – Molybdenite identified in Cerdeirinha mine. **a)** Backscattered electrons image of molybdenite intergrown with pyrite. **b)** Energy-dispersive X-ray spectroscopy – spectrum of molybdenite.

Bi, Au, Ag, Te, Pb, In, Ni and Mo are related among themselves. However, they are not related with arsenopyrites (nor Fe, S, As in arsenopyrite) (fig. 91 and table 25), with the exception of Ni. Therefore, they can possibly be related with hosting of native phases to low temperature sulfides in arsenopyrite fractures (fig. 83). The correlation was established regarding correlation coefficient ( $R^2$ ;  $0 < R^2 \leq 1$ ).

Several other metals that seem to be close to correlate are noted with an yellow circumference in figure 91. Among these, Sb seems to correlate with Fe and As, while Ni seems to correlate with Fe and S. Attention should be drawn to W and Au that present some values below detection limit.

Table 25 – L.A.-I.C.P.-M.S. calibration and control standards measurements regarding arsenopyrites measurements.

	<sup>107</sup> Ag	<sup>197</sup> Au	<sup>209</sup> Bi	<sup>59</sup> Co	<sup>115</sup> In	<sup>55</sup> Mn	<sup>95</sup> Mo	<sup>58</sup> Ni	<sup>208</sup> Pb	<sup>125</sup> Sb	<sup>118</sup> Sn	<sup>183</sup> W	<sup>66</sup> Zn	<sup>128</sup> Te
calibration st. NIST-630	251	23.6	384	410	434	444	417	458.7	426	396	430	444	460	302
Sample Arsenopyrite	<b>0.572</b>	<b>3.002</b>	1543.573	1306.562	<b>0.439</b>	<b>1.908</b>	<b>1.686</b>	<b>356.151</b>	<b>0.800</b>	<b>96.142</b>	<b>0.243</b>	<b>2.506</b>	<b>0.646</b>	<b>6.294</b>
control st. BHVO-2G			0.01	44	<b>0.1</b>	1317	<b>3.8</b>	<b>116</b>	<b>1.7</b>	0.3	2.6	0.23	<b>102</b>	
rel. error			-995.30%	4.36%	-4.38%	2.18%	15.7	6.76%	0.38%	-55.20%	-32.76%	-181.40%	13.68%	
control st. BCR-2G	<b>0.5</b>		0.05	38	<b>0.11</b>	1550	270	13	11	0.35	<b>2.6</b>	<b>0.5</b>	125	
rel. error	-9.98%		140.00%	-1.60%	-1.90%	-1.67%	-4.30%	-5.30%	-3.66%	-5.20%	-17.68%	18%	23.43%	
control st. MASS-1	67	<b>47</b>	7	67	50	<b>260</b>	61	86.5	74	<b>55</b>	55		210000	
rel. error	2.38%	-30.86%	856.26%	-4.64%	2%	-1.80%	-11.90%	14.60%	-1.36%	16.36%	7.76%		11.20%	
	ok	probably vary uncertain	ok	ok	ok	ok	ok	ok	perfect	ok		ok		

\*red - far below the detection

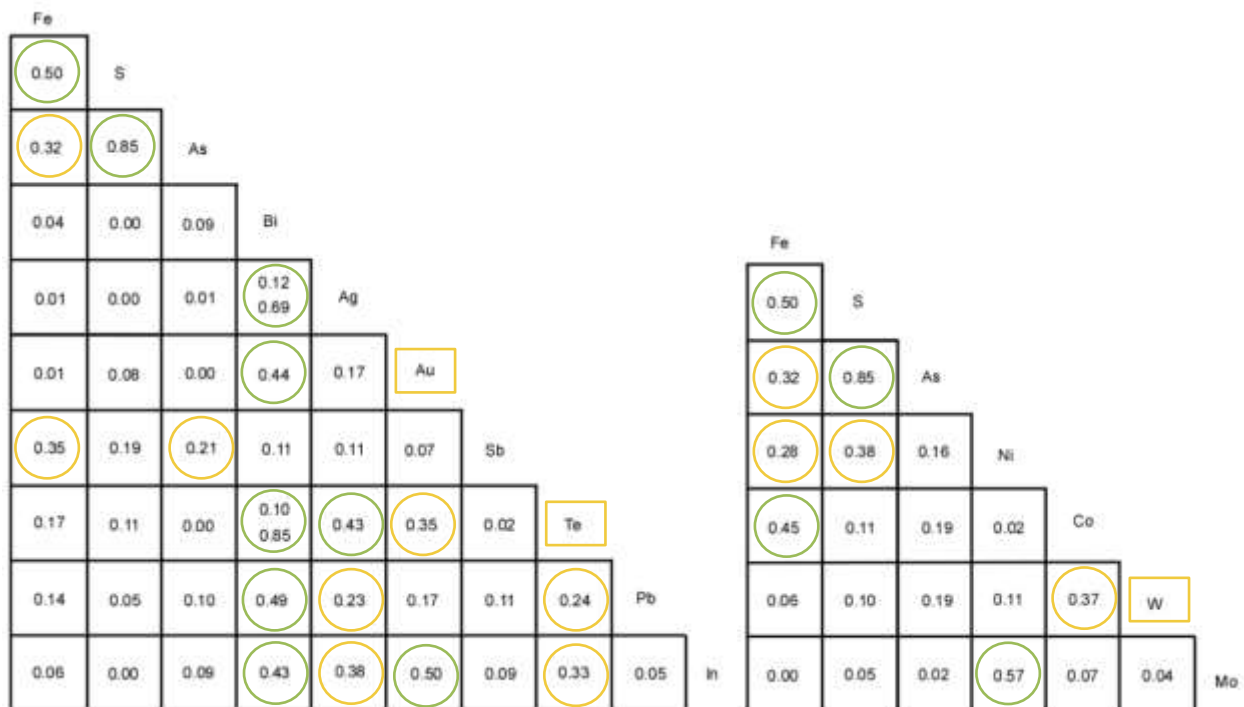


Figure 91 – Paragenetic correlation diagram of metallic trace-elements in arsenopyrite. Green circumferences highlight the best correlations, while the yellow ones indicate the second best. Yellow rectangle evidence the elements that caution should be taken regarding elations.

Regarding the figure 92, where Au, Ag and Bi content are present (fig. 92 b)), is possible to conclude that the arsenopyrite including Au-Ag alloy have low gold values in its crystal net. Therefore the Au present in the Au-Ag alloy was remobilized from a source that was not the arsenopyrite crystal net, and it was latter installed in the transpressive fracture, once the arsenopyrite is a sulfide mineral with the most fragile behaviour. This suggests that arsenopyrite is a favourable place from the mechanic point of view, and therefore takes in the latter fluids (opens space to gold precipitation). Besides, 2 hypothesis are presented in figure 92 d): (1) previous presence of lollingite later affected by transpressive bismuth installation or (2) a former transpressive crack with Bi content and latter lollingite installation.

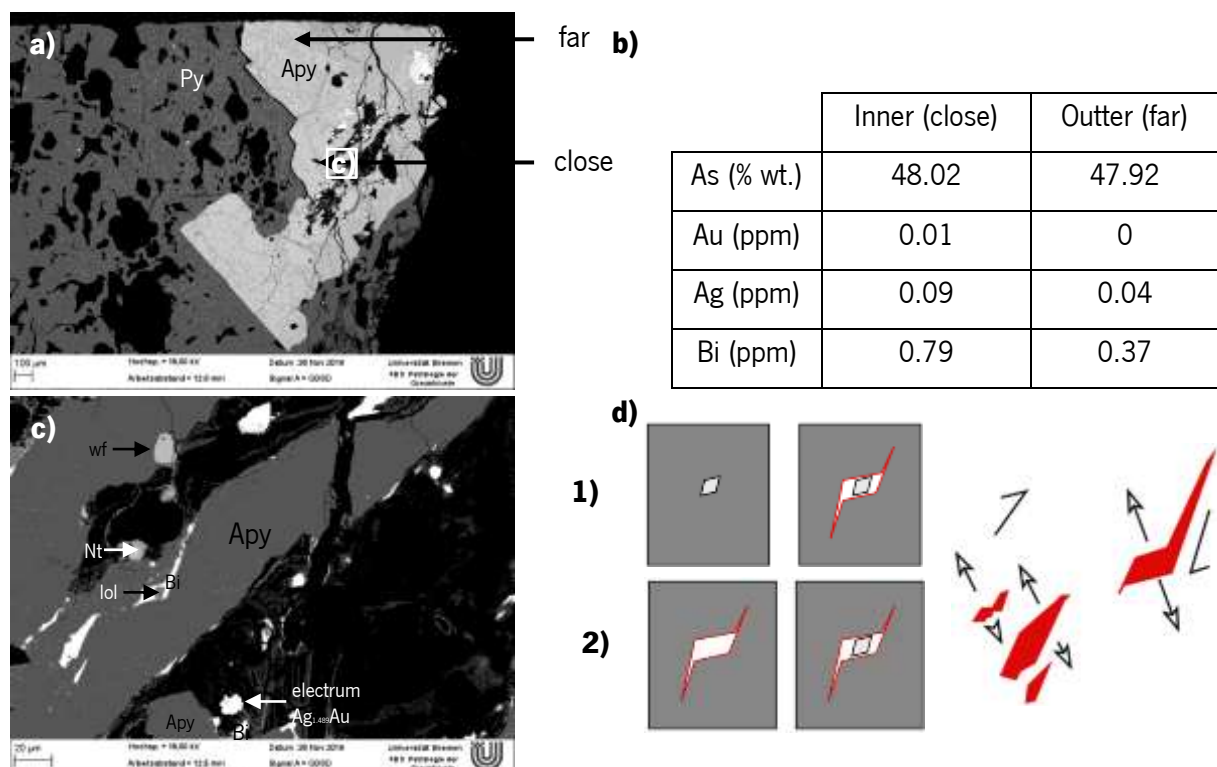


Figure 92 – Non-auriferous arsenopyrite. **a)** Backscattered electrons image of the porphyroblastic arsenopyrite and the location of their measurements found in b). **b)** Table with the content present in a), regarding As, Au, Ag and Bi. **c)** Detail of a). **d)** Representative scheme of the genesis of lollingite particle included in Bi, included in arsenopyrite (hypothesis 1 and 2).

Also, an arsenopyrite, that exsolves or includes lollingite and contains some metalliferous data in its interface, was identified. Arsenopyrite below (fig. 93) was not included in the plots nor diagram plot once it presented high values of Co, Ni, Ag, Au, Te, Bi and one of the highest of Pb values comparing with the other samples. Sb and In in this arsenopyrite measurements belong to the range values present in the figure 93.

Lollingite was not measured under microprobe, therefore its Fe and As (wt. %) was calculated as seen below, in order to establish the normalization of the L.A.-I.C.P.-M.S. elements measurements.

$$FeAs_2 = \frac{A_{Fe}}{M_{FeAs_2}} = \frac{55.845}{55.845 + (2 \times 74.922)} \cong 0.2715 = 27.15\% \text{ of } Fe$$



$$FeAs_2 = \frac{2 \times A_{As}}{M_{FeAs_2}} = \frac{2 \times 74.922}{55.845 + (2 \times 74.922)} \cong 0.7285 = 72.85\% \text{ of As}$$

The arsenopyrite measurement that is close to lollingite contains higher values of all the elements present in the table 26 comparing with outer zone. However, lollingite followed the inner sector of arsenopyrite high values, except for Bi and Ni, which their highest was here observed. These arsenopyrite contents were not present in the correlation diagram, once it suggests that these high metallic values can be explained by the exsolution of native Bi in the border of arsenopyrite-lollingite, and not in the arsenopyrite crystal net.

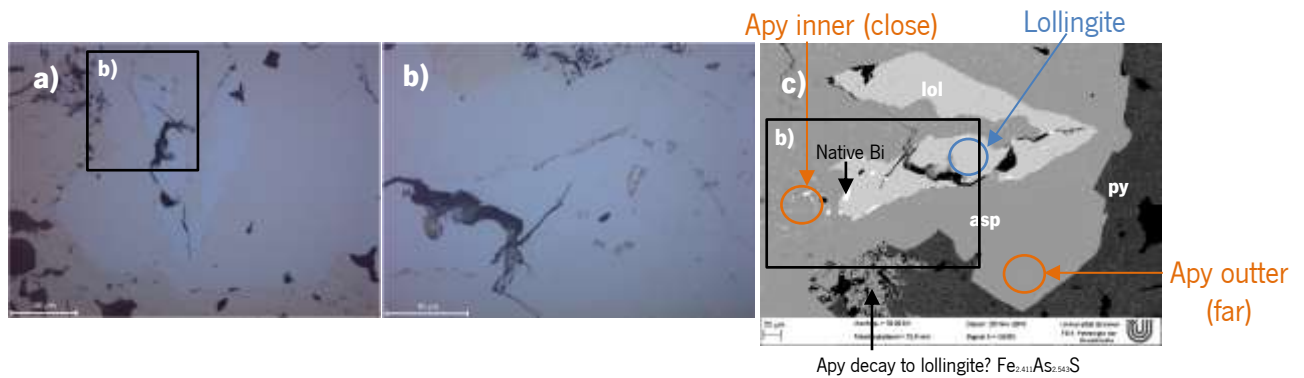


Figure 93 – Lollingite exsolution from arsenopyrite, with native bismuth in the contact of the arsenic minerals. **a)** Reflected light image of lollingite included in arsenopyrite that is in contact with pyrite. **b)** Detail of a). **c)** Backscattered electrons image of a) with overlap of the L.A.-I.C.P.-M.S. spots locations present in table 26.

Table 26 – Data from the laser ablation spots present in figure 92 c).

	Arsenopyrite		Lollingite
	Inner (close)	Outer (far)	
As (% wt.)	48.27		72.85
Fe (% wt.)	34.36		27.15
Au (ppm)	188.21	0.14	3.23
Ag (ppm)	69.93	0.17	6.30
Bi (ppm)	7948.79	6.26	16113.54
Te (ppm)	25.81	0.48	4.51
Co (ppm)	2272.60	736.85	1968.91
Ni (ppm)	1634.44	69.20	2361.84
In (ppm)	0.35	0.32	0.60
Pb (ppm)	2.82	0.07	0.95
Sb (ppm)	65.77	49.94	59.26

### 7.2.1.2. Pyrite

Now focusing only in pyrite, there is a small distinction in its As contents (fig. 94). Pyrite that was included in pyrrhotite and close to the center of the spheroid nucleus presented the lowest As content. The highest As content was identified in the border zone of the spheroid in a pyrite-pyrrhotite decay texture.

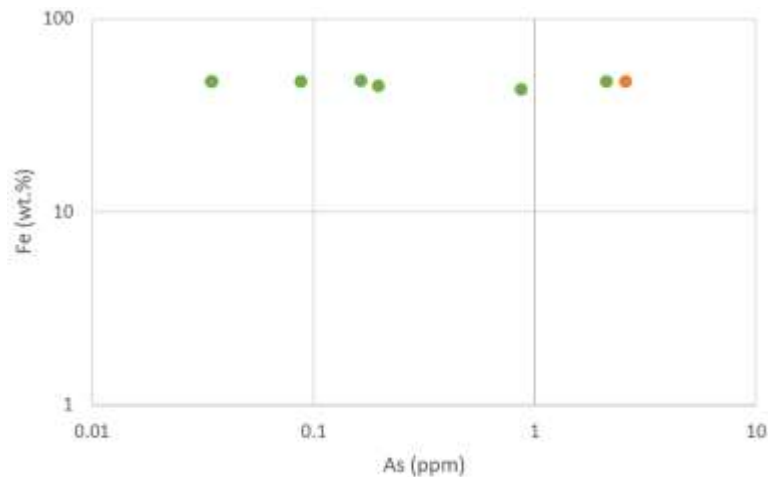


Figure 94 – Binary plot of Fe and As content in pyrite from samples CW05n and CWW-3A. Consult figure 81 for symbology meaning.

Furthermore, the textural transformation and coupled dissolution/precipitation in pyrite is documented using Ag vs. Ni plots with associated defined fields (*i.e.*, diagenetic *versus* metamorphic) (fig. 95). Given the existence of the event-specific element associations, several plots specifically designed address and potentially constrain the nature of the mineralizing fluid, the stages (*i.e.*, number of events) involved in the mineralizing processes, and the origin of elements (*i.e.*, orogenic versus diagenetic) (Gourcerol *et al.*, 2018a). Large *et al.* (2009) *in* Gourcerol *et al.* (2018a) studied four sediment-hosted gold deposits (Sukhoi Log, Bendigo, Spanish Mountain and North Carlin Trend) and reported L.A.-I.C.P.-M.S. data from early diagenetic pyrite and their corresponding recrystallized metamorphic/hydrothermal pyrite within orogenic and Carlin-type settings. For instance, Sukhoi Log (Large *et al.* (2007) *in* Gourcerol *et al.* (2018a)), where it was shown that paragenetically early, framboid-textured pyrite is metal-rich (including Au) and the later recrystallized equant pyrite is metal depleted. This observation provided the basis for their model transformation of this early pyrite to the later pyrite liberates Au which forms concentrations in orogenic style deposits (Large *et al.* (2009) *in* Gourcerol *et al.* (2018a)). Using the analytical data, authors defined empirically based discrimination fields based on the observation of data for different textural varieties of pyrite (early framboidal versus later metamorphic) from these deposit settings are distributed differently in a binary Ag versus Ni plot (fig. 95). Although this diagram is empirically based, it is nevertheless used to establish several inferences:

- (1) Distinguish the origin of various pyrites (primary versus recrystallized pyrite);

- (2) Determine potential element sources and associations within these sulfides;
- (3) Assess the geochemical nature of the gold event(s).

Hence, overlapping the pyrite data collected with the Gourcerol *et al.* (2018) work a binary plot of Ag versus Ni (ppm) for pyrite from four different sediment-hosted gold deposits (using data presented in Large *et al.* (2009) on Sukhoi Log, Bendigo, Spanish Mountain, and the North Carlin Trend), it is possible to conclude that by this method these pyrites are present only in the field of *Metamorphic/Hydrothermal Pyrite* (fig. 95).

Large *et al.* (2019) in Gourcerol *et al.* (2018a) studied the contents of trace elements in pyrites of different origins and

used the changes in their Ni–Au contents to discriminate between pyrites formed by diagenesis and/or hydrothermal processes. In the Ni vs. Au discrimination diagram (fig. 96 a)), the samples with pyrite measurements (CW05n and CWW-3A) fall within or close to the field of hydrothermal pyrite. The same happen in the Zn vs. Pb discrimination diagram (fig. 96 b)), where majority of the samples fall within and near the field of hydrothermal pyrite. However, as written before, the majority of Au measurements are below detection limit and Zn data content in pyrite and pyrrhotite is not close to any calibration standard, therefore these elements must not be taken as reliable indicators.

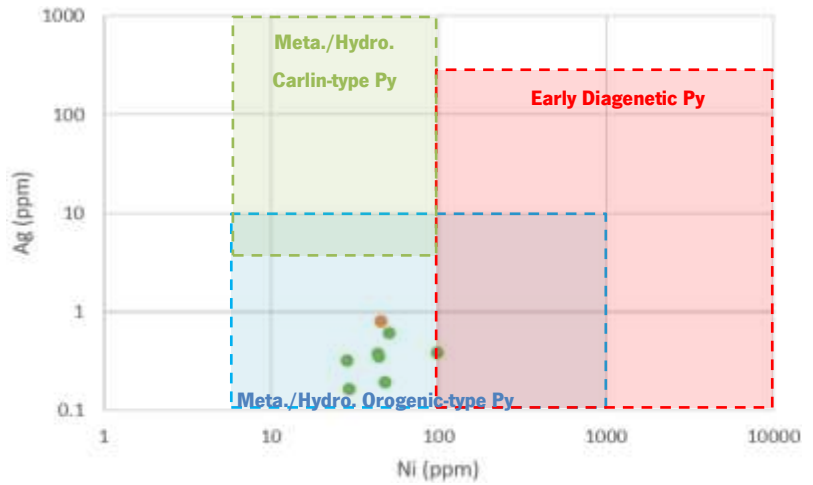


Figure 95 – Binary plot of Ag versus Ni (ppm) for pyrite from four different sediment-hosted gold deposits using data presented in Large *et al.* (2009) on Sukhoi Log, Bendigo, Spanish Mountain, and the North Carlin Trend. The distribution of the trace elements in these pyrites provides the basis for distinguishing early diagenetic (red field), versus metamorphic/ hydrothermal orogenic (blue field) and Carlin-type (green filed) pyrite via decoupling/precipitation processes. The green circles are from CW05n pyrite and the orange spot is from CWW-3A. Consult figure 81 for symbology meaning.

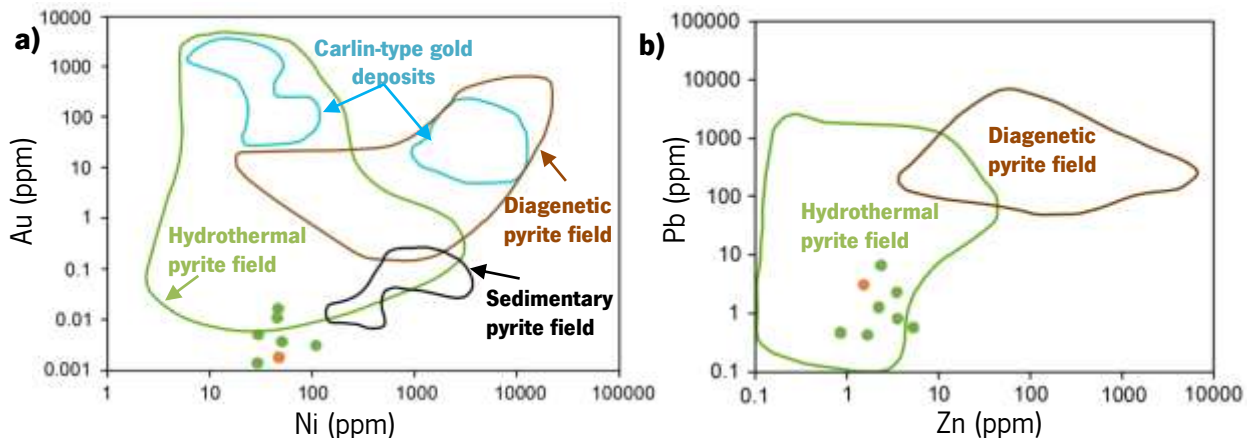


Figure 96 – Genesis determination of pyrite and pyrrhotite. **a)** Ni vs. Au diagram **b)** Zn vs. Pb diagram. Data of sedimentary pyrite are from Gregory *et al.* (2015) in Liu *et al.* (2018). (Modified after Liu *et al.*, 2018.). Consult figure 81 for symbology meaning.

### 7.2.1.3. Pyrite and Pyrrhotite

Although Ni does not discriminate the samples, pyrite and pyrrhotite Co content allow to discriminate the samples, whether they are pyrite or pyrrhotites (fig. 97).

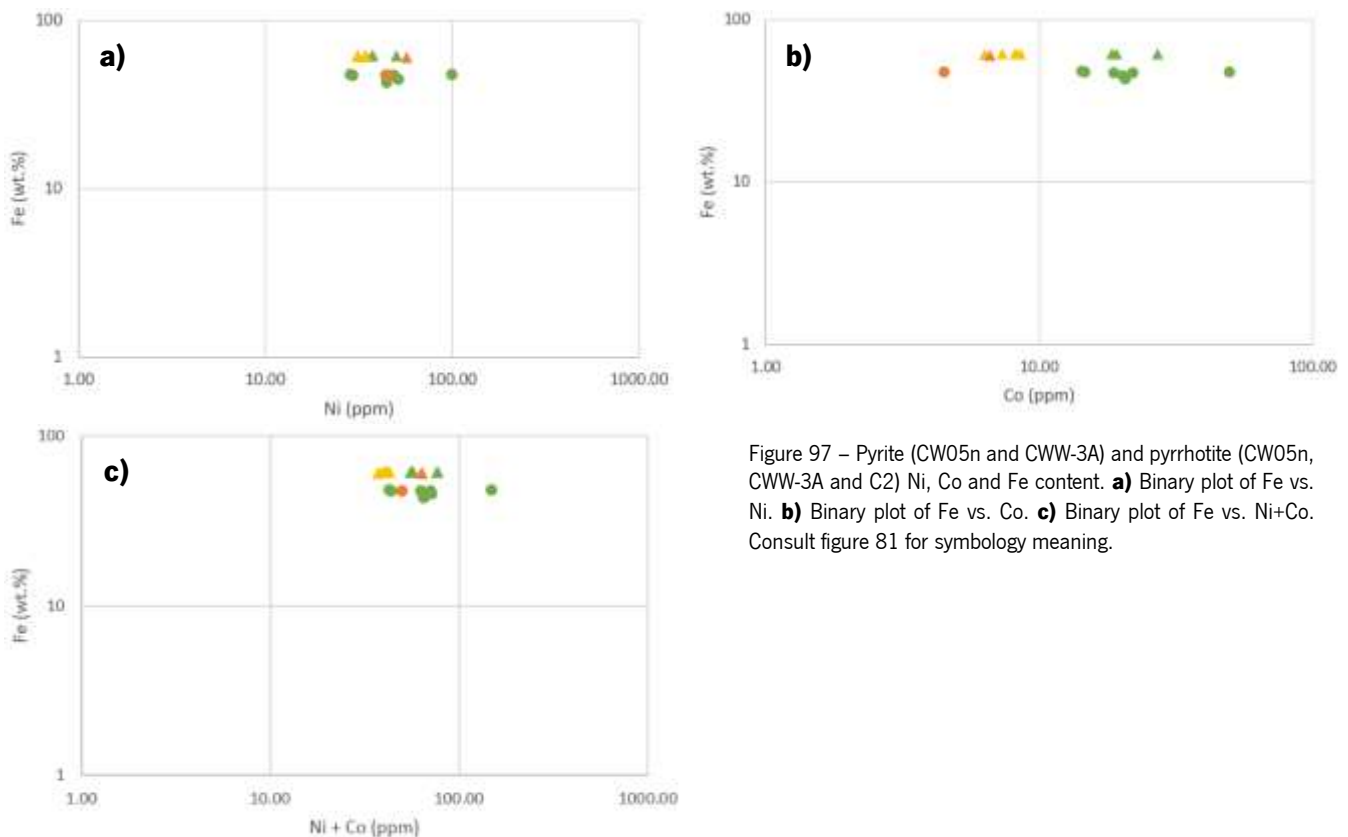


Figure 97 – Pyrite (CW05n and CWW-3A) and pyrrhotite (CW05n, CWW-3A and C2) Ni, Co and Fe content. **a)** Binary plot of Fe vs. Ni. **b)** Binary plot of Fe vs. Co. **c)** Binary plot of Fe vs. Ni+Co. Consult figure 81 for symbology meaning.

In the Co vs. Ni discrimination diagram (fig. 98), the pyrite and pyrrhotite of CW05n (*spheroid – apical sulfide domain with mound structure*) mainly fall within the field of *sedimentary field (V)* – which was expected once it is a nodule – but very close to *deposit related to magmatic-hydrothermal solution (I)* frontier. While C2 (*sulfide arcs periphery – distal relatively to apical mounds domain*) pyrrhotite mainly fall within the *sedimentary field (V)*, and CWW-3A (*attributed to sulfide-calcsilicate rock interface in the proximal tubform structural domain*) fall in the border of *sedimentary field (V) - sedimentary-reformed field (VI)*.

There is not a clear distinction between pyrite and pyrrhotite minerals from the same samples.

The Ni and Co trace element concentrations indicate that the ore-forming materials are principally originated from the *sedimentary field (V)*. However, Au vs. Ni and Pb vs. Zn contrast with the *hydrothermal pyrite field* (fig. 96). Although sedimentary-hydrothermal contrast is not very enhance in Ni vs. Co plot, they might be related to the mixing of crustal materials regarding Liu *et al.* (2018) (due to the comparison of previous diagrams).

The Dongguashan copper (gold) deposit, a stratabound *skarn*-type ore deposit associated with magma intrusion activity (during the Yanshanian Period) presented majority data of the latter one fell in

magmatic–hydrothermal genesis (III and IV), where the ore-forming conditions were medium–high temperature, high sulfur fugacity and medium-shallow depth (Liu *et al.*, 2018). Comparing these data with Cerdeirinha, these data suggest that pyrite and pyrrhotite were not strictly correlated with a magmatic genesis, but instead with *sedimentary field (V)*.

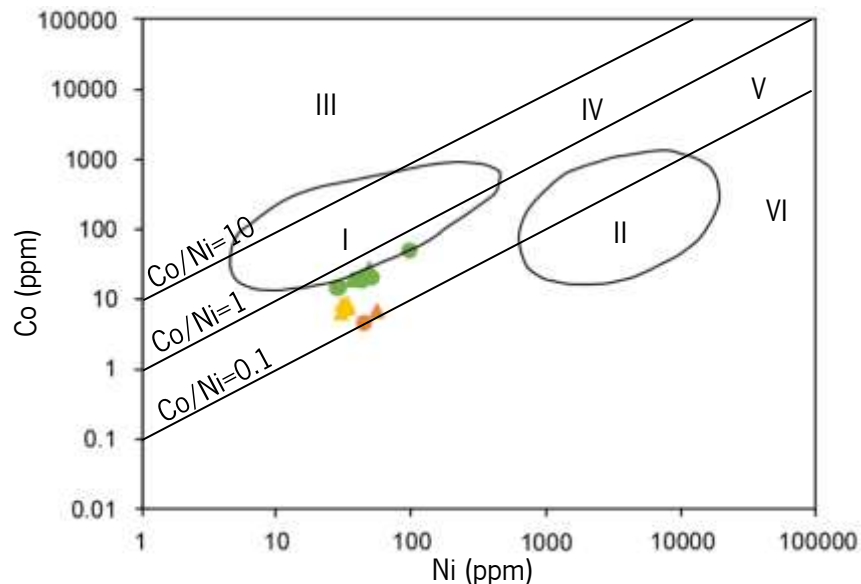


Figure 98 – Ni vs. Co diagrams for pyrite and pyrrhotite from massive and lamellar ores of the Dongguashan copper (gold) deposit (Chen (1995) and Bajwah *et al.* (1987) in Liu *et al.* (2018)). I: deposit related to magmatic–hydrothermal solutions; II: Cu–Ni sulfide deposit; III, IV: magmatic and hydrothermal fields; V, VI: sedimentary and sedimentary-reformed field. Consult figure 81 for symbology meaning.

#### 7.2.1.4. All sulfidic phases

Quantitative L.A.-I.C.P.-M.S. element distribution analysis represents a relatively new and powerful approach to assess gold mineralizing processes (Gourcerol *et al.*, 2018a). The nature of the mineralizing fluid is investigated by studying Ni and Co variations in the sulfide grains in environments ranging from ultramafic to felsic, whereas upgrading of gold tenor within an ore deposit is identified using Au vs. Ag plots (fig. 84) grouped by element association and elemental geochemical affinity.

Compilation of the trace-element data for several rock types (felsic to ultramafic) from the Superior Province (Canada) (Gourcerol *et al.*, 2018a) was used to construct the following series of diagrams: Co/Ni vs. Ni, Co vs. Co/Ni; and Ni vs. Co (fig. 99). These plots allow to constrain the nature of the mineralizing fluids and to detect *fluid:rock* interaction along the fluid pathway.

The application and use of the Co and Ni data is illustrated in figure 99 using data from several pyrite (n = 8), pyrrhotite (n = 9) and arsenopyrite (n = 13) samples from the Cerdeirinha. Importantly, these data can not be compared directly to each other, as they are for different sulfide phases. Once there was no accordance regarding a possible genesis for CW05n (*spheroid – apical sulfide domain with*

*mound structure*) pyrites (fig. 95 and 96 with fig. 98), these were also plotted in this diagram (fig. 99). However, these samples suggest that the fluids responsible for pyrite and pyrrhotite deposition at Cerdeirinha were likely derived from or interacted with intermediate (close to felsic) rocks/melt having intrinsically variable contents of Ni and Co (fig. 99).

Besides, some arsenopyrites content suggest to be related with ultramafic setting (figs. 99 a) and c)). This contrasting expression seem to fit with the bimodal volcanism setting presented by Dias (2011) (?) (fig. 21).

This interpretation is, of course, based on the assumption that factors controlling element partitioning between fluid and sulfide remain constant. Caution should be taken, once the number of average measurements plotted is low.

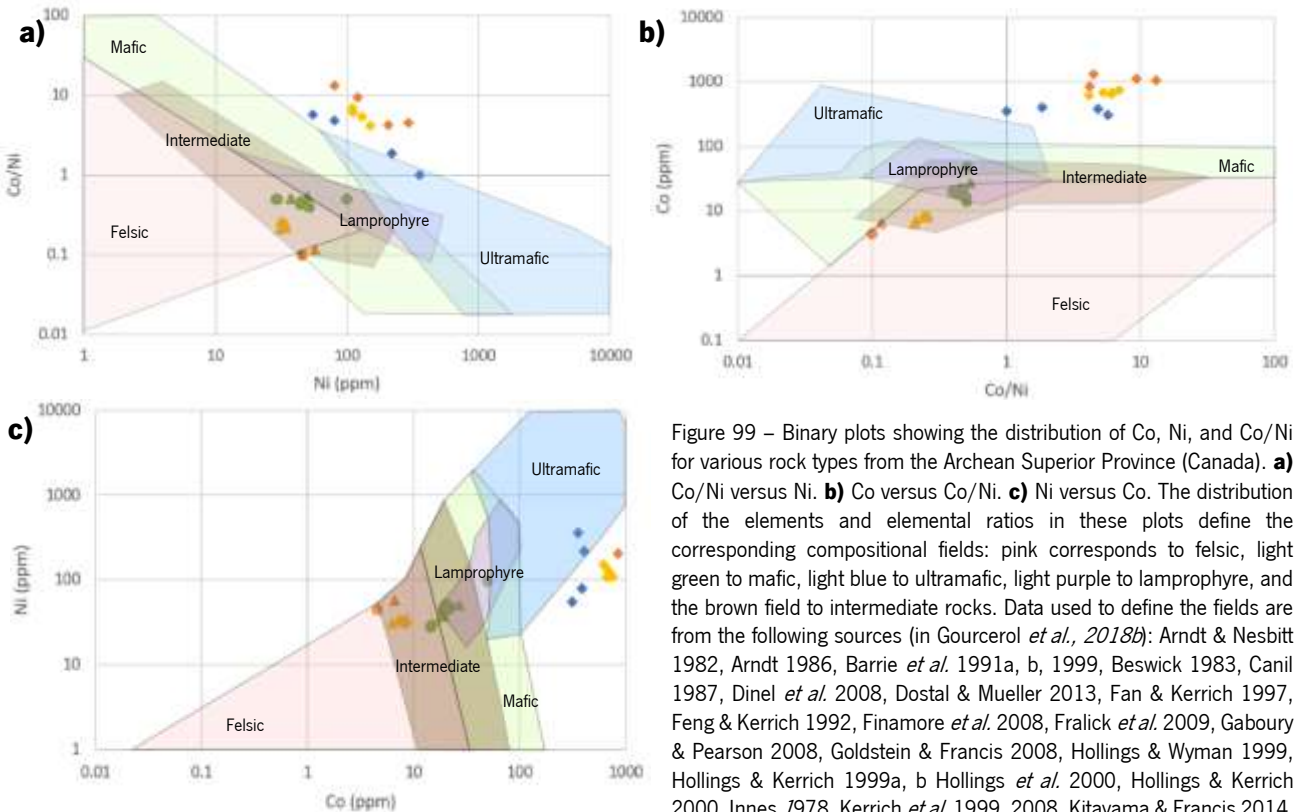


Figure 99 – Binary plots showing the distribution of Co, Ni, and Co/Ni for various rock types from the Archean Superior Province (Canada). **a)** Co/Ni versus Ni. **b)** Co versus Co/Ni. **c)** Ni versus Co. The distribution of the elements and elemental ratios in these plots define the corresponding compositional fields: pink corresponds to felsic, light green to mafic, light blue to ultramafic, light purple to lamprophyre, and the brown field to intermediate rocks. Data used to define the fields are from the following sources (in Gourcerol *et al.*, 2018b): Arndt & Nesbitt 1982, Arndt 1986, Barrie *et al.* 1991a, b, 1999, Beswick 1983, Canil 1987, Dinel *et al.* 2008, Dostal & Mueller 2013, Fan & Kerrich 1997, Feng & Kerrich 1992, Finamore *et al.* 2008, Fralick *et al.* 2009, Gaboury & Pearson 2008, Goldstein & Francis 2008, Hollings & Wyman 1999, Hollings & Kerrich 1999a, b, Hollings *et al.* 2000, Hollings & Kerrich 2000, Innes 1978, Kerrich *et al.* 1999, 2008, Kitayama & Francis 2014, La Fleche *et al.* 1992, La Fleche & Dupuy 1992, Lafrance *et al.* 2000, Lahaye *et al.* 1995, Lahaye & Arndt 1996, Maurice *et al.* 2003, 2009, Mercilangevin *et al.* 2007, Nesbitt *et al.* 2009, Parks *et al.* 2014, Picard & Piboule 1986, Piercey *et al.* 2008, Polat *et al.* 1999, 2012, Polat & Kerrich 2000, Polat & Münker 2004, Polat 2009, Rinne & Hollings 2013, Sproule *et al.* 2002, Stone *et al.* 1993, 1995, 1996, Stone & Stone 2000, Thurston & Fryer 1983, Ujike & Goodwin 1987, Ujike *et al.* 2007, Wyman & Kerrich 1993, Wyman & Kerrich 1993, 2009, Wyman & Hollings 1998, Wyman 1999, Wyman *et al.* 2000, 2002. Consult figure 81 for symbology meaning.

Regarding the figure 100, a trend was verified in a Ni+Co (ppm) vs As + Fe (ppm), where it is possible to distinguish pyrites from pyrrhotites by As + Fe content. And, these two from the arsenopyrites, due to Ni + Co, besides As + Fe content.

In figure 101, sulfides present similar content in Bi, so its discrimination is done by the content of Au+Ag.

In the three sulfides (arsenopyrite, pyrite and pyrrhotite), Au and Bi were mostly connected to arsenopyrite, but Ag was not (fig. 102).

Considering that the detection limit of L.A.-I.C.P.-M.S. is 0.01 ppm, one should notice that in the case of Au the majority of the measurements are below that, so the values can be just a *background noise*. Therefore, it is just

possible to say that arsenopyrite seems to contain slightly higher Au content than the two other sulfide phases. This agrees with what was present in figure 101, because several sulfides seem to be depleted in Au and Ag. Otherwise, auriferous arsenopyrites were found, but all from shear-zoning (latter enrichment) containing 0.04 wt. % (Leal Gomes *et al.* (2011 and 2015) and 338 ppm and <180 ppm (Araújo & Leal Gomes, 2014). Besides this, gold content in Covas, Serro and Cumieira - Picoto do Carvalho was identified, notice that Dias & Leal Gomes (2015) found around 600 ppm Au in arsenopyrite from Covas (Valdarcas) (fig. 17). In Cerdeirinha, they identified a pyrite with about 200 ppm and pyrrhotite close to 800 ppm of Au content.

The Ag content should have been latter added, being of low temperature (83 a)), and therefore related with hydrothermal process. Ag presents in pyrite has a similar behaviour to the Ag present in pyrrhotite, however this behavior is distinct of the arsenopyrite (fig. 102 b)).

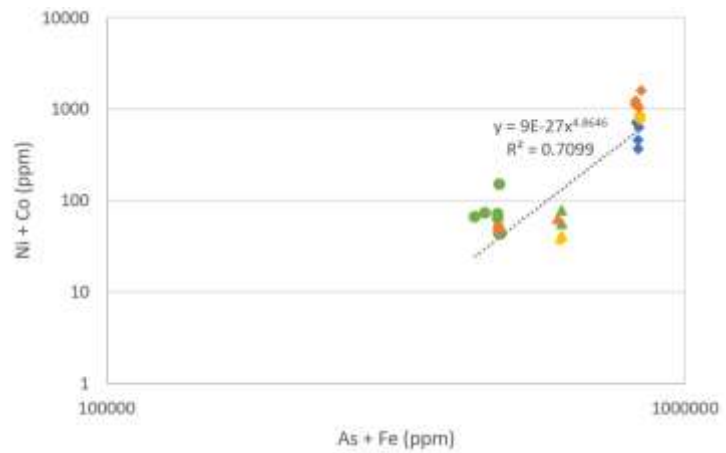


Figure 100 – Binary plot of Ni +Co and As + Fe. Pyrite (CW05n and CWW-3A) and pyrrhotite (CW05n, CWW-3A and C2) and arsenopyrite (CWW-3A, C2, and CW05) Ni, Co and Fe content. Consult figure 81 for symbology meaning.

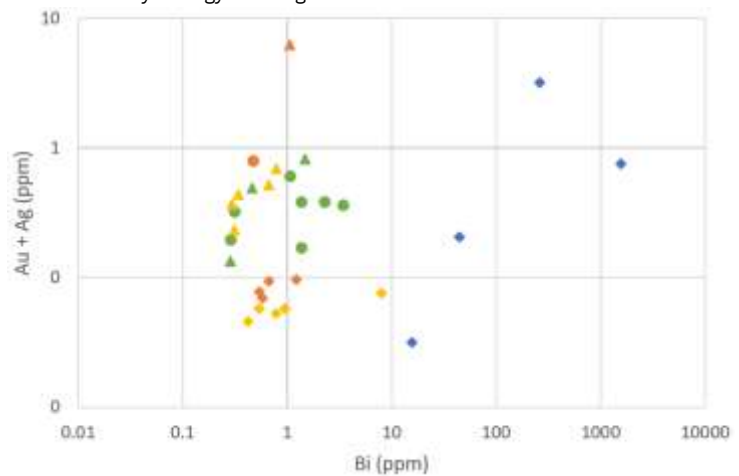


Figure 101 – Binary plot of Au + Ag and Bi. Pyrite (CW05n and CWW-3A) and pyrrhotite (CW05n, CWW-3A and C2) and arsenopyrite (CWW-3A, C2, and CW05) Au, Ag and Bi content. Consult figure 81 for symbology meaning.

In the case of Bi, there are higher values in arsenopyrite net than the ones verified in pyrite and pyrrhotite. In the arsenopyrite data present in figure 102 d), one Bi measurement (1543.57 ppm) was removed, once it would bias the results.

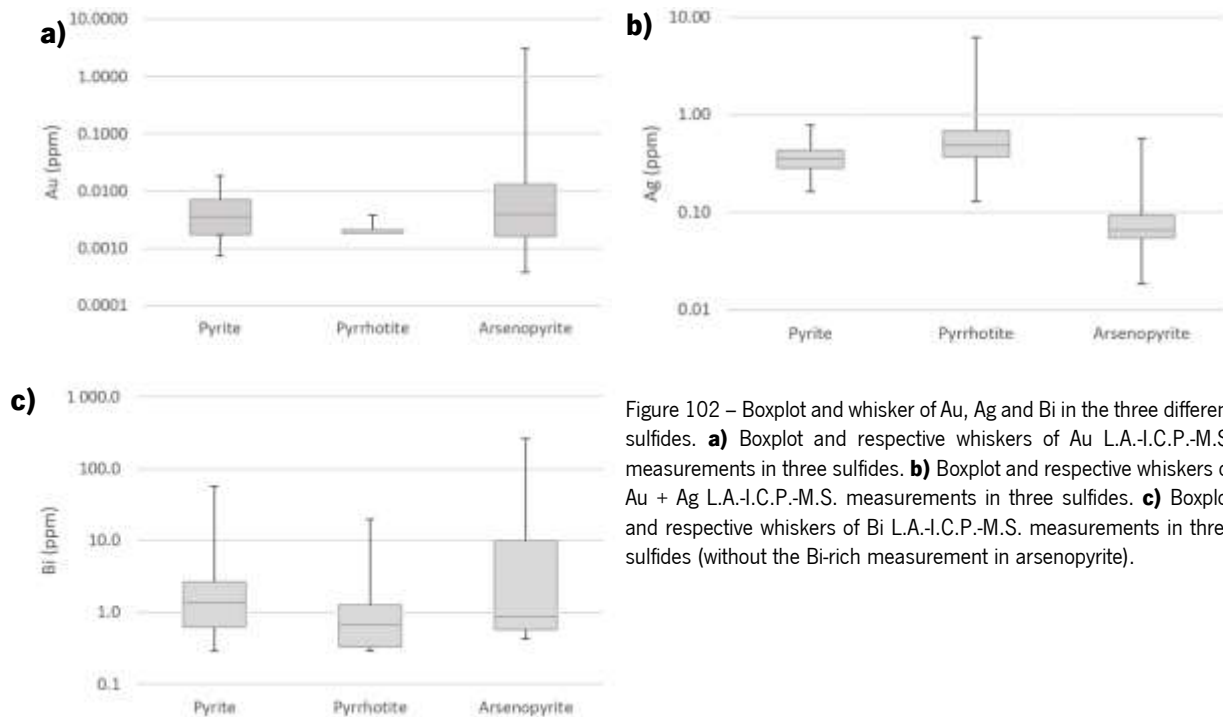


Figure 102 – Boxplot and whisker of Au, Ag and Bi in the three different sulfides. **a)** Boxplot and respective whiskers of Au L.A.-I.C.P.-M.S. measurements in three sulfides. **b)** Boxplot and respective whiskers of Au + Ag L.A.-I.C.P.-M.S. measurements in three sulfides. **c)** Boxplot and respective whiskers of Bi L.A.-I.C.P.-M.S. measurements in three sulfides (without the Bi-rich measurement in arsenopyrite).

#### 7.2.1.5. Summary

Bi, Au, Ag, Te, Pb, In, Ni and Mo are related among themselves. However, they are not related with arsenopyrites (nor Fe, S, As in arsenopyrite) (fig. 91), except Ni. Therefore, they can possibly be related with hosting of native phases to low temperature in arsenopyrite fractures (fig. 83).

On one hand, most of the graphics confirmed the hydrothermal hypothesis *with Metamorphic/Hydrothermal Pyrite* (fig. 95) and *Hydrothermal pyrite field* (fig. 96). This agrees with the SEDEX hypothesis, however it can also be related with the *skarn* formation, once it is also a hydrothermal deposit. On the other hand, pyrite and pyrrhotite phases were not strictly correlated with a magmatic genesis, but instead with *sedimentary and sedimentary-reformed field (V/VI)* (fig. 98), which may also support the primordial SEDEX setting, that latter suffered metamorphism and *skarn* installation. Sedimentary-hydrothermal contrast is not very enhance in Ni vs. Co plot, therefore they might be related with the mixing of crustal materials (fig. 99) regarding Liu *et al.* (2018), (due to the comparison of previous diagrams).

These samples suggest that the fluids responsible for pyrite and pyrrhotite deposition at Cerdeirinha were likely derived from or interacted with intermediate (close to felsic) rocks/melt having intrinsically variable contents of Ni and Co. However, some arsenopyrites contents suggest to be related with ultramafic setting (fig. 99 a) and c)). This contrasting expression seem to fit with the bimodal



volcanism setting presented by Dias (2011) (?) (fig. 21). However, it can be co-related with the different metal content that each sulphide mineral can afford in its net.

For last but not least, the *mixed phases*, that were similar to *mineral clusters*, presented greater concentration of metallic trace-elements than the previous individualized sulfide minerals. Might this suggest that these are latter (remobilized?) phases, richer in trace metals identified than the ones verified in the others sulfide phases.

#### 7.2.2. REE fractionation

The petrographic and mineralogical study of the facies patent in some anomalous levels of the Silurian lithostratigraphy from Cerdeirinha provided knowledge of some petrogenetic trends. For some of Cerdeirinha facies, specific minerals were REE analysed, in order to seek primary evolutionary trends and other related to metasomatism, with a view to deducing a protolithic nature.

Although several minerals were analysed regarding their REE content (table 27), three minerals group allowed to establish diverse generations:

- Scheelite: with high REE content and Eu negative anomaly *vs.* with low REE and with low Eu negative anomaly.
- Apatite: with high REE content and with strong Eu anomaly *vs.* with REE low content.
- Vesuvianite: with high REE content and Eu anomaly *vs.* with low Eu anomaly.

Table 27 – Mineral groups with or without REE.

<b>Minerals</b>	<b>Without REE</b>	<b>With REE</b>
Scheelite	<b>CEE-S</b>	<b>C2</b> and <b>CW05</b>
Apatite		<b>C2</b> , <b>CEE-S</b> and <b>CW05.n</b>
Pyroxene (diopside & hedenbergite)	<b>CEE-S</b>	
Wollastonite	<b>CEE-S</b>	
Ferberite		<b>C2</b>
Wolframite		<b>C2</b>
Vesuvianite		<b>CEE-S</b>

Once attention was not drawn towards apatite and scheelite during the microprobe measurements, these data is only speculative, although scheelite and apatite elements contents allow to compare with possible magmatic source or high grade metamorphism. However, it allows to compare the same mineral elements contents and, hence establish the same mineral generations (fig. 103).

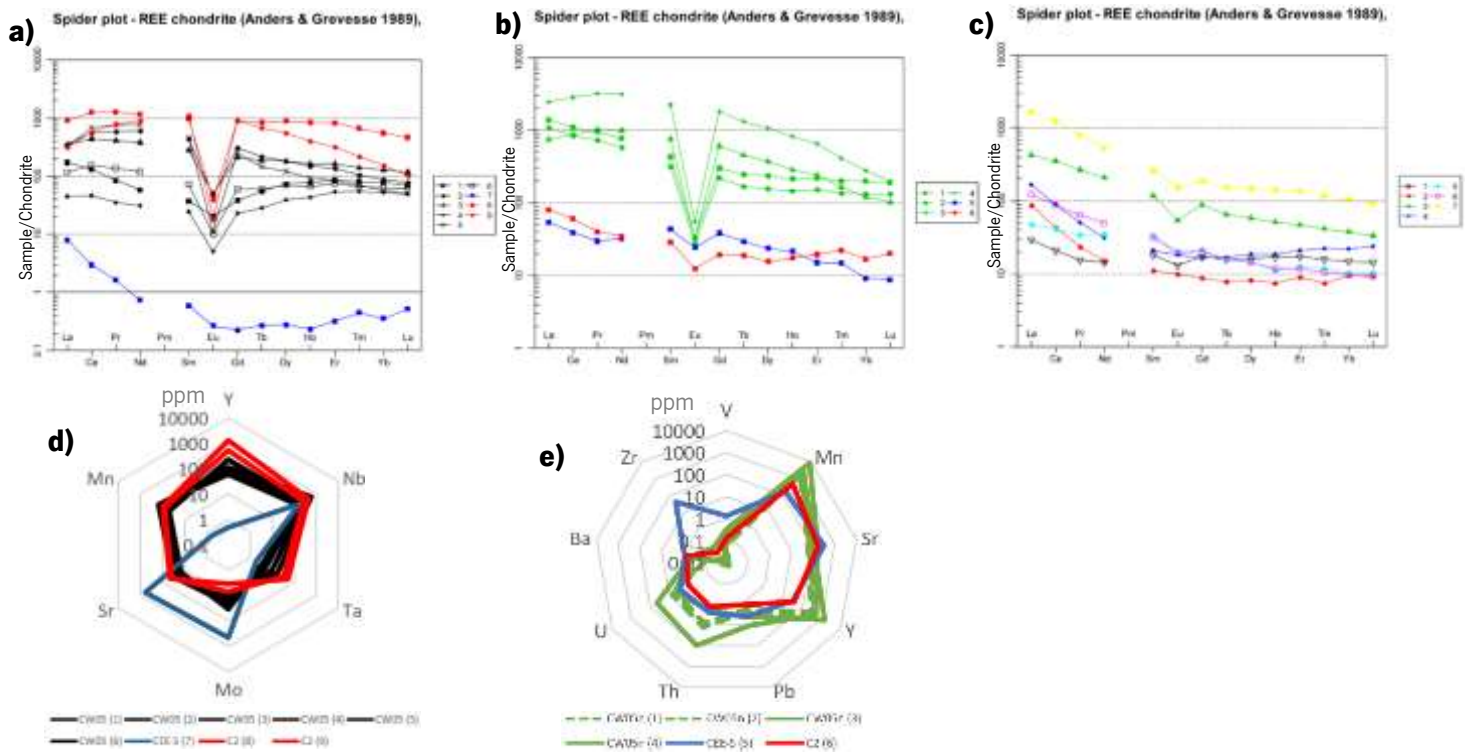


Figure 103 – L.A.-I.C.P.-M.S. scheelite and apatite data treatment. The data is in ppm. **a)** REE-scheelite spider plot. **b)** REE-apatite spider plot. **c)** REE-vesuvianite spider plot. **d)** Discernible elements of scheelite in a radar plot. **e)** Discernible elements of apatite in a radar plot.

### 7.2.2.1. Scheelite

Variations of Eu anomalies and trace element compositions in scheelite can be used to decipher the origin and processes of tungsten mineralization. Regarding scheelite, two mineral generations are easily identified: with high and low REE content (fig. 103 a)). Early scheelite (C2) display significantly negative Eu anomalies and have high REE, Nb and Ta contents, suggesting that the initial ore-forming fluids were of magmatic origin (Zhang *et al.*, 2018). Petrographically, in C2 sample, two scheelite crystals were analysed by L.A.-I.C.P.-M.S., one was automorphic, contained wolframite included and the crystal was included in biotite matrix, while the other was a smaller crystal without any inclusion and it was surrounded by pyrrhotite. However, regarding the plots (figs. 103 a) and d)), that can be considered as the earliest generation observed. Deposition of the early tungsten minerals would lower REE, Nb and Ta in the mineralizing fluids, leading to depletion of these elements in the late ones (Zhang *et al.*, 2018). This generation would be followed by the CW05 scheelite sample. Under microscope, these scheelites were not euhedric crystals, but they were intergrown with quartz, pyrite and arsenopyrite, which suggest a strong latter hydrothermal remobilization.

Notice that in the scheelites from C2, followed by CW05 and finally CEE-S generation order are supported by the registered increase in Mo content (Mo enrichment tend to be accompanied by increasing of  $fO_2$  (Hsu, 1977)) and a decrease in Y and Ta.

In contrast, regarding the latter scheelite, LREE/HREE ratios (C2: 3.6 – 4.8, CW05: 2.0 – 15.5, and CEE-S: 19.2 ppm) and REE total (C2: 1508.0 – 2478.3, CW05: 96.3 – 1078.5, and CEE-S: 4.5 ppm), Eu/Eu\* (C2: 0.02 – 0.04, CW05: 0.03 – 0.55, and CEE-S: 0.73 ppm), Sr (C2: 38.0 – 45.6, CW05: 14.5 – 33.6, and CEE-S: 593.6 ppm) abundances can be explained not by the decomposition of plagioclase and K-feldspar, but because it was included in a calc-silicate rock, where the referred minerals are absent and therefore they do not take in Sr (Zhang *et al.*, 2018). Notice that the normalized Eu anomaly (Eu/Eu\*) for scheelite, apatite, and vesuvianite was calculated by the following equation:  $Eu/Eu^* = \frac{Eu_{CN}}{(Sm_{CN} \times Gd_{CN})^{\frac{1}{2}}}$  (Tobia & Shangola (2016) and Mazumder (2017)), where the subscript *CN* denotes chondrite normalized values (Taylor and McLennan, 1985).

#### 7.2.2.2. Apatite

In what apatite minerals concerned, 2 apatites generations were clearly seen: with high and low REE content. However, in the CW05n apatites spider plot seem to exist 2 sub generations, once 2 apatites measurements intersect with the others 2. No petrographical difference was noticed. Regarding figure 103 e) CW05n apatites are enriched in Mn, Y, Pb, Th and U content, compared with the other samples. The crystallization of these elements would impoverish the fluid in this content and that would be reflected in the others apatite generations, as it is verified. Still in the same figure (fig. 103 e)), C2 apatite suggest to be an intermediate generation between CW05n and CEE-S. Besides the impoverishment, also Sr, Ba, Zr and V enrichment can be seen from CW05n, followed by C2 and then CEE-S. Therefore, 3 apatites generations seem to be observed (figs. 103 b) and d)).

Comparing the same parameters as presented in scheelite: LREE/HREE ratios (CEE-S: 5.5 ppm, C2: 6.7, and CW05n: 7.9 – 11.3) and REE total (CW05n: 1277.4 – 5155.2, C2: 95.3, and CEE-S: 81.3 ppm) Eu/Eu\* (CW05n: 0.03 – 0.10, C2: 0.53, and CEE-S: 0.60 ppm), Sr (CW05n: 60.0 – 168.4, C2: 171.0, and CEE-S: 328.3 ppm) abundances. Overall, these comparisons, CW05n apatites suggest that this sector was formed first, then C2, and latter CEE-S. This is supported by the REE scheelite content that suggests that C2 is the earliest one, followed by CW05 and for last CEE-S. However, C2 and CEE-S contained scheelite, and this mineral can incorporate REE, leaving less REE for apatites. Moreover, CEE-S also contained vesuvianite that also takes in REE. In general, the amplitude of Eu anomalies in apatites increases towards more fractionated rocks and probably is controlled by the crystallisation of feldspars, which concentrate  $Eu^{2+}$  from the melt (Budzinski and Tischendorf (1989) *in* Belousova *et al.*, 2002). This

supports what was written before, once Eu anomaly increase, REE total decrease and Sr abundance increase, the crystallization order verified was CW05n, C2 and CEE-S.

Some authors such as Parak (1975) in Mokhtari *et al.* (2014) considered apatites of Kiruna-type iron ores to be sedimentary. However, the REE content and patterns show that the apatites of Kiruna-type ores are different from sedimentary apatites. The content of REE in the apatites of Kiruna iron ores is about 2000–7000 ppm (Frietsch & Perdahl (1995) in Mokhtari *et al.* (2014)) Here, REE<sub>total</sub> content in CW05n sample ranges between ≈1277 and 5155 ppm, while C2 (95ppm) and CEE-S (81 ppm)). Ce deficiency, characterizing marine apatites is not seen in igneous apatites (Laajoki (1975); Altschuler (1980) in Mokhtari *et al.* (2014)). Therefore, apatites in this study are mainly possible igneous.

The Zr content present in CEE-S apatite, might be explained due to whole rock being a calc-silicate rock, and without biotite nor zircon that could undertake the Zr content (as seen in C2 – fig. 104). Still in CEE-S, also vesuvianites contained a higher Eu anomaly than scheelite and apatite (CEE-S: 0.40 – 1.09 ppm) and Sr (44.4 – 137.4) (fig. 103 c)). Its V and Cr content ranges

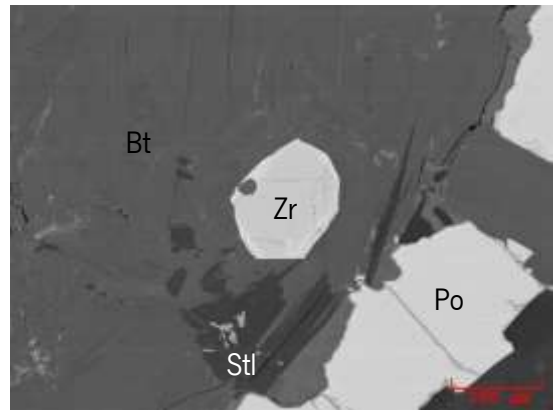


Figure 104 – Zircon in biotitic matrix, found in C2 sample. It did not contain chemical difference in the border, even though they are brighter.

between 72.0 to 206.5 ppm and 0.7 to 636.4 ppm, respectively. While, in diopside V content goes from 8.0 to 63.1 ppm and Cr from 13.9 to 240.7 ppm, and in hedenbergite was 6.0 to 13.3 ppm of V and 7.5 to 35.7 ppm of Cr. Wollastonite was the most depleted (V: 0.0 to 0.2 ppm, and Cr: 0.5 to 2.1 ppm). Therefore the highest V and Cr content were verified in vesuvianite.

Regarding apatites, besides distinguish its possible generations, also a speculative genesis was established, as it can be seen below.

The Sr and Y contents of apatites vary widely and show a strong negative correlation (fig. 105 a)), because Sr concentrations decrease with the degree of magmatic fractionation (from ultramafic rocks to mafic/intermediate rocks to granites and granitic pegmatites), while Y contents increase (Belousova *et al.*, 2002). A clearer distinction is established between apatites from mafic rocks or iron ores, and those from granitoids (fig. 105 b)). Also, their REE total content and the degree of LREE enrichment, from different rock types were individualized (fig. 105 c)). Belousova *et al.* (2002) also decreases from mafic/ultramafic rocks (including carbonatites) through mafic and intermediate rocks to granitoids and to highly fractionated rocks such as granite pegmatites, this trend is not clearly related to total REE

content. The low LREE/HREE of these evolved granitic rocks is partly due to high HREE contents, which are reflected in high Y contents (fig. 105 d)).

Overall, CW05n apatites seem to be highly correlated with a granitoid source considering figure 105.

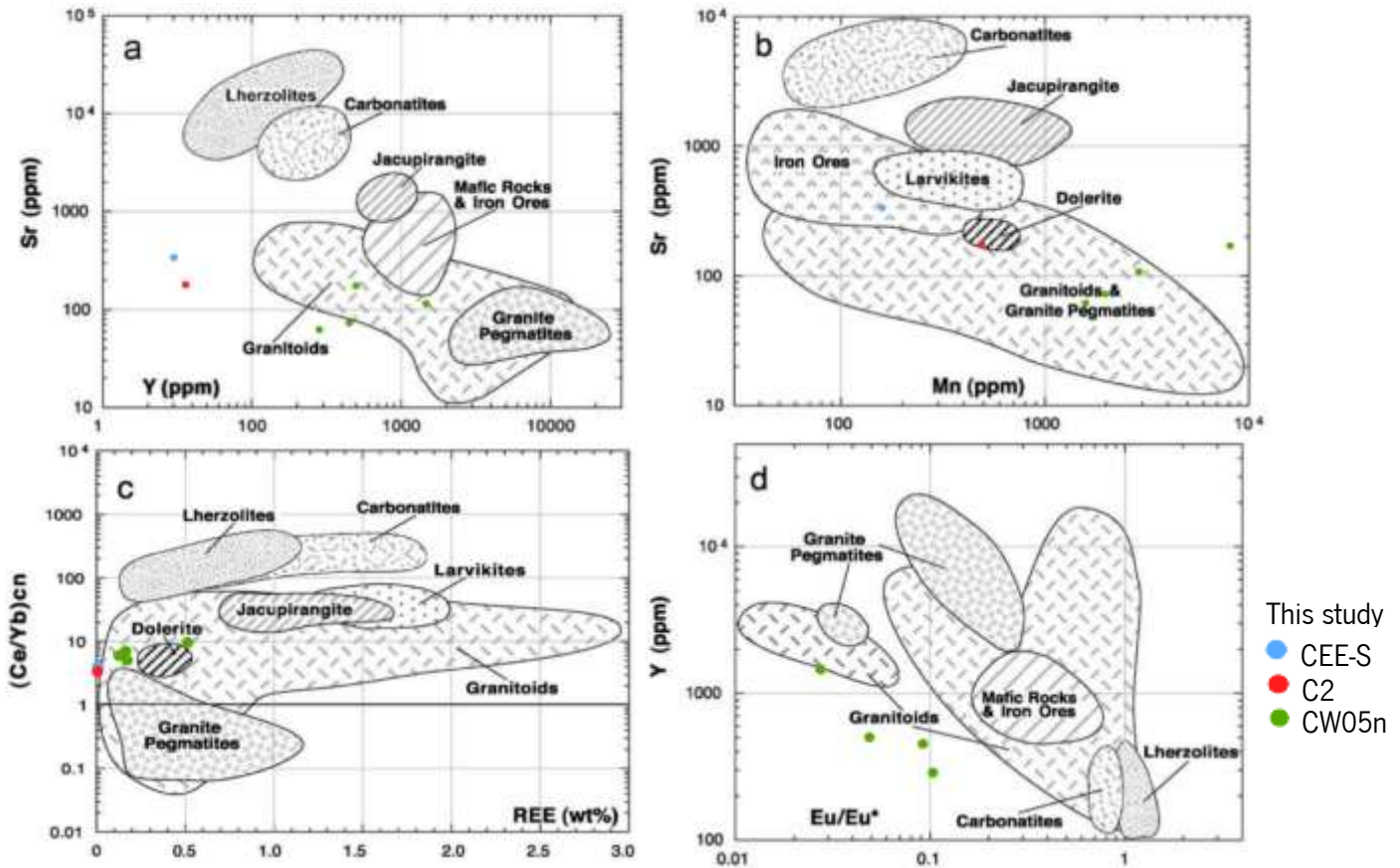


Figure 105 – Fields of apatite composition from different rock types, proposed as discriminant plots. **a)** Binary-plot of Sr vs. Y. **b)** Binary plot of Sr vs. Mn. **c)** Binary plot of  $(Ce/Yb)_{cn}$  vs. REE (wt%). **d)** Binary plot of Y vs.  $Eu/Eu^*$ . (Modified after Belousova *et al.*, 2002).

Discriminant functions DP1-1 vs. DP1-2 (fig. 106) separate most of the apatite data from carbonatites, various mineralized systems, and the unmineralized rocks.

DP1 – 1

$$= -0.06461 \cdot \log Mn - 1.56 \cdot \log Sr + 2.609 \cdot \log Y + 0.3631 \cdot \log La - 1.766 \cdot \log Ce + 0.6243 \cdot \log Eu - 3.642 \cdot \log Dy + 0.7086 \cdot \log Yb - 1.178 \cdot \log Pb + 0.4161 \cdot \log Th + 0.963 \cdot \log U + 6.589$$

DP1 – 2

$$= 0.2073 \cdot \log Mn - 1.035 \cdot \log Sr + 15.1 \cdot \log Y + 4.995 \cdot \log La - 5.804 \cdot \log Ce + 0.1741 \cdot \log Eu - 8.771 \cdot \log Dy - 4.326 \cdot \log Yb + 2.022 \cdot \log Pb - 0.6719 \cdot \log Th + 0.02096 \cdot \log U - 10.45$$

The apatites from MORs can be further discriminated by their relatively high Zr and low Sr contents (fig. 106 b)), coupled with their relatively high Mg and W contents.

Regarding this, all the apatites fit in *ore deposit* setting (fig. 106). However, CEE-S (calc-silicate sample; *proto-travertine* (Dias, 2011)) composition suggest it can be MOR related.

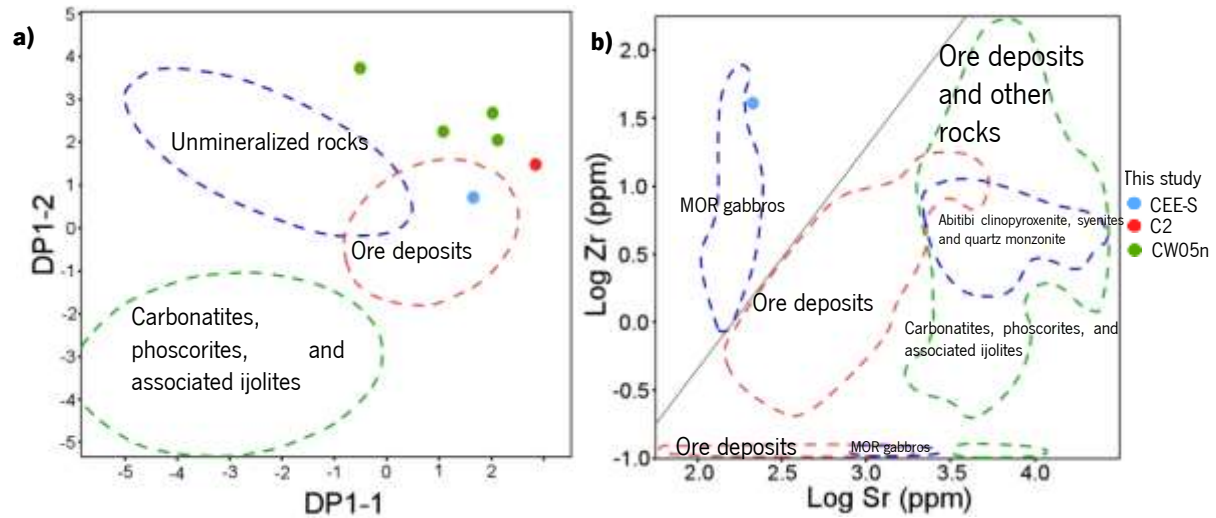


Figure 106 – Discrimination diagrams for apatites from carbonatites, various ore deposits, and rocks that are not associated with mineralization. Also shown are literature data (Belousova *et al.*, 2002; Cao *et al.*, 2012 in Mao *et al.* 2016) that were not used in DPA for construction of the discrimination diagrams. **a)** The first discriminant function (DP1-1) vs. the second discriminant function (DP1-2), showing contours of constant Mahalanobis distance outlining bulk of the data in each group. **b)** Log Sr (ppm) vs. log Zr (ppm) with boundary separating bulk of the data for mid-ocean ridge (MOR) from ore deposits and other rocks based on the lowest Mahalanobis distance. (Modified after Mao *et al.* (2016)).

The following graphics (fig. 107) allow to differentiate the mineralized apatites into the main deposit types: porphyry Cu-Au-Mo, epithermal Au-Ag, IOCG, *skarn*, orogenic Au, and orogenic Ni-Cu ore systems. Six discriminant functions from three different sets of DPA using Mn, Y, Ce, Eu, Dy, Yb, Th, and U ( $\pm$  Mg  $\pm$  Sr  $\pm$  Pb) were found to effectively discriminate these groups. The two axes (DP2-1-1 vs. DP2-1-2) from the DP2 discriminate >90% of apatites from iron oxide-associated deposits (IOCG breccia and Kiruna-type) from the other groups (fig. 107) (Mao *et al.*, 2016).

Three of the samples fall in *Au-Co, Cu, and Pb-Zn skarns*, however 2 of them fall in *Porphyry Cu-Mo-Au and epithermal Au-Ag*. One measurement of CW05n and C2 fall close to *W skarns*. Yet, it is not possible to achieve a concrete conclusion, because for further diagrams of these authors, Mg had to be previously measured.

$$DP2 - 1 - 1$$

$$= -2.275 \cdot \log Mn - 1.429 \cdot \log Sr + 1.504 \cdot \log Y + 3.247 \cdot \log Ce - 1.088 \cdot \log Eu + 0.1925 \cdot \log Dy + 0.7636 \cdot \log Yb - 0.05301 \cdot \log Th - 1.538 \cdot \log U - 3.655$$

$$DP2 - 1 - 2$$

$$= 1.321 \cdot \log Mn + 1.576 \cdot \log Sr + 14.63 \cdot \log Y - 0.005804 \cdot \log Ce + 1.605 \cdot \log Eu - 16.53 \cdot \log Dy + 3.251 \cdot \log Yb - 0.2426 \cdot \log Th - 1.155 \cdot \log U - 20.30$$

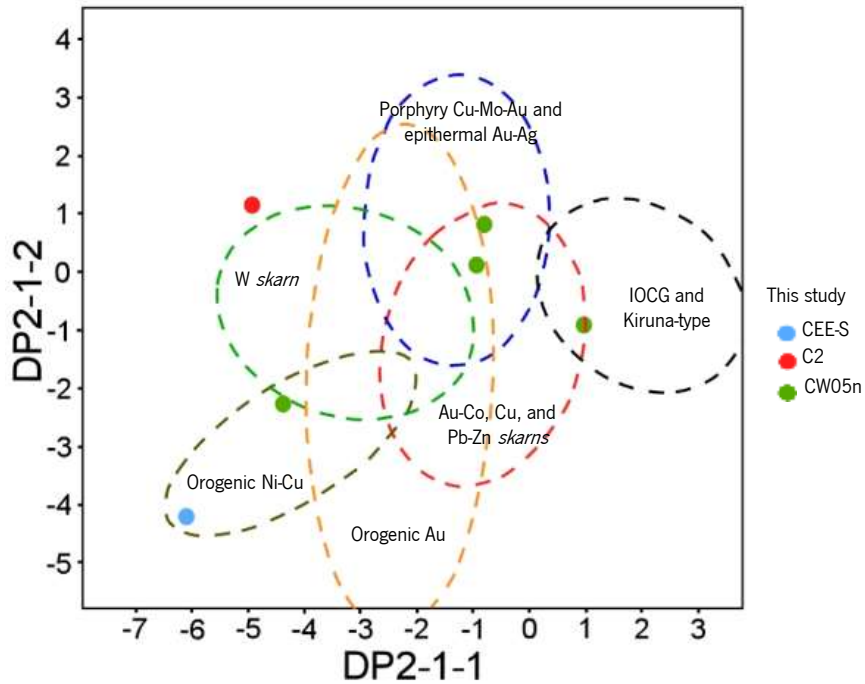


Figure 107 – Discrimination diagrams for apatites from different ore deposits, showing contours of constant Mahalanobis distance outlining bulk of the data in each group. Also shown are literature data (Belousova *et al.*, 2002; Cao *et al.*, 2012 in Mao *et al.*, 2016) that were not used in DPA for construction of the discrimination diagrams. The first discriminant function (DP2-1-1) vs. the second discriminant function (DP2-1-2). (Modified after Mao *et al.*, 2016)

Regarding apatite composition, its data was plotted below in order to attempt to better define its genesis. However, there results were not clear. Besides, in some cases all apatites measurements fitted the graphic, in other case they did not. The large variations in the size of negative Eu anomalies (fig. 108) may reflect early plagioclase fractionation or partial melting of source rocks that retained feldspar (Watson and Green (1981); Piccoli and Candela (2002); Tollari *et al.* (2008) in (Mao *et al.*, 2016)).

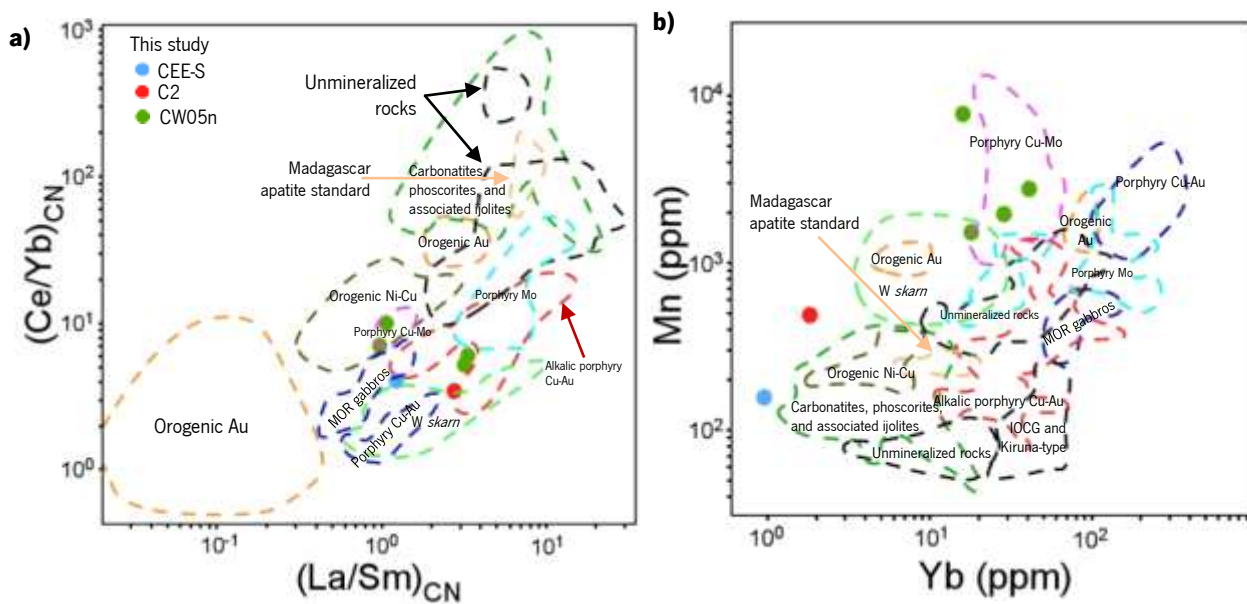


Figure 108 – Scatterplots for apatites. **a)**  $(La/Sm)_{CN}$  vs.  $(Ce/Yb)_{CN}$ . **b)** Yb (ppm) vs. Mn (ppm). (Modified after Mao *et al.*, 2016)

Although a comparison between Leal Gomes (1994) bulk data spectra (fig. 109) and apatite and scheelite from Cerdeirinha was attempted, the spectra geometry and fractionation of these minerals seem to be more correlated with high grade metamorphism (fig. 110) than with Leal Gomes (1994) data.

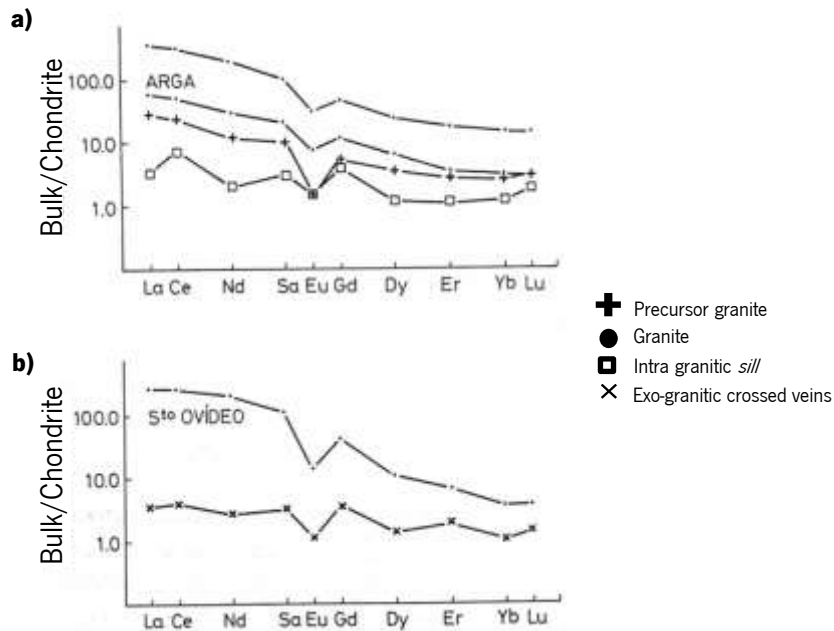


Figure 109 – REE profiles normalized. (Composition of chondrite: C1 of Evensen *et al.* (1978) in Leal Gomes (1994)). (From Leal Gomes, 1994)

Comparing this study values with the whole-rock REE measurements (Dias, 2011), the REE-depleted scheelite contained lower values and was not verified before in Covas Dome (fig. 110 a)). While apatite CW05n presented higher REE values than the verified in the whole-rock data from Covas (fig. 110 b)).

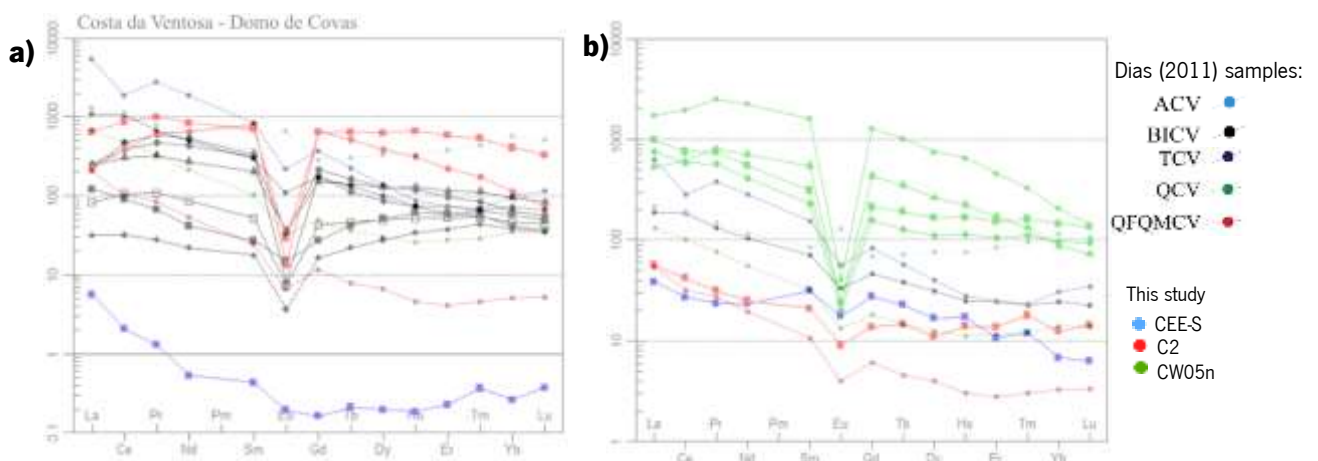


Figure 110 – Spectra comparison related to phyllic and quartzophilitic facies of Costa da Ventosa – Covas Dome (Dias, 2011). **a)** Comparison with scheelite. **b)** Comparison with apatite. Micaceous tourmalinite with coarse tourmaline porphyroblasts, hosting of quartz-micaceous vein segregations (TCV); muscovitic-biotitic banded quartzphyllite with tourmaline (QFQMCV); tourmalinitic phyllite with garnet (QCV); biotite (BICV); coarse apatite with micaceous matrix that occurs segregated in the periphery of quartz-micaceous venulations (ACV)



### 7.2.3. Mn-indetermination

Two spots of an indetermined crystal (with composition close to ilmenite) rich in Mn (B and C in table 28) were found close to the centre of the spheroid nucleus (CW05n – *spheroid – apical sulfide domain with mound structure*) (fig. 111).

This oxide weight percentage content (measured in microprobe) is even higher than the Mn rich ilmenites verified by Jian *et al.* (1996) and Cassidy *et al.* (1988). Ilmenites with highest MnO content in each study case are present in table 28, including highest MnO contents regarding representative compositions of ilmenite from metamorphosed mafic and ultramafic rocks from low (metaperidotite), medium (komatiitic metabasalt) and high (tholeiitic metagabro) grade domains (western Australian shield) was present in the same table.

Ilmenite, in the Broken Hill district (Australia), occurs as a metamorphic mineral (Plimer (1990) in Jian *et al.* (1996)) with the Mn level of the ilmenite controlled by the availability and concentration of Mn in the protolith. An ilmenite grain in a regional clastic metasedimentary rock from Aldridge Formation (which hosts the Sullivan deposit) also was found to have slightly high (7 wt. %) MnO content (Leitch (1992) in Jian *et al.* (1996)). Also in this study, slightly high MnO content were found: 9.89 wt. % (D; CW05n), 10.75 wt. % (E; C2), and 10.25 wt. % (F; C2) (table 28). The elevated Mn levels locally in the shallow footwall and peripheral to the Sullivan deposit are considered to be an indication of submarine Mn-rich exhalations (Leitch (1992), Slack (1993) in Jian *et al.* (1996)). Slack further suggested that stratiform tourmalinite that contains in excess of 19% fine-grained, spessartine-rich garnet is the product of Fe-Mn-B precipitation in a pool of dense brine (Jian *et al.*, 1996).

Thus, the high Mn content found in this study can possibly be related with primordial Mn nodule (and be an indication of submarine Mn-rich exhalations) (?).

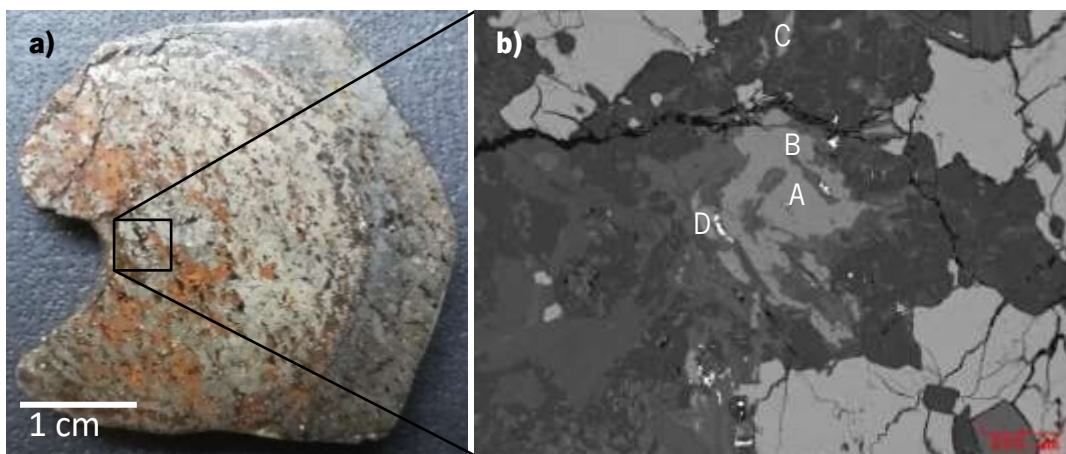


Figure 111 – Mn-indetermination in CW05.n. **a)** Spheroid sample where Mn-indetermination was identified. **b)** Backscattered electrons image of spots of microprobe analyses; the content present in the letters can be found in the table 28.

Table 28 – TiO<sub>2</sub>, FeO and MnO wt.% content in several ilmenites and indetermination.

		<b>Oxide Wt. %</b>		
		<b>TiO<sub>2</sub></b>	<b>FeO</b>	<b>MnO</b>
Ilmenite (NMNH 96189) (standard)		46.08 ± 0.01	46.22 ± 0.01	4.95 ± 0.04
A (CW05n)		50.62 ± 0.42	38.85 ± 0.27	5.03 ± 0.19
B (CW05n)		51.38 ± 0.43	16.13 ± 0.11	32.56 ± 1.21
C (CW05n)		49.74 ± 0.41	18.98 ± 0.13	28.87 ± 1.07
D (CW05n)		51.70 ± 0.43	37.08 ± 0.25	9.89 ± 0.37
E (C2)		50.19 ± 0.42	35.92 ± 0.25	10.75 ± 0.40
F (C2)		50.53 ± 0.42	36.49 ± 0.25	10.25 ± 0.39
Jian <i>et al.</i> (1996)		51.91	29.45	16.66
Cassidy <i>et al.</i> (1988)	Low grade	46.81	37.13	5.30
	Medium grade	52.08	38.49	7.96
	High grade	52	42	4

## 8. DISCUSSION AND CONCLUSIONS

The pressure ( $(3.80 \pm 0.35)$  Kbar) and temperature ( $(718.0 \pm 23.0)$  °C) determinations in hornblende and plagioclase are in accordance with data from Dias (2011) and Dias & Leal Gomes (2013a) (P-T conditions of 2.9-4.2 Kbar and 650-710 °C) for  $D_2$  and the metamorphic evolution between  $D_2$  and  $D_3$ , in the C.D.F.. Chlorites crystallization temperatures calculated by the empirical method of Kranidiotis & MacLean (1987), owing to the presence of pseudothuringite gave the maximum values of 416.13 °C to 419.72 °C, while the minimum was obtained due to brunsvigite (257.13 °C and 311.81 °C).

In ore mineralogy, arsenopyrite appear in several generations that represent a primitive equilibrium followed by *annealing/recovery* readjustments related with primordial metamorphism/metasomatism (from 634 °C to 491 °C). All the arsenopyrites analysed by Leal Gomes (1994), Araújo & Leal Gomes (2014) and Leal Gomes *et al.* (2015), whose compositions and pyrite equilibrium suggest hydrothermal precipitation or deuteric alteration temperatures under  $\approx 490$  °C to  $\approx 395$  °C. Furthermore, it seems to exist some compositions resulting from cataclastic readjustment and remobilization/recrystallization at low temperature (mesothermal domain; 360 °C to 330 °C).

The comparison of chlorites temperatures (416.13 °C–419.72 °C, 355 °C to 375 °C and 257.13–311.81 °C) (Kranidiotis & MacLean, 1987) with arsenopyrite temperature (564 °C–557 °C) (Kretschmar & Scott, 1976) only in C2 sample, suggest that a prior arsenopyrite was formed under higher temperatures, and latter, at lower temperatures, chlorites crystallized in pseudothuringite, ripidolite, brunsvigite compositional domain).

L.A.-I.C.P.-M.S. measurements in arsenopyrite allowed to establish that, even though arsenopyrites were gold depleted, electrum particles were found included in it and Sb and Ag seem to be well correlated in CWW-3A arsenopyrites ( $R^2=0.9015$ ). Bi seems to correlate well with most of others metals presence, except Sb. Although it is not possible to evaluate Te accuracy, its correlation with Bi might be explained by the formation of tetradyomite.

Arsenopyrite seems to contain slightly higher Au content than the pyrite and pyrrhotite. In fact all the sulfides seem to be depleted in Au and Ag. Although Dias & Leal Gomes (2015) found auriferous arsenopyrite (600 ppm Au) in Covas structures (Valdarcas), specifically in Cerdeirinha ores they only found gold contents in pyrite and pyrrhotite, 200 ppm and 800 ppm, respectively. Also, Araújo & Leal Gomes (2014) found auriferous arsenopyrites in shear-zones.

Ag present in pyrite has a similar behaviour to the Ag present in pyrrhotite, yet this behavior is distinct from the one found in arsenopyrite. In the case of Bi, there are higher values in arsenopyrite.

Arsenopyrite presented major Ni + Co content comparing with other sulfide phases. The major Bi content was found in arsenopyrite in CW05.

Mo and Sn indicate higher and positive correlations. Although the W-Mo correlation are not enhanced in the arsenopyrite crystal net, it was identified scheelite, wolframite and ferberite (W-carriers) and molybdenite (Mo-carrier). Moreover, Dias *et al.* (2010) previously found W-molybdenite in Serro, which they correlate it with a possible exhalitic remobilization (oxidizing evolved environment that would promote the deposition of vein tourmalinites (Cr-rich dravite) in tuffitic protoliths with W-molybdenite included). The primitive introduction of W in the system, possibly accompanied water-interaction, concomitant with the deposition of sulfide mineralization, in a VHMS type model (Dias *et al.*, 2010).

Pyrite genesis, could be *Metamorphic/Hydrothermal*, which could be related with both a SEDEX hypothesis or a latter *skarn* formation, once both are compatible with deposits. In general, iron sulfide compositions seem to be compatible with *sedimentary and sedimentary-reformed* generation signature, which may support the primordial SEDEX setting, that latter suffered metamorphism and *skarn* metassomatism. Although sedimentary-hydrothermal contrast is not strictly clear, these samples suggest that the fluids responsible for pyrite and pyrrhotite deposition at Cerdeirinha were likely derived from or interacted with intermediate (close to felsic) rocks/melt, having intrinsically variable contents of Ni and Co. However, some arsenopyrites content suggest to be related with ultramafic setting. This contrasting expression seem to fit with the bimodal volcanism setting (mixing of crustal materials) proposed by Dias (2011).

The REE scheelite and apatite contents indicate an order of crystallization of fluid increasing crystal fractionation following the order: CW05n, C2, CW05 and for last CEE-S (fig. 112). Bayer (1968) *in* Dias & Leal Gomes (2013b) considered:

- The earliest scheelite appears to be disseminated in calc-silicate beds with wollastonite and vesuvianite in amphibolites and in primitive sulfide-rich layer;
- *Generation 2* is represented by automorphic disseminated scheelite in calc-silicate rocks or sulfide rich layers, generally as pseudomorphic ferberite or reinite;
- *Generation 3* concerns epitaxial scheelite around wolframite, observed in plagioclasic and apatitic late apatite-rich lithologic supports.

From apatite compositions seems that in part they are related to granitoid genesis, although all of them are plotted close to an ore deposit field.

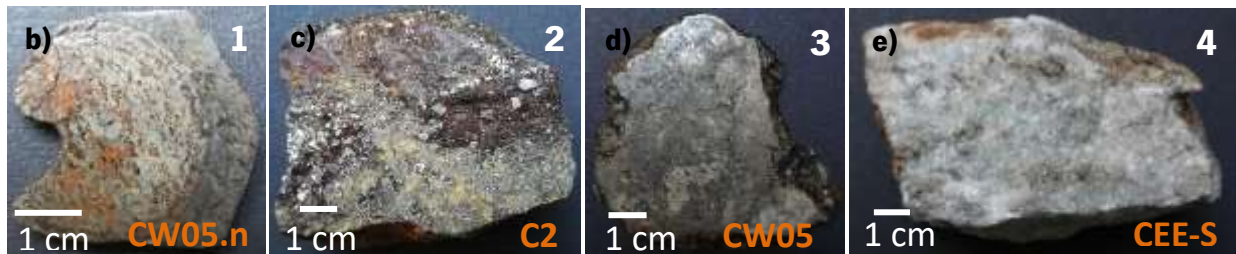
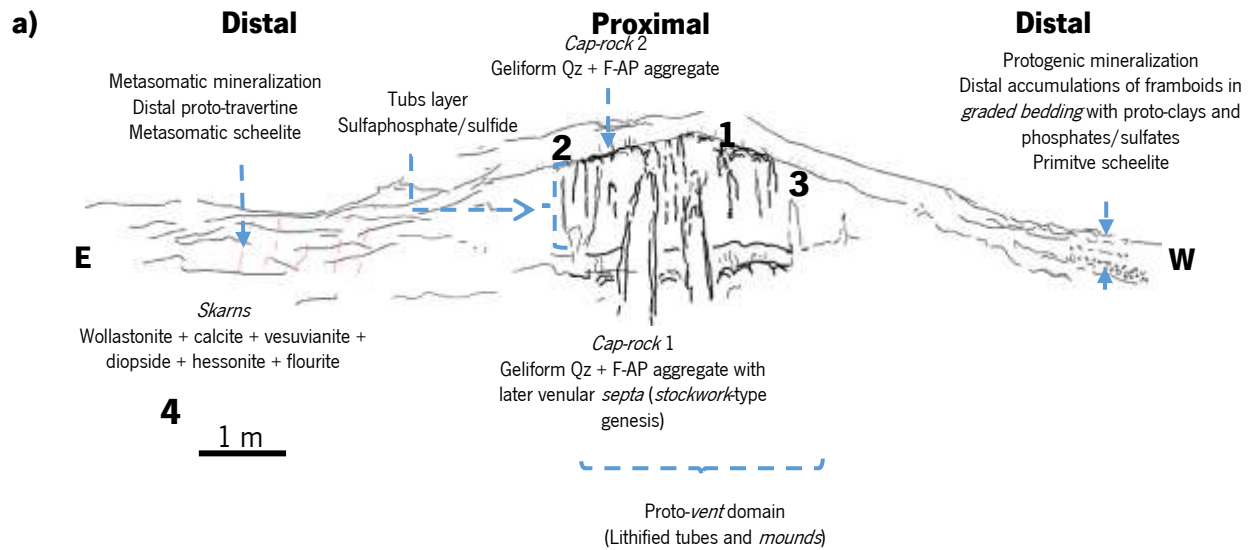


Figure 112 – REE conclusion. **a)** Protolith structures generalized conceptual profile of Cerdeirinha mine latter overprinted by igneous fluid. The number represent the order of crystallization. **b), c), d),** and **e)** hand samples and polished sections that allowed the production of thin-sections that allowed to achieve this conclusion.

Comparing scheelite and apatite L.A.-I.C.P.-M.S. spectrums with the ones from Covas (Dias, 2011), a REE depletion was observed.

The spheroid of CW05.n sample allowed to establish the hornblende-plagioclase geothermobarometry for pyrite and pyrrhotite associated genesis. It is not clear if that can be correlated with a sedimentary-exhalative setting or with a sedimentary setting that was latter hydrothermally affected. Small scheelite crystals were only found close to the center of the spheroid, and a pyrite with higher W content was found in the same crystal. Still in this sample also a Mn-rich indetermination was found. This Mn content was higher than the findings of others authors (Cassidy *et al.* (1988) and Jian *et al.* (1996)) that attributed their values to several grades of metamorphism and an exceptional high 16.7 wt. % MnO that reflected the remobilization of Mn within the local environment (Jian *et al.*, 1996). Jian *et al.* (1996) both types of Mn-rich ilmenite were considered to be derived from Mn originally concentrated in pools of dense brine that formed during syn-sedimentary, submarine-exhalative mineralization, and are considered to be an indication of submarine Mn-rich exhalations (Leitch (1992), Slack (1993) in Jian *et al.* (1996)).

In the results that are now presented, temperatures, sulfides and apatites compositions, Au enrichment in some phases, are in fact in argument with the hypothesis proposed by Leal Gomes et al. (2011) and Dias (2011) of exhalative protogenesis, this could represent the residual Paleothetis opening, that was latter aborted, which agrees with a low oxygenation basin, with high S content and volcanic affinity in C.D.F. (fig. 113).

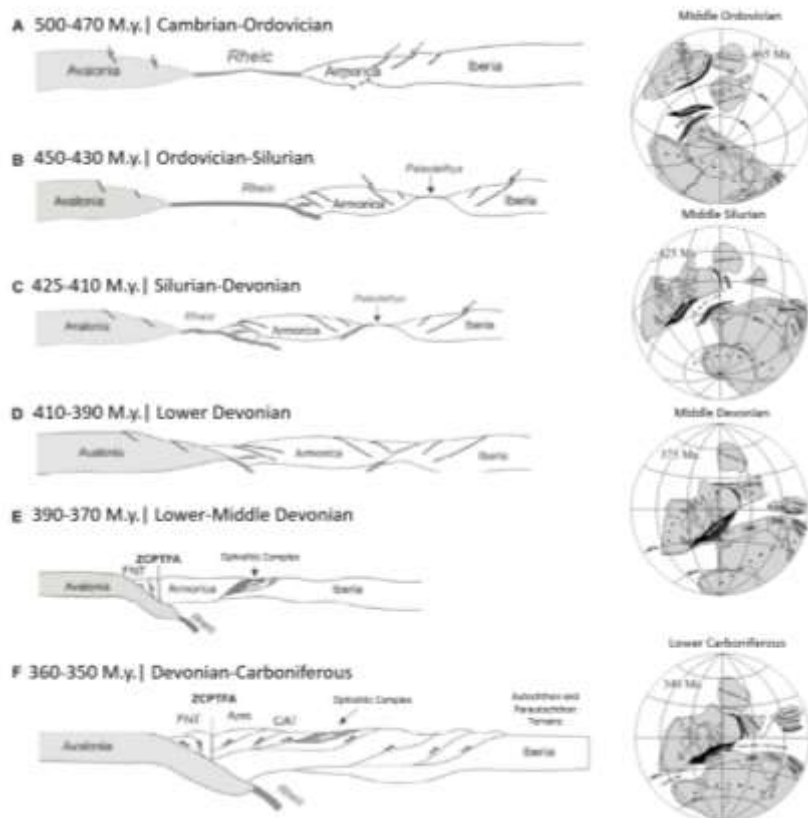


Figure 113 – Current conception of paleogeography, in the context of the Ordovician to the Carboniferous, of the NW Gondwana margin (modified after Ribeiro *et al.* (2007) e Matte (2001) in Dias (2011)).

According to the petrological study of the hosting and parental metamorphic facies Dias

(2011) establish a possible parental affinity for some relevant constituents hosted in rock surrounding Cerdeirinha deposit (Dias, 2011):

- B: related to a syngenetic exhalative and hydrothermal to metasomatic state linked to alkaline magmatism;
- P: volcanogenic bonded to alkaline rocks and easily adsorbed on sedimentary organic matter;
- S: volcanogenic linked to calc-alkaline to transitional felsific rocks as well as exhalative;
- Li: volcanogenic and possibly also evaporitic.

Although metamorphic-metasomatic remobilizations have been important, it is possible to attribute these formations to a primitive volcano-sedimentary and sedimentary-exhalative polygenic nature that can contribute to the final mineralogical concentration from an early metallic stock (Dias, 2011).

The idea of an overprinting *skarn* was also observed in Cardona *et al.* (2015) and in Canet *et al.* (2003). Canet *et al.* (2003) highlights the importance of Silurian deposits in the Iberian Massif (Moro *et*

*al.* (1995) in Canet *et al.* (2003)). Notice that Cerdeirinha is inserted in Galizia-Trás-os-Montes Zone, which belongs to Iberian Massif sector.

Besides the explanation present in Leal Gomes *et al.* (2011), Cerdeirinha open pit structures seem to be similar to the ones verified in a preliminary description of the origin of a sedimentary-exhalative ore deposit in Mexico (Cerecedo-Sáenz *et al.*, 2018) (fig. 114). The presented studied is from Jurassic

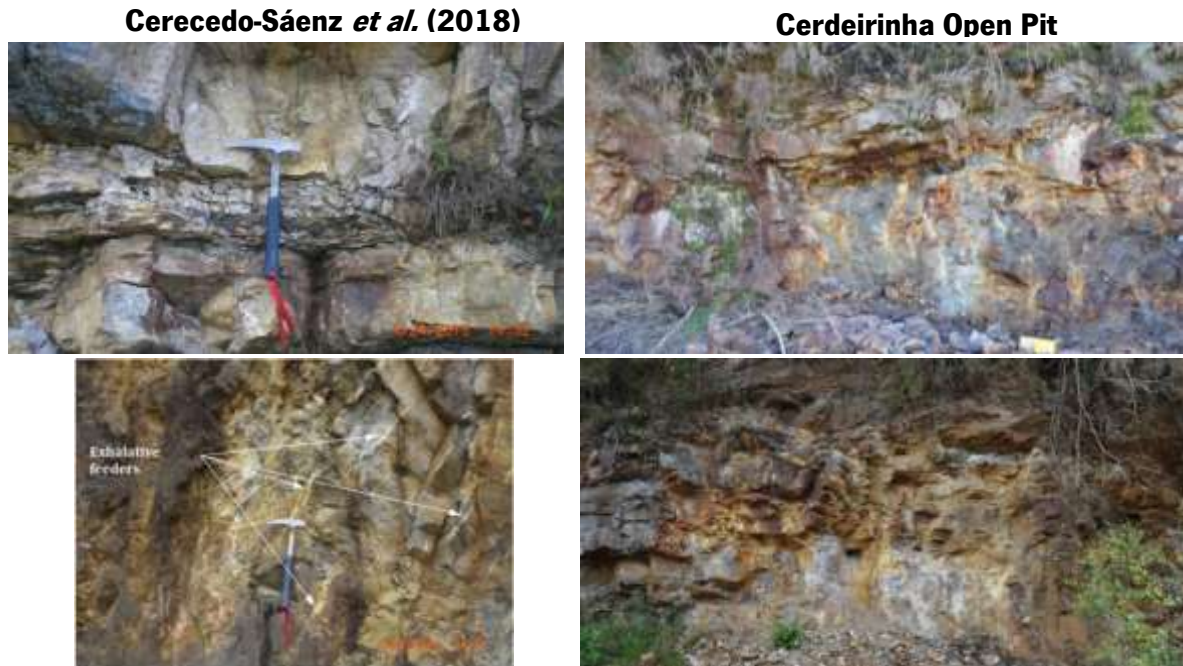


Figure 114 – Comparison between Cerecedo-Sáenz *et al.* (2018) and Cerdeirinha open pit field structures.

and therefore the structure seem to be better preserved than the Cerdeirinha open pit (C. Leal Gomes personal communication, 2019).

In what the *skarn* overprint concerns, it is important to highlight that there is no specific age attributed to *skarns*, so far. However, the protolith is considered Silurian and co-related with *Valença e Vila Nune* unit (in sheet 1 of Portugal Geological map at scale 1: 200 000). Until now, no granitic body was found correlated with the *skarns*. Therefore, the metasomatic alteration have been correlated with more or less diffuse hydrothermal activity of regional character sometimes focused in thrust fault sectors of the 2<sup>nd</sup> Variscan phase where granitoids were also installed, and especially high dimension aplite-pegmatite and pegmatite bodies. These influenced the paragenetic calc-silicate modifications (C. Leal Gomes personal communication, 2019). A reference age materialized by generation of intra-pegmatitic contaminations can be about 330 M.y. – age group of synthectonic granitoids installed in 2<sup>nd</sup> deformation phase structures and related with aplite-pegmatites (C. Leal Gomes personal communication, 2019).

Extrapolating this new data for Covas Dome, at least, the last episodes of the hydrothermal reset seem to be documented in some marker phases. In previous works, in particular in Cerdeirinha, possible primordial seamounts, smoker-like structures and sulfide-sulfates graded bedding were observed.

In case this hypothesis is latter confirmed this would change the Covas Dome exploration perspective, once this would no longer be looked at as only a tungstiferous *skarn* deposit, but also as a primordial SEDEX deposit.



## REFERENCES

- Anderson, J. L. & Smith, D. R. (1995). 'The effect of temperature and oxygen fugacity on Al-in-hornblende barometry'. *AM MINERAL* pp. 80, 549-59.
- Anderson, J. L. (1996). 'Status of thermobarometry in granitic batholiths'. *Transactions of the Royal Society of Edinburgh: Earth Sciences*, 87, pp 125-138.
- Araújo, P.; Leal Gomes, C. (2014). 'Análise geométrica e cinemática das partículas de Au acolhidas em arsenopirite no corredor de cisalhamento de Argas-Cerquido-Serra de Arga (Minho)'. *Comunicações Geológicas* (2014) 101, Especial I, 243-246.
- Bajwah, Z.U.; Seccombe, P.K.; Offler, R. (1987). 'Trace element distribution, Co/Ni ratios and genesis of the Big Cadia iron-copper deposit, New South Wales, Australia'. *Miner. Depos.* 22, 292–300. [CrossRef]
- Belousova, E.A.; Griffin, W.L.; O'Reilly, Suzanne Y.; Fisher, N.I. (2002). 'Apatite as an indicator mineral for mineral exploration: trace-element compositions and their relationship to host rock type'. *Journal of Geochemical Exploration* 76 (2002) 45–69
- Berglund, S & Ekström, T.K. (1980). 'Arsenopyrite and sphalerite as T-P indicators in sulfide ores from northern Sweden'. *Mineral. Deposita* 15, 175-187.
- Blundy, J. D. & Holland, T. J. B. (1990). 'Calcic amphibole equilibria and a new amphibole-plagioclase geothermometer'. *CONTRIB MINERAL PETROL* 104, 208-24.
- Bourdelle, F.; Parra, T.; Chopin C.; Beyssac, O. (2013). 'A new chlorite geothermometer for diagenetic to low-grade metamorphic conditions.' *Contrib Mineral Petrol* (2013) 165:723-735
- Canet, C.; Alfonso, P.; Melgarejo, J.-C.; Jorge, S. (2003). 'PGE-Bearing Minerals in Silurian Sedex Deposits in the Poblet Area, Southwestern Catalonia, Spain'. *The Canadian Mineralogist*. Vol. 41, pp. 581-595.
- Cardona, S.; Torró, L.; Campeny, M.; Andreu, E.; Melgarejo, J. C.; Proenza, J. A.; De Witt, M. C. J.; Bruchs, J. M.; Lewis, J. F. (2015). 'Proterozoic metallogeny in the NW border of Botswana'. *Mineral Deposit Research For A High-Tech World*. 12th SGA Biennial Meeting 2013. Proceedings, Volume 3. Pp. 1247-1250.
- Caritat, P.; Hutcheon, I.; Walshe, J. (1993). 'Chlorite Geothermometry: A REVIEW'. *Clays and Clay Minerals*, Vol.41, No. 2, 219-239, 1993.

Cassidy, H. F.; Groves, D. I. ; Binns, R. A. (1988). 'Manganoan Ilmenite Formed During Regional Metamorphism Of Archean Mafic And Ultramafic Rocks From Western Australia'. *Canadian Mineralogist*. Vol. 26, pp. 999-1012 (1998)

Cathelineau, M. (1998). 'Cation site occupancy in chlorites and illites as a function of temperature'. *Clay Minerals*. V.23, p.471-485.

Cathelineau, M. & Neiva, D. (1985). 'A chlorite solid solution geothermometer: The Los Azufres (Mexico) geothermal system'. *Contributions to Mineralogy and Petrology*, v.91, p. 235-244.

Cerecedo-Sáenz, E.; Rodríguez-Lugo, V.; Ávila, J. H.; Mendoza-Anaya, D.; Reyes-Valderrama, M. I.; Vázquez-García, R. A.; Salinas-Rodríguez, E. (2018). 'Preliminary Description of the Origin of a Sedimentary – Exhalative Ore Deposit, in Molango, Hidalgo Mexico'. *Preprints* (www.preprints.org). doi:10.20944/preprints201803.0020.v1

Chace, F.M. (1956). 'Abbreviations In Field And Mine Geological Mapping'. Scientific Communications. *Economic Geology*, v.51, pp. 712-723

Chen, D.F. (1995). 'Characteristics of main metallic minerals in some copper-nickel sulfide deposits of China'. *Acta Petrol. Miner.* 1995, 14, 345–354. (In Chinese)

Coelho, J. (1993). 'Os "skarns" cálcicos pósmagmáticos, mineralizados em scheelite, do distrito mineiro de Covas, Vila Nova de Cerveira (Norte de Portugal)'. PhD dissertation, Univ. Porto, Porto, 570p.

Couto, M. H. M. (1993). 'As Mineralizações de Sb-Au da Região Dúrico-Beirã'. Porto. Faculdade de Ciências da Universidade do Porto. Centro de Geologia da Universidade do Porto. Tese de Doutoramento. 647 pages.

Craig, J. R.; Vaughan, D. J (1994). *Ore Microscopy and ore petrography*. 2nd ed. New York: John Wiley & Sons Ltd, 1994. 434 p.

Deer, W.A.; Howie, R.A. and Zussman, J. (1992). 'An Introduction to the Rock Forming Minerals'. Longman Scientific & Technical, England; Wiley, New York.

Dias, P. (2011). 'Análise Estrutural e Paragenética de Produtos Litológicos e Mineralizações De Segregação Metamórfica - Estudo de veios hiperaluminosos e protólitos poligénicos Silúricos da região da Serra de Arga (Minho)'. PhD dissertation, Universidade do Minho, Portugal. 546 pag.

Dias, P.; Leal Gomes, C. (2015). 'Silurian protholits hosting syngenetic gold in the Serra de Arga region (Northern Portugal) – sources for orogenic reset'. X Congresso Ibérico de Geoquímica. 74-77pgs. (in Portuguese)

Dias, P.; Leal Gomes, C. (2013a). 'Considerações sobre a natureza vulcanogénica e exalativa de algumas formações metamórficas da Serra de Arga – Minho – Portugal – consequências para a cartografia'. *Geodinâmica e Tectónica global; a Importância da Cartografia Geológica*. Livro de actas da 9ª Conferência Anual do GGET-SGP

Dias P.; Leal Gomes, C. (2013b). 'Sedex signatures in Covas Tungsten Deposits – Northern Portugal'.

Dias, P.A.; Leal Gomes, C. (2010). 'Petrogenetic repositioning of W-Mo from Silurian to late-D3 remobilization – Serra de Arga (Minho)'. VIII Congresso Nacional de Geologia. Geosciences On-line Journal. E-Terra: Revista Eletrónica de Ciências da Terra. GEOTIC – Sociedade Geológica de Portugal. ISSN 1645-0388. (in Portuguese).

Dias, P.; Leal Gomes, C. (2008). 'Study of the volcano-sedimentary nature of the Serro formations – Silurian terranes of Serra de Arga – Minho (Northern Portugal)'. *Revista eletrónica de Ciências da Terra*. GEOTIC – Sociedade Geológica de Portugal. Volume 5 – nº 9. ISSN 1645-0388

Dias, P.; Leal Gomes, C. (2007). 'Estudo da natureza protolítica das formações de Serro – Serra de Arga, Minho, Portugal – Contributo para o conhecimento da poligénese vulcano-sedimentar dos terrenos Silúricos'. *Actas do VI Congresso Ibérico de Geoquímica e XV Semana de Geoquímica*, Vila Real, Portugal.

Dias, P. A.; Gomes, C. Leal; Guimarães, F. (2010). 'W-molybdenite in Silurian meta-volcanic rocks of Northern Portugal' [Poster]. In: IMA2010, 20th General Meeting of the International Mineralogical Association, Budapest, Hungary, 21-27 August, 2010. Acta Mineralogica-Petrographica. Abstract series

Doolan, B. L.; Evans, B. W.; Gilbert, M. C.; Helz, R. T.; Klein, C.; Laird, J.; Popp, R. K.; Robinson, P.; Schaumacher, J. C. and Spear, F. S. (1982). 'Amphiboles: Petrology and Experimental Phase Relations'. *Reviews in Mineralogy*. Volume 9B. Mineralogical Society of America.

Essene, E.J. (1982). 'Geologic thermometry and barometry. In Characterization of Metamorphism Through Mineral Equilibria' (J.M. Ferry, ed.). Mineral. Soc. Amer., Rev. Mineral. 10, 153-206.

Evans, A. (1993). 'Ore Geology and Industrial Minerals: An Introduction'. Chapter 15. 3<sup>rd</sup> Edition. Blackwell Science.

Gourcerol, B.; Kontak, D. J.; Thurston, P. C.; Petrus, J. A. (2018a). 'Application of LA-ICP-MS sulfide analysis and methodology for deciphering elemental paragenesis and associations in addition to multi-stage processes in metamorphic gold settings'. *The Canadian Mineralogist*. Vol. 56 (1): 39-64.

Gourcerol, B.; Kontak, D. J.; Thurston, P. C.; Petrus, J. A. (2018b). 'Results of LA-ICP-MS sulfide mapping from Algoma-type BIF gold systems with implications for the nature of mineralizing fluids, metal sources, and deposit models'. *Mineralium Deposita*. Springer-Verlag GmbH Germany.

Gregory, D.D.; Large, R.R.; Halpin, J.A.; Lounejeva, E.B.; Lyons, T.W.; Wu, S.; Danyushevsky, L.V.; Sack, P.; Chappaz, A.; Maslennikov, V.V. (2015). 'Trace element content of sedimentary pyrite in black shales'. *Econ. Geol.* 2015, 110, 1389–1410. [CrossRef]

Hawthorne, F. C. and Oberti R. (2007). 'Amphiboles: Crystal Chemistry'. *Reviews in Mineralogy & Geochemistry* Vol. 67, pp. 1-54. Mineralogical Society of America

Hawthorne, F.C. (1981). 'Crystal Chemistry of the Amphiboles'. *Canadian Mineralogist*, 21, 173-480

Hey, M. H. (1954). 'A new review of chlorites'. *The mineralogy magazine and journal of the mineralogical society*, 30, (224) 278-292, 1954

Holland, T. and Blundy, J. (1994). *Plagioclase-Hornblende Thermobarometry*. Excel sheet: 9<sup>th</sup> May, 2019.

Jian, S.Y.; Palmer, M. R.; Slack, J. F. (1996). 'Mn-rich ilmenite from the Sullivan Pb-Zn-Ag deposit, British Columbia'. *The Canadian Mineralogist*. Vol. 34, pp. 29-36 (1996)

Kalogeropoulos, S.I. (1984). 'Composition of arsenopyrite from the Olympias Pb-Zn massive sulphide deposit, Chalkidiki Peninsula, N. Greece'. *Neues Jahrb. Mineral. Monatsh.*, 296-300.

Klein, E. L.; Harris, C.; Giret, A.; Moura, C. (2006). 'The Cipoeiro gold deposit, Gurupi Belt, Brazil: Geology, chlorite geochemistry, and stable isotope study'. *Journal of South American Earth Sciences* pp. 23 (2007) 242–255.

Klein, E.L.; Koppe, J.C. (2000). 'Chlorite geothermometry and physicochemical conditions of gold mineralization in the Paleoproterozoic Caxias deposit, São Luís Craton, northern Brazil'. *Geochimica Brasiliensis* 14(2):219-232, 2000.

Kretschmar, U.; Scott, S.D. (1976). 'Phase relations involving arsenopyrite in the system Fe-As-S and their application'. *Can. Mineral.* 14, 364-386.

Leake, B.E. (1978). 'Nomenclature of amphiboles. *American Mineralogist*, 63, 1023–1052.

Leake, B. E.; Woolley, A. R.; Arps, C. E.S.; Birch, W. D.; Gilbert, M. C.; Grice, J. D.; Hawthorne, F. C.; Kato A.; Kisch H. J.; Krivovichev V. G.; Linthout, K.; Laird, J.; Mandarino, J. A.; Maresch, W. V.; Nickel, E. H.; Rock, N. M.S.; Schumacher, J. C.; Smith, D. C.; Stephenson, N. C.N.; Ungaretti, L.; Whittaker, E. J.W.; Youzhi, G.. (1997). 'Nomenclature of Amphiboles: Report of the Subcommittee on

Amphiboles of the International Mineralogical Association, Commission on New Minerals and Mineral Names'. *The Canadian Mineralogist* Vol. 35, pp. 219-246

Leal Gomes, C. (1994). 'Estudo estrutural e paragenético de um sistema pegmatóide granítico - O campo filoniano de Arga - Minho (Portugal)'. Tese de Doutoramento; Univ. Minho, Braga, 695 p..

Leal Gomes, C.; Araújo, P.; Dias, P. (2015). 'Petrofabric e composição do ouro orogénico associado a cisalhamentos nos terrenos Silúricos da Serra de Arga – Norte de Portugal'. X Congresso Ibérico de Geoquímica. 102-105 p..

Leal Gomes, C.; Verduzco, G.; Dias, P. A. (2011). 'Vestígios de actividade fumaroliana litificados no nível com sulfuretos do jazigo da cerdeirinha, Caminha, N Portugal'. VIII Congresso Ibérico de Geoquímica- XVII Semana de Geoquímica, Castelo Branco.

Li, L.; Lin, S.; Xing, G.; Jiang, Y. and He, J. (2017). 'First Direct Evidence of Pan-African Orogeny Associated with Gondwana Assembly in the Cathaysia Block of Southern China'. *Tectonics of South China*

Liu, Z.; Shao, Y.; Zhou, H.; Liu, N.; Huang, K.; Liu, Q.; Zhang, J.; Wang, C. (2018). 'Major and Trace Element Geochemistry of Pyrite and Pyrrhotite from Stratiform and Lamellar Orebodies: Implications for the Ore Genesis of the Dongguashan Copper (Gold) Deposit, Eastern China'. *Minerals*. doi.org/10.3390/min8090380

Lowell, G.R. & Gasparri, C. (1982). 'Composition of arsenopyrite from topaz greisen veins in southeastern Missouri'. *Mineral. Deposita* 17, 229-238

Mao, M.; Rukhlov, A. S.; Rowins, S. M.; Spence, J.; Coogan, L. A. (2016). 'Apatite Trace Element Compositions: A Robust New Tool for Mineral Exploration'. *Economic Geology*, v. 111, pp. 1187–1222

Mazumder, R. (2017). Sediment Provenance: Influence on Compositional Change From Source to Sink. Sediment Provenance. Influences on Compositional Change from Source to Sink. Pages 1-4. Elsevier

Mokhtari, M. A. A.; Zadeh, G. H.; Emami, M. H. (2014). 'Genesis of iron-apatite ores in Posht-e-Badam Block (Central Iran) using REE geochemistry'. *Journal of earth system science* 2013 v.122 no.3 pp. 795-807

N'Diaye, I.; Essaifi A.; Dubois, M.; Lacroix, B. (2015). 'Implication of Mineral Geochemistry and Stable Isotopes in the Kettara Pyrrhotite-Rich Massive Sulphide Deposit (Central Jebilet, Hercynian, Morocco)'. Mineral Resources in a Sustainable World. 13th Biennial SGA Meeting 24-27 August 2015, Nancy, France.

Neiva, A. M. R.; Moura, A.; Leal Gomes, C. A.; Pereira, M. F.; Corfu, F. (2019). 'The granite-hosted Variscan gold deposit from Santo António mine in the Iberian Massif (Penedono, NW Portugal): constraints

from mineral chemistry, fluid inclusions, sulfur and noble gases isotopes'. *Journal of Iberian Geology*, Springer, Vol. 45, Issue 3, pp 443–469.

Nelson, S. A. (2015). 'Phyllosilicates (Micas, Chlorite, Talc, & Serpentine)'. Mineralogy Tulane University.

Oliveira, M. (2017). 'Caracterização Materialográfica de Minerais Industriais'. Work developed for Valorização de Recursos Minerais subject.

Otten, M. T. (1984). 'The origin of brown hornblende in the Artfjället gabbro and dolerites'. *Contributions to Mineralogy and Petrology*. Volume 86, Issue 2, pp 189–199.

Rajabpour S.; Behzadi M.; Jiang, S.; Rasa I.; Lehmann B.; Ma Y. (2017). 'Sulfide chemistry and sulfur isotope characteristics of the Cenozoic volcanic-hosted Kuh-Pang copper deposit, Saveh county, northwestern Central Iran'. *Ore Geology Reviews* 86.

Ribeiro, A.; Munhá, J.; Dias, R.; Mateus, A.; Pereira, E.; Ribeiro, L.; Fonseca, P.; Araújo, A.; Oliveira, T.; Romão, J.; Chaminé, H.; Coke, C.; Pedro J. (2007). 'Geodynamic evolution of the SW Europe Variscides'. *Tectonics*. 26 (6)

Rodrigues, J.; Pereira, E.; Ribeiro, A. (2013). 'Complexo de Mantos Parautóctones do NE de Portugal: Estrutura interna e Tectonoestratigrafia'. In: Geologia de Portugal (R. Dias, A. Araújo, P. Terrinha & J. Kullberg Eds.). *Escolar Editora*, pp.275-332.

Safei, K.; Arian, M.; Mirhosseini, S. H. M. Z. (2015). 'Mineral Chemistry and Geothermometry of Amphibole and Plagioclase in the Metabasites, Located at the Tanbour Metamorphic Complex in Southern Iran'. *Open Journal of Geology*, 5, 795-808. Scientific Research Publishing.

Schiffman, P. & W. D. Howard (1995). Low-Grade Metamorphism of Mafic Rocks. Special Paper. *Geological Society of America*. 192 pages

Schmidt, M. W. (1992). 'Amphibole composition in tonalite as a function of pressure: an experimental calibration of the Al-in-hornblende barometer'. *CONTRIB MINERAL PETROL* 110, 304-10.

Scott (1983). 'Chemical behaviour of sphalerite and arsenopyrite in hydrothermal and metamorphic environments'. *Mineral. Mag.* 47, 427-435.

Sharp, Z. D.; Essene E. J.; Kelly, W. C. (1985). 'A Re-Examination of the Arsenopyrite Geothermometer: Pressure Considerations and Applications to Natural Assemblages'. *Canadian Mineralogist* Vol. 23, pp. 517-534.

Souto & Leal Gomes (2017). 'Dispositivos Estruturais Exalativos em níveis Estratiformes Silúricos com Sulfuretos da região de Caminha'. I Encontro de Jovens Investigadores – Património e Território, EJI PATER, Braga, Portugal.

Souto, A. S. (2017). 'Dispositivos Estruturais Exalativos em Níveis Estratiformes com Sulfuretos da região de Caminha'. Bachelor dissertation. Faculty of Sciences. University of Minho. (in portuguese)

Souto & Leal Gomes (2018). 'Orbicular To Framboidal Textures In Sulphide Layers From Cerdeirinha Mine – Caminha, Northern Portugal – Paragenesis And Its Relation With The Tungsten Mineralizations'. X Congresso Nacional de Geologia, Azores, Portugal.

Souto, A. S. & C. Leal Gomes (2019). Orbicular to framboidal textures in sulphide layers from Cerdeirinha Mine – Caminha, Northern Portugal – paragenesis and its relation with the tungsten mineralizations. *Comunicações Geológicas*. In Portuguese. (*in press*)

Mikrosondenstandards (2015). Mikrosondenlabor. Petrologie der Ozeankruste. Universität Bremen

Taylor, S.R. & McLennan, S.M., (1985). *The Continental Crust: Its Composition and Evolution*. Blackwell, Oxford.

Tindle, A. G. and Webb, P. C. (1994). 'PROBE-AMPH An amphibole structural formula calculator and classifier (with barometers)'. *Computers & Geosciences. Elsevier*. Vol. 20, Issues 7–8, August–October 1994, Pages 1201-1228.

Tobia, F. H. & Shangola S. S. (2016). Mineralogy, geochemistry, and depositional environment of the Beduh Shale (Lower Triassic), Northern Thrust Zone, Iraq. *Turkish Journal of Earth Sciences*.

Whitney, D. L.; Evans, B. W. (2010). 'Abbreviations for names of rock-forming'. *American Mineralogist*, Volume 95, pages 185–187.

Winter, J. D. (2014). *Principles of Igneous and Metamorphic Petrology*. Chapter 25. Second Edition. Pearson New International Edition.

Zhang, Q.; Zhang, R.-Q.; Gao, J.-F.; Lu, J.-J.; Wu, J.-W. (2018). 'In-situ LA-ICP-MS trace element analyses of scheelite and wolframite: Constraints on the genesis of veinlet-disseminated and vein-type tungsten deposits, South China'. *Ore Geology Reviews*. Volume 99, August 2018, Pages 166-179

## WEBGRAPHY

“Electron probe microanalysis” in *en – Petrology of the Ocean Crust*. <https://www.ozeankruste.uni-bremen.de/index.php/en/laboratories/electronmicroprobe.html> [24<sup>th</sup> of June of 2019].

“LA-ICP-MS” in *en – Petrology of the Ocean Crust*. <https://www.ozeankruste.uni-bremen.de/index.php/en/laboratories/la-icp-ms/81-la-icp-ms-txt-en.html> [24<sup>th</sup> of June of 2019].

“REM & EDX” in *en – Petrology of the Ocean Crust*. <https://www.ozeankruste.uni-bremen.de/index.php/en/laboratories/rem-en.html> [24<sup>th</sup> of June of 2019].

“Translucent and opaque mineral microscopy” in *en – Petrology of the Ocean Crust*. <http://petrologyservices.com/transmitted-and-reflected-light-microscopy> [24<sup>th</sup> of June of 2019].

IUPAC Periodic Table of Elements (2019). <https://iupac.org/what-we-do/periodic-table-of-elements/>, on 31<sup>st</sup> July, 2019.



# ANNEX I – FIGURE OF MINERAL INTERGROWTH

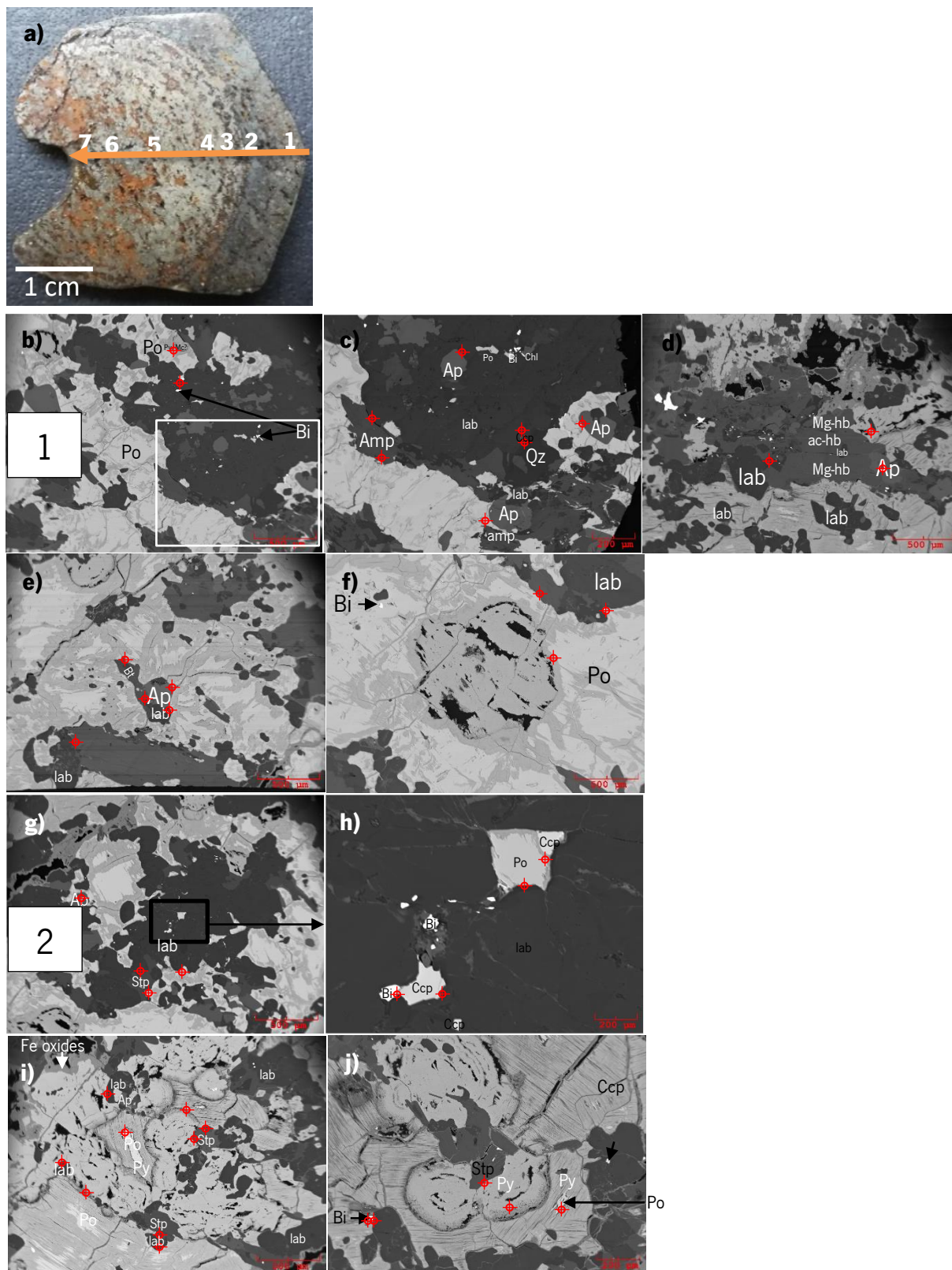


Figure I.1 – CW05.n sample. **a)** General image with sector location. **Sector 1:** Periphery of the nodule. **b)** Amphibole, labradorite, apatite, quartz, pyrite, pyrrhotite, scheelite and native bismuth intergrowth. **c)** Detail of a). **d)** Amphibole intergrown with labradorite and pyrite. **e)** Amphibole intergrown with pyrite. **f)** Bird-eye feature. **Sector 2:** **g)** Amphibole and plagioclase intergrown with pyrite. **h)** Detail of f). **i)** Decay of pyrrhotite to pyrite. **j)** Detail of the decay of pyrrhotite to pyrite (marcasite?).

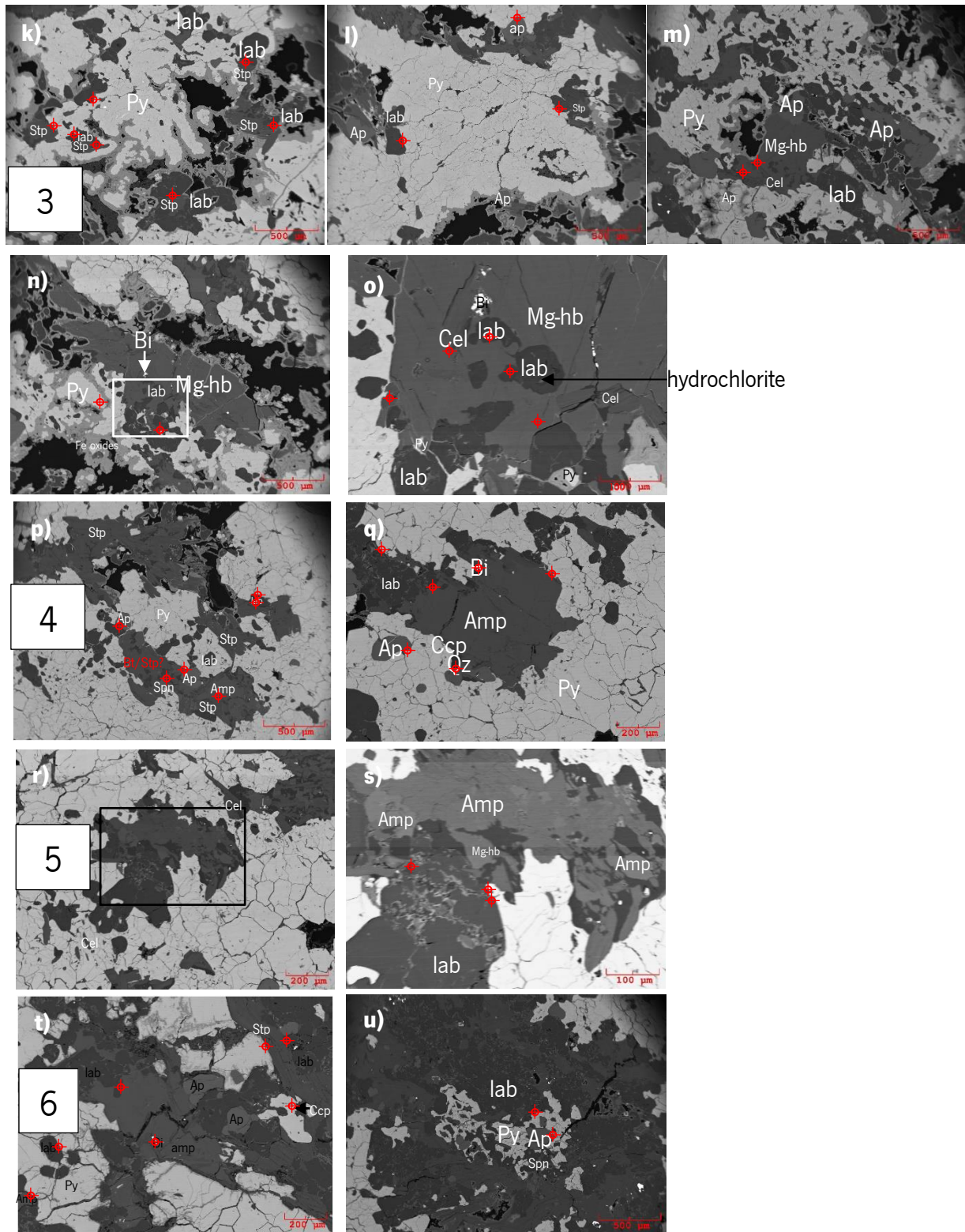


Figure I.1 – CW05.n sample. **Sector 3:** **k)** Pyrite, Fe oxide and amphibole. **l)** Pyrite. **m)** Amphibole intergrown with apatite, pyrite and plagioclase. **n)** Amphibole and plagioclase intergrown with pyrite. **o)** Detail of n. **Sector 4:** **p)** Intergrowth of amphibole, pyrite and apatite. **q)** Amphibole, quartz, bismuth and pyrite. **Sector 5:** **r)** Amphibole and plagioclase intergrowth. **s)** Detail of r). **Sector 6:** **t)** Amphibole, plagioclase and apatite intergrowth. **u)** Apatite involved by pyrite. (to be continued)

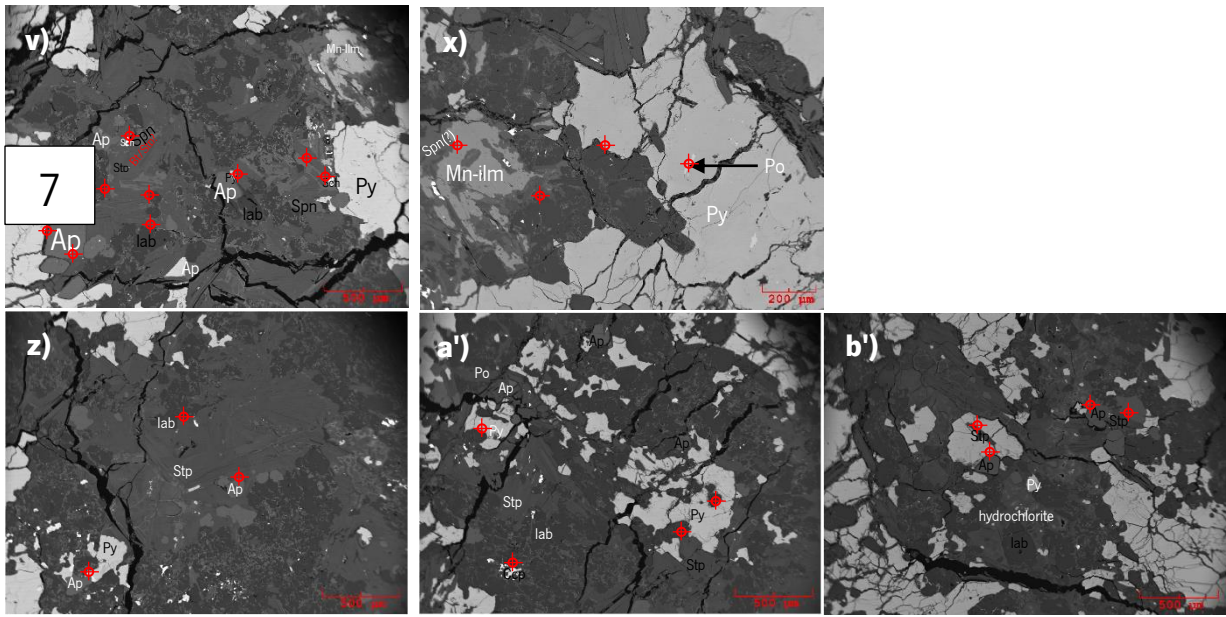


Figure I.1 – **Sector 7:** close to nuclear sector. **v)** Amphibole, plagioclase, apatite, pyrite and ilmenite sector. **x)** Pyrrhotite included in pyrite and Mn rich ilmenite crystal. **z)** Micaceous character. **a')** Amphibole, plagioclase and pyrite intergrowth. **b')** Hydrochlorite, apatite, stilpnomelane and pyrite. (Concluded)

## Other sulphides

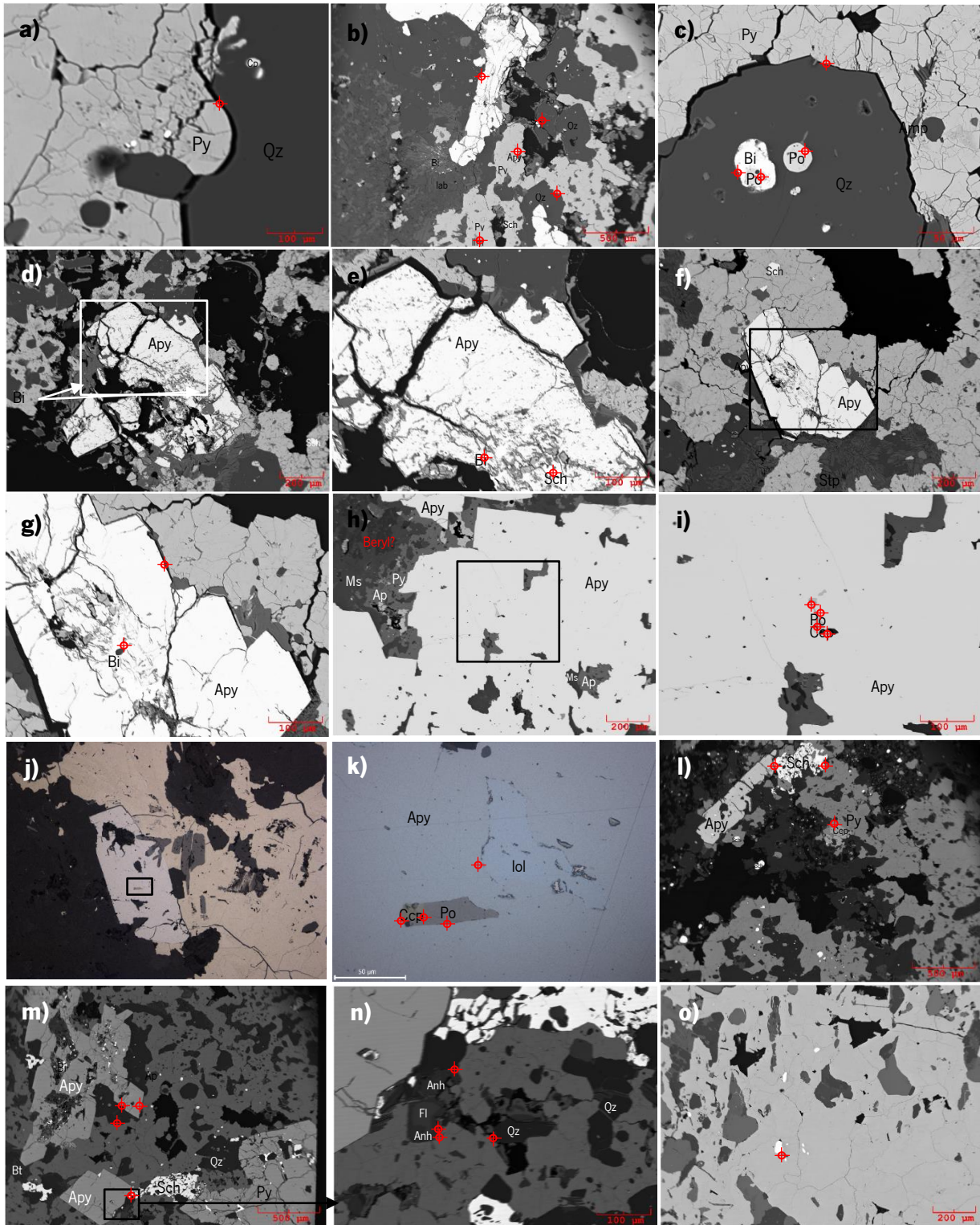


Figure 1.2 – Backscattered electron and reflected light microscopy images of sulphidic assemblages (to be continued). **a)** Pyrite intergrown with quartz. **b)** Pyrite, arsenopyrite, scheelite, native bismuth and labradorite intergrown close to the CW05 “nucleus”. **c)** Bismuth involving pyrrhotite in a quartzitic sector. **d)** Arsenopyrite with inclusions (or exsolution?) of native bismuth and scheelite. **e)** Detail of d). **f)** Arsenopyrite (with native bismuth inclusion or exsolution (?)) intergrown with arsenopyrite and quartz. **g)** Detail of f). **h)** Chalcopyrite and pyrrhotite included in porphyroblast of arsenopyrite. **i)** Detail of h). **j)** Porphyroblast arsenopyrite (with inclusions of chalcopyrite, pyrrhotite and lollingite) intergrown with pyrite and ilmenite. **k)** Detail of h). **l)** Arsenopyrite, scheelite and pyrite intergrown. **m)** Porphyroblastic arsenopyrites with and without native bismuth inclusions and scheelite and pyrite intergrown. **n)** Detail for fluorite-pyrite reaction that generated the anhydrite (?). **o)** W-minerals in pyritic matrix. (to be continued)

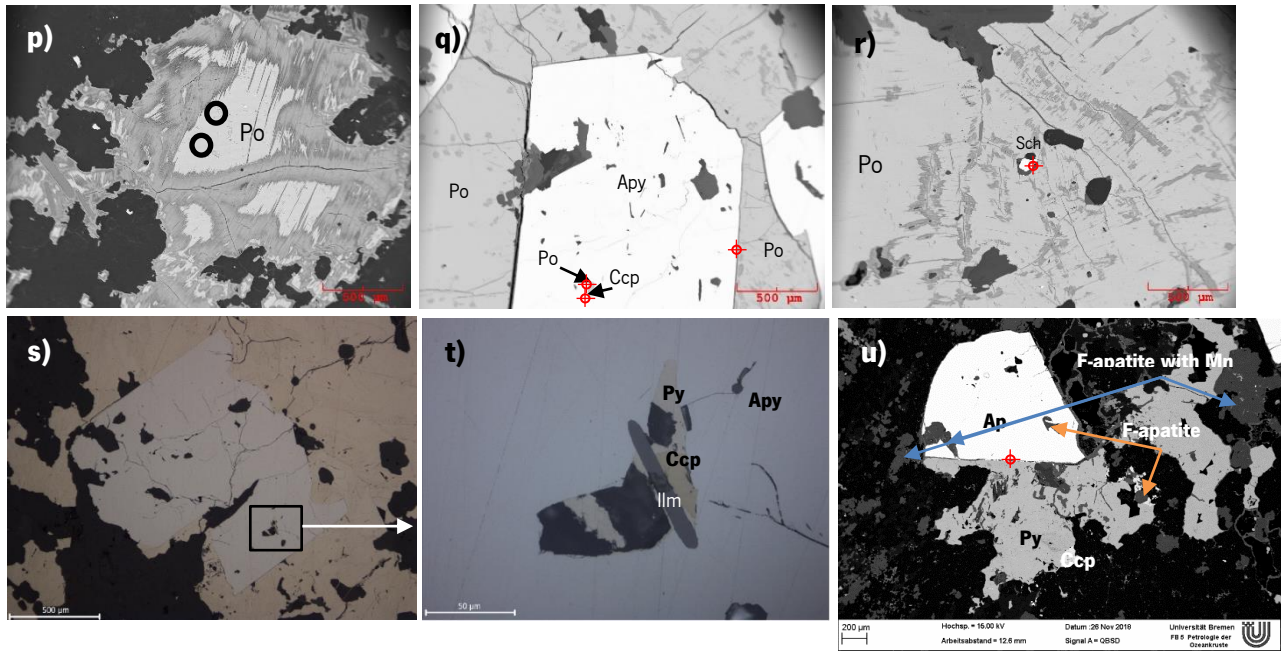
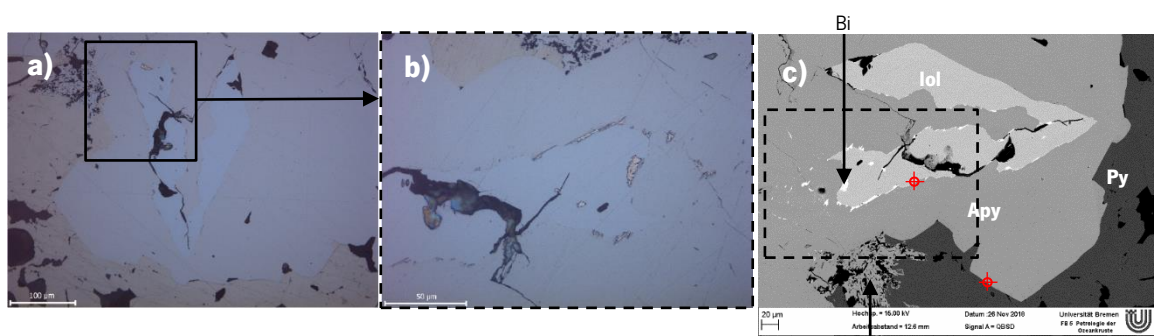


Figure I.2 – Backscattered electron and reflected light microscopy images of sulphidic assemblages (continuation). **p)** Pyrrhotite included in a plagioclase matrix. Black circles indicated the spots of L.A.-I.C.P.-M.S. measurements. **q)** Porphyroblastic arsenopyrite with pyrrhotite and chalcopyrite inclusions. **r)** Scheelite included in pyrrhotite. **s)** Porphyroblastic arsenopyrite with inclusions of pyrite, chalcopyrite and ilmenite. **t)** Detail of s). **u)** Sulphides involved with mica and F-apatite with and without Mn content. (concluded)



Figure I.3 – Latter chalcopyrite comparing with pyrite.



Apy decay to lollingite?  $\text{Fe}_{2.411}\text{As}_{2.542}\text{S}$

Figure I.4 – Lollingite exsolution from arsenopyrite, with native bismuth in the contact of the arsenic minerals. **a)** Reflected light image of lollingite included in arsenopyrite that is in contact with pyrite. **b)** Detail of a). **c)** Backscattered electrons image of a) with overlap of the laser ablation spots locations present in table 26.

## Calc-silicate sample

Some short notes about particular aspects:

It seems that the fluids flew from two different directions, and where they intersected promoted the deposition/recritalization of native Bi.

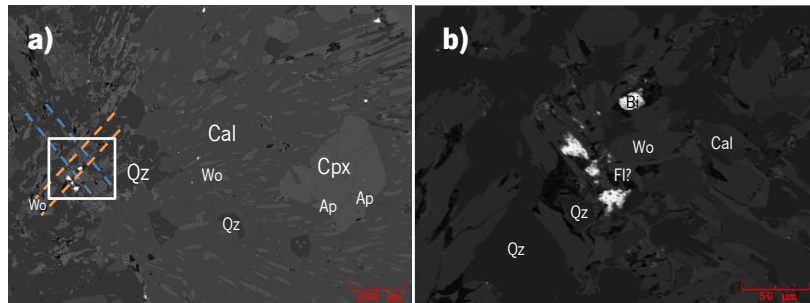


Figure I.5 – High weight minerals in backscattered electrons image. **a)** Backscattered electron images of high weight minerals in a wollastonite, fluorite, quartz matrix. **b)** Detail of a).

## Vesuvianite-fluorite interaction

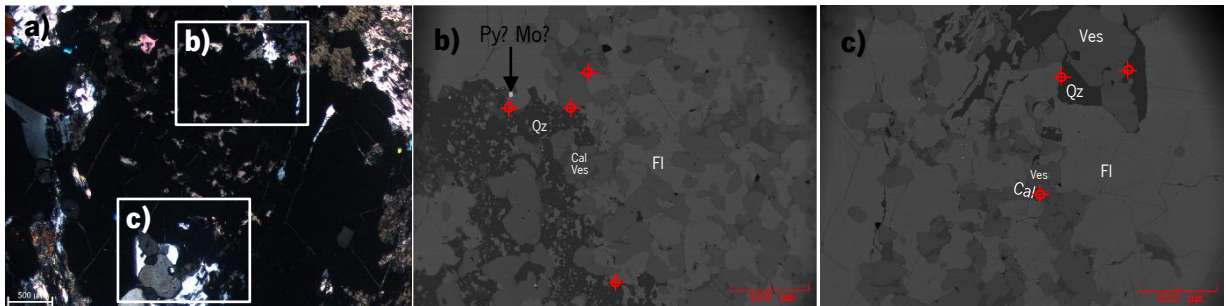


Figure I.6 – Vesuvianite-fluorite interaction. **a)** Transmitted light microscopy (crossed polarizers). **b)** Backscattered electron image of a) detail. **c)** Backscattered electron image of a) detail.

## Apatite

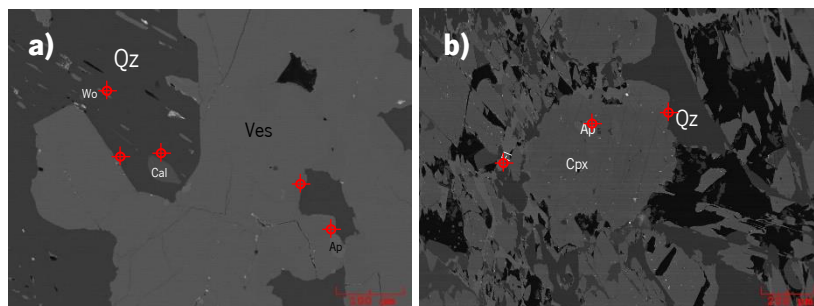


Figure I.7 – Apatite intergrowths. **a)** Apatite included in vesuvianite. **b)** Apatite included in clinopyroxene.

There is the presence of clinopyroxene (diopside). Pyroxene in contact with quartzitic matrix presents hedenbergite (in this zone although it was quartzous, some fluorite content was also found). In yet another reaction zone between quartz and fluorite, it was possible to verify a type of reactional texture. In this sector there was the presence of zoned clinopyroxene, but all of it only diopside. In the CEE-5b sample, in the carbonate sector, in calcitic matrix was observed pyroxene, apatite, vesuvianite. Quartz appears to be replacing vesuvianite (?) – CEE-5b. Pyroxene might be later as it including calcite, quartz, fluorite and native Bi.

### Wollastonite intergrowths

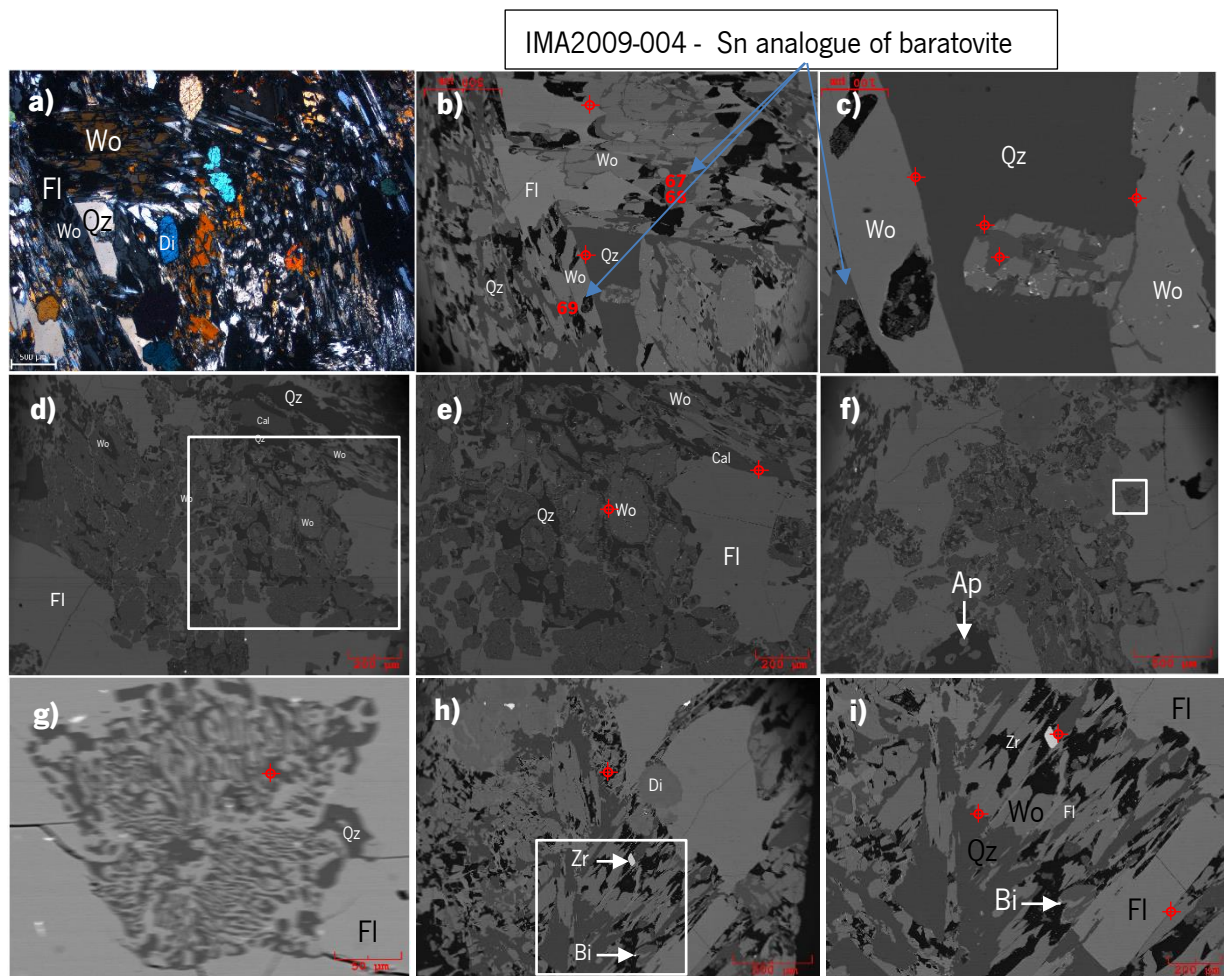


Figure 1.8 – Wollastonite intergrowths. **a)** Transmitted light microscopy image (crossed polarizers) wollastonite with allongated aspect. **b)** Backscattered electrons image of a). **c)** Detail of b). **d)** “Wollastonite mixture” latter than the wollastonite crystals in a quartz-fluorite matrix. **e)** Detail of d). **f)** Sector of quartz- fluorite reaction. **g)** Detail of f). **h)** Zircon and native bismuth in calc-silicate sample. **i)** Detail of h).

## Main vesuvianite intergrowths

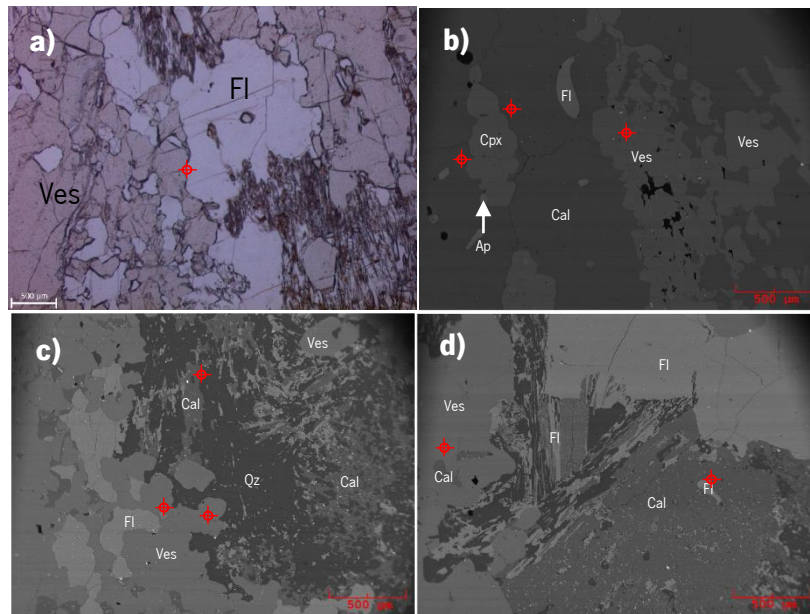


Figure 1.9 – Vesuvianite intergrowths. **a)** Transmitted light microscopy image (crossed polarizers) of vesuvianite intergrown with fluorite. **b)** Backscattered electrons image of vesuvianite included in a calcitic matrix. **c)** Vesuvianite intergrown with fluorite and quartz. **d)** Vesuvianite intergrown with calcite and fluorite.



## ANNEX II – COMPOSITIONS OF THE DIVERSE MINERALS APPLIED AS GEO THERMOMETERS (MICROPROBE DATA)

Table II.1– Microprobe analysis of the chlorites in C2 sample.

	Na <sub>2</sub> O	MgO	K <sub>2</sub> O	CaO	TiO <sub>2</sub>	FeO	MnO	P <sub>2</sub> O <sub>5</sub>	SiO <sub>2</sub>	Al <sub>2</sub> O <sub>3</sub>	Total
<b>C2-1</b>	0.07	7.71	1.29	0.06	1.13	30.02	0.99	0.00	28.80	18.04	88.10
<b>C2-2</b>	0.00	8.13	2.08	0.01	0.42	27.67	1.11	0.00	25.66	20.69	85.78
<b>C2-3</b>	0.15	9.12	2.57	0.07	0.23	27.11	0.96	0.02	28.21	19.86	88.29
<b>C2-4</b>	0.09	8.98	0.04	0.01	0.08	31.07	1.20	0.00	23.24	22.03	86.74
<b>C2-5</b>	0.00	7.72	0.06	0.03	0.13	31.85	1.22	0.03	23.84	22.61	87.49
<b>C2-6</b>	0.04	7.58	0.06	0.05	0.05	31.87	1.52	0.01	23.49	22.71	87.37
<b>C2-7</b>	0.00	7.65	0.01	0.00	0.05	32.40	1.15	0.00	23.86	22.29	87.41
<b>C2-8</b>	0.08	7.91	0.05	0.00	0.09	32.12	1.42	0.00	23.39	22.25	87.30
<b>C2-9</b>	0.04	7.81	0.02	0.01	0.04	33.00	1.26	0.05	23.52	22.49	88.23
<b>C2-10</b>	0.02	7.91	0.02	0.02	0.08	33.16	1.17	0.07	23.50	22.75	88.68
<b>C2-11</b>	0.03	8.29	0.02	0.03	0.10	31.41	1.34	0.19	23.62	22.64	87.67
<b>C2-12</b>	0.00	8.36	0.01	0.04	0.09	31.63	1.13	0.10	23.25	22.62	87.23
<b>C2-13</b>	0.01	8.12	0.00	0.03	0.09	31.97	1.34	0.04	23.67	22.09	87.37
<b>C2-14</b>	0.02	8.15	0.00	0.00	0.12	32.29	1.21	0.04	23.82	22.32	87.99
<b>C2-15</b>	0.01	8.06	0.00	0.01	0.05	32.04	1.34	0.05	23.56	22.88	88.00
<b>C2-16</b>	0.06	7.61	0.01	0.01	0.14	32.50	1.43	0.27	23.53	22.30	87.87
<b>C2-17</b>	0.01	10.15	0.00	0.00	0.04	30.05	0.75	0.00	26.28	20.20	87.49
<b>C2-18</b>	0.01	7.57	0.00	0.03	0.07	31.68	1.34	0.01	19.95	21.59	82.24
<b>C2-19</b>	0.05	7.77	0.01	0.00	0.01	31.78	1.35	0.06	19.68	21.08	81.79
<b>C2-20</b>	0.03	10.13	0.03	0.03	0.05	29.99	0.93	0.00	25.80	21.00	88.00
<b>C2-21</b>	0.00	9.21	0.09	0.01	0.09	31.31	0.83	0.00	25.69	20.57	87.80
<b>C2-22</b>	0.03	7.76	0.01	0.00	0.07	32.11	1.37	0.04	23.48	22.77	87.64
<b>C2-23</b>	0.06	7.70	0.02	0.01	0.04	32.34	1.39	0.00	23.67	22.43	87.67
<b>C2-24</b>	0.04	9.63	0.03	0.00	0.00	29.88	0.74	0.00	25.82	20.99	87.14

Table II.2 – A.p.f.u. calculation of the chlorites in C2 sample (data obtained by microprobe analysis).

Samples	tetrahedral		octahedral									Total	VI Total	Fe/Fe+Mg	Si/Al <sup>IV</sup>	Ca+K+N	K. & M. (1987)		Z. & F. (1995)	
	Si	Al <sup>IV</sup>	Al <sup>VI</sup>	Ti	Fe <sup>3+</sup>	Fe <sup>2+</sup>	Mn	Mg	Ca	Na	K						Al <sup>IV</sup> <sub>cor</sub>	T (°C)	Al <sup>IV</sup> <sub>cor</sub>	T (°C)
<b>C2-1</b>	6.13	1.87	2.72	0.18	0.51	4.83	0.18	2.44	0.01	0.06	0.70	19.63	11.63	0.69	3.27	0.77	2.35	267.52	1.57	184.34
<b>C2-2</b>	5.62	2.38	3.04	0.07	0.18	4.89	0.21	2.65	0.00	0.00	1.16	20.21	12.21	0.66	2.36	1.17	2.84	318.85	2.10	240.64
<b>C2-3</b>	5.94	2.06	2.95	0.04	0.20	4.58	0.17	2.86	0.02	0.12	1.38	20.30	12.30	0.63	2.88	1.52	2.50	283.00	1.81	210.02
<b>C2-4</b>	5.16	2.84	2.92	0.01	0.03	5.73	0.22	2.97	0.00	0.08	0.02	19.99	11.99	0.66	1.81	0.10	3.31	368.54	2.56	289.70
<b>C2-5</b>	5.23	2.77	3.10	0.02	0.20	5.65	0.23	2.53	0.01	0.00	0.03	19.76	11.76	0.70	1.89	0.04	3.26	363.22	2.45	277.99
<b>C2-6</b>	5.18	2.82	3.10	0.01	0.15	5.73	0.28	2.49	0.01	0.03	0.03	19.84	11.84	0.70	1.84	0.08	3.31	369.00	2.50	283.10
<b>C2-7</b>	5.26	2.74	3.06	0.01	0.18	5.79	0.22	2.51	0.00	0.00	0.00	19.77	11.77	0.70	1.92	0.00	3.24	361.07	2.42	274.92
<b>C2-8</b>	5.18	2.82	2.99	0.02	0.09	5.86	0.27	2.61	0.00	0.07	0.03	19.92	11.92	0.69	1.83	0.10	3.31	368.88	2.51	284.21
<b>C2-9</b>	5.17	2.83	3.00	0.01	0.09	5.97	0.23	2.56	0.00	0.03	0.01	19.90	11.90	0.70	1.82	0.04	3.33	370.47	2.51	284.37
<b>C2-10</b>	5.14	2.86	3.01	0.01	0.09	5.97	0.22	2.58	0.00	0.01	0.01	19.90	11.90	0.70	1.79	0.03	3.36	373.68	2.55	287.87
<b>C2-11</b>	5.18	2.82	3.06	0.02	0.14	5.62	0.25	2.71	0.01	0.02	0.01	19.84	11.84	0.68	1.84	0.04	3.29	367.05	2.52	284.86
<b>C2-12</b>	5.13	2.87	3.03	0.02	0.11	5.73	0.21	2.75	0.01	0.00	0.01	19.87	11.87	0.68	1.79	0.02	3.34	372.23	2.57	290.09
<b>C2-13</b>	5.22	2.78	2.98	0.01	0.13	5.77	0.25	2.67	0.01	0.01	0.00	19.84	11.84	0.69	1.88	0.02	3.26	363.23	2.47	279.68
<b>C2-14</b>	5.22	2.78	3.00	0.02	0.13	5.78	0.22	2.66	0.00	0.02	0.00	19.84	11.84	0.69	1.87	0.02	3.27	364.13	2.47	280.34
<b>C2-15</b>	5.16	2.84	3.07	0.01	0.13	5.73	0.25	2.63	0.00	0.01	0.00	19.84	11.84	0.69	1.81	0.01	3.33	370.57	2.53	286.63
<b>C2-16</b>	5.19	2.81	3.01	0.02	0.13	5.87	0.27	2.51	0.00	0.05	0.01	19.86	11.86	0.71	1.85	0.06	3.30	367.77	2.48	281.34
<b>C2-17</b>	5.67	2.33	2.82	0.01	0.28	5.14	0.14	3.26	0.00	0.01	0.00	19.65	11.65	0.62	2.43	0.01	2.77	311.81	2.08	238.97
<b>C2-18</b>	4.74	3.26	2.82	0.01	0.00	6.47	0.27	2.68	0.01	0.00	0.00	20.27	12.27	0.71	1.45	0.01	3.76	416.13	2.94	329.41
<b>C2-19</b>	4.70	3.30	2.70	0.00	0.00	6.62	0.27	2.77	0.00	0.05	0.01	20.41	12.41	0.70	1.43	0.06	3.79	419.72	2.98	333.37
<b>C2-20</b>	5.54	2.46	2.88	0.01	0.23	5.15	0.17	3.24	0.01	0.02	0.02	19.73	11.73	0.62	2.25	0.05	2.90	325.23	2.21	252.42
<b>C2-21</b>	5.57	2.43	2.85	0.01	0.24	5.44	0.15	2.98	0.00	0.00	0.05	19.72	11.72	0.66	2.29	0.05	2.89	324.25	2.15	246.10
<b>C2-22</b>	5.17	2.83	3.08	0.01	0.14	5.76	0.26	2.54	0.00	0.03	0.01	19.83	11.83	0.70	1.82	0.03	3.32	370.32	2.52	284.97
<b>C2-23</b>	5.21	2.79	3.05	0.01	0.13	5.82	0.26	2.53	0.00	0.05	0.01	19.85	11.85	0.70	1.87	0.06	3.28	365.82	2.47	279.95
<b>C2-24</b>	5.58	2.42	2.96	0.00	0.29	5.12	0.13	3.10	0.00	0.04	0.02	19.66	11.66	0.64	2.31	0.06	2.86	321.46	2.16	246.79

Table II.3 – Calculations of this study arsenopyrites.

Sample	Mineral Assemblage	Wt. %			At. %			a.p.f.u.		
		Fe	As	S	Fe	As	S	Fe	As	S
Asp A	<b>Apy + Po</b> ( $\pm$ Ilm $\pm$ Po $\pm$ Ap $\pm$ Zr inclusions)	34.67	48.66	18.75	33.42	34.95	31.48	1.06	1.11	1.00
Asp B	<b>Apy + Po</b> ( $\pm$ Po $\pm$ Ccp inclusions)	34.68	48.68	18.88	33.33	34.87	31.60	1.05	1.10	1.00
Asp C	<b>Apy + Po</b> + Bt $\pm$ ferb ( $\pm$ Spn $\pm$ Ilm $\pm$ Sch inclusions)	35.05	48.37	18.95	33.62	34.59	31.66	1.06	1.09	1.00
Asp D	Apy + Bt + Sch ( $\pm$ Spn $\pm$ Ilm inclusions)	34.89	48.56	18.71	33.62	34.88	31.40	1.07	1.11	1.00
Asp E	<b>Apy</b> + Bt ( $\pm$ <b>Po</b> inclusion)	34.99	48.71	18.77	33.60	34.87	31.39	1.07	1.11	1.00
Asp F	<b>Apy + Po</b> + Bt ( $\pm$ <b>Po</b> inclusion)	34.97	48.58	18.77	33.61	34.80	31.42	1.07	1.11	1.00
CWW-3A-1-ASPjuntaoAu	<b>Apy + Py</b> ( $\pm$ electrum (close))	34.18	48.02	18.75	33.25	34.82	31.77	1.05	1.10	1.00
CWW-3A-2-ASPjuntaoAu+afastado	<b>Apy + Py</b> ( $\pm$ electrum (distant))	34.28	47.92	19.14	33.11	34.51	32.20	1.03	1.07	1.00
CWW-3A-7-ASPemcontactoomLollingite-ASP	<b>Apy</b> + Py ( $\pm$ <b>lol</b> inclusion)	34.63	48.55	18.44	33.27	34.84	31.79	1.08	1.13	1.00
CWW-3A-8-ASPemcontactocomPo-ASP	<b>Apy</b> + Py ( $\pm$ <b>Po</b> inclusion)	33.84	50.22	17.33	33.24	36.77	29.66	1.12	1.24	1.00
CWW-3A-14	<b>Apy</b> + Ap + Pl ( $\pm$ <b>Po</b> inclusion)	34.16	48.97	18.20	33.30	35.58	30.90	1.08	1.15	1.00
CWW-3A-11ASPemcontactocomPo&Chalcopyrite-ASP	<b>Apy</b> + Py + Ap + Ilm + Spn + Rt + Ab ( $\pm$ <b>Po</b> $\pm$ Ccp inclusions)	34.57	48.54	19.00	33.23	34.78	31.80	1.04	1.09	1.00
CWW-3A-10	<b>Apy</b> + Py + ( $\pm$ <b>lol</b> + Native Bi + Ap inclusions)	34.17	48.48	18.66	33.17	35.08	31.56	1.05	1.11	1.00
CWW-3A-6-ASP	<b>Apy</b> + Py + Ab ( $\pm$ <b>Py</b> inclusion)	34.68	47.41	19.48	33.33	33.97	32.62	1.02	1.04	1.00
A	<b>Apy + Py</b> + Qz + Stp	35.01	47.98	19.07	33.64	34.37	31.92	1.05	1.08	1.00
B	<b>Apy + Py</b> + Qz ( $\pm$ native Bi + Qz + Sch inclusions)	34.87	47.49	18.91	33.75	34.26	31.88	1.06	1.07	1.00
C1	Apy + Sch	34.87	48.52	18.17	33.92	35.18	30.79	1.10	1.14	1.00
C	<b>Apy</b> + Py + Qz ( $\pm$ <b>Po</b> + Qz inclusions)	35.10	47.45	18.89	33.93	34.19	31.81	1.07	1.07	1.00
D	<b>Apy</b> + Py + Qz ( $\pm$ <b>lol</b> + Sch + Qz + native Bi)	34.63	48.55	18.44	33.58	35.10	31.15	1.08	1.13	1.00
E	<b>Apy</b> + Py + Qz + Stp ( $\pm$ <b>Po</b> inclusions)	35.00	48.06	18.85	33.70	34.50	31.63	1.07	1.09	1.00

Table II.5 – Atomic percentage calculations of the shear zone Argas-Cerquido-Serra de Arga and shear zone networking in Serra de Arga Silurian Terrains, obtained by electron microprobe. (Data from Araújo & Leal Gomes (2014) and Leal Gomes et al. (2015).)

Table II.4 – Calculations of Leal Gomes (1994) arsenopyrites (a.p.f.u.).

	As	Fe	S	As	Fe	S
a	1.00	1.01	1.02	34.43	33.46	32.11
b	1.00	1.10	1.22	33.35	33.70	32.95
b	1.00	1.12	1.23	31.26	33.57	35.17
c	1.00	1.12	1.25	31.09	32.32	36.59
c	1.00	1.09	1.26	31.29	32.40	36.31
c	1.00	1.11	1.23	30.94	32.31	36.74
d	1.00	1.13	1.25	29.69	34.07	36.24
e	1.00	1.14	1.32			

## ANNEX III – TRACE-ELEMENTS CONCENTRATIONS OF THE DIVERSE MINERALS (L.A.-I.C.P.-M.S. DATA)

Table III.1 –Sulphides trace elements contents.

Samples		<sup>55</sup> Mn	<sup>59</sup> Co	<sup>60</sup> Ni	<sup>63</sup> Cu	<sup>66</sup> Zn	<sup>95</sup> Mo	<sup>107</sup> Ag	<sup>115</sup> In	<sup>118</sup> Sn	<sup>121</sup> Sb	<sup>128</sup> Te	<sup>182</sup> W	<sup>197</sup> Au	<sup>208</sup> Pb	<sup>209</sup> Bi	
Pyrite	090_CW05n-1-pyrite-1 & 091_CW05n-1-pyrite-2 & 092_CW05n-1	0.55	21.96	48.44	0.02	0.82	0.23	0.19	0.00	0.05	0.06	0.12	1949.76	0.00	0.51	0.29	
	109_CW05n-8-pyrite-1 & 110_CW05n-8-pyrite-2 & 111_CW05n-8	5.51	20.53	44.37	0.38	3.37	0.12	0.34	0.00	0.27	0.02	0.00	0.12	0.02	0.88	3.46	
	112_CW05n-9-pyrite-1 & 116_CW05n-9-pyrite-2 & 117_CW05n-9	11.65	18.70	43.80	0.14	2.24	0.18	0.37	0.01	0.98	0.20	0.17	2191.01	0.01	7.06	1.37	
	121_CW05n-12-pyrite-2 & 122_CW05n-12-pyrite-1	4.48	20.14	51.24	0.06	3.32	0.18	0.60	0.00	0.11	0.06	0.00	6.44	0.00	2.46	1.07	
	123_CW05n-14-pyrite-1 & 124_CW05n-14-pyrite-2 & 126_CW05	1.98	49.57	98.69	0.50	4.97	0.25	0.38	0.00	0.05	0.13	0.13	948.86	0.00	0.63	2.32	
	127_CW05n-15-pyrite-1 & 128_CW05n-15-pyrite-2	1.08	14.65	29.24	0.24	2.11	0.30	0.16			0.06	0.05	0.02	988.53	0.01	1.38	1.38
	132_CW05n-18-pyrite-1 & 133_CW05n-18-pyrite-2 & 134_CW05	0.16	14.27	28.43	0.38	1.61	0.22	0.32			0.07	0.12	0.17	351.20	0.00	0.47	0.32
	172_CWW3A-3-1 & 173_CWW3A-3-2	0.53	4.48	45.28	6.42	1.46	0.16	0.79	0.00	0.06	0.19	0.13	655.37	0.00	3.28	0.48	
	184_CW05-11-1 & 185_CW05-11-2	3.79	2.66	15.92	20.16	1.41	0.17	0.72			0.36	1.04	0.16	2646.43	0.02	3.89	57.10
	098_CW05n-3-pyrrhotite-1 & 099_CW05n-3-pyrrhotite-2	1.29	19.10	37.56	0.05	1.12	0.23	0.82	0.00	0.22	0.16	0.06	5.22	0.00	2.35	1.49	
Pyrrhotite	106_CW05n-7pyrrhotite-1 & 107_CW05n-7pyrrhotite-2 & 108_C	1.26	18.43	37.05	0.42	0.52	0.13	0.13	0.02	0.19	0.03	0.00	0.06	0.00	1.35	0.28	
	120_CW05n-13pyrrhotite	3.84	27.08	50.04	0.35	0.72	1.20	0.49	0.05	0.00	0.21	0.40	0.16	0.00	0.79	0.46	
	144_C2-1-1-pyrrhotite & 145_C2-1-2-pyrrhotite	0.62	8.14	34.15	0.00	0.46	0.41	0.37	0.00	0.06	0.04	0.27	0.03	0.00	0.35	0.30	
	146_C2-1-3-pyrrhotite & 147_C2-1-4-pyrrhotite	0.65	8.22	31.31	0.03	0.59	0.16	0.69	0.00	0.16	0.29	0.08	0.02	0.00	0.58	0.78	
	148_C2-2-1-pyrrhotite & 149_C2-2-2	0.25	7.34	34.39	0.11	0.71	0.32	0.43	0.00	0.10	0.02	0.00	0.00	0.00	0.11	0.34	
	153_C2-3-1 & 154_C2-3-2	0.31	6.32	30.88	0.08	0.62	0.25	0.23	0.00	0.11	0.12	0.09	0.00	0.00	0.38	0.31	
	158_C2-6-1-pyrrhotite & 160_C2-6-2-pyrrhotite	0.95	15.61	33.63	0.10	1.06	0.53	2.07	0.06	0.37	4.71	0.00	0.58	0.04	4.66	14.40	
	165_C2-8-1 & 166_C2-8-2	0.57	8.52	34.03	0.28	0.84	0.21	0.52	0.01	0.18	0.05	0.46	0.00	0.00	0.58	0.67	
	174_CWW3A-3-3	0.00	6.62	56.95	17.36	5.54	0.26	6.23	0.00	0.45	0.00	1.03	770.86	0.00	5.35	1.05	
	177_CWW3A-8-1	34.62	5.22	41.87	3.83	0.00	0.46	1.49	0.11	0.75	2.87	0.00	0.00	0.00	48.46	19.55	
Arsenopyrite	193_CW05-4-1-asp & 194_CW05-4-2-asp	1.68	407.16	220.55	3.80	0.49	0.33	0.57	0.40	0.12	64.84	6.29	1.48	0.18	0.80	1543.57	
	198_CW05-18-1 & 199_CW05-18-2	0.28	312.60	54.89	0.40	0.46	0.01	0.02	0.32	0.08	52.95	0.65	2.51	0.01	0.30	15.52	
	201_CW05-17-1 & 202_CW05-17-2	1.91	383.46	79.91	2.35	0.59	0.04	0.21	0.33	0.06	65.34	0.42	1.54	0.00	0.27	44.58	
	203_CW05-14-1 & 204_CW05-14-2	0.97	355.67	356.15	0.23	0.65	1.69	0.18	0.44	0.24	96.14	1.06	0.04	3.00	0.38	262.20	
	212_C2-3-1-AspC & 213_C2-3-2-AspC	0.16	680.14	110.58	0.06	0.33	0.44	0.05	0.33	0.07	65.49	0.26	0.00	0.00	0.07	0.95	
	210_C2-1-1AspA & 211_C2-1-2AspA	0.17	620.22	150.34	0.00	0.35	0.23	0.06	0.31	0.12	73.76	0.30	0.00	0.01	0.19	8.02	
	214_C2-AspD-1 & 215_C2-AspD-2	0.09	684.99	129.84	0.07	0.35	0.15	0.05	0.32	0.09	65.22	0.31	0.00	0.00	0.02	0.79	
	216_C2-AspE-1 & 217_C2-AspE-2	0.13	661.49	110.41	0.01	0.33	0.10	0.06	0.26	0.13	63.82	0.46	0.09	0.00	0.34	0.54	
	218_C2-AspF-1 & 219_C2-AspF-2 & 220_C2-AspF-3	0.10	756.15	109.10	0.06	0.23	0.03	0.04	0.33	0.04	68.17	0.13	0.00	0.00	0.07	0.42	
	232_CWW-3a-2-1 & 233_CWW-3a-2-2	0.13	1115.88	120.21	0.21	0.26	0.03	0.07	0.35	0.03	41.62	0.76	0.48	0.00	0.06	0.58	
234_CWW-3a-2-1 & 235_CWW-3a-2-2	0.00	1052.48	80.59	0.03	0.28	0.01	0.09	0.35	0.10	80.93	0.56	0.01	0.00	0.12	0.66		
236_CWW-3a-8-1asp & 237_CWW-3a-8-2asp	0.16	1306.56	293.72	0.00	0.35	0.13	0.08	0.34	0.07	52.19	0.98	0.00	0.02	0.07	1.22		
239_CWW-3A-14-1 & 240_CWW-3A-14-2	0.06	849.67	204.40	0.01	0.30	0.05	0.07	0.34	0.06	49.66	1.02	0.00	0.01	0.04	0.54		

Table III.2 – Scheelite trace elements contents.

<b>Scheelites</b>	<b>Ca (wt.%)</b>	<b><sup>55</sup>Mn</b>	<b><sup>88</sup>Sr</b>	<b><sup>89</sup>Y</b>	<b><sup>93</sup>Nb</b>	<b><sup>95</sup>Mo</b>	<b><sup>139</sup>La</b>	<b><sup>140</sup>Ce</b>	<b><sup>141</sup>Pr</b>	<b><sup>146</sup>Nd</b>	<b><sup>147</sup>Sm</b>	<b><sup>151</sup>Eu</b>	<b><sup>158</sup>Gd</b>	<b><sup>159</sup>Tb</b>	<b><sup>161</sup>Dy</b>	<b><sup>165</sup>Ho</b>	<b><sup>166</sup>Er</b>	<b><sup>169</sup>Tm</b>	<b><sup>172</sup>Yb</b>	<b><sup>175</sup>Lu</b>	<b><sup>181</sup>Ta</b>	<b>Eu/Eu*</b>
1 254_ScheeliteCanto	13.92	151.38	33.64	112.94	306.73	12.84	40.40	79.10	7.53	26.30	5.50	1.15	7.48	1.99	17.66	4.33	13.53	1.96	12.81	1.68	9.39	0.55
2 scheelite-inclusa-em-py	13.92	51.73	14.47	223.90	211.68	34.92	83.55	334.30	52.62	274.87	63.67	2.52	59.68	7.78	44.81	8.31	21.81	2.50	14.24	1.89	3.75	0.13
3 258_Scheelite-inclusa-em-arseno	13.92	49.71	19.84	235.32	204.87	26.12	80.20	264.29	36.22	172.21	41.21	2.78	41.71	6.76	43.99	9.02	25.81	3.38	20.56	2.85	3.31	0.21
4 260_scheelite-asp	13.92	148.44	33.62	60.64	143.34	12.78	10.54	27.82	3.13	13.94	3.59	0.28	4.55	1.04	9.53	2.41	8.53	1.32	8.47	1.20	5.04	0.21
5 263_scheelite-incluir-py+asp-py	13.92	103.07	29.46	109.82	582.21	7.82	75.91	412.33	67.90	339.89	67.00	0.63	49.64	5.26	29.34	5.14	13.38	1.69	9.13	1.25	16.62	0.03
6 264_scheelite-incluir-py+asp-as	13.92	122.78	32.06	83.88	202.81	21.39	27.34	92.19	12.14	54.29	10.57	0.56	11.79	2.18	17.08	3.67	11.93	1.61	10.23	1.50	5.20	0.15
7 333_CEE-5a-scheelite-1	13.92	0.54	593.57	0.48	172.37	445.46	1.86	1.79	0.14	0.33	0.09	0.01	0.04	0.01	0.07	0.01	0.05	0.01	0.06	0.01	1.86	0.73
8 278_scheelite-1	13.92	97.22	45.57	1355.11	437.55	3.41	214.73	758.29	112.64	530.89	142.36	2.23	176.25	30.28	215.43	46.75	131.27	16.14	89.76	11.25	51.38	0.04
9 341_C2-scheelite-1	13.92	83.93	37.96	530.00	272.33	6.88	73.96	346.46	69.74	412.91	161.67	1.02	180.42	24.39	132.89	22.22	49.69	5.24	25.00	2.45	31.62	0.02

Table III.3 – Apatites trace elements contents.

<b>Apatites</b>	<b>Ca (wt.%)</b>	<b><sup>51</sup>V</b>	<b><sup>55</sup>Mn</b>	<b><sup>88</sup>Sr</b>	<b><sup>89</sup>Y</b>	<b><sup>90</sup>Zr</b>	<b><sup>137</sup>Ba</b>	<b><sup>139</sup>La</b>	<b><sup>140</sup>Ce</b>	<b><sup>141</sup>Pr</b>	<b><sup>146</sup>Nd</b>	<b><sup>147</sup>Sm</b>	<b><sup>151</sup>Eu</b>	<b><sup>158</sup>Gd</b>	<b><sup>159</sup>Tb</b>	<b><sup>161</sup>Dy</b>	<b><sup>165</sup>Ho</b>	<b><sup>166</sup>Er</b>	<b><sup>169</sup>Tm</b>	<b><sup>172</sup>Yb</b>	<b><sup>175</sup>Lu</b>	<b><sup>208</sup>Pb</b>	<b><sup>232</sup>Th</b>	<b><sup>238</sup>U</b>	<b>Eu/Eu* (La/Yb)<sub>CN</sub></b>	
1 303_CW05n-apatite-1	39.33	0.06	1978.68	71.25	448.44	0.02	0.08	324.37	655.58	84.68	346.61	63.07	1.85	58.93	8.99	57.07	11.82	34.63	4.86	32.12	4.60	2.41	12.76	7.08	0.09	6.82
2 307_CW05n-apatite-4	39.33	0.20	1565.85	60.00	282.84	0.01	0.10	252.08	506.14	64.64	258.78	46.54	1.55	43.82	6.02	37.79	8.01	24.10	3.30	21.45	3.22	1.92	8.29	4.81	0.10	7.94
3 309_CW05n-apatite-5	39.33	0.34	8055.38	168.39	494.55	0.08	0.42	175.67	526.05	90.08	447.20	111.41	1.85	118.98	16.45	89.65	15.80	38.48	3.97	19.42	2.46	10.75	97.41	45.32	0.05	6.11
4 311_CW05n-apatite-6-1	39.33	0.19	2869.36	108.63	1445.86	0.01	0.41	570.19	1698.47	282.69	1403.00	328.27	3.06	353.63	47.85	258.69	45.83	103.72	9.89	45.04	4.83	4.06	1.97	5.03	0.03	8.55
5 014_CEE-5a-64-4	39.33	1.37	158.47	328.30	29.82	40.20	0.84	12.68	23.54	2.64	14.63	6.40	1.36	7.56	1.07	5.75	1.20	2.40	0.36	1.49	0.21	4.06	2.44	2.68	0.60	5.74
6 325_C2-apatite-4	39.33	0.13	489.72	170.96	35.98	0.04	0.73	18.82	36.19	3.56	15.67	4.25	0.70	3.79	0.69	3.79	0.97	3.10	0.54	2.74	0.49	1.05	1.37	0.99	0.53	4.64

Table III.4 – Wolframite and ferberite trace elements contents.

<b>Wolframite &amp; Ferberite</b>	<b>Fe (wt.%)</b>	<b><sup>139</sup>La</b>	<b><sup>140</sup>Ce</b>	<b><sup>141</sup>Pr</b>	<b><sup>146</sup>Nd</b>	<b><sup>147</sup>Sm</b>	<b><sup>151</sup>Eu</b>	<b><sup>158</sup>Gd</b>	<b><sup>159</sup>Tb</b>	<b><sup>161</sup>Dy</b>	<b><sup>165</sup>Ho</b>	<b><sup>166</sup>Er</b>	<b><sup>169</sup>Tm</b>	<b><sup>172</sup>Yb</b>	<b><sup>175</sup>Lu</b>
1 275_wolframite-1	9.21	4.29	10.65	1.14	5.73	1.13		1.26	0.28	4.84	1.73	10.23	3.01	34.10	5.73
2 276_wolframite-2	9.21	1.60	3.80	0.47	2.54	1.00	0.05	1.35	0.53	6.93	2.49	13.29	3.31	33.29	5.68
3 277_ferberite	18.39	139.36	477.99	64.59	260.82	48.57	1.63	40.86	6.88	49.94	11.46	35.21	5.52	38.96	4.86
4 339_C2-ferberite-1	18.39	84.97	222.13	33.93	169.44	45.91	0.40	35.99	5.90	36.91	6.55	17.45	2.33	14.99	1.95
5 340_C2-ferberite-2	18.39	97.30	242.97	32.67	147.04	31.60	0.27	21.84	3.90	24.13	4.29	12.34	1.78	13.48	1.87

Table III.5 – Vesuvianites trace elements contents.

<b>Vesuvianites</b>	<b>Ca (wt.%)</b>	<b><sup>51</sup>V</b>	<b><sup>53</sup>Cr</b>	<b><sup>139</sup>La</b>	<b><sup>140</sup>Ce</b>	<b><sup>141</sup>Pr</b>	<b><sup>146</sup>Nd</b>	<b><sup>147</sup>Sm</b>	<b><sup>151</sup>Eu</b>	<b><sup>158</sup>Gd</b>	<b><sup>159</sup>Tb</b>	<b><sup>161</sup>Dy</b>	<b><sup>165</sup>Ho</b>	<b><sup>166</sup>Er</b>	<b><sup>169</sup>Tm</b>	<b><sup>172</sup>Yb</b>	<b><sup>175</sup>Lu</b>
1 032_CEE-5a-50	25.69	89.97	46.94	6.86	12.60	1.38	6.49	2.65	0.73	3.38	0.57	3.97	0.94	2.73	0.38	2.41	0.35
2 033_CEE-5a-49	25.49	118.04	13.12	20.17	26.04	2.08	6.78	1.64	0.56	1.74	0.29	1.99	0.42	1.42	0.18	1.54	0.23
3 047_CEE-5a-53a	25.35	107.11	636.43	99.69	213.39	23.78	94.28	17.35	3.04	17.33	2.38	14.18	2.85	7.45	1.01	6.17	0.81
4 061_CEE-5b-7-3	25.35	98.24	0.70	30.65	29.84	1.76	3.52	0.93	0.38	0.83	0.18	1.68	0.43	1.50	0.29	2.20	0.42
5 067_CEE-5b-7-a	25.35	92.28	3.49	20.92	19.49	1.19	3.06	0.57	0.33	0.73	0.15	1.20	0.27	1.08	0.24	1.67	0.32
6 068_CEE-5b-7-b	25.35	117.75	12.03	66.58	112.55	10.59	35.99	7.73	2.38	8.12	1.50	10.80	2.43	7.40	1.08	6.92	1.00
7 069_CEE-5b-7-c	25.35	77.05	33.07	11.05	24.63	3.05	15.77	4.86	1.15	4.22	0.56	3.57	0.62	2.00	0.29	1.67	0.25
8 074_CEE-5a-11a	25.35	72.03	35.32	29.33	49.48	5.15	20.26	4.54	0.93	4.45	0.65	3.74	0.72	1.99	0.26	1.45	0.18
9 075_CEE-5a-11b	25.35	82.42	33.26	34.97	68.43	7.69	29.90	5.55	1.26	4.62	0.65	4.15	0.75	2.12	0.30	1.83	0.23
10 076_CEE-5a-11c	25.35	121.62	22.92	29.45	54.26	6.05	24.09	5.22	1.27	3.83	0.54	3.14	0.55	1.78	0.25	1.71	0.24
11 077_CEE-5a-11d	25.35	93.31	28.61	22.88	39.81	4.24	15.61	3.22	0.80	3.12	0.49	2.83	0.61	1.56	0.21	1.37	0.23
12 078_CEE-5a-11e	25.35	175.58	44.40	324.37	536.65	50.96	174.17	30.12	6.85	30.97	4.68	30.97	6.99	20.05	2.59	16.90	2.28
13 079_CEE-5a-11f	25.35	206.48	98.20	456.94	966.88	94.06	308.82	46.64	10.23	43.04	6.52	41.19	8.53	23.51	3.05	17.53	2.24

Table III.6 – Pyroxene trace elements contents.

<b>Pyroxene</b>	<b>Ca (wt.%)</b>	<b><sup>139</sup>La</b>	<b><sup>140</sup>Ce</b>	<b><sup>141</sup>Pr</b>	<b><sup>146</sup>Nd</b>	<b><sup>147</sup>Sm</b>	<b><sup>151</sup>Eu</b>	<b><sup>158</sup>Gd</b>	<b><sup>159</sup>Tb</b>	<b><sup>161</sup>Dy</b>	<b><sup>165</sup>Ho</b>	<b><sup>166</sup>Er</b>	<b><sup>169</sup>Tm</b>	<b><sup>172</sup>Yb</b>	<b><sup>175</sup>Lu</b>
1 009_CEE-5a-64-1	17.267	0.01	0.01	0.00	0.01	0.05	0.00	0.01	0.00	0.00	0.00	0.00	0.00	0.00	
2 019_CEE-5a-66-1	17.034	0.01	0.02	0.00	0.02	0.03	0.01	0.01	0.00	0.01	0.00	0.01	0.00	0.01	0.01
3 022_CEE-5a-72	17.373	0.01	0.01		0.03	0.02		0.00		0.00	0.00		0.00	0.01	
4 024_CEE-5a-24	17.355	0.01	0.01		0.01	0.00			0.00	0.00	0.00	0.00	0.00	0.00	
5 029_CEE-5a-34-2	17.141		0.01	0.00	0.00	0.00	0.01	0.00	0.00			0.00	0.00	0.01	
6 039_CEE-5a-112	17.256	0.03	0.08		0.04	0.03	0.02	0.00	0.00	0.02		0.01	0.00	0.03	0.00
7 041_CEE-5a-97	17.348				0.00	0.08		0.00	1.10	0.00	0.00	0.01	0.00	0.00	0.02
8 044_CEE-5a-108	17.764		0.03		0.02	0.03	0.02	0.03	0.00			0.01	0.01	0.00	0.00
9 046_CEE-5a-78	17.138	0.01	0.01					0.00	0.00	0.01	0.00	0.01	0.00	0.03	0.00
10 066_CEE-5b-130	17.664	0.06			0.00		0.13		0.03		0.01	0.00	0.01	0.00	0.02
11 316_CEE-5a-pyroxene-1	17.138	0.03	0.08	0.01	0.05	0.01	0.02	0.01	0.00	0.01	0.00	0.01	0.00	0.02	0.01
12 318_CEE-5a-pyroxene-inlcusa	17.291	0.03	0.05	0.01	0.02	0.06	0.03	0.01		0.01	0.00	0.00	0.00	0.01	0.02

Table III.7 – Hedenbergite trace elements contents.

<b>Hedenbergite</b>	<b>Ca (wt.%)</b>	<b><sup>139</sup>La</b>	<b><sup>140</sup>Ce</b>	<b><sup>141</sup>Pr</b>	<b><sup>146</sup>Nd</b>	<b><sup>147</sup>Sm</b>	<b><sup>151</sup>Eu</b>	<b><sup>158</sup>Gd</b>	<b><sup>159</sup>Tb</b>	<b><sup>161</sup>Dy</b>	<b><sup>165</sup>Ho</b>	<b><sup>166</sup>Er</b>	<b><sup>169</sup>Tm</b>	<b><sup>172</sup>Yb</b>	<b><sup>175</sup>Lu</b>
13 028_CEE-5a-34-1	17.141	0.01	0.00		0.02	0.01		0.00	0.00		0.00			0.01	
14 040_CEE-5a-101	17.189	0.01	0.02	0.02	0.05	0.00	0.03		0.00		0.00	0.03	0.01	0.02	0.01
15 045_CEE-5a-111	16.773	0.03	0.07		0.12		0.00	0.00	0.01	0.00		0.02	0.00	0.00	0.02
16 065_CEE-5b-128	16.993		0.01		0.16	0.27					0.04		0.00	0.04	

Table III.8 – Wollastonite trace elements contents.

<b>Wollastonite</b>	<b>Ca (wt.%)</b>	<b><sup>139</sup>La</b>	<b><sup>140</sup>Ce</b>	<b><sup>141</sup>Pr</b>	<b><sup>146</sup>Nd</b>	<b><sup>147</sup>Sm</b>	<b><sup>151</sup>Eu</b>	<b><sup>158</sup>Gd</b>	<b><sup>159</sup>Tb</b>	<b><sup>161</sup>Dy</b>	<b><sup>165</sup>Ho</b>	<b><sup>166</sup>Er</b>	<b><sup>169</sup>Tm</b>	<b><sup>172</sup>Yb</b>	<b><sup>175</sup>Lu</b>
17 012_CEE-5a-61	33.988	0.02	0.03	0.01	0.02	0.00	0.01	0.00	0.01	0.03	0.01	0.02	0.01	0.09	0.02
18 013_CEE-5a-62	33.843	0.04	0.04		0.04		0.02	0.03	0.01	0.07	0.02	0.11	0.02	0.25	0.05
19 018_CEE-5a-60	34.031	0.09	0.15	0.01	0.08	0.06	0.02	0.04	0.02	0.25	0.09	0.37	0.07	0.82	0.19
20 027_CEE-5a-31	33.984									0.04		0.16		0.13	0.00
21 034_CEE-5a-52	34.069	0.04	0.04	0.00	0.01	0.02	0.02	0.01	0.01	0.02	0.01	0.05	0.02	0.19	0.03
22 042_CEE-5a-102	33.817	0.07	0.11	0.03	0.00		0.04	0.03	0.02	0.09	0.03	0.18	0.04	0.51	0.08
23 043_CEE-5a-102	33.817	0.14	0.30	0.03	0.19	0.05	0.03	0.02	0.01	0.07	0.03	0.11	0.02	0.20	0.03

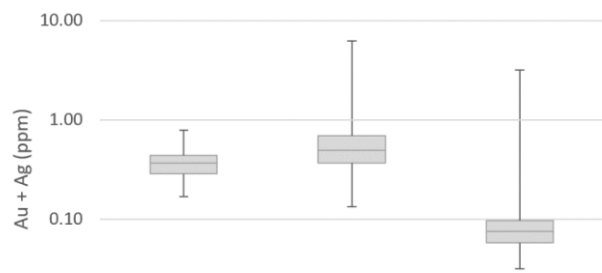


Figure I.1 – Boxplot and whisker of Au, Ag and Bi in the three different sulphide minerals. Boxplot and respective whiskers of Au L.A.-I.C.P.-M.S. measurements in three sulphides.

## ANNEX IV – LOCATION OF L.A.-I.C.P.-M.S. MEASUREMENTS

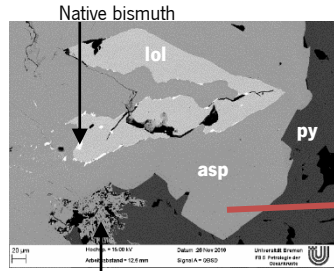
Table IV.1 – Location and respective Fe wt. % applied to each arsenopyrite crystal.

	Code	Color	Fe wt. %	Local	image
1	193_CW05-4-1-asp & 194_CW05-4-2-asp	<b>black</b>	34.627	With lollingite and scheelite (?) inclusions	
2	198_CW05-18-1 & 199_CW05-18-2	<b>black</b>	34.995	With included pyrrhotite	
3	201_CW05-17-1 & 202_CW05-17-2	<b>black</b>	35.005	Without inclusions	
4	203_CW05-14-1 & 204_CW05-14-2	<b>black</b>	34.871	arsenopyrite with Qz and included Bi	
5	210_C2-1-1AspA & 211_C2-1-2AspA	<b>red</b>	34.673	Included in pyrrhotite, with inclusions of ilmenite and pyrrhotite,	



				apatite and zircon.	
6	212_C2-3-1-AspC & 213_C2-3-2-AspC	red	35.047	With inclusions of pyrrhotite, titanite, and ilmenite.	
7	214_C2-AspD-1 & 215_C2-AspD-2	red	34.893	With inclusions of ilmenite and sphene.	
8	216_C2-AspE-1 & 217_C2-AspE-2	red	34.991	With pyrrhotite inclusions	
9	218_C2-AspF-1 & 219_C2-AspF-2 & 220_C2-AspF-3	red	34.973	With pyrrhotite inclusion	
10	232_CWW-3a-2-1	brown	34.276		

11	233_CWW-3a-2-2	<b>brown</b>	34.176		<p>233_CWW-3A-2-2</p>
12	234_CWW-3A-2-1 & 235_CWW-3A-2-2	<b>brown</b>	34.675	With pyrrhotite inclusions	<p>176_CWW-3A-6-2 175_CWW-3A-6-1</p> <p>235_CWW-3A-6-2</p> <p>234_CWW-3A-6-1</p>
13	236_CWW-3a-8-1asp & 237_CWW-3a-8-2asp	<b>brown</b>	33.841	With inclusions of pyrrhotite and apatite, bismuth and lollingite	<p>236_CWW-3A-8-1-asp</p> <p>237_CWW-3A-8-2-asp</p>
14	239_CWW-3A-14-1 & 240_CWW-3A-14-2	<b>brown</b>	34.164	With inclusion of pyrrhotite	<p>albite (?)</p> <p>ortoclase</p> <p>239_CWW-3A-14-1</p> <p>240_CWW-3A-14-2</p>
15	241_CWWA-7-1	<b>brown</b>	34.356	With lollingite and bismuth inclusion	<p>241_CWW-3A-7-1</p> <p>Native bismuth</p> <p>asp</p> <p>ASP decay to lollingite? <math>Fe_{2.41}As_{2.543}S</math></p>

16	242_CWWA-7-2	<b>brown</b>	34.356	With lollingite and bismuth inclusion	 <p>Native bismuth lol asp py</p> <p>20 µm Hochsp. = 10.00 kV Datum: 28 Nov 2016 Universität Bremen Abt. Erdwissenschaften FB 9 Petologie der Ozeantruste</p> <p>ASP decay to lollingite? <math>Fe_{2.411}As_{2.545}S</math></p>
----	--------------	--------------	--------	---------------------------------------	--

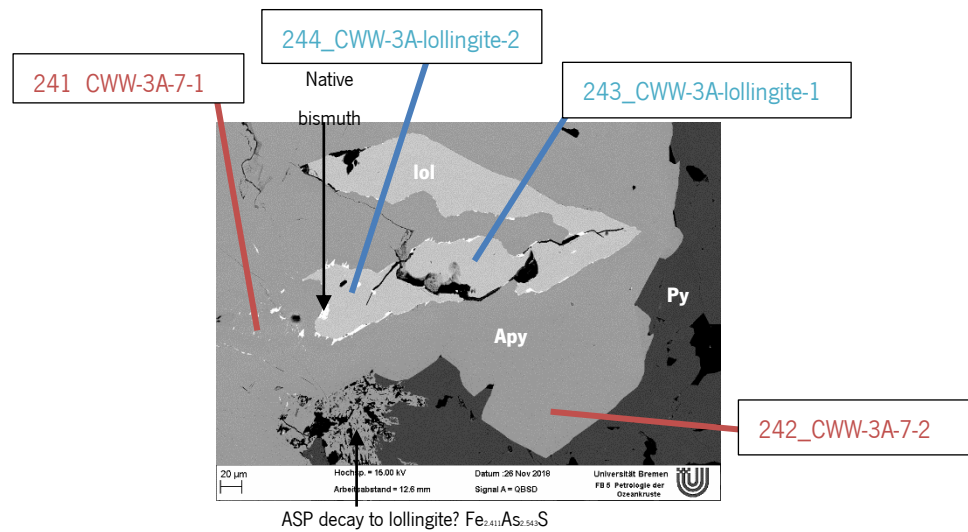


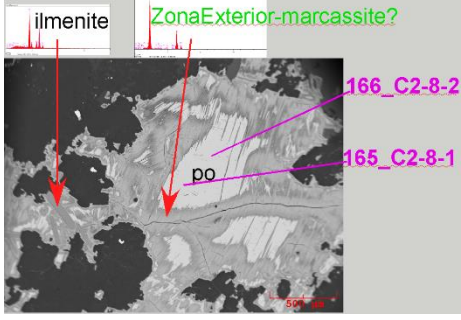
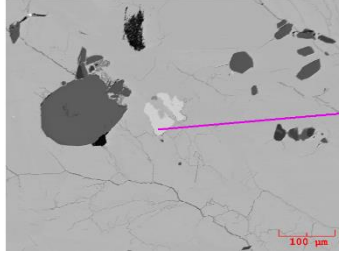
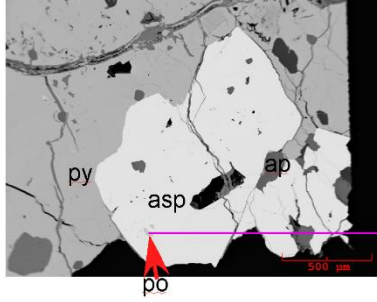
Figure IV.1 – Lollingite exsolution from arsenopyrite, with native bismuth in the contact of the arsenic minerals.

# Pyrrhotite

Table IV.2 – Location and respective Fe wt. % applied to each pyrrhotite crystal.

	Code	Color	Fe wt. %	Local	image
1	098_CW05n-3-pyrrhotite-1 & 099_CW05n-3-pyrrhotite-2	orange	61.407	Outer zone	
2	106_CW05n-7pyrrhotite-1 & 107_CW05n-7pyrrhotite-2 & 108_CW05n-7pyrrhotite-3	orange	61.281	Border zone	
3	120_CW05n-13pyrrhotite	orange	61.349	Border zone; included in pyrite	
4	144_C2-1-1-pyrrhotite & 145_C2-1-2-pyrrhotite	red	61.014		
5	146_C2-1-3-pyrrhotite & 147_C2-1-4-pyrrhotite	red	61.327		

6	148_C2-2-1- pyrrhotite & 149_C2-2-2	red	61.364		
7	153_C2-3-1 & 154_C2-3-2	red	60.644	Included in apyC	
8	155_C2-4-1 & 156_C2-4-2	red	61	Included in apyC	
9	158_C2-6-1- pyrrhotite & 160_C2-6-2- pyrrhotite	red	60.798	Included in apyE	
10	161_C2-7-1 & 162_C2-7-2	red	61		

11	165_C2-8-1 & 166_C2-8-2	<b>red</b>	61.13		 <p>ilmenite    ZonaExterior-marcassite?</p> <p>166_C2-8-2 165_C2-8-1</p> <p>po</p> <p>50 µm</p>
12	174_CWW3A- 3-3	<b>brown</b>	60.198	Included in pyrite matrix	 <p>174_CWW-3A-3-3</p> <p>100 µm</p>
13	177_CWW3A- 8-1	<b>brown</b>	60.329	Included in pyrite	 <p>py    ap</p> <p>asp</p> <p>po</p> <p>177_CWW-3A-8-1</p> <p>500 µm</p>

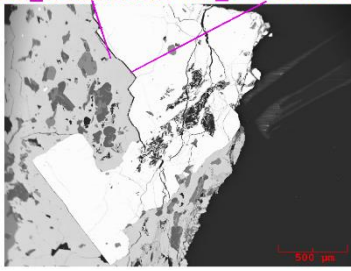
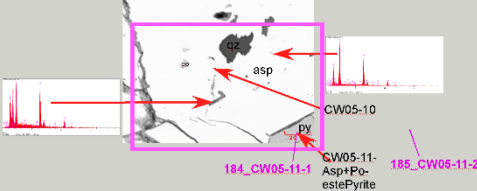
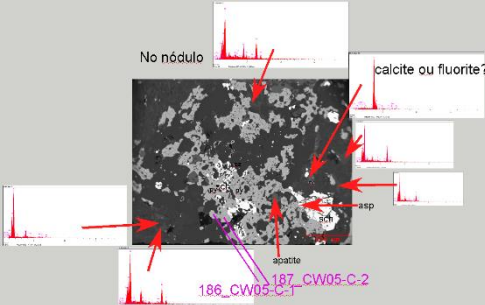
# Pyrite

Table IV.3 – Location and respective Fe wt. % applied to each pyrite crystal.

	Code	Color	Fe wt. %	Local	image
1	090_CW05n-1- pyrite-1 & 091_CW05n-1- pyrite-2 & 092_CW05n-1- pyrite-3	orange	47.553		<p>amphibola? não pode ser muscovite, porque contém Mg</p> <p>Bi</p> <p>CW05n-1-2 CW05n-1-3 pyrite CW05n-1</p> <p>Pyrrhotite</p> <p>Qz</p> <p>Fe</p> <p>CW05n-1-1</p>
2	109_CW05n-8- pyrite-1 & 110_CW05n-8- pyrite-2 & 111_CW05n-8- pyrite-3	orange	43.341		<p>Fe oxide</p> <p>py</p> <p>pyrrhotite</p> <p>labradorite</p> <p>CW05n-8-1 CW05n-8-3 CW05n-8-2</p>
3	112_CW05n-9- pyrite-1 & 116_CW05n-9- pyrite-2 & 117_CW05n-9- pyrite-3	orange	47.573		<p>CW05n-9-3 CW05n-9-1 CW05n-9-2</p> <p>Fe oxides</p> <p>Qz</p> <p>pyrrhotite</p> <p>pyrite</p> <p>apatite</p> <p>galena</p> <p>stilpnomelane</p> <p>labradorite</p> <p>Wante? este tem Au</p>
4	121_CW05n-12- pyrite-2 & 122_CW05n-12- pyrite-1	orange	45.241		<p>pyrite</p> <p>pyrite</p> <p>pyrrhotite</p> <p>122_CW05n-12-1 CW05n-12-2</p> <p>Bi</p> <p>stilpnomelane</p> <p>chalcopyrite</p>

5	123_CW05n-14-pyrite-1 & 124_CW05n-14-pyrite-2 & 126_CW05n-14-pyrite-3	orange	47.853		
6	127_CW05n-15-pyrite-1 & 128_CW05n-15-pyrite-2	orange	47.697		
7	132_CW05n-18-pyrite-1 & 133_CW05n-18-pyrite-2 & 134_CW05n-18-pyrite-3	orange	48.178		
8	172_CWW3A-3-1 & 173_CWW3A-3-2	brown	47.595		
9	175_CWW3A-6-1 & 176_CWW3A-6-2	brown	47.055		



10	178_CWW3A-2-1 & 179_CWW3A-2-2	<b>brown</b>	1		179_CWW-3A-2-2 178_CWW-3A-2-1 
11	184_CW05-11-1 & 185_CW05-11-2	<b>black</b>	47.607		
12	186_CW05-C-1 & 187_CW05-C-2	<b>black</b>	1		

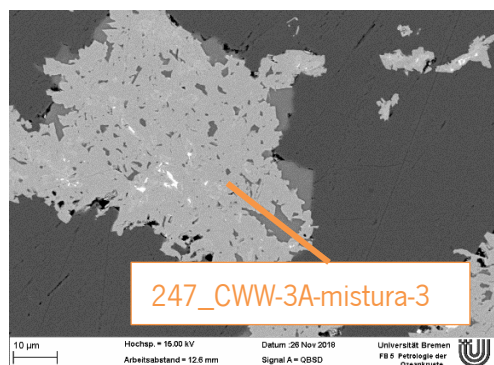
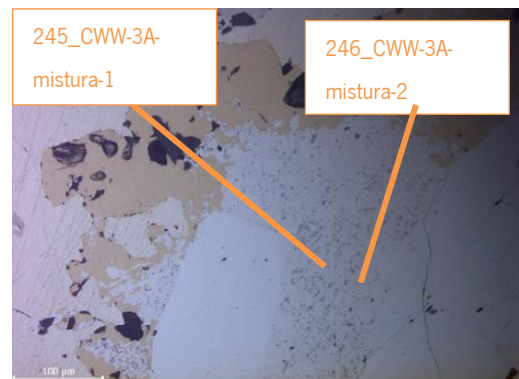
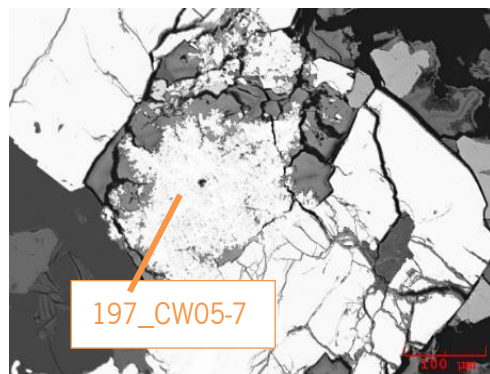


Figure IV.3 – Location and code of *mixed phases* and *mineral cluster* measurement.

Table IV.4 – Location and respective Fe wt. % applied to each *mixture phase* and *mineral cluster*.

	Code	Color	Fe wt. %	Local
1	245_CWW-3A- mistura-1	<b>black</b>	1	CWW-3A
2	246_CWW-3A- mistura-2	<b>black</b>	1	CWW-3A
3	247_CWW-3A- mistura-3	<b>black</b>	33.059	CWW-3A
4	197-CW05-7-mistura	<b>black</b>	57.197	CW05

## ANNEX V – NOTES ABOUT THE GEOLOGICAL SETTING

Regarding NW from Gondwana margin evolution, the scheme that has been affirmed as the most appropriate to explain the structure of these lands, presupposes the opening of an ocean – Rheic – between the NW portion of Gondwana (which included Iberia and Armorica, Cadomian Orogeny) and Avalonia, individualized from Gondwana as a result of the Cambric-Ordovician distension (500-470 Ma) (fig. V.1).

For the evolution of the Ordovician to the Silurian (430-390 M.y.), it is considered that the SE margin of the Rheic Ocean was subducted to which the Paleothetys retro-arc opening is related (Pin *et al.* (2002) and Ribeiro *et al.* (2007)), also referred to as Galicia Central Massif Ocean (OGMC) in Matte (2001). Namelly, the parautochthonous (referred to as the Peritranmontan Domain (Ribeiro, 1974)), comprises metasedimentary sequences from the Superior Ordovician to

the Devonian deposited on the continental, distal, North-Gondwanic margin, with metamorphism equivalent to that observed in the autochthonous (ZCI) and with which manifests paleogeographic correlation (Ribeiro *et al.*, 1990). The strong thickness of the Silurian sequence led to the consideration of the deposition of metasediments in a highly subsidence basin (Farias *et al.*, 1987). Parautochthonous formations, attributed to the Silurian, suggest deposition in confined, low-oxygen, epicontinental basins (Pereira, 1987). From this context, lithologies such as black schists are typical.

As in other situations described in the literature, high alkali metal concentrations, including Li, may be related to endorheic basin volcanism in the early stages of continental rifting. This is the most

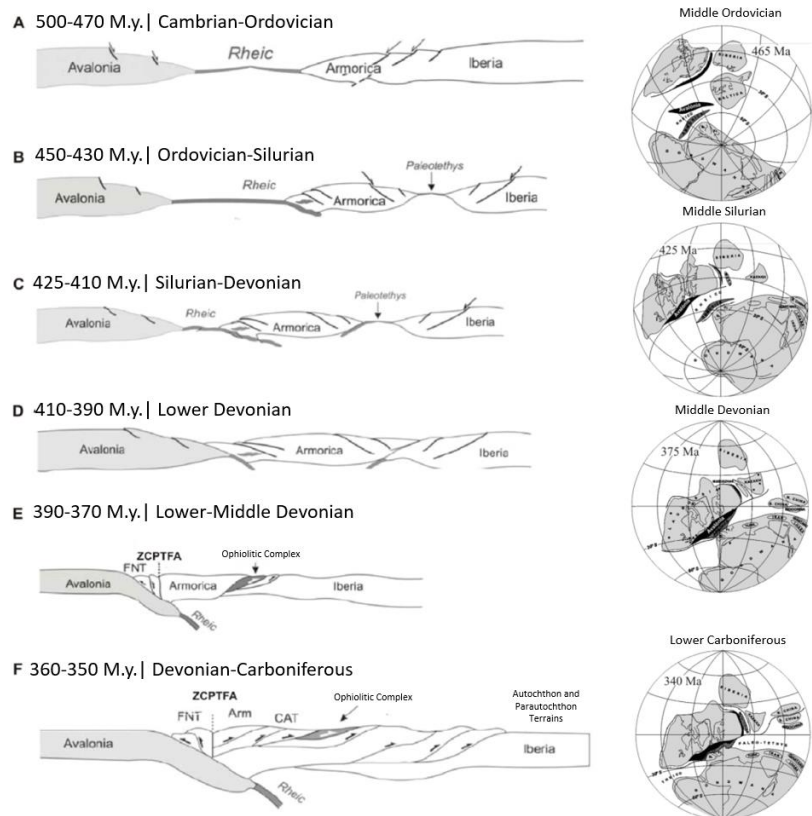


Figure V.1 – Current conception of paleogeography, in the context of the Ordovician to the Carboniferous, of the NW Gondwana margin (modified after Ribeiro *et al.* (2007) e Matte (2001) in Dias (2011)).

likely situation in the Silurian basin for this sector of the Varisca chain, according to petrogenetic arguments, given the set of polygenic lithologies that have been selected for petrographic study by Dias (2011).